CHEMICAL REVIEWS

Review

Cite This: *Chem. Rev.* 2018, 118, 3121−3207

pubs.acs.org/CR

Localized Surface Plasmon Resonance in Semiconductor Nanocrystals

Ankit Agrawal,[†] Shin Hum Cho,[†] Omid Zandi,[†] Sandeep Ghosh,[†] Robert W. Johns,[‡,†] and Delia J. Milliron*[,†]

[†]McKetta Department of Chemical Engineering, The University of Texas at Austin, Austin, Texas 78712, United States

[‡]Department of Chemistry, University of California Berkeley, Berkeley, California 94720, United States

ABSTRACT: Localized surface plasmon resonance (LSPR) in semiconductor nanocrystals (NCs) that results in resonant absorption, scattering, and near field enhancement around the NC can be tuned across a wide optical spectral range from visible to far-infrared by synthetically varying doping level, and post synthetically via chemical oxidation and reduction, photochemical control, and electrochemical control. In this review, we will discuss the fundamental electromagnetic dynamics governing light matter interaction in plasmonic semiconductor NCs and the realization of various distinctive physical properties made possible by the advancement of colloidal synthesis routes to such NCs. Here, we will illustrate how free carrier dielectric properties are induced in various semiconductor materials including metal oxides, metal chalcogenides, metal nitrides, silicon, and other materials. We will highlight the applicability and limitations of the Drude model as applied to semiconductors considering the complex band structures and crystal structures that predominate and quantum effects that emerge at nonclassical sizes. We will also emphasize the impact of dopant hybridization with bands of the host lattice as well as the interplay of shape and crystal structure in determining the LSPR characteristics of semiconductor NCs. To illustrate the discussion regarding both physical and synthetic aspects of LSPR-active NCs, we will focus on metal oxides with substantial consideration also of copper chalcogenide NCs, with select examples drawn from the literature on other doped semiconductor materials. Furthermore, we will discuss the promise that LSPR in doped semiconductor NCs holds for a wide range of applications such as infrared spectroscopy, energy-saving technologies like smart windows and waste heat management, biomedical applications including therapy and imaging, and optical applications like two photon upconversion, enhanced luminescence, and infrared metasurfaces.

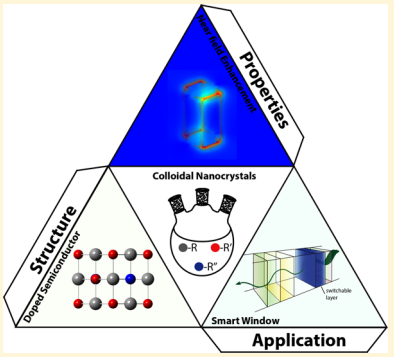

CONTENTS

Special Issue: Plasmonics in Chemistry

Received: October 11, 2017
Published: February 5, 2018

DOI: 10.1021/acs.chemrev.7b00613
Chem. Rev. 2018, 118, 3121−3207

1. INTRODUCTION

The glass of the Lycurgus cup, created by the Romans in 400 A.D., is a prototypical early example of a dichroic material, where the colors observed in transmission and in reflection differ. It is also one of the earliest known objects in which the material derives its properties from nanoscopic plasmonic particles embedded in the glass that exhibit what we now know as a localized surface plasmon resonance (LSPR). Since 400 A.D., our understanding of LSPR of metals, especially gold (Au) and silver (Ag) whose interesting optical effects most often lie in the visible spectral range, has now been well-established.[1−7] What remains now, as a frontier in materials, are questions about how LSPRs differ in materials that are not classical metals.[8−13] With the advances in colloidal synthesis and a better understanding of free carrier properties in semiconductors, LSPR properties have now been actively explored in several NC material classes, including metal oxides, metal chalcogenides, metal nitrides, and silicon (Si).[14−22] In nanoparticles of metals like Au and Ag, high charge carrier concentration (on the order of 10^{22} cm^{-3}) causes the natural resonance frequencies for LSPR to lie in the visible spectrum; large particles or complex morphologies are required to shift the optical response to the near-infrared (NIR) or mid-infrared (MIR).[3,23−30] By contrast, in semiconductor nanocrystals (NCs), the carrier concentration is tunable (10^{19}−10^{21} cm^{-3}) via chemical doping or post synthetic chemical, photochemical, and electrochemical reactions.[13,14,20,31−46] Control over the carrier concentration allows tuning the LSPR across a wide range of the optical spectrum from visible to far-infrared in colloidally synthesized semiconductor NCs, even those with simple shapes and sizes less than 50 nm.

LSPR and its origins in colloidally synthesized semiconductor NCs is the focus of this review. As with most optical properties, the response of a conductive medium to the incident electromagnetic field (light) depends on the material's complex polarizability or dielectric function.[5,47,48] The dielectric function describes the bulk properties of a material, it includes contributions from transitions between electronic bands, excitation of vibrational modes, and the movement of free carriers (electrons or holes).[25,26,47,49−51] The free carrier contribution to the dielectric function depends on the free carrier concentration and characteristics like crystal structure and band structure.[52−59] These encompass the intrinsic properties of the material.

Geometrical and environmental features, on the other hand, such as shape and size of NCs and the dielectric properties of the surrounding medium, must also be considered to understand the nature of light−matter interactions and the ultimately resultant optical phenomena. In thin films, depending upon the angle of incidence and frequency of the incoming light, the oscillation of electronic charge at the metal−air interface due to the incident oscillating field leads to surface plasmon resonance (SPR).[5,6] Conversely, if the object is spatially limited in all dimensions (as in nanoparticles or NCs), the interaction between the light and the conductive NC leads to confinement of a high intensity nonpropagating wave inside the volume of the NC known as LSPR.[5,47]

The LSPR characteristics of semiconductor NCs depend on NC shape and size as well as dopant type, dopant concentration, and dopant distribution inside the NCs. There are three general observations that guide design of LSPR-active semiconductor NCs: (1) increasing activated dopant concentration increases the free carrier concentration, thereby shifting LSPR toward higher

DOI: 10.1021/acs.chemrev.7b00613
Chem. Rev. 2018, 118, 3121−3207

energy, (2) dopant choice and spatial distribution changes overall electron scattering, impacting the near field enhancement (NFE) around the NC, and (3) shape and size of the NC in conjunction with the intrinsic dielectric properties determine the NC LSPR characteristics. In the last two decades, researchers have achieved precise control over the geometric and intrinsic dopant properties of NCs through colloidal synthesis.

The principle art of colloidal NC synthesis is the control of nucleation and growth, which dictates the resulting size, shape, uniformity, and even composition of the NCs.[14,18,19,32,60−63] This control is realized experimentally by establishing macroscopic thermodynamic parameters such as temperature and concentration but is informed by microscopic chemical considerations such as balancing precursor reactivities, tuning ligand binding strengths, selecting the valence of metal precursors, comparing ionic sizes, and so forth.[64−67] These considerations ultimately dictate the synthetic mechanisms that give rise to different NC products, for example, shifting the focus between kinetics and thermodynamics in describing strategies for controlling NC synthesis. The nucleation stage is typically intended to last only a short time in the early stages of crystallization, and the resulting seeds act as sites for depositing additional monomers during growth of LSPR-active NCs. Diffusion-limited growth occurs after nucleation, and this process can be tuned in some cases to produce batches of highly uniform NCs to minimize heterogeneous broadening of the collective LSPR response.[60,68,69] Kinetics often strongly influence NC growth in colloidal synthesis, allowing synthetic methods to be employed to tailor and design materials' physical and optical properties. Examples of NCs that deviate from expectations based on thermodynamics alone include the incorporation of substantial concentrations of extrinsic dopants (e.g., Al:ZnO), and realizing faceted, anisotropic NC shapes.[62,64,65,70,71] In colloidal synthesis, surfactants passivate dangling bonds at NC surfaces and balance surface charges.[15,66,67,71−73] Their role as capping ligands allows synthesized NCs to exhibit LSPR signatures characteristic of isolated particles and to be dispersible in solution, facilitating scalable deposition onto substrates by low-cost techniques such as blade-, spin-, and spray-coating and enabling integration into composites.[74,75]

NCs can be controllably synthesized by colloidal, solvothermal, or nonthermal plasma methods based on the principles of nucleation and growth.[14,16,18,62,76−79] A wide selection of host materials among metal oxides, metal chalcogenides, metal nitrides, and silicon can be made plasmonic by extending the previously established chemical toolbox to controllably introduce defects (impurities or vacancies). Metal oxide NCs are formed by established reaction mechanisms such as thermolysis, hydrolysis, alcoholysis, and aminolysis where ligand-coordinated metal precursors undergo assisted decomposition to monomers and ultimately NCs; these are extended by including precursors to dopant impurities along with the host metal cations.[45,68,72,80−90] Metal chalcogenides can be synthesized from ligand-coordinated chalcogenide species that bind to metal precursors leading to monomers; metal-chalcogen ratios are then tuned to provide stoichiometric variations and metal ion vacancies.[19,21,32,91−99] Nonthermal plasma synthesis allows synthetic access to NC materials such as metal nitrides or silicon that have high melting points that make them challenging to crystallize in solution under typical conditions used for colloidal synthesis.[100−107] In plasma synthesis, the high energy reaction conditions circumvent the requirement for precise reactivity balance between host and dopant precursors.

Synthetically, free carrier concentrations and mobilities in doped semiconductors can be controlled by the composition of the host material and dopant type and the dopant concentration. The different types of chemical doping are vacancy doping, aliovalent substitutional doping, and interstitial doping.[31,34,35,56,58,59,108−113] In self-doped or vacancy-doped NCs, control over the stoichiometry (for example, Cu vacancies in $Cu_{2-x}S$, O vacancies in WO_{3-x}) allows tuning of the free charge carrier density.[19,21,32,97] Vacancies can introduce either free holes or free electrons without requiring extrinsic dopant ions. In metal chalcogenide NCs, cation vacancies are typically a source of free holes that determine the LSPR characteristics.

Aliovalent doping is the incorporation of elemental impurities inside the host lattice via a substitutional or interstitial doping mechanism that are capable of donating a free hole or free electron to the valence band or conduction band, respectively.[11,31,34,35,59,108,114−116] Extrinsic substitutional or interstitial doping in NCs can be synthetically achieved by balancing reactivity between the precursors for the dopants and the host material during NC growth.[14,31,117] Building on established host NC material synthesis, hard−soft acid−base (HSAB) theory provides a chemical framework for strategically incorporating dopants into NCs as they grow.[17,118−120] Affinity between metal ion Lewis acids (e.g., Al^{3+}, Zn^{2+}, and In^{3+}) and organic ligand Lewis bases (e.g., stearate and acetylacetonate) in the reaction must be considered and balanced so that the dopant precursors can decompose with kinetics that allow their incorporation into the growing NC commensurate with the rate of decomposition of the host material precursor and its consolidation to form the NCs via nucleation and growth.

The ionic radius of substitutional dopant ions influences lattice strain within the host NC and contributes to the energetic cost of defect formation; excessive strain constrains the incorporation of higher dopant concentrations.[59,70,86,115] Considering dopant reactivity and ionic radius comparisons between the dopant and host metals allows doping without disruption of the crystallographic phase and ideally allows straightforward tuning of carrier concentration and thus LSPR optical behavior with minimum perturbation by defect clusters or other structural perturbations in doped NCs. More advanced dopant incorporation strategies can control the spatial distribution of dopants within each NC by timely addition of dopant precursors to the reaction or by controlling the relative rate of dopant precursor decomposition.[68,69,117,121] Co-doping, where both cations and anions are partially substituted by aliovalent dopants or two different cationic dopants are incorporated, has the potential to substantially expand the synthetic space of achievable compositions in extrinsic aliovalent-doped NCs and has led to higher carrier concentrations and blue-shifted LSPR response compared to single dopant NCs.[89,122]

To boost NFE, and to understand phase-dependent LSPR properties in semiconductor NCs, the following design rules have been proposed: (1) minimize the oxygen vacancy concentration in metal oxide NCs to reduce the scattering due to the doubly charged vacancy sites, (2) the size of a cationic or anionic dopant should closely match size of the host cation or anion to minimize strain, (3) the dielectric function in anisotropic crystal structures is dependent on crystallographic direction, and the interplay between shape and crystalline anisotropy determines both near field and far field LSPR characteristics of NCs of such materials.

DOI: 10.1021/acs.chemrev.7b00613
Chem. Rev. 2018, 118, 3121−3207

Beyond managing the reaction kinetics to achieve dopant incorporation, one must consider the defect chemistry of the crystals and the material's electronic structure to understand how dopants change free carrier concentration, perturb the host lattice, and ultimately determine the properties of the material (see refs 35, 58, 59, 108, 109, 111, 114, and 115). For example, Sn content in Sn:In_2O_3 NCs impacts the concentration of activated $Sn_{In}^{\cdot}$ substitutional defects, oxygen vacancies $V_O^{\cdot\cdot}$, and $Sn_{In}^{\cdot} - O_i''$ clusters that can act as deep traps for electrons. The concentrations of the activated dopant sites and oxygen vacancies determine the free carrier concentration, thereby the LSPR energy of the NCs.

In addition to determining the free carrier concentration, dopants also influence the scattering of free charge carriers inside the NC.[59,123−126] If the dopant states hybridize strongly with states near the conduction band minimum (CBM) or valence band maximum (VBM), oscillating charge carriers may experience strong ionized impurity scattering due to the dopant sites. For example, in the In_2O_3 host lattice, Sn dopant orbitals hybridize far more strongly than Ce orbitals near the CBM, which leads to greater ionized impurity scattering in Sn:In_2O_3 than Ce:In_2O_3.[59] The stronger the scattering of the charge carriers, the lower the NFE will be around LSPR-active NCs. Improving the potential for impactful near field properties is a major focus of current research on LSPR-active semiconductor NCs. Although the presence of free charge carriers within the NC already implies interactions with incident light that will be observable in the far field as absorption and perhaps scattering by the NC LSPR, maximizing the near-field enhancement of light requires strict synthetic shape control with well-defined NC morphology. Shape control is achievable by extending considerations of kinetic and thermodynamic shape control during colloidal NC synthesis to the more complicated case of doped NCs.[71,127−132] Selection of surface capping agents such as halogens and organic ligands provides an additional avenue for shape control in colloidally synthesized metal oxide and metal chalcogenide NCs. Selectivity is determined by the relative affinity of capping agents for specific crystallographic facets and is guided by the HSAB theory as it relates to the interactions between ligands and surface-terminal metal cations. This theory at least provides some intuitive guide to pursue rational synthetic control over NC morphologies designed to achieve higher NFE or other shape-dependent LSPR properties.

Control over shape of the NCs allows control over NC LSPR in the following ways: (1) NC shape determines the potential LSPR modes that contribute to the spectral line shape. In a symmetric shape like a cube there are often three different geometric modes localized, respectively, at the vertices, edges, and faces of the NC. On the other hand, in anisotropic shapes such as nanorods and nanodisks there exist directionally dependent longitudinal and transverse modes;[5,133,134] (2) the sharpness of the NC morphologies determines the NFE strength around the NC;[28,135] and (3) synergistic effects of anisotropic NC shape and anisotropic crystal structure determine the LSPR and NFE characteristic of a NC.[56]

Semiconductor NCs with multifunctional properties have been synthesized by either codoping with dopants that introduce different attributes, such as magnetic response, or by creating heterostructures where each domain introduces distinct functionality. By codoping, the introduction of multifunctionality such as localized magnetic spin together with delocalized free charge carriers is possible.[136,137] For example, Fe,Sn-codoped In_2O_3 NCs display both magnetic and LSPR characteristics. Heterostructures, typically those incorporating elemental metal and doped semiconductor domains, have been explored either for enhancing optical extinction or use as tandem electronic systems where excitations within the LSPR-active semiconductor enhance the functional properties of the metal.[138−143] For example, in CuS-Pd heterostructures, hot electrons created by photoexcitation of LSPR in the CuS enhance the catalytic activity of Pd for several organic reactions.[144]

Owing to the semiconducting nature of the host materials, LSPR of degenerately doped NCs can be dynamically modulated by tuning their carrier concentration. Postsynthetic control over LSPR characteristics adds a dynamic tuning knob in semiconductor NCs that far exceeds what is possible with metal nanoparticles. Dynamic LSPR tuning has been demonstrated using three different approaches: (1) chemical redox reactions, which involve electron transfer to and from NCs when exposed to reducing or oxidizing agents,[34,43,46,46,145,146] (2) photochemical charging, which is usually achieved through illumination with above band gap energy light under anaerobic conditions in a presence of a hole scavenger to stabilize free electrons in the NC conduction band,[38,39,54,79,147−150] (3) ultrafast modulation, which relies on the LSPR relaxation dynamics on the picosecond time scale, and (4) electrochemical charging and discharging: the Fermi level and thus the concentration of conduction band electrons or valence band holes is shifted through applying an electrochemical potential, usually to samples in the form of films or assemblies.[41,74,75,151−156] Dynamic and external control over LSPR has led to promising applications in IR electrochromic smart windows, redox sensors, and electro-optical modulators.

The potential of resonant absorption and scattering as well as NFE characteristics of LSPR-active semiconductor NCs has been explored for several applications. High absorption cross section may enable photothermal applications in biomedical therapy and imaging as well as for enhanced waste heat recovery.[157−164] High NFE leads to strong coupling with other resonant phenomena (excitons, vibrational excitations, or phonons) to enhance the signal of weak optical processes.[89,165−170] These interations suggest applications such as surface-enhanced infrared absorption (SEIRA), surface-enhanced Raman scattering (SERS), two photon upconversion, and enhanced photoluminescence. Moreover, generation of hot electrons or holes makes these optical resonances promising for enhanced catalytic applications.[171−173]

1.1. Outline

The physics of LSPR in colloidal semiconductor NCs and its suitability for various applications depend on aspects of the material's structure and chemistry that result from how the NCs are synthesized and treated postsynthetically. To systematically address each of these aspects, this review is divided into 4 major sections: physics (section 2), synthesis (section 3), post synthetic LSPR modulation (section 4), and applications (section 5).

In the physics section (section 2) of this review, our discussion will begin with an examination of the fundamental physical principles that govern light−matter interactions based on the dielectric properties of a material (section 2.2). Within this subsection, we will discuss the origin of free carriers in semiconductors, the conventional treatment of free carrier optical response using the Drude-Lorentz model, a general overview of LSPR in semiconductor NCs, and limitations of the Drude-Lorentz model as applied to semiconductor NCs. After setting the stage for in-depth discussion of LSPR in semiconductors, in the next subsection (section 2.3), we discuss

DOI: 10.1021/acs.chemrev.7b00613
Chem. Rev. 2018, 118, 3121−3207

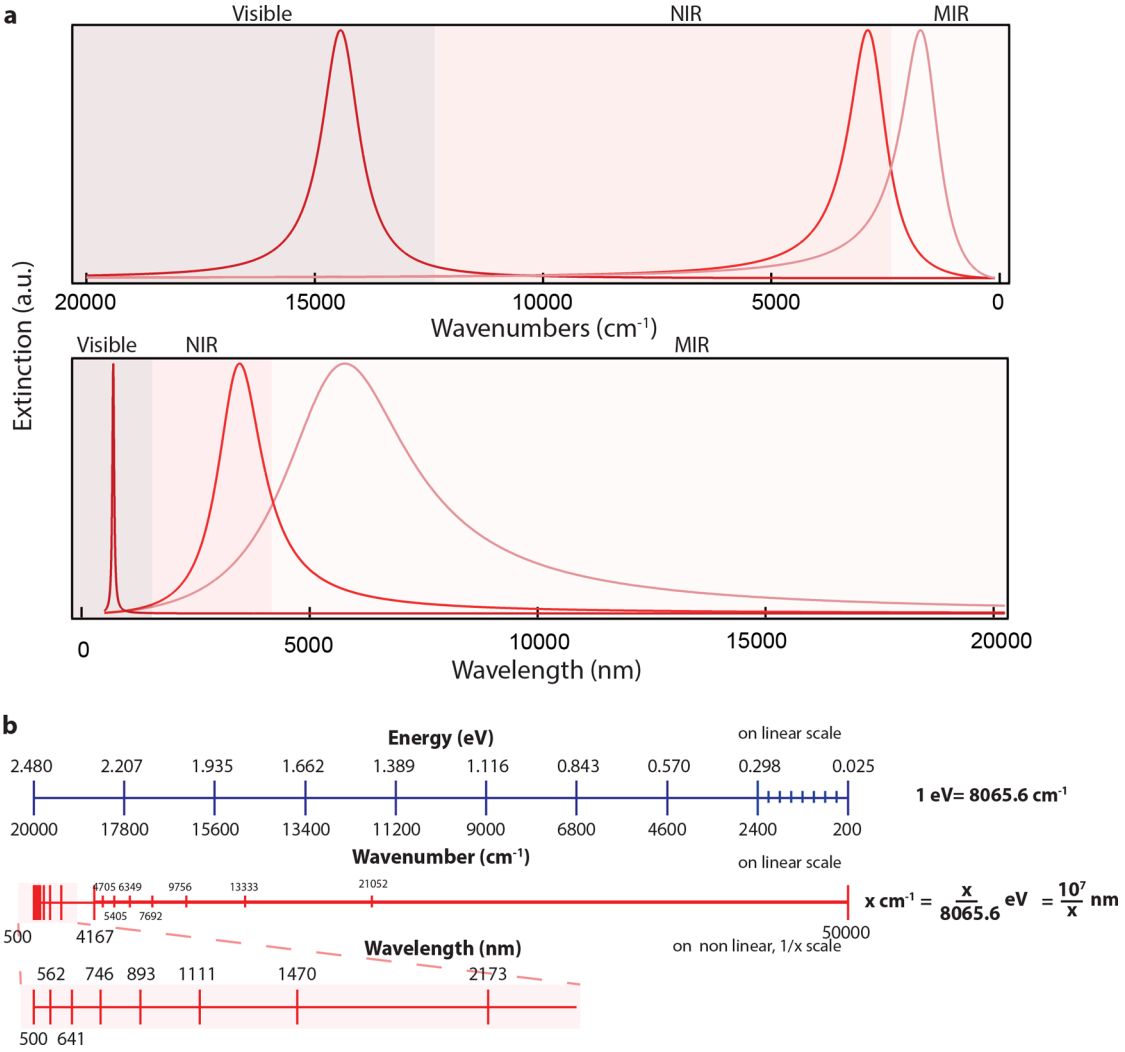

Figure 1. Spectral Analysis. (a) Optical resonance on wavelength, nm (red curves) and wavenumber, cm^{-1} (blue curves) scales in different spectral ranges. In the visible range (dark red), the response appears sharper when plotted in wavelength (bottom) instead of energy (top). In the NIR (red), optical spectra on both wavelength (bottom) and energy (top) scales have similar line width but very different lineshapes. In the MIR (light red), optical spectra on a wavelength scale (bottom) appear much broader than on an energy scale (top). (b) Interconversion between different units of energy and wavelength are shown. The energy scale is plotted linearly (blue line) with energy in eV on top and in wavenumbers below. The wavelength corresponding to each tick mark on the blue energy scale is shown as a red tick mark on the wavelength scale. Due to the inverse relationship between energy and wavelength, the wavelength scale is nonlinear.

LSPR in metal oxide NCs, more specifically, how doping in metal oxide NCs influences their LSPR properties followed by a discussion of LSPR dependence on shape, size, crystal structure, and dopant distribution inside the NC. We also briefly discuss the stability of metal oxide NCs under ambient conditions, LSPR in heterostructures, and further discuss other promising metal oxide materials which are intrinsically metallic. The next subsection (section 2.4) focuses on LSPR in metal chalcogenide materials, wherein we discuss the correlation between the extent of self-doping and crystal structure in copper chalcogenide NCs and how it influences their LSPR properties. This subsection also includes the discussion on extrinsically doped, alloyed, and ternary metal chalcogenide NCs, NC ambient stability, NC phase transformations, and metal chalcogenide-containing heterostructures. Following this subsection (section 2.5) is a discussion of other semiconductor materials such as Si, metal nitrides, and other semiconductors. This subsection, as an outlook, ends by outlining some of the unanswered questions in the field.

In the synthesis section (section 3) of this review, we begin by outlining the principles behind colloidal synthesis and chemistry leading to NC formation (section 3.1). This includes a background in classical nucleation and growth, precursor and monomer chemistry for metal oxides and metal chalcogenides, along with hard−soft acid−base (HSAB) theory as it relates to balancing reactivity. Having established this context, we overview doping strategies used to introduce free charge carriers in semiconductor NCs leading to LSPR (section 3.2). The strategies discussed for doping LSPR-active metal oxide and metal chalcogenide NCs include vacancy doping, interstitial doping, and substitutional aliovalent doping. We will also highlight advanced doping methods such as codoping and controlling the spatial distribution of dopants in a case study format. Then, we continue the section with a discussion of synthetic shape control in LSPR-active semiconductor NCs (section 3.3), highlighting thermodynamic and kinetic control, capping agents, and dopant-induced shape changes reported in LSPR-active metal oxide and metal chalcogenide NCs.

DOI: 10.1021/acs.chemrev.7b00613
Chem. Rev. 2018, 118, 3121−3207

Complementing our main focus on solution-based colloidal synthesis, case studies of nonthermal plasma synthesis of high-melting point LSPR-active NC materials will be presented (section 3.4) with notes on the advantages and key differences from solution phase colloidal synthesis. We will provide a survey (section 3.5) of the characterization tools used to evaluate outcomes of doping chemistry such X-ray diffraction (XRD) for crystal structure and strain, inductively coupled plasma-atomic emission spectroscopy (ICP-AES) for dopant quantification, X-ray photoelectron spectroscopy (XPS) for oxidation state and dopant distribution, and X-ray absorption spectroscopy (XAS) for dopant oxidation state assessment. We will conclude with (section 3.6) a summary, prospective questions, and outlook.

In the post synthetic LSPR modulation section (section 4), we will discuss four different controls employed to modulate the LSPR in semiconductor NCs. The first subsection will highlight chemical control of semiconductor NCs (section 4.2) using oxidizing and reducing agents to reversibly tune the intensity or peak energy of NC LSPR. The second subsection will be a discussion of photochemical control of semiconductor NC LSPR (section 4.3) including the photodoping process, proton coupled electron transfer following photoexcitation, and effects of chemical doping on further charging by photodoping. Here, we will also discuss how photocharging modulates IR intraband transitions in semiconductor quantum dots as it relates to understanding LSPR modulation. The third subsection on ultrafast modulation (section 4.4) will examine recombination dynamics of photoexcited plasmonic semiconductor NCs, a comparative look at different semiconductors and metals, as well as the applicability to applications such as ultrafast optical modulators. The final subsection addresses electrochemical control of NC LSPR (section 4.5) and covers how capacitive and intercalation charging of LSPR-active semiconductor NC films impacts their optical properties. Here, we also discuss how semiconductor properties such as electronic structure and crystal structure play crucial roles in determining the optical switching response and impact the suitability of such materials for applications such as smart windows.

In the application section (section 5), the discussion is focused on emerging and potential applications that utilize different characteristics of semiconductor NC LSPR. The first subsection (section 5.1) addresses applications based on light absorption due to LSPR, including biomedical applications and waste heat recovery. In the second subsection (section 5.2), we discuss near field coupling between LSPR and other optical excitations for applications such as two photon upconversion, SEIRA and SERS. The third subsection (section 5.3) explains how hot carriers in LSPR-active NCs can enhance the catalytic properties of metal catalysts. The last subsection (section 5.4) discusses other potential applications that are presently not realized in NCs but have been studied in thin films, leading us to finish this section with unanswered questions in the field.

The final section (section 6) of this review summarizes the overall field of semiconductor NC LSPR and lays out aspirational goals for future developments, which if accomplished could reveal new insights and lead to novel and interesting applications.

1.2. Analysis of Optical Spectra

Two informative parameters typically extracted from any resonant optical spectrum are the peak frequency/wavelength/energy and the full-width half-maximum (fwhm). One parameter which is often used to gauge "quality" of LSPR optical resonances especially is the quality factor. Quality factor is defined as $\omega_{resonance}/fwhm_{resonance}$, where $\omega_{resonance}$ is the central resonance frequency in energy units (eV or cm^{-1}) and $fwhm_{resonance}$ is the fwhm in energy units (eV or cm^{-1}). Thus, quality factor can be increased by either decreasing the peak width or increasing the peak energy. The quality factor denotes how fast the resonator will relax absent any external perturbation; loosely, it describes the number of coherent oscillations following excitation. Quality factor LSPR is also positively correlated with NFE around the NC (section 2.3.4). In the LSPR literature, the routine practice has been to compare the fwhm of different spectra across different spectral ranges to roughly assess relative quality factors. However, this can lead to erroneous and misleading comparisons, especially if spectra are analyzed in wavelength units, due to the nonlinearity between different scales used to plot spectra: wavelength, frequency, and energy. Here, we have plotted a hypothetical LSPR using three different scales for the photon energy (Figure 1). All the spectra shown here were generated with the same damping constant, which is the physical parameter controlling peak width, and three different resonant frequencies. As illustrated here, the apparent line shape and fwhm when using wavelength versus energy scales are vastly different. In the visible spectral range, the same resonance response can look much sharper when plotted on a wavelength scale than on a linear energy scale. In the NIR regime, the fwhm in both wavelength and energy scales is comparable, but the line shape changes significantly. In the MIR regime, the spectrum is much broader when plotted on a wavelength scale than on an energy scale and differences in the lineshapes are exaggerated. Considering these substantial changes in apparent spectral characteristics when using wavelength and energy scales, caution should be employed while comparing different spectra qualitatively. For this reason, special care is taken while comparing spectra in this review. Spectra are presented on various scales, both wavelength (nm) and energy (eV and cm^{-1}), consistent with the widely varying practices in the literature.

2. LIGHT MATTER INTERACTION IN SEMICONDUCTOR NCS

2.1. Introduction

Light matter interaction in a closed system consisting of an arbitrary shaped particle and surrounding medium with the dielectric properties, ε_p and ε_m, respectively, is governed by the fundamental laws of electromagnetism.[5,48] Oscillatory charges set into motion inside a material by incoming oscillatory electromagnetic waves lead to reradiation of light by matter in all directions, referred to as scattering, and thermal losses associated with the interaction, referred to as absorption. Given the incident electromagnetic field and the shape and size of the particle, resultant electric and magnetic fields inside the closed system can be solved using macroscopic Maxwell equations. In a simplified case where the material's magnetic permeability is unity, Maxwell equations can be simplified into one equation to solve for the electric field inside the closed system (eq 1). Then, based on the electric field inside the closed system, optical properties like scattering, absorption, and extinction of the particle can be evaluated.

$$\nabla \times \nabla \times E = -\mu_0 \frac{\partial D}{\partial t} \tag{1}$$

where E is the electric field, μ_0 is the free space magnetic permeability, and D is the displacement field.

DOI: 10.1021/acs.chemrev.7b00613
Chem. Rev. 2018, 118, 3121−3207

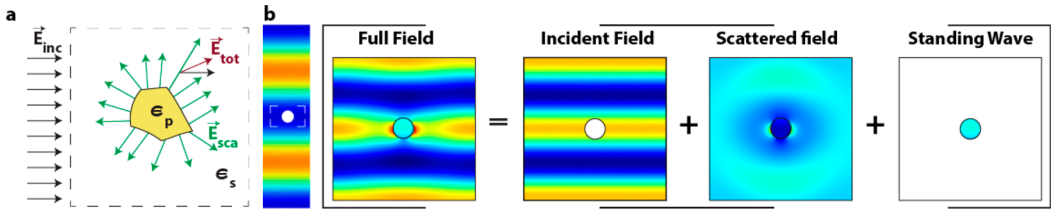

Figure 2. Light Matter Interaction. (a) Schematic depicting the interaction of light with an object of a given shape, size, and dielectric function resulting in the net electric field as the sum of scattered and incident fields. Adapted from ref 4. Copyright 2011 American Chemical Society. (b) Total, incident, scattered, and standing electric field for the semiconductor NC. Each plot is normalized and the color scale ranges from +1 (blue) to −1 (red).

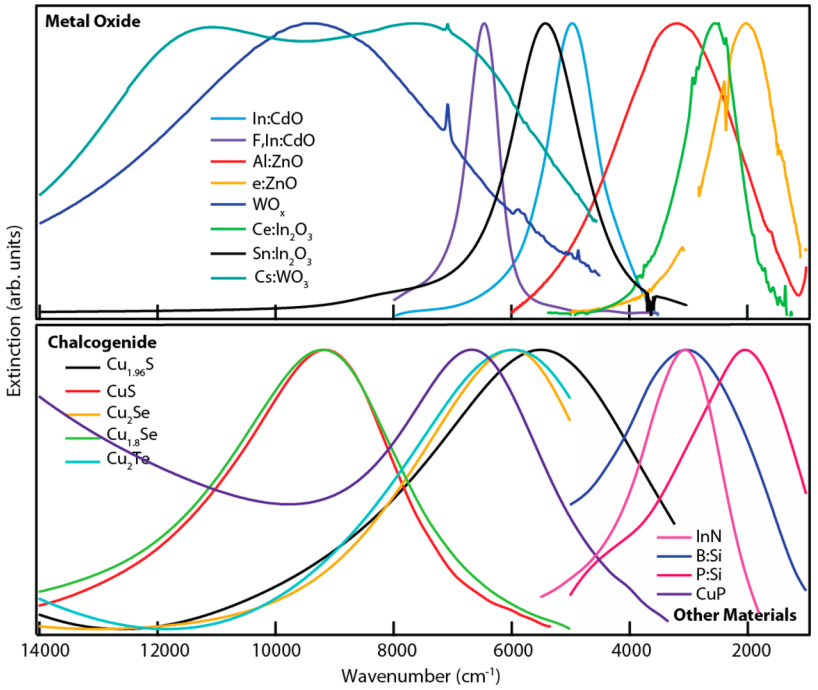

Figure 3. LSPR in different semiconductor NCs. Normalized LSPR extinction spectra of semiconductors spanning the visible spectrum to the MIR spectrum. Included are (top) metal oxides such as CdO, ZnO, In_2O_3, and WO_{3-x} and (bottom) metal chalcogenides such as $Cu_{2-x}E$ (E = S,Se,Te) as well as Si, metal nitride, and metal phosphide materials, highlighting the wide range of semiconductor materials demonstrating LSPR. In all of these materials, LSPR can be tuned via chemical doping, photodoping, electrochemical charging, or shape- or crystal-phase control during colloidal synthesis. LSPR spectra were adapted from refs 35, 56, 59, 84, 106, 112, 113, 122, 124, 146, and 195−201.

To visualize the particle interaction with the incident light, the electric field at any point in space surrounding the particle can be decomposed into two components, the incident field, $\overrightarrow{E_{inc}}$ and scattered radiation from the particle surface, $\vec{E}_{sca}$ (Figure 2).From $\vec{E}_{inc}$ and $\vec{E}_{sca}$, extinction is calculated as the sum of the two contributions to obtain the total electric field outflowing from the particle surface. Energy outflow or power of the scattered light is determined by $\vec{E}_{sca}$, while absorption is obtained from the difference between extinction and scattering losses.

$$E_{out}(x, y, z) = E_0\hat{z} - \left[\frac{\epsilon_p - \epsilon_m}{\epsilon_p + 2\epsilon_m}\right]a^3E_0\left[\frac{\hat{z}}{r^3} - \frac{3z}{r^5}(x\hat{x} + y\hat{y} + z\hat{z})\right] \quad (2)$$

$$E_{in}(x, y, z) = \left[\frac{3\epsilon_p}{\epsilon_p + 3\epsilon_m}\right]E_0\hat{z} \quad (3)$$

where E_{out} and E_{in} are the net electric fields outside and inside the particle, respectively, E_0 is the magnitude of incident electric field ($\overrightarrow{E_{inc}}$), x, y, and z are the spatial coordinate relative to the center of the particle, $\hat{x}$, $\hat{y}$, $\hat{z}$ are the unit vectors, and r is the distance from the center.

For a spherical particle, the electric field inside and outside of the particle can be analytically solved using Mie theory (eqs 2 and 3), but for all other geometries, Maxwell's equations need to be solved numerically.[2,4] There are several computational methods available, including the discrete dipole approximation,[174,175] finite element method,[176,177] boundary value problem,[6,178,179] and finite difference time domain.[133] Using Mie theory approximations for a spherical particle under the quasistatic approximation (applicable when the size of the particle is much smaller than wavelegnth of light), the absorption and scattering cross sections can also be analytically solved (eqs 4 and 5). These expressions demonstrate that while the extinction of small objects or NCs will primarily lead to absorption of light, above a diameter threshold of approximately $d = \lambda_{LSPR}/20$, NCs will begin to scatter light with increasing efficiency.

$$C_{ext}(\omega) = 4\pi R^2[k(\epsilon_H)^{1/2}R]\mathrm{Im}\left\{\frac{\epsilon_p(\omega) - \epsilon_H}{\epsilon_p(\omega) + 2\epsilon_H}\right\} \quad (4)$$

DOI: 10.1021/acs.chemrev.7b00613
Chem. Rev. 2018, 118, 3121−3207

$$C_{sca}(\omega) = 4\pi R^2[k(\epsilon_H)^{1/2}R]^4 \left| \frac{\epsilon_p(\omega) - \epsilon_H}{\epsilon_p(\omega) + 2\epsilon_H} \right|^2 \quad (5)$$

Here, k represents the wavevector of the light, R the NC radius, and ϵ_H is the dielectric constant of the environment surrounding the NCs.

The dielectric function directly affects the scattering cross sections defined in eqs 4 and 5, and so the form of the dielectric function, whether it is real ($\epsilon_p = \epsilon_1$) or complex ($\epsilon_p = \epsilon_1 + i\epsilon_2$), with a positive or negative real component ($\epsilon_1 < 0$ or $\epsilon_1 > 0$), dictates the type of optical interaction. If the dielectric function is a positive real function, the optical interactions will consist of pure scattering with no absorption. If the dielectric function is complex with a positive real component, the optical interactions will include Rayleigh scattering. A special case and point of interest in this review is when the dielectric function is complex with a negative real component. As is evident from the extinction cross-section expression (eq 4), if the real part of the dielectric function goes negative, or more specifically when $\epsilon_p(\omega) = -2\epsilon_H$, extinction is maximized. This resonant optical phenomenon is the physical basis of LSPR. This behavior of the dielectric function, one that is complex but has a negative real component, is often displayed by conductive materials with high free carrier density. Thus, common materials that possess such characteristics are metals such as Ag[25,180,181] or Au,[26,182] or degenerately doped semiconductors such as Sn:In_2O_3,[87,183−185] In:CdO,[111,124,186,187] copper-deficient Cu_2S,[19,99,188,189] and highly doped n-type Si[106,190] (Figure 3).

Coherent collective oscillation of free carriers within NCs in response to an oscillating electromagnetic field that leads to an LSPR response depends on free carrier density, size, and shape of the NC, and the surrounding dielectric environment. The central resonance frequency is known as the LSPR frequency (ω_{LSPR}), and the associated resonance line width is $fwhm_{LSPR}$. ω_{LSPR} is primarily dictated by the free carrier concentration and the carrier effective mass(es), while $fwhm_{LSPR}$ is determined by the scattering or damping of free carrier motion. At ω_{LSPR}, both extinction and electric field around the NC (eq 2) are maximized, and this concentration of electric field at the NC surface is termed the NFE. Both ω_{LSPR} and $fwhm_{LSPR}$ observed as a far field optical response are directly correlated with the NFE; a high NFE is usually suggested by a high LSPR quality factor, where the LSPR quality factor is defined as $Q_{LSPR} = \omega_{LSPR}/fwhm_{LSPR}$.

LSPR phenomena have been studied in great detail for metals such as Ag or Au. The LSPR wavelength of sub-100 nm spherical Ag nanoparticles, depending on the nanoparticle size and surrounding dielectric, lies in between 320 and 450 nm.[191] To extend the LSPR frequency to lower energy, researchers have either increased the size of the nanoparticles or synthesized elongated (rod-shaped or ellipsoidal), hollow, or complex branched nanoparticles.[191] Star-like branched Ag nanoparticles display multimodal LSPR response that extends to 1100 nm in the NIR spectrum.[192] To further extend the LSPR frequency to MIR using Ag or Au particles, researchers have fabricated coupled nanostrucutres such as helices,[193] split-ring resonators,[194] or asymmetric coupled rods.[30] The remarkable progress in metal plasmonics over the past two decades has given rise to a diverse array of applications in the fields of spectroscopy, imaging, biomedical therapy, sensing, catalysis, electrooptics, and energy harvesting (sections 4 and 5). But the efficacy of Au or Ag is quite low for some of the applications that require both sub-100 nm nanoparticle size and LSPR in the infrared spectrum. In the recent decade, LSPR in conductive semiconductors such as degenerately doped metal oxides like Sn:In_2O_3[87,183−185] and In:CdO,[111,124,186,187] metal chalcogenides like copper-deficient Cu_2S,[19,99,188,189] and III−V/Group IV semiconductors like highly doped n-type Si[106,190] has been explored as a possible alternative to metals. Semiconductors offer certain unique advantages over metals such as the capability to tune LSPR properties via chemical doping, accessible LSPR frequencies spanning a wide optical range from visible to FIR, even for small NCs (NC size less than 200 nm), and flexibility to post synthetically tune the LSPR characteristics over a broad range of intensities and frequencies. Oxygen vacancy doped metal oxide (WO_{3-x}, MoO_{3-x}) and cation vacancy doped metal chalcogenide ($Cu_{2-x}S$, $Cu_{2-x}Se$) NCs of size less than 20 nm displays LSPR in the range of 8000−14000 cm^{-1} (700−1250 nm); this spectral range overlaps with that achievable only with much larger nanoparticles of Au or Ag (Figure 3). Furthermore, with impurity-doped semiconductors (Sn:In_2O_3, In:CdO, B−Si, etc.), the LSPR can be extended into the FIR spectrum. But due to lower carrier concentrations and high-electron damping, the extinction coefficients of vacancy-doped semiconductor NCs are much lower than those of metal nanoparticles. The high damping also limits the NFE around the NCs and increases the LSPR fwhm. Despite these drawbacks, the possibility of LSPR in NIR spectrum for sub-20 nm NCs has encouraged researchers to explore these materials for several applications (sections 4 and 5).

Before delving into the more intricate material-specific details regarding these semiconductor materials and their impact on LSPR, we will first discuss the origins of free carrier properties in semiconductors and how these impact dielectric properties. In the next section, we will discuss mathematical models used to express free carrier properties and the assumptions and limitations underlying such models. After getting a general sense of how semiconductors support free carrier optical phenomena and the limitations of the current models used to express these phenomena mathematically, we will discuss LSPR in three classes of semiconductor materials: metal oxides, metal chalcogenides, and III−V/Group IV semiconductors. We will end this section with a discussion of some other new promising semiconductor materials that have been explored for their LSPR properties and highlight remaining open questions with regard to the physical understanding of LSPR in semiconductor systems.

2.2. Dielectric Properties of Semiconductors

Upon excitation with an external light source, the charge distribution inside a material depends on several components of the dielectric function, including electronic effects from interband or intraband excitation ($\epsilon_{electronic}$), atomic effects from vibrational or phonon excitation (ϵ_{atomic}), or conduction hole or electron excitations ($\epsilon_{conduction}$). The dielectric function or polarizability of a material is an additive property and expressed as,

$$\epsilon = \epsilon_{electronic}(\omega) + \epsilon_{atomic}(\omega) + \epsilon_{conduction}(\omega) \quad (6)$$

In this review, our focus will be on the optical properties originating from conduction or free carriers. But since the light matter interaction depends upon the overall dielectric properties, it is crucial to consider how each of the polarizability components affects the overall dielectric function. The free carrier contribution to the dielectric function depends on the free carrier concentration and is expressed using the Drude model, details of which are discussed later in this text (section 2.2).

DOI: 10.1021/acs.chemrev.7b00613
Chem. Rev. 2018, 118, 3121−3207

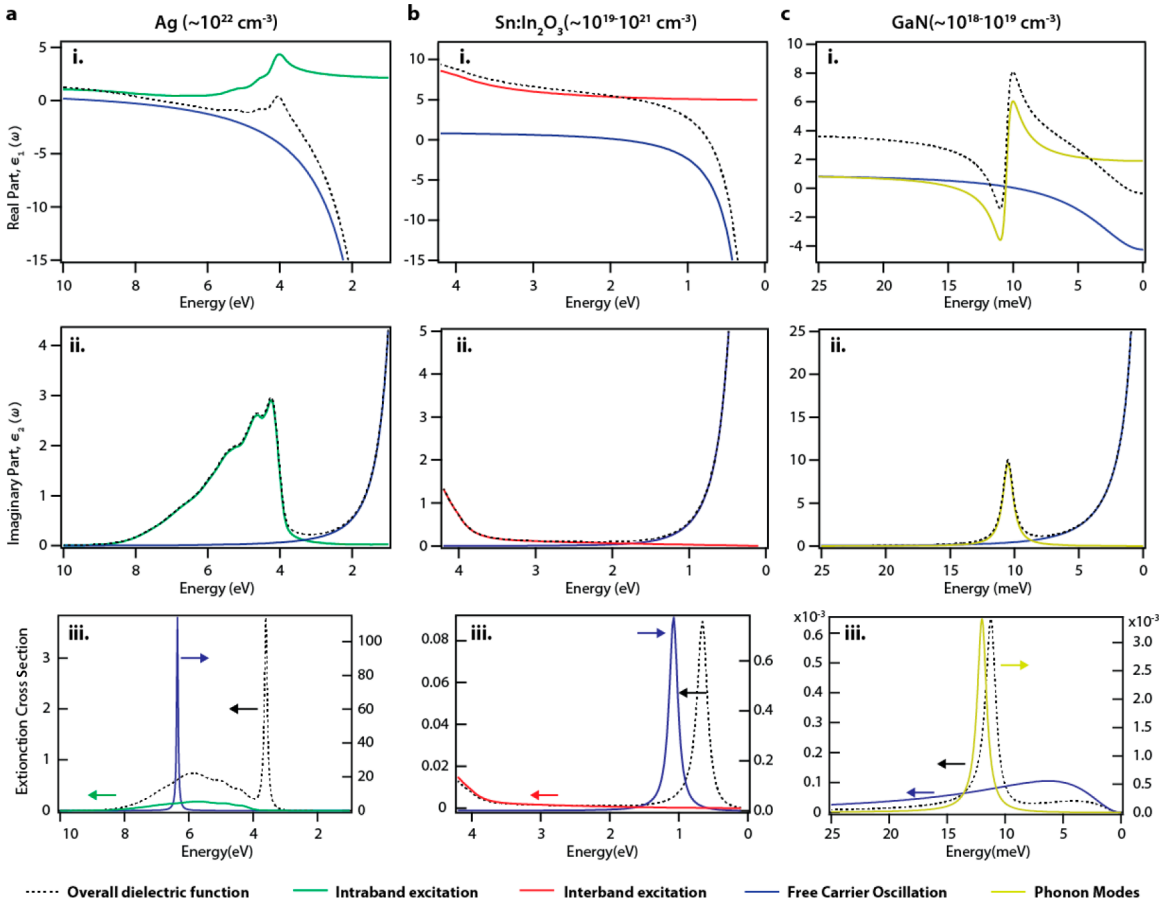

Figure 4. Dielectric function of materials in different carrier density regimes. (a) Dielectric function of Ag (black) is the sum of contributions from free charge carriers (blue) and intraband excitations (green). Similar overlap between intraband and free charge carrier excitations is observed in Au. (b) Dielectric function of Sn:In_2O_3 shows relatively low overlap between different frequency dependent optical processes such as free charge carrier (in IR spectrum, blue) and interband excitation (in UV−visible spectrum, red). (c) In material with ultralow carrier concentration, such as GaN, there exists a strong overlap between the free charge carrier contribution (blue) and low energy optical phonon modes (yellow). Synergistic interaction between dielectric contributions from discrete transition like intraband (a-iii), interband (b-iii), or phonon transitions (c-iii) and free carrier excitations results in shifting LSPR to lower energy. Data used in this figure were adapted from refs 25, 50, and 202.

At high carrier concentration (10^{22} cm^{-3} commonly found in metals such as Ag or Au), the onset of the free carrier dielectric contribution is at around 10 eV (Figure 4a, i−ii, blue curve). As the carrier concentration is reduced, the onset of the free carrier contribution moves toward lower energy. For example, in degenerately doped semiconductors like Sn:In_2O_3, where the free carrier density is on the order of 10^{19}−10^{20} cm^{-3}, the onset of the free carrier contribution to the dielectric function shifts to around 4 eV, leading to LSPR in the infrared energy spectrum (Figure 4b, i−ii, blue curve). Similarly, if the carrier density is further lowered to represent systems like GaN (10^{18} cm^{-3}), the onset of the free carrier contribution shifts to around 25 meV corresponding to the far-infrared regime. Irrespective of the carrier concentration, in all cases (Figure 4, panels a−c), the overall dielectric function cannot be expressed accurately with sole consideration of the free electron contribution and is greatly perturbed by the presence of other polarizabilities. The contribution from other optical phenomenon such as intraband transition in Ag, interband transition in Sn:In_2O_3, or phonon modes in GaN changes both the magnitude of the dielectric value at a given frequency and other important overall benchmarks in a dielectric curve such as the crossover frequency (i.e., frequency at which real part of dielectric function switches from positive to negative). Ultimately, it is the overall dielectric function of the material that determines the extinction cross section of a NC. To expand on the point of how the additive effect of different polarizability effects changes the extinction of a NC, we simulated the extinction cross section of Ag, Sn:In_2O_3, and GaN depicting the various contributions to the dielectric function and revealing their effects on the final extinction spectra (Figure 4, panels a−c (iii). From all the three material systems shown, the following observations are clear: (i) LSPR peak position shifts to lower energy upon addition of secondary components beyond the free carrier contribution and (ii) the absolute extinction decreases as the LSPR shifts to lower energy. Furthermore, interaction between different polarizabilities can provide additional electron-scattering pathways that further perturb the observed LSPR phenomena (discussed in section 2.2.2). Here, it is important to emphasize that it is the polarizability of the material or the dielectric function that is additive. The extinction is not additive as is often misrepresented or misanalysed in the literature. A complete approach to consider the multiple contributions should include experimental measurement of the material dielectric function by ellipsometry of a film or extinction measurements of NCs.

2.2.1. Free Carrier Contribution to the Dielectric Function and Its Origin in Semiconductor NCs. Optical properties of conducting materials are dominated by the

DOI: 10.1021/acs.chemrev.7b00613
Chem. Rev. 2018, 118, 3121−3207

collective optical transitions within the conduction or valence band where electrons or holes behave as a free carrier gas. The dielectric function of conductive materials demonstrating the collective oscillation of free electrons is expressed using the Drude-Lorentz model (see refs 4, 8, 10, 35, 50, 59, 111, 183, 186, and 187). This model is simplistic and makes the following assumptions: (i) free carrier motion is unimpeded by any potential energy function and follows Brownian motion and (ii) the dielectric properties of any material with free carrier concentration (n) can effectively be expressed using only three additional properties [i.e., charge +e/−e (hole or electron), carrier damping, and effective mass, m_e].

Despite these simplistic assumptions and nonconsideration of band structure, the Drude-Lorentz model has been found to be widely applicable with reasonable precision in predicting and modeling the behavior of both metal[7,203] and semiconductor LSPR.[50,111,187] The Drude-Lorentz dielectric function (eqs 7−10) is a complex function.

$$\epsilon_p(\omega) = \epsilon_1(\omega) + i\epsilon_2(\omega) \tag{7}$$

$$\epsilon_1 = \epsilon_\infty - \frac{\omega_p^2}{\omega^2 + \gamma^2} \quad \epsilon_2 = \frac{\omega_p^2 \gamma}{\omega(\omega + \gamma^2)} \tag{8–9}$$

Here, the function ϵ_p is the dielectric function of the material, ϵ_1 and ϵ_2 are the real and imaginary parts of the dielectric function, respectively, ϵ_∞ is the high frequency dielectric constant of the material, γ is the damping constant that represents scattering of free carriers, and ω_p is the plasma frequency, that is expressed as,

$$\omega_p = \sqrt{\frac{ne^2}{m_e \epsilon_0}} \tag{10}$$

Here, n is the free carrier concentration, m_e is the free carrier effective mass, which accounts for deviations in behavior from the free electron gas approximation caused by material-specific electronic band dispersion.

For most cases, the high frequency dielectric constant is assumed to be frequency-independent, and as in most of the semiconductor materials such as metal oxides[59,183,187] and metal chalcogenides,[12,19,20,42] the contribution to polarizability from bound electrons going through interband transitions do not overlap energetically with free carrier transitions like LSPR. For this reason, their contribution to polarizability can be treated as a constant value (Figure 4b). In some cases, however, there is energetic overlap between these transitions, so the frequency dependence of bound electronic transitions must be accounted for, instead of using a constant ϵ_∞. In these cases, application of the Drude-Lorentz dielectric function to describe LSPR behavior is inappropriate and more complex analytical models should be employed or, more commonly, numerical dielectric functions extracted from experimental data should be employed as is almost the universal practice in analysis of coinage metal LSPR.[25,26]

The effect of free carrier concentration on the free carrier dielectric function is quantitatively reflected in the plasma frequency with the plasma frequency being directly proportional to the square root of the free carrier concentration. Metals like Ag and Au which are traditional plasmonics materials, have a carrier concentration of the order of 10^{22} cm^{-3}. Such high free carrier concentration results in a high plasma frequency (60000−70000 cm^{-1}) that essentially confines optical phenomenon such as surface plasmon resonance (SPR), LSPR in nanosystems (size less than 200 nm), or episolon near zero (ENZ) to the visible energy spectrum. In the past decade, researchers[9,11,12,20] have been exploring doped semiconductors in which, depending upon the dopant type (n or p) and concentration, free carrier concentration (electron or hole) can be tuned from 10^{18}−10^{21} cm^{-3}. This low carrier concentration shifts plasma frequency and resultant plasmonic phenomenon toward the infrared range. There are three classes of semiconductor materials that have been extensively studied for plasmonic applications: metal oxides[9,11,12,20,35] (In_2O_3, ZnO, CdO, WO_3, and MoO_3), metal chalcogenides[13,19,20] (CuE and HgE, where E = S, Se, or Te), and III−V compounds[22,204] and Group IV elements[10,106,205] (Si, Ge, nitrides, or phosphides).

Depending on the oxidation state of the dopant relative to host ions, the free carriers in doped semiconductors can be either electrons (n-type dopant) or holes (p-type dopant) (Figure 5a). Either n-type and p-type doping at high concentrations is

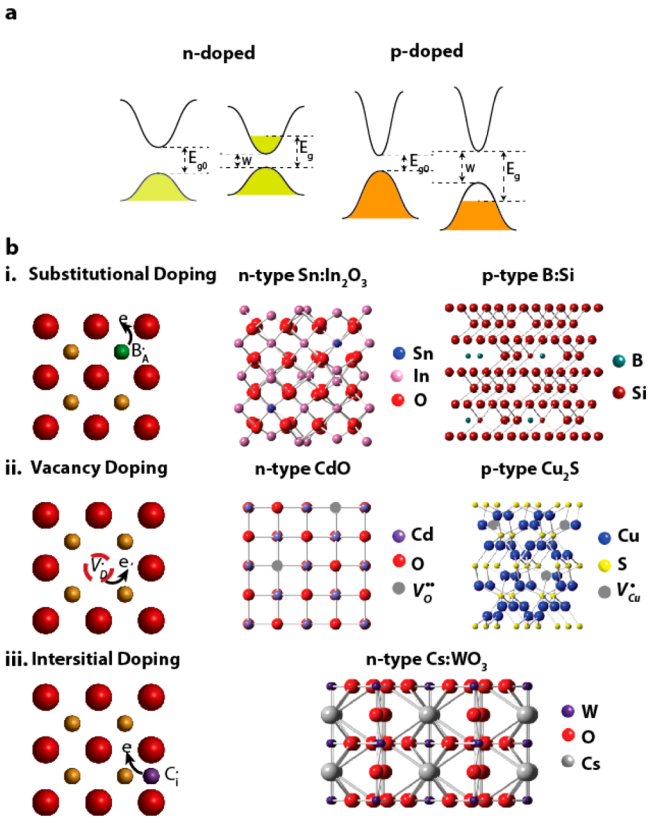

Figure 5. Doping semiconductors. (a) Schematics of the band structure of n-type and p-type semiconductors. When the stoichiometric material is doped either via n- or p-type doping, introduction of dopant perturbs the band gap of the host lattice. In the case of n-type doping such as Al:ZnO, the electronic band gap shrinks, while the Fermi level moves up in conduction band, determining the net optical band gap. In contrast, p-type doping such as introducing copper vacancies in $Cu_{2-x}S$ increases the electronic band gap and moves the Fermi level into the valence band, thereby increasing the optical band gap with increasing dopant concentration. Adapted from ref 13 with permission from The Royal Society of Chemistry. (b) Schemes of common doping mechanisms with host cations (orange spheres) and anions (red spheres) and corresponding examples of n- and p-type-doped semiconductor systems. Three common donor doping types are (i) aliovalent substitutional impurities, (ii) vacancies, and (iii) interstitial impurities. Schematics are reprinted from ref 35. Copyright 2014 American Chemical Society.

DOI: 10.1021/acs.chemrev.7b00613
Chem. Rev. 2018, 118, 3121−3207

necessary to induce a plasmonic response. However, this high concentration can also significantly perturb the band structure of the host material such as through hybridization or distortion in the host lattice that then impacts the band structure and the mobility of free carriers within the material. Several types of defects occur in semiconductors, each with their own impact on the band structure of the material. Intrinsic doping by vacancies (Figure 5b, top), extrinsic aliovalent substitutional doping to introduce free carriers (Figure 5b, middle), and extrinsic interstitial doping compensated by free carriers (Figure 5b, bottom) have all been discussed in the literature.[11,35]

Most metal oxides (In_2O_3,[206] CdO,[187] ZnO,[54,207] MoO_3,[158] cubic WO_3,[45,113] and monoclinic WO_3[113]) are n-type intrinsically doped with some equilibrium oxygen (anion) vacancy concentration. In such cases, equilibrium vacancy concentration can be controlled by adjusting oxygen partial pressure or kinetically trapping a nonequilibrium concentration. In contrast, metal chalcogenides (Cu_2E,[19,98,146,189] where E = S, Se, or Te) are p type intrinsically doped with a Cu (cation) vacancy concentration. The Cu vacancy concentration can be controlled using oxidation/reduction and cation exchange.[42,43,112,146,208]

Aliovalent doping [e.g., Sn:In_2O_3 (87, 184, 185, 195, and 209−212), In:CdO (111, 124, 135, 186, and 213), Al:ZnO (54, 70, 84, 86, 207, 214, and 215), P:Si (57, 106, 107, 190, and 200), B:Si (107, 200, and 216), and CuSSe (217−219 etc.) has been widely used in the semiconductor industry for tuning the electronic properties of materials. Here, a lattice atom is substituted by an atom of higher or lower valence to n- or p-dope the material. Depending on the energy equilibrium of a given doped semiconductor, these n- or p-doping sites can contribute free carriers to the material, (i.e., they are activated) or they can be compensated by cation or anion vacancies or interstitial oxygen or other defects. Incorporation of aliovalent dopants in metal oxides, metal chalcogenides, III−V materials, or elemental semiconductors, and its impact on free carrier optical properties is discussed in detail later in this text.

Extrinsic interstitial doping can also introduce electrons into the conduction band of semiconductor metal oxides. Some metal oxides like M_xWO_3 (M = Cs, K, Li, Na, etc.) allow intercalation of ions due to a relatively open crystal lattice, resulting in accumulation of delocalized free electrons in the conduction band.[56,113,220,221] Several researchers have shown that lithiation of crystalline tungstate materials enhances light absorption.[37,74,75,222,223] Yang et al.[224] demonstrated with density functional theory (DFT) that lithiation of tungsten oxide leads to substantial free carrier density.

Dopants, along with introducing free carriers, also modify the crystal structure of the host material. Several researchers have shown that depending upon the Cu vacancy concentration, $Cu_{2-x}E$ materials have different equilibrium phases moving from low symmetry hexagonal phase for low Cu deficiency to more symmetric FCC phase for highly deficient Cu stoichiometry.[13,19,21,188] In the case of an aliovalent dopant, Radovanovic et al.[209,225] observed two products from a single reaction; NCs 5 nm in diameter trapped in the metastable corundum (rh-Sn:In_2O_3) phase and larger (>10 nm) NCs in the cubic bixbyite phase (bcc-Sn:In_2O_3). These phases have distinctly different dopant-dependence of their optical response. Furthermore, Mattox et al.[113] showed that Cs incorporation in monoclinic tungsten oxide leads to NC phase change to hexagonal crystal structure. Phase control and its impact on plasmonic properties is a major discussion point later in this review (sections 2.3.5 and 2.4.1).

2.2.2. Free Carrier Scattering. While increasing the carrier concentration shifts plasma frequency toward higher energy, it also causes the imaginary part of the dielectric function to increase, and thus leads to optical loss. The other crucial parameter that quantifies the optical loss per the Drude-Lorentz model is the damping constant which can be qualitatively understood as the rate of energy loss from a free carrier excitation. There are several scattering mechanisms that impact free carrier energy loss in plasmonic systems such as electron−electron or hole−hole scattering (γ_{e-e} or γ_{h-h}), electron/hole-phonon scattering ($\gamma_{e/h-ph}$), interband transition scattering (γ_{ib}), surface scattering (γ_s), and electron/hole-impurity scattering ($\gamma_{e/h-i}$) as well as material and morphologically specific scattering mechanisms. These scattering mechanisms are additive via Matthiessen's rule, leading to the overall scattering function of the material[35,111,114,125,226] (eq 11),

$$\gamma = \sum \gamma_i = \gamma_{e-e/h-h} + \gamma_{e/h-ph} + \gamma_{ib} + \gamma_s + \gamma_{e/h-i} + .. \quad (11)$$

Some loss processes are intrinsic, such as the case of the d-d transition intraband scattering (γ_{ib}) characteristic of gold.[26] On the other hand, silver does not have significant intraband scattering due to little overlap between such transitions and the LSPR frequency.[25] Semiconductors typically have little overlap between intra or interband excitation and free carrier excitation, so interband or intraband scattering does not significantly impact the LSPR excitation. Electron (hole)−phonon scattering $\gamma_{e/h-ph}$ is strongly temperature-dependent and makes a significant contribution to overall scattering only at high temperatures.[111,227] Electron−electron/hole−hole ($\gamma_{e-e/h-h}$) scattering is a minor contributor due to minimal interaction between electrons/holes. Impurities and vacancies in semiconductors, however, can lead to significant defect scattering ($\gamma_{e/h-i}$), which becomes an important source of damping. In NCs with sizes less than the electron mean free path, surface scattering (γ_s) can also be a significant contributor to damping. Since surface scattering is NC specific, however, generalizing this phenomenon using the Drude model is difficult, and failure to treat surface scattering is usually considered as a limitation of the Drude model (section 2.2.3.2). The optical properties of semiconductors (metal oxides, metal chalcogenides, or III−IV systems) are ultimately determined by the choice of dopant type, carrier concentration, and free carrier scattering by the host matrix that lead to distinct dielectric properties, which then dictate the localized surface plasmon resonance (LSPR) of semiconductor NCs as will be discussed in the next sections (section 2.3−2.5).

2.2.3. Limitations of Conventional Treatment of LSPR. The Drude-Lorentz model is a simple model that treats the conduction electrons as a free gas, but it still sufficiently explains macroscopically observable optical phenomena like LSPR with reasonable accuracy. Having been applied to semiconductor systems, which possess complex electronic structure and low free carrier density, the validity of the model has been tested again, and some of the major questions that have been addressed by researchers are as follows. (1) How does nonparabolicity of the conduction band at high dopant concentrations affect the applicability of the Drude model? (2) What happens at ultralow free carrier density (1−10 electrons per NC)? Do the NCs still behave like continuum materials? (3) How does quantum confinement at small sizes change the free carrier optical dynamics?

DOI: 10.1021/acs.chemrev.7b00613
Chem. Rev. 2018, 118, 3121−3207

2.2.3.1. Nonparabolic Bands. Plasma frequency is the Drude parameter that macroscopically captures the impact of the electronic structure via changes in the free carrier effective mass. The effective mass ($m_e = \frac{h^2}{d^2E/dk^2}$ where h is Planck's constant, E is the density of states, and k is the wavevector), depends on the curvature around the CBM for electrons and VBM for holes.[227] This treatment is valid only for parabolic bands, and it neglects the true nature of band structure, which can deviate significantly from parabolicity at energies relevant to degenerately doped systems. Specifically, when a semiconductor is highly doped, electronic states far from the band edges become occupied, and these states far from the band edge may more likely be influenced by the nonparabolicity of the band structure.[52,187]

To address this impact of band structure nonparabolicity and its influence on LSPR properties, Jung and Pedersen[52] computationally demonstrated the effects of nonparabolic bands on crucial optical parameters such as the plasma frequency. In their work, plasma frequency was calculated considering the full band structure, the latter being calculated using the empirical pseudopotential method. In addition to taking into account the nonparabolic band structure, calculation of the full band structure allows the study of plasma frequency dependence on crystalline anisotropy and the relative polarization of light. Their calculation showed that if the Fermi level is close to the conduction band edge, the effective mass approximation yields a similar result to the full band calculation. But if the Fermi level is deep inside the band, for either n- and p-type doping, the plasma frequency reaches saturation due to saturation in electronic density of states (EDOS) arising from the nonparabolic bands (Figure 6). These results showed that for n-type material, deriving plasma frequency based on the effective mass approximation from experimental extinction spectra would severely underestimate the free carrier density. Similar observations were made for a broad range of semiconductor plasmonic materials, including Si, Ge, GaAs, ZnO, and GaN. For ZnO, the authors proposed a 3D-band based effective mass formulation (eq 12), with one free parameter, α, that expresses the asymptotically linear nature of the conduction band.

$$\omega_p^2 = \frac{e^2 n_e}{\epsilon_0 m_e} \frac{1}{\sqrt{1 + (9\pi^2 n_e)^{2/3} h^2/(m_e \alpha)}} \quad (12)$$

Comprehensive experimental or theoretical studies taking into account detailed electronic and crystal structures of semiconductors and their implications for optical properties are few, and this area warrants further detailed study.

2.2.3.2. Small Sizes and Low Carrier Density. Size-dependent optical properties such as photoluminescence (PL) are among the most studied properties of semiconductor NCs. Similar to PL, LSPR properties of semiconductor NCs are size-dependent.[228−234] For LSPR, reduction in NC size results into two changes. First, when the size of the NC is less than the mean free path, free carriers experience substantial surface scattering. Increasing surface scattering as NC size decreases results in an overall increase in free carrier scattering.[228,229,234,235] Second, decrease in NC size leads to quantum confinement effects on the states near the CBM/VBM that cause the continuous distribution of states found in bulk semiconductors to become discretized into particle-in-a-spherical well-like states. Confinement results in IR absorption transitioning from continuum LSPR absorption to more discrete intraband absorption (see Figure 7).

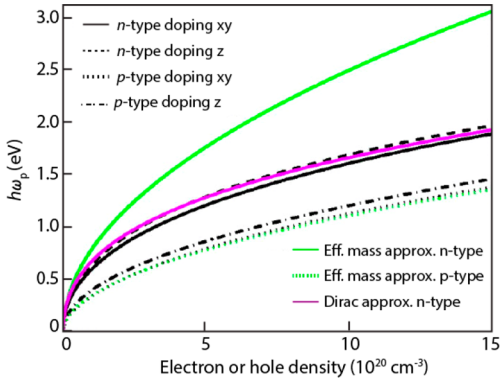

Figure 6. Nonparabolic band. Calculated plasma frequency ω_p (in eV) as a function of free carrier concentration in n- and p-doped ZnO. The calculated plasma frequency based on the full band structures (black curves) diverges from the parabolic band approximation for both n- and p-type systems (green curves). Additionally, calculations based on full band structures show polarization-dependent optical characteristics. Prediction based on the Dirac effective mass model corrected for nonparabolic bands (magenta curve) agrees well with the full band calculations. Reprinted with permission from ref 52. Copyright 2013 American Institute of Physics.

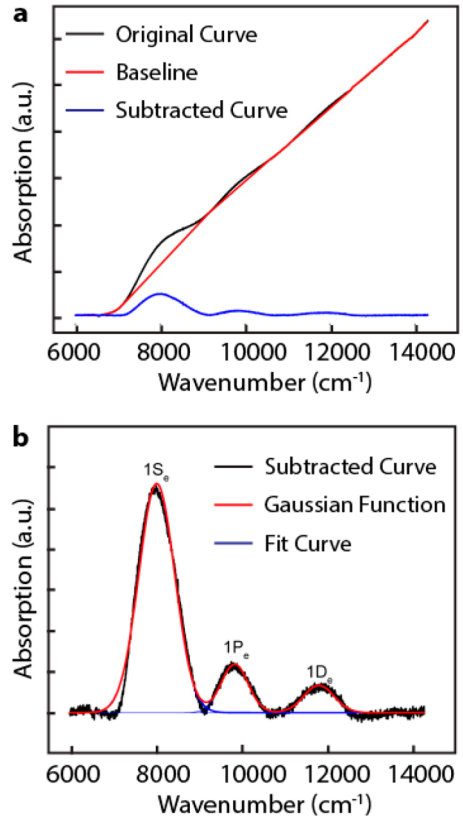

Figure 7. Band splitting in quantum confined systems. (a) Absorption spectrum of 5.7 nm HgS quantum dots (black) along with the baseline (red) and the subtracted curve (blue). (b) The subtracted curve and the corresponding three Gaussian functions that possibly corresponds to the first nine quantum confined states arising from the conduction band, $1S_e$ (1 state), $1P_e$ (3 state), and $1D_e$ (5 states). Reprinted with permission from ref 230. Copyright 2016 American Chemical Society.

DOI: 10.1021/acs.chemrev.7b00613
Chem. Rev. 2018, 118, 3121−3207

Due to reduction of size of the NC below the mean free path, the electronic density profile extends beyond the physical surface, popularly known as the spillover effect.[228,229,235,236] The importance of spillover increases as NC size decreases, which results in higher surface scattering. Using the conventional treatment of surface scattering developed for plasmonic metal nanoparticles, overall LSPR scattering coming from the bulk and surface scattering can be expressed as,

$$\gamma = \gamma_b + \frac{A\nu_F}{D} \tag{13}$$

Here, γ is the overall scattering, γ_b is the bulk scattering, ν_F is the Fermi velocity, D is diameter of the NC, and A is an empirical constant that can be set using fits of experimental data. This increase in electron scattering results in red-shifting of LSPR peak energy and broadening of LSPR spectra, which has been observed in metal and semiconductor metal chalcogenide LSPR. Recently, Monreal et al.[228,229] published theoretical work on surface scattering in ultralow electron density LSPR materials suggesting that in addition to the spillover effect due to nanoscale size, there is a substantial increase in diffuse surface scattering due to the roughness of the NC surface, further broadening the LSPR spectrum.

Moreover, exceptionally small NCs exhibit quantum confinement effects on the states near the CBM that causes the continuous distribution of states from bulk to become discretized into particle-in-a-spherical well-like states.[54,230,231] The first 9 quantum confined states to emerge from the CBM are assigned as the $1S_e$ (1 state), $1P_e$ (3 states), and $1D_e$ (5 states). When one or more of these states are filled, new electronic transitions emerge for the $1S_e \rightarrow 1P_e$ and the $1P_e \rightarrow 1D_e$ transitions (with some contribution from $1S_e \rightarrow 1D_e$ if the symmetry of the orbitals is broken and parity selection rules are relaxed). Similar band splitting takes place near VBM and new hole transitions emerge in corresponding p-type quantum-confined NCs. These so-called "intraband transitions" can be observed at IR frequencies and are size-dependent since the spacing between these electronic states increases as NC size decreases (Figure 9a). These electronic transitions are clearly quantum mechanical in nature and simulation shows they can arise under the same conditions that cause semiconductor NCs to be plasmonic (occupation of electrons in the conduction band reaching carrier concentrations above 10^{19} cm^{-3}).

This change from intraband transitions to LSPR with increasing size can complicate the interpretation of the spectral signatures. Though the spectral change from intraband transitions to LSPR may appear seamless, the conceptual change is significant as it requires a switch from a framework consisting of discrete states that enable PL to that of a free electron gas with a continuum of states available for ensemble electron excitation giving rise to a plasmon[230] (Figure 8a). An addendum to the latter is that the continuum of states is achieved when intraband states are energetically spaced less than k_bT, and in that case, the LSPR takes the place of the lowest energy intraband transition. However, one may anticipate still being able to see $1S_e \rightarrow 1D_e$ transition in addition to an LSPR at this limit. Making sense of experimental observations of this gradual evolution even in systems with carrier Bohr radii that are quite large requires considering the impact of inhomogeneous broadening on the intraband transitions measured.

Inhomogeneous broadening can emerge from the influence of charged defects (either dopants or surface adsorbed species) on the electronic transitions. DFT studies[54] that compared the

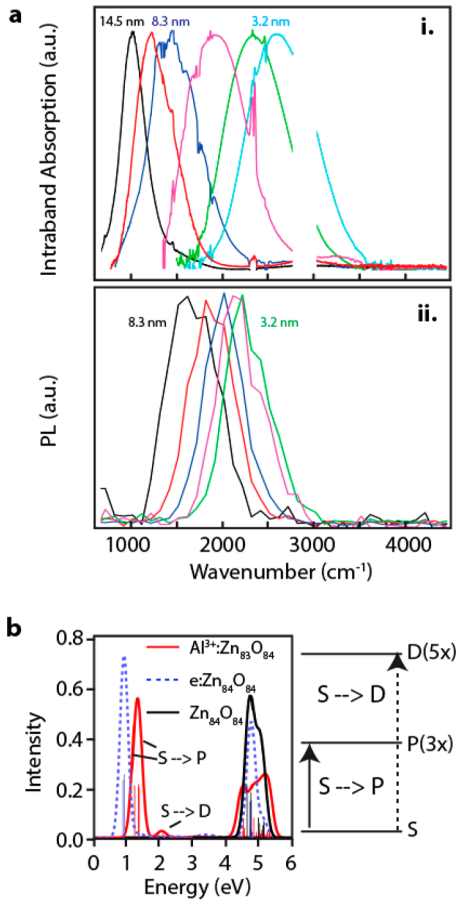

Figure 8. Transition between intraband and LSPR excitation. (a) Normalized absoprtion and PL spectra of HgS quantum dots. Absorption spectra show that as the NC size increases, the nature of optical absorption evolves from intraband band transitions to free carrier excitation. For the smaller NCs, where intraband transitions are dominant, distinct PL features can be observed from the relaxation of the excited states. Reprinted from ref 230. Copyright 2016 American Chemical Society. (b) Calculated absorption spectra of $Zn_{33}O_{33}$ QDs containing a single Al^{3+} dopant (red solid line), a single added e_{CB}^- (blue dashed line), or neutral (undoped) (black dotted line). Broken symmetry due to the introduction of an Al^{3+} dopant weakly allows S → D transitions on the top of S → P transitions observed in calculated spectra. Schematic of superorbital transitions illustrates the possible transitions. Reprinted from ref 54. Copyright 2014 American Chemical Society.

orbital structure of the quantized conduction band states for an electron in ZnO with no point charge compensation versus that of ZnO with a single Al^{3+} dopant show how dopant placement affects the selection rules for intraband transitions. In the spherically symmetric case, only the S → P and P → D transitions appear, while no S → D is observed since this is parity forbidden. When a defect is located near the surface, breaking the spherical symmetry, the charged defect distorts the orbitals to the point that the S → P, P → D, and S → D transitions are all observed and the broken degeneracy of orbitals leads to a general broadening of the otherwise discrete transition (Figure 8b). Size heterogeneity will also lead to broadening of these discrete states as the energy spacing of the conduction band orbitals is strongly size dependent (approximately scaling with $1/R^2$). Additionally, in charged quantum dots with only a few electrons per dot (often 1−4 for the smallest NCs), though the average charge per NC may be, for example, only 2 electrons per NC,

DOI: 10.1021/acs.chemrev.7b00613
Chem. Rev. 2018, 118, 3121−3207

there will be a distribution of total charge per individual NCs that also broadens the intraband spectra.[196] That is why observed intraband peaks tend to be much broader experimentally than the LSPR peak observed at larger sizes (though this broadening could include contributions due to surface scattering damping in an LSPR).

Similar to the quantum size effect, low carrier density (1−5 electron per NC) in a nonquantum confined particle reveals a similar crossover between intraband transition and LSPR excitation. In his theoretical work on LSPR in low carrier density materials, Jain[233] argued that quantum mechanical intraband transitions dominate in the low carrier regime, followed by an intermediate regime, where both intraband and plasmon excitations coexist, and then at higher carrier density, plasmon excitation dominates the overall extinction. More extensive time-dependent DFT performed by Zhang et al.[231] for CdSe and $Cu_{2-x}S$ gave similar results (Figure 9b). The calculation showed that in the low carrier density regime, peak plasmon energy approaches a constant value rather than zero as predicted by classical plasmon theory. Both Jain[233] and Zhang et al.[231] suggested that overall peak extinction frequency can be expressed as,

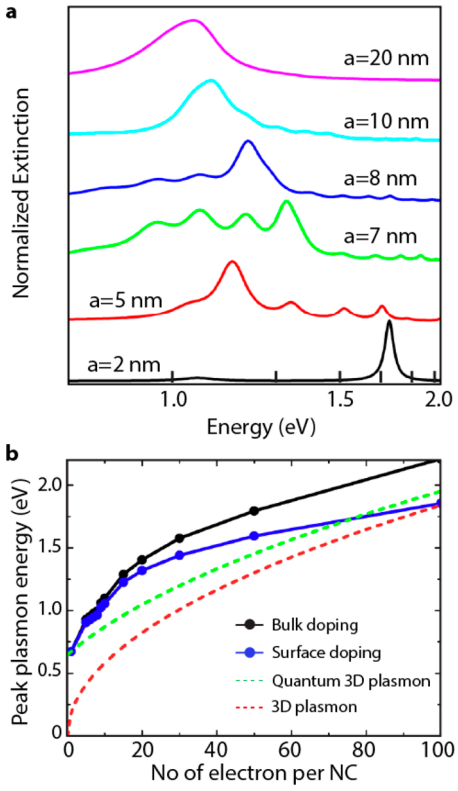

Figure 9. Extinction in quantum-confined systems. (a) Emergence of intraband transitions is observed in calculations performed for quantum-size confined systems. As the size of the NC decreases, carriers become quantum confined and the spectrum determined by collective excitation at large sizes starts displaying discrete quantum mechanical transitions. Reprinted from ref 233. Copyright 2014 American Chemical Society. (b) DFT calculated peak plasmon energy as a function of the number of electrons per NC in CdSe. As predicted by the classical 3D plasmon model, LSPR frequency should approach zero as the number of electrons approaches zero, but instead due to the origin of intraband transitions at lower carrier count, overall peak plasmon energy approaches a constant value both for surface and bulk-doped systems. Reprinted from ref 231. Copyright 2014 American Chemical Society.

$$\omega_r^2 = \omega_{qm}^2 + \omega_{LSPR}^2 \tag{14}$$

or

$$\omega_r^2 = \omega_{qm}^2 + \frac{\omega_p^2}{\epsilon_\infty + 2\epsilon_m} \tag{15}$$

where ω_r is the overall peak extinction frequency, ω_{qm} is the quantum mechanical transition frequency, and ω_{LSPR} is the LSPR frequency.

Surface scattering effects and evolution of LSPR toward intraband extinction both due to quantum confinement and low carrier density warrants in-depth validation of the conventional Drude model whenever it is applied to a semiconductor system. To complement the discussion in this section, we have also included a discussion on photocharging of quantum confined semiconductor NCs and its impact on the associated intraband transitions later in this review (section 4.3).

2.3. Metal Oxide NCs

2.3.1. Doping Metal Oxides. Plasmonic metal oxides (ZnO,[54,207,214] CdO,[111,187,237] In_2O_3,[211] WO_3,[56,74,75,220,224] and MoO_3[158,238]) always possess some equilibrium oxygen vacancies, the concentration of which is governed by the thermodynamics of defect formation. Often, the contribution of electrons from oxygen vacancies leads to intrinsic degenerate doping in these semiconductors. And while incorporating aliovalent dopants or deliberate defects into the crystal lattice generates additional free carriers in metal oxides, one must consider how different defect equilibria influence one another to predict the change in overall carrier concentration. For example, substitutional doping of Sn in $Sn:In_2O_3$ donates charge carriers but also impacts the thermodynamic equilibrium for creating oxygen vacancies, another electron donor. In general, doping in metal oxides can be divided into three distinct regimes: intrinsic, extrinsic, and compensation (Figure 10a).

In the intrinsic regime, aliovalent dopants are either not present or are at a low concentration. The free carriers in the conduction band are charge-compensated dominantly by intrinsic oxygen vacancies. Equilibrium oxygen vacancy concentration can be controlled by adjusting oxygen partial pressure while at sufficiently high temperature to enable diffusion, and then vacancies can be kinetically trapped by cooling. Several researchers have observed that oxygen vacancy concentration in intrinsically doped metal oxides can be controlled by tuning the effective oxygen partial pressure during NC synthesis.[56,239,240] Since oxygen vacancies are each compensated by two free electrons in order to maintain charge neutrality, these defects can generate carrier concentrations on the order of 10^{19} cm^{-3}, rendering even undoped metal oxide NCs plasmonic.

Second, in the extrinsic regime, lattice atoms are substituted by aliovalent dopants to raise or lower the Fermi level. Depending on the energetic proximity of the dopant orbitals to the bands of the metal oxide and the energy cost of creating other lattice defects, free carriers can result (i.e., the dopants are activated), or they can be compensated by other defects such as cation vacancies or interstitial oxygen forming various defect complexes inside the host lattice. (This latter effect is dominant in the third regime−compensation.) Several recent studies (see refs 35, 58, 59, 108, 114, 115, and 241−244) have focused on studying complex defect equilibrium dynamics of oxygen vacancies, activated dopant ions, and defect complexes and the impact of their concentrations on optical properties arising from LSPR.

DOI: 10.1021/acs.chemrev.7b00613
Chem. Rev. 2018, 118, 3121−3207

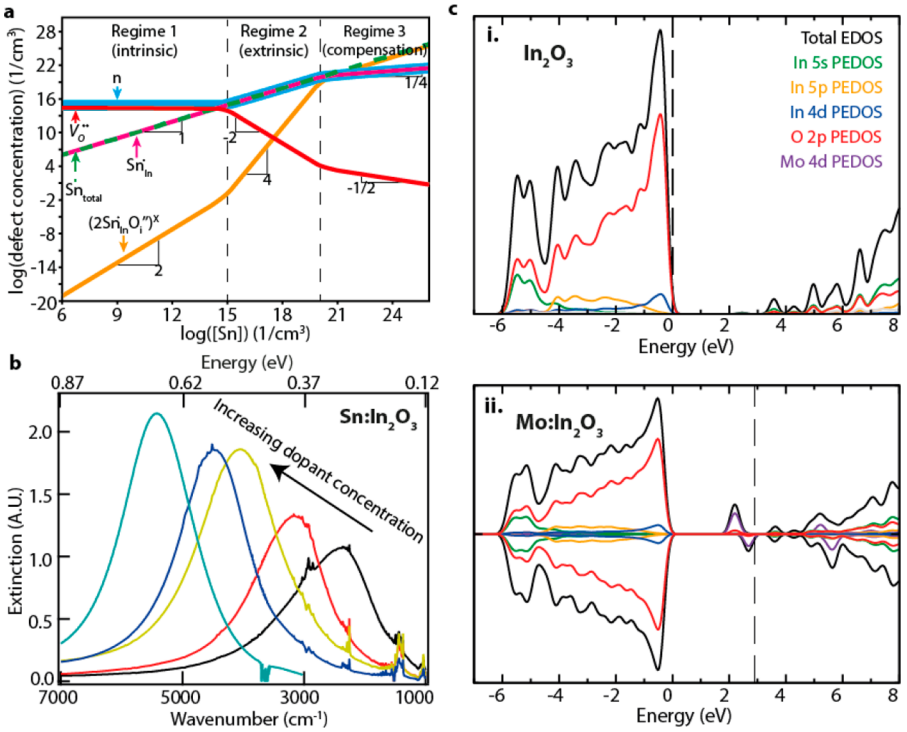

Figure 10. Doping metal oxide semiconductors. (a) Brouwer defect equilibrium diagram for [Sn] and oxygen vacancies in In_2O_3 at fixed partial pressure of O_2. The free electron concentration depends upon the relative concentrations of activated Sn dopant $Sn_{In}^{\cdot}$, oxygen vacancies $V_O^{\cdot\cdot}$, and $(2Sn_{In}^{\cdot} - O_i'')$ complexes. Reprinted from ref 35. Copyright 2014 American Chemical Society. Original graphic from ref 35 adapted with permission from ref 114. Copyright 2000 Elsevier. (b) FTIR spectra of $Sn:In_2O_3$ NCs at various dopant concentrations (0−5 at % Sn); oxygen vacancies in In_2O_3 lead to a LSPR at approximately 2,000 cm^{-1} (black). As expected from the Brouwer diagram, increasing Sn concentrations (all other colors) leads to LSPR shifting toward higher energy, and at high dopant concentration LSPR saturates at approximately 5500 cm^{-1}. Reprinted with permission from ref 11. Copyright 2017 Annual Reviews. (c) Calculated total and partial electronic density of states (EDOS and PEDOS, respectively) for (i) pure In_2O_3 and (ii) one Mo dopant on the 8*b* site in a 40-atom primitive cell. The dashed lines indicate the highest occupied states. The absence of Mo 4d state density near the CBM leads to a low free electron ionized impurity scattering by the $Mo_{In}^{\cdot}$ defect site. Reprinted from ref 110. Copyright 2015 American Chemical Society.

Ágoston et al.[108] and Hwang et al.,[114] studied $Sn:In_2O_3$ defect chemistry to elucidate the interplay between Sn doping and other defect compensation (Figure 10a). They showed that carrier concentration depends on the relative contribution of oxygen vacancies (intrinsic), substitutional Sn^{4+} atoms (extrinsic), and oxygen interstitial atoms which compensate for Sn and form $(2Sn_{In}^{\cdot} - O_i'')$ defect complexes (compensation). High Sn dopant concentration in the compensation regime leads to saturation effects in which Sn no longer increases free electron concentrations at high dopant concentration. These regimes are apparent in observing the LSPR energy as a function of Sn concentration. Undoped In_2O_3 NCs exhibit a low energy LSPR that blue shifts with the addition of Sn, but eventually adding more Sn cannot further blue shift the LSPR and may even lead to a red shift[151,211,212,245] (Figure 10b). Similar behavior has been reported by Sachet et al.[58] for Dy:CdO thin films, Taha et al.[115] for Al:ZnO and Ga:ZnO NCs, and Fang et al.[242] for $Ti:In_2O_3$ and $Sb:In_2O_3$. Sachet et al.[58] proposed the following defect reaction mechanism to understand the defect equilibria in the Dy:CdO system.

$$Cd_{Cd}^{x} + O_o^{x} \Leftrightarrow Cd_{Cd}^{x} + V_O^{\cdot\cdot} + 2e^{-} + \frac{1}{2}O_2\ (g) \tag{16}$$

$$Dy_2O_3 \xrightarrow{CdO} 2Dy_{Cd}^{\cdot} + O_o^{x} + 2e^{-} + \frac{1}{2}O_2\ (g) \tag{17}$$

They argued that in intrinsic cadmium oxide, electrons originate from doubly ionized O vacancies (eq 16). By changing oxygen partial pressure, one can modulate O vacancy concentration. Further doping with aliovalent cations, here Dy, will act as an extrinsic donor (eq 17). By Le Chatelier's principle, increasing the Dy concentration will drive the oxygen vacancy equilibrium backward. At high concentrations of Dy, clustering of dopants is favored in CdO. These parameters have important impacts on the dielectric function as the $Dy_{Cd}^{\cdot}$ and $V_O^{\cdot\cdot}$ concentrations will shift the plasma frequency of the metal oxide, while defects can also change the damping constant of the material.

The charge of the donor sites (Z) influences the strength of ionized impurity scattering. In fact, the impurity or defect scattering potential scales with Z^2. As a result, dianion oxygen vacancy sites contributing two electrons will scatter more than two singly ionized aliovalent sites. Depending on the relative defect equilibria, tunable carrier concentration and low scattering can be achieved by an optimal ratio of extrinsic and intrinsic doping.

Sachet et al.[58] also discussed the role of strain in scattering and mobility within metal oxides. Since Dy^{3+} and Cd^{2+} have similar ionic radii, CdO experiences less lattice perturbation from Dy doping than from O vacancies. Runnerstrom et al.[59] and Fang et al.[242] have recently generalized this concept in NCs of In_2O_3. Runnerstrom et al.[59] argued that due to relatively similar sizes of the Ce^{4+} and In^{3+} ions, lattice strain in $Ce:In_2O_3$ is minimal. A similar argument is presented by Fang et al.[242] for $Ti:In_2O_3$ and $Sb:In_2O_3$.

DOI: 10.1021/acs.chemrev.7b00613
Chem. Rev. 2018, 118, 3121−3207

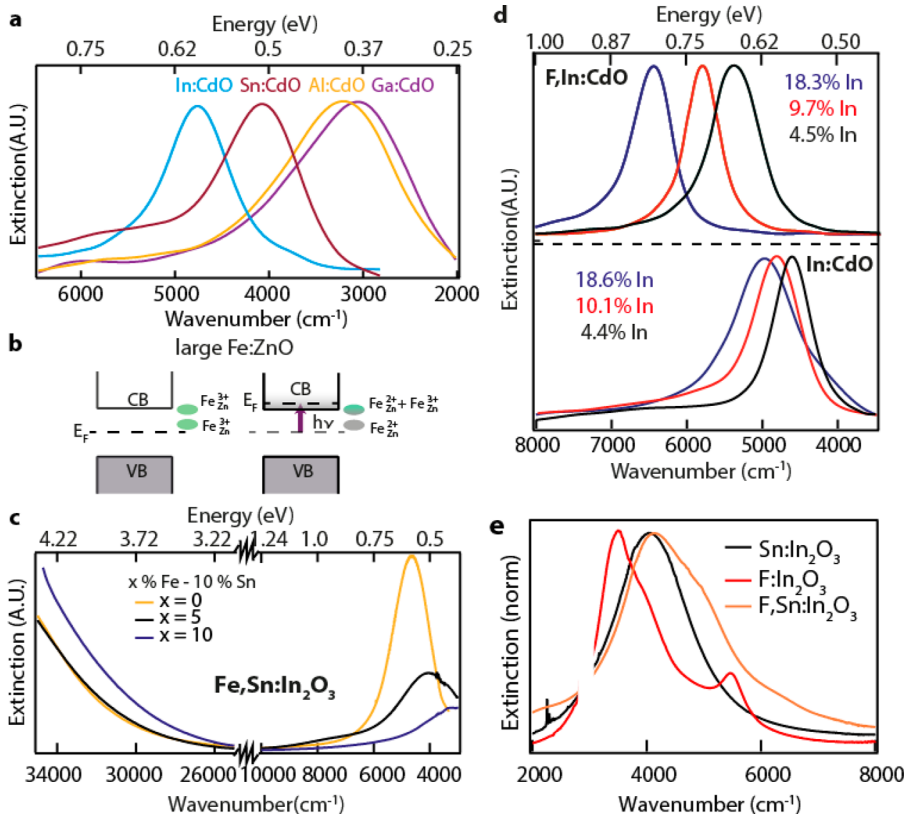

Figure 11. LSPR in doped metal oxide NCs. (a) Normalized extinction spectra of doped CdO NCs dispersed in tetrachloroethylene (TCE). Due to the different extents of dopant incorporation into the NCs during colloidal synthesis and different defect equilibrium dynamics, different dopants such as In (blue), Sn (red), Al (yellow), and Ga (violet) show LSPR saturation at different frequencies. Adapted from ref 123. Copyright 2014 American Chemical Society. (b) Schematic band diagram for Fe-doped ZnO NCs before and after raising the Fermi level by photodoping. Incorporation of Fe into the ZnO lattice leads to deep trap states, which effectively reduces the overall photoinduced free electron concentration. CB and VB denote conduction band and valence band, respectively. Adapted with permission from ref 246. The Royal Society of Chemistry. (c) The reduction of overall free electron concentration resulting from codoping Fe with Sn in In_2O_3 NCs leads to a redshift of LSPR spectra, denoting a decrease in free carrier density as electrons localize on Fe sites. Adapted from ref 136. Copyright 2014 American Chemical Society. (d) Normalized extinction spectra of codoped F,In:CdO NCs and In:CdO NCs dispersed in tetrachloroethylene. Incorporation of F^- as a codopant gives access to higher-energy LSPR compared to In:CdO samples with similar In doping levels. Reprinted from ref 122. Copyright 2014 American Chemical Society. (e) Normalized extinction spectra of $Sn:In_2O_3$, codoped $F,Sn:In_2O_3$ NCs, and $F:In_2O_3$ NCs dispersed in TCE. Incorporation of F^- as a dopant lowers the overall damping in the material. Adapted from ref 89. Copyright 2017 American Chemical Society.

Though strain negatively impacts mobility, doping can lead to changes in the band structure that even more significantly impact the resulting LSPR. Using Ce instead of Sn as a dopant results in a decrease in LSPR line width by 30%; however, the LSPR saturates in the mid-IR while Sn doping can reach NIR resonance. Using electronic structure calculations, similar results were earlier postulated by Bhachu et al.[110] for $Mo:In_2O_3$ and later expanded on by Runnerstrom et al.[59] for $Ce:In_2O_3$ and by Fang et al.[242] for $Ti:In_2O_3$ and $Sb:In_2O_3$. Electronic structure calculations of $Mo:In_2O_3$ showed that states near the bottom of conduction band are primarily of In 5s and O 2p character (Figure 10c), similar to that of undoped In_2O_3. This means that if the dopant orbitals do not have good energy overlap with these orbitals they will not hybridize well near the CBM, resulting in free carriers being effectively electrostatically screened from significant dopant-based ionized impurity scattering. Compared to $Sn:In_2O_3$, $Ti:In_2O_3$, or $Sb:In_2O_3$, in which dopants hybridize well near the CBM and induce high overall scattering, Mo and Ce orbitals hybridize with states much higher in energy than the CBM. Indeed, scattering in $Mo:In_2O_3$ or $Ce:In_2O_3$ materials is less prevalent, resulting in a substantial decrease in LSPR line width. Moreover, Bhachu et al.[110] observed that in $Mo:In_2O_3$, Mo has +4 oxidation state and not +6. As evident from the electronic structure calculations, they argued that Mo has strong 4d character both above and below the CBM. More specifically, there are two localized t_{2g} α-spin states in the band gap, below the CBM, and there is one t_{2g} β-spin state above the CBM. These calculations for various In_2O_3 systems show that dopant hybridization with the host lattice greatly impacts the free carrier concentration and ionized impurity scattering, both of which are crucial in determining LSPR properties in metal oxide NCs.

Control over dopant type and dopant concentrations and the impact on LSPR is a nontrivial aspect of understanding LSPR in metal oxide NCs. Irrespective of the origin of the free electrons, photodoped ZnO NCs are spectroscopically similar to compositionally doped Al:ZnO NCs. Both show metallic behavior as characterized by EPR.[39,247] However, both theoretical[54] and experimental studies[84] have indicated that the presence of the Al^{3+} ion changes the LSPR damping.[70,123] Also, incorporation of different dopants into the same lattice can lead to very different energies and peak shapes in the LSPR within the same host material, as in the case of CdO[123] (Figure 11a). Similar observations have been made for In_2O_3[59,151,209,242,248] and ZnO[115,247,249] systems. As discussed earlier, different dopants

DOI: 10.1021/acs.chemrev.7b00613
Chem. Rev. 2018, 118, 3121−3207

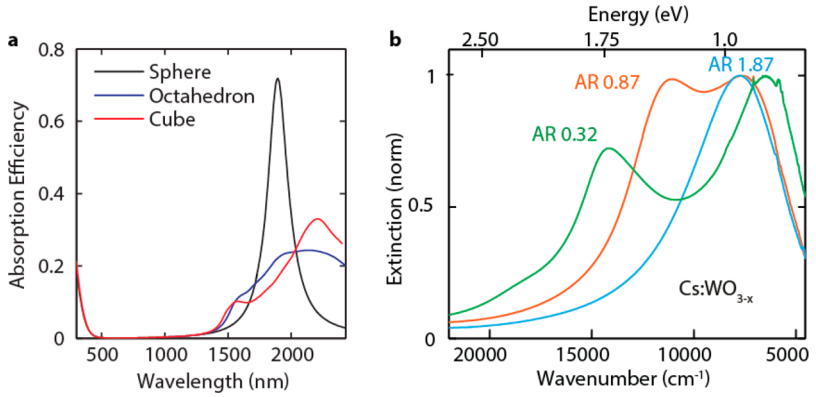

Figure 12. LSPR dependence on NC shape and crystal structure. (a) Calculated extinction spectra of differently shaped In:CdO NCs with a carrier density of 1.11×10^{21} cm^{-3}. The spectra of cube and octahedron show multipeak absorption profiles corresponding to different geometrical LSPR modes. Reprinted from ref 135. Copyright 2015 American Chemical Society.(b) Normalized optical absorption spectra of hexagonal $Cs:WO_3$ NC samples of platelets (green), isoprisms (red), and rods (blue) dispersed in TCE. Spectra show strong aspect ratio (AR) dependence of the LSPR response, which was explained by accounting for both shape and crystalline anisotropy in these NCs. Reprinted from ref 56. Copyright 2016 American Chemical Society.

hybridize differently with the host matrix bands, which results in different dopant concentration-dependent electron effective mass. Moreover, Fang et al.[242] argued that due to the formation of deep defect states within the band gap of $Ti:In_2O_3$, for the same Sb or Ti doping percentage, the LSPR frequency of $Ti:In_2O_3$ is always at lower energy compared to $Sb:In_2O_3$. Such phenomena are widely reported across several metal oxide systems.

2.3.2. Co-Doping Metal Oxides. Incorporating multiple types of substitutional doping in the same material can lead to opening a large dynamic range for the carrier concentration. In the case of CdO, both In^{3+} and F^- substitutional dopants are defects that contribute one electron to the conduction band.[122] Interestingly, though, even after In doping saturates at high dopant concentrations (~20%), codoping with F can lead to a substantially higher carrier concentration beyond that point (Figure 11, panels d and e) and is accompanied by a decrease in line width at similar dopant concentrations. This effect shows that using multiple dopants in the same material can introduce multiple benefits, not only by boosting carrier concentration with multiple electron sources but also by enhancing carrier mobility like in the case of F in CdO. Similarly, Agrawal et al.[89] observed reduction in electron damping on introduction of F as the codopant in $Sn:In_2O_3$ lattice. They argued that fluorine ions likely occupy oxygen sites ($F_O^{\cdot}$), contribute free electrons, and decrease the oxygen vacancy concentration. Because the extent of ionized impurity scattering is directly proportional to the square of ionic charge (Z^2), $F_O^{\cdot}$ defects scatter electrons more weakly than oxygen vacancies ($V_O^{\cdot\cdot}$). This results in reduced LSPR damping while producing a high carrier concentration in F, Sn codoped In_2O_3 NCs (Figure 11e). Furthermore, Agrawal et al.[89] also argued that F atoms act as a capping agent during colloidal synthesis, driving the shape of the NC from pseudospherical to faceted cubes. Dependence of metal oxide LSPR on shape of the NC is discussed in the next section.

Some dopants such as Fe^{3+}, Mn^{3+} do not introduce any substantial free electrons but will induce additional paramagnetic properties along with typical LSPR behavior.[136,137,246] As codopants are not mutually exclusive, addition of Fe leads to the formation of a deep donor state in the band gap ZnO (Figure 11b). Photodoping has been shown to convert Fe^{3+} to Fe^{2+} before starting to add charge carriers to the conduction band[136,246] (see section 4.3 for further description of photodoping). Similarly, in Fe, Sn codoped In_2O_3, any addition of Fe reduces the free carrier concentration, thereby red shifting the LSPR spectrum[136] (Figure 11c).

Co-doping the metal oxide with different dopants is a relatively new field of research and has already been shown to promote several valuable material properties such as high free carrier concentration in cation and anion codoped CdO, reduced damping and driving NC shape in In_2O_3, and multifunctional magnetic/plasmonic propertues in Fe/Mn, Sn codoped indium oxide.

2.3.3. Doping and Shape of Metal Oxide NCs. Doping strongly perturbs the electronic structure of the host lattice and is a powerful tool for tuning the LSPR properties of semiconductor NCs. In addition to the free carrier concentration modulation, dopant incorporation, along with the reactivity of ligand−metal complexes used as precursors during NC synthesis, determines the shape and crystal structure of NCs, all of which substantially influences LSPR.

Runnerstrom et al.[59] demonstrated that the shape of $Ce:In_2O_3$ NCs can be tuned between spherical and cubic through choice of precursor. Further, Della Gaspera et al.[70] showed that even the dopant element choice can impact the shape of doped ZnO NC ranging from pseudospherical with Ga and In to elongated pyramids with Al. In all the above cases as well as in a computational study by Agrawal et al.,[135] it has been observed moving from spherical to faceted NCs, LSPR response broadens and the one fundamental dipolar mode in a sphere splits into at least three geometric dipolar modes with field localized at corners, edges, and faces of the NCs, respectively. In far field extinction spectra, these modes are observed either as distinct peaks or shoulders with field localized around the corners at low energy and moving toward faces at high energies[135] (Figure 12a).

2.3.4. Near Field Enhancement. In addition to the far field optical response, the localization of electromagnetic radiation into near-field electronic polarization via plasmonic resonances is a major topic of research in plasmonics. Recently, Agrawal et al.[89] mapped the different plasmonic modes (dipolar corner, face, and edge geometrical modes) supported by F, Sn codoped In_2O_3 NCs (Figure 13a). The observations of plasmonic modes were consistent with simulated electric field maps and previous simulation work done on similar materials such as In:CdO[135] as

DOI: 10.1021/acs.chemrev.7b00613
Chem. Rev. 2018, 118, 3121−3207

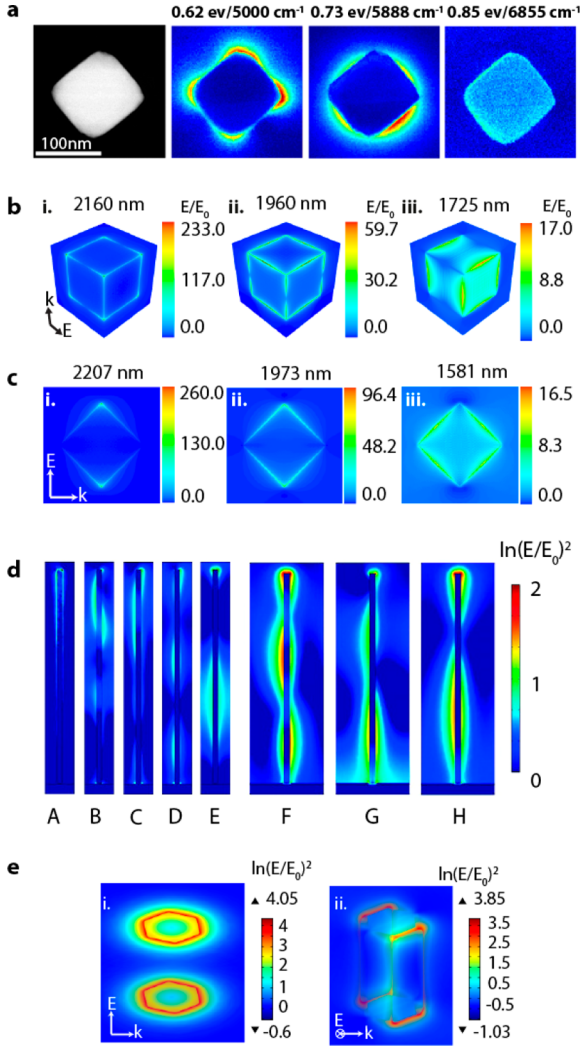

Figure 13. Near field enhancement. (a) Spatial distribution of geometric LSPR modes extracted, using non-negative matrix factorization (NMF) method, from spectral images acquired by scanning transmission electron microscopy-electron energy loss spectroscopy (STEM-EELS) for a single 100 nm F,Sn-codoped In_2O_3 NC. Reprinted with permission from ref 89. Copyright 2017 American Chemical Society. (b and c) Simulated near-field enhancement (NFE) map of (b) an In:CdO cube and (c) an octahedron using the discrete dipole approximation. For both shapes, similar to the EELS modes (in a), fundamental corner, edge, and face geometrical modes were observed (from left to right). Reprinted with permission from ref 135. Copyright 2015 American Chemical Society. (d) Near field intensity (on log scale) in a periodic structure of $Sn:In_2O_3$ nanorods with interparticle spacings of (A−E) 600 nm and (F−H) 1500 nm. Interparticle coupling between standing waves and dipolar plasmon modes leads to different near-field profiles. Reprinted from ref 184. Copyright 2011 American Chemical Society. (e) Near-field intensity map on a log scale for a $Cs:WO_3$ hexagonal rod excited at the two LSPR peak frequencies corresponding to longitudinal and transverse plasmon modes. Due to strong crystalline anisotropy in hexagonal-phase $Cs:WO_3$, almost equal enhancement could be sustained by excitation of either mode. Reprinted from ref 56. Copyright 2016 American Chemical Society.

well as experimental work on metallic nanoparticles.[250,251] Previously, Agrawal et al.[135] used the discrete dipole approximation to simulate enhancement by In:CdO NCs. Despite the lower carrier concentration compared to metals, suppressed electron scattering in CdO allows these NCs to efficiently concentrate IR light. A maximum NFE of the order of 10^5 was calculated and was shown to be significantly reduced with rounding of sharp corners and edges (Figure 13, panels b and c).

Plasmon coupling in extended assembled structures leads to modified LSPR modes supporting more intense and higher volumetric density of near field hot spots compared to isolated NCs. Computations of hot spot formation between coupled In:CdO NC dimers indicated that coupling can lead to an order of magnitude improvement in NFE.[135] Moreover, Li et al.[184] studied the effect of interparticle spacing on the optical response of random and periodic assemblies of $Sn:In_2O_3$ nanorods. The periodic $Sn:In_2O_3$ nanorod array demonstrated a narrower plasmon peak and several small features in the p-polarized reflection spectrum, indicative of coupling between dipole (multipole) modes and standing waves in the $Sn:In_2O_3$ nanorods (Figure 13d). Recently, Kuznetsov[252] demonstrated computationally that although individual metal oxide NCs have weaker NFE than metal nanoparticles, they can be packed into tighter assemblies without losing NFE due to long-range coupling. When ordered into a higher spatial hot spot density, coupled metal oxide structures have higher volumetrically average NFE than similar metallic nanostructures. Moreover, Gordon et al.[124] showed that self-assembly of metal oxide NCs into large scale periodic structures is feasible. Using this approach of self-assembly, Agrawal et al.[89] computationally and experimentally showed the NC size-dependent far field spectrum and enhancement of near field intensity; the maximum NFE was increasing with size of the NCs, keeping the interparticle spacing constant. With promising NFE surrounding single NCs and in periodic structures, metal oxide NC plasmonics are attracting more attention for a diverse range of applications that may take advantage of their light absorption as well as their NFE.

2.3.5. Phase and Its Impact on Metal Oxide LSPR. Dopant-dependent phase transformation has been widely reported in metal chalcogenide semiconductors, while there are only a few reports discussing the correlation between crystal phase and LSPR properties of metal oxide NCs. While synthesizing In_2O_3 NCs, Radovanovic et al.[209,225] observed two products from a single reaction: NCs 5 nm in diameter trapped in the metastable corundum (rh-$Sn:In_2O_3$) phase and larger (>10 nm) NCs in the stable cubic bixbyite phase (bcc-$Sn:In_2O_3$). These phases have distinctly different dopant-dependence of their optical responses. While bcc-$Sn:In_2O_3$ NCs have strong dopant concentration dependence of LSPR frequency, rh-$Sn:In_2O_3$ has a small free carrier density and does not exhibit a plasmonic response at any dopant concentration. Differences in the CBM vs the Sn^{4+} donor state lead to drastically differing degrees of donor activation.

Further, Kim et al.[56] showed that depending on synthetic conditions, $Cs_y:WO_{3-x}$ can be formed in the hexagonal (Cs-doped) phase, consistent with results previously reported by Mattox et al.[113] or in cubic or monoclinic phases of WO_{3-x} that are not Cs-doped (Figure 12b). In contrast to the symmetric cubic phase, optical spectra of hexagonal phase tungsten oxide can only be explained via a cooperative influence of crystalline and shape anisotropies. The role that intrinsic crystalline anisotropy plays in magnifying the dependence of LSPR directionality is substantial and can cause peak splitting in LSPR as a result of the crystallographic orientation. This effect became apparent in cesium tungstate NCs by synthetically varying NC aspect ratios. Integration of spectroscopic observations (Figure 12b) and electromagnetic near-field simulations (Figure 13e) revealed that unlike classical metal

DOI: 10.1021/acs.chemrev.7b00613
Chem. Rev. 2018, 118, 3121−3207

platelets or rods in which one resonance mode dominates based on the NC shape, here cesium tungstate NCs sustain strong dipolar LSPR modes both along the *c* axis and parallel to the basal plane regardless of physical aspect ratio. Simulations of LSPR must account for anisotropic crystal structures as well as shape in order to properly model spectra in materials with significant crystalline anisotropy. This aspect of synergistic dependence of LSPR on both shape and crystalline anisotropy is discussed in more detail for metal chalcogenide materials in section 2.4.1 of this review.

2.3.6. Dopant Distribution Inside Metal Oxide NCs. One of the most contentious discussions in metal oxide plasmonics is the frequency dependence of ionized impurity scattering. For Sn:In_2O_3 thin films, Hamberg and Granqvist[183] applied the method developed by Gerlach and Goose[125] to calculate the frequency dependence of ionized impurity scattering. In this method, scattering interactions are calculated assuming scattering centers oscillate relative to stationary sea of electrons. When assessing the complex dynamical resistivity, the real part of this function takes on a constant value at low frequencies which is roughly equivalent to the DC resistivity of the material since the electrons are able to screen ionized impurities during the relatively large amplitude of oscillation. At high frequencies, the electrons are no longer able to fully screen scattering centers and the total ionized impurity scattering value decreases as the frequency continues to increase. One can think of this effect as the amplitude of oscillation decreasing at higher frequencies, causing electrons to sample less of the material before they change direction, decreasing the probability of scattering events. This frequency dependence of scattering leads to an asymmetrical peak shape in the LSPR. Given that scattering by ionized impurities is at a maximum at low frequency (γ_L) and decreases to a minimum scattering (γ_H) at high frequency, there are several empirical functions that have been proposed to express this behavior mathematically (e.g., eqs 18 and 19).

$$\gamma = \gamma_L - \frac{\gamma_L - \gamma_H}{\pi}\left(\operatorname{atan}\left(\frac{\omega - \gamma_x}{\gamma_w}\right) + \frac{\pi}{2}\right) \tag{18}$$

$$\gamma = \gamma_L f(\omega) - (1 - f(\omega))\gamma_H\left(\frac{\omega}{\gamma_x}\right)^{3/2}, \text{ where } f(\omega) = \frac{1}{1 + \exp\left(\frac{\omega - \gamma_x}{\gamma_w}\right)} \tag{19}$$

This function has γ_L as the low frequency damping, γ_H as the high frequency damping, γ_X as the crossover frequency, and γ_W as the crossover width.

The frequency-dependent scattering model above is an empirical and simplistic model and is not necessarily applicable to all metal oxide materials systems. For example for In:CdO, Mendelsberg et al.[187] found that at high frequencies, a high background dielectric value of the host crystal led to impurities being screened efficiently. Ce doping instead of Sn doping in In_2O_3 leads to effectively no frequency-dependent scattering in the material.[59] It is important to take into account the very different values of ω_p observed across the different metal oxide materials and consider not only which dopants will hybridize with the CBM in a way that causes them to introduce ionized impurity scattering but also which energy regimes are relevant for screening effects changing appreciably across the line width of the LSPR.

Dopant hybridization with the host lattice and substantial scattering due to ionized impurity scattering makes it important to rationalize how the spatial distribution of dopants in the NC affects the LSPR properties. Lounis et al.[35,195] demonstrated that two common synthetic methods for making Sn:In_2O_3 NCs actually result in different dopant distributions within NCs: one homogeneous and another surface-rich in dopant.[195] In the case of homogeneously doped particles, the LSPR exhibits a strongly asymmetric line shape that is indicative of strong frequency-dependent scattering. Conversely, surface-doped NCs exhibit a symmetric line shape, meaning no significant frequency dependence of scattering. This suggests that dopants, when located near the surface of NCs, can contribute electrons to the conduction band but still be spatially separated enough from the free carriers' path within the NCs that they do not significantly dampen the LSPR. Since minimizing scattering in these materials is crucial to many applications, surface segregation of dopants may be a useful strategy. Yet, NCs with dopants near the surface have a lower carrier-to-dopant ratio, indicating that it is easier for other defects to compensate aliovalent dopants that are near the surface, making doping less efficient and stable. Moreover, Crockett et al.[121] and Jansons et al.[68,69,117] performed a comprehensive study on the effect of dopant segregation by precisely controlling the radial dopant placement inside spherical NCs by a slow growth synthesis method. Crockett et al.[121] demonstrated the change in LSPR by controllably placing dopants in two distinct ways: in the first, the core was Sn:In_2O_3 and different thickness shells of undoped In_2O_3 were overgrown (Figure 14b), while in the second, the core was undoped In_2O_3 and different thickness shells of Sn:In_2O_3 were overgrown (Figure 14a). In the first case, they first observed the blue shift in LSPR due to increased activation of the dopant ions near the surface of the doped cores and on further growth of undoped In_2O_3, due to the dilution of the carriers over a larger volume, LSPR starts red shifting. While in the second case, with increasing shell thickness of a doped shell on an undoped core, the LSPR moves progressively toward high energy due to increasing concentration of free carriers. In both types of core/shell NCs, overall damping decreased relative to homogeneously doped NCs, due to the presence of a dopant-free region. The observation of reduced scattering with dopant localization inside the NC offers an additional control strategy to reduce damping, which can lead to higher NFE. The current treatment of dopant segregation and its implication on LSPR properties is based on the assumption that, irrespective of dopant position, free electrons are delocalized throughout the NC. The validity of this assumption, along with the more detailed study on NFE as a function of dopant placement remains open to inquiry in this area of metal oxide NC plasmonics.

2.3.7. Ensemble Broadening Due to Internanocrystal Heterogeneities. Both the control over dopant distribution within a single NC and control over the NC dopant concentration heterogeneity among an ensemble of NCs continue to be major challenges, and their impacts on the observed optical properties of any given material remain largely unknown. Moreover, dopant heterogeneity is convoluted with shape and size heterogeneity effects. All the sources of heterogeneity combined will broaden the ensemble spectra, which gives rise to a lower apparent optical mobility derived from ensemble spectra compared to the true, intrinsic material property. To better quantify the correlation between the NC

DOI: 10.1021/acs.chemrev.7b00613
Chem. Rev. 2018, 118, 3121−3207

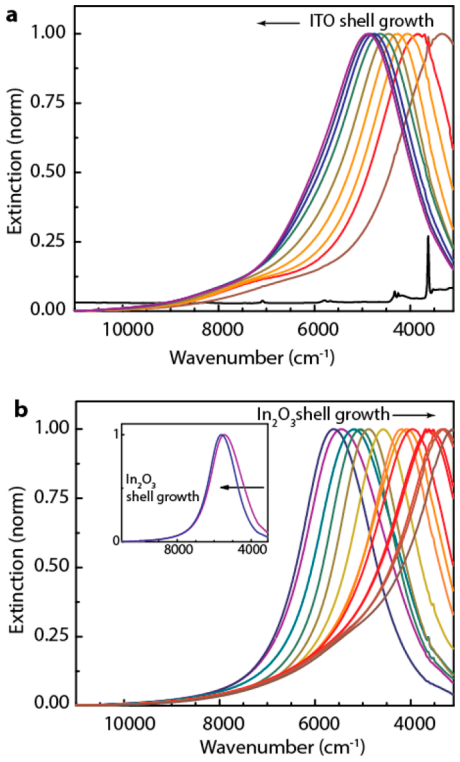

Figure 14. LSPR dependence on dopant distribution inside the NC. (a) Normalized extinction spectra of the In_2O_3/Sn:In_2O_3 core−shell NCs for progressive growth of the Sn:In_2O_3 shell. As the Sn:In_2O_3 shell grows thicker, LSPR blue shifts. This behavior was attributed to overall increase in free carrier concentration throughout the NC. (b) Normalized extinction spectra of the Sn:In_2O_3/In_2O_3 core−shell NCs for progressive growth of the In_2O_3 shell. First Sn:In_2O_3/In_2O_3 core−shell NCs show an initial blue-shift in the LSPR due to slight increase in surface Sn dopant activation (inset, b). As the In_2O_3 shell grows thicker due to overall dilution of free carrier density, LSPR red shifts. Reprinted from ref 121. Copyright 2017 American Chemical Society.

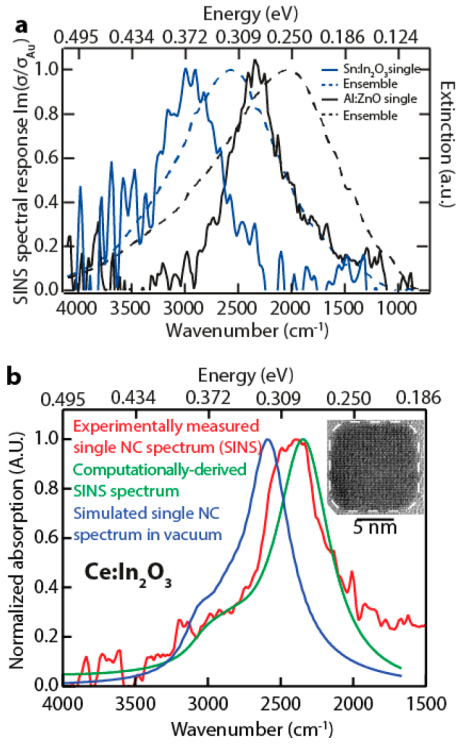

Figure 15. Single NC optical measurements. (a) Ensemble spectra measured by conventional transmission FTIR on KBr substrates (dashed lines) and single-NC synchrotron infrared nanospectroscopy (SINS) spectra of Al:ZnO and Sn:In_2O_3 shows substantial NC−NC heterogeneity broadening in ensemble spectra. Single NC measurement show lower fwhm compared to the ensemble spectrum. Reprinted with permission from ref 126. Copyright 2016 Nature Publishing Group. (b) Dielectric function evaluation of Ce:In_2O_3 NCs (inset) via fitting experimental spectrum (red) by using electromagnetic simulations (green) of the SINS experimental setup. The obtained dielectric function was used to simulate the absorption spectrum of a single isolated NC. Reprinted from ref 59. Copyright 2016 American Chemical Society.

material and its optical properties, the study of single NC optical responses is well motivated. Optical spectra of single NCs with IR response are difficult to measure as the diffraction limit is orders of magnitude larger than nanoscale crystals. Using a bright and spectrally broad IR synchrotron radiation source, Johns et al.[126] probed the full LSPR line shape of single NCs. The authors used the technique known as synchrotron infrared nano-spectroscopy (SINS), where using the heterodyne or homodyne interferometric amplification it is possible to probe light matter interaction with spatial resolution 1000 times greater than conventional FTIR microscopy. In this work, Johns et al.[126] observed significant particle-to-particle variability in LSPR energy as well as line width and line shape in Al:ZnO and Sn:In_2O_3 NCs. For the materials studied, the minimum single NC LSPR line width (Figure 15a) is less than half the line width of the corresponding ensemble indicating that dopant integration is quite heterogeneous in doped metal oxide NCs with some synthetic methods. Runnerstrom et al.[59] performed single particle measurements on Ce:In_2O_3 NCs and used the measured optical spectra to obtain a more accurate value for the NC dielectric function without the convolution imposed by ensemble broadening. The methodology introduced by Runnerstrom et al.[59] deconvoluted the NC optical response from the measured optical response of coupled tip-NC-substrate system (Figure 15b). Derivation of actual dielectric properties free of any ensemble broadening will facilitate the accurate design of materials specifically aiming to optimize performance in diverse optical systems.

2.3.8. Surface Depletion and Its Impact on Metal Oxide LSPR. Earlier in this review (section 2.2.3), we discussed the limitations of the Drude model as applied to semiconductor plasmonic materials. The underlying assumption of treating degenerately doped semiconductors as metals ignores any band structure modification at interfaces and its implication for NC LSPR. The presence of surface defect states, trap states, or surface bound/attached molecules modifies the near-surface electronic structure. Native surface states can pin the Fermi level at the surface potential leading to the formation of a depletion layer near the surface of semiconductor NCs in which the charge carrier density is much reduced compared to the core of the NC. The depleted shell shields the active plasmonic core from the surrounding environment, directly impacting its properties including sensitivity and NFE. Recently, using Sn:In_2O_3 as a model system, Zandi et al.[153] demonstrated that the depletion layer on the NC surface reduces NFE around the NC and decreases LSPR sensitivity to changes in their surroundings. The depleted NC volume relative to the total NC volume decreases with increasing NC size and increasing Sn doping level. As a result, deviation from the ideal behavior increased with

DOI: 10.1021/acs.chemrev.7b00613
Chem. Rev. 2018, 118, 3121−3207

decreasing size and with decreasing Sn doping level (Figure 16a). Furthermore, the near-field intensity enhancement surrounding

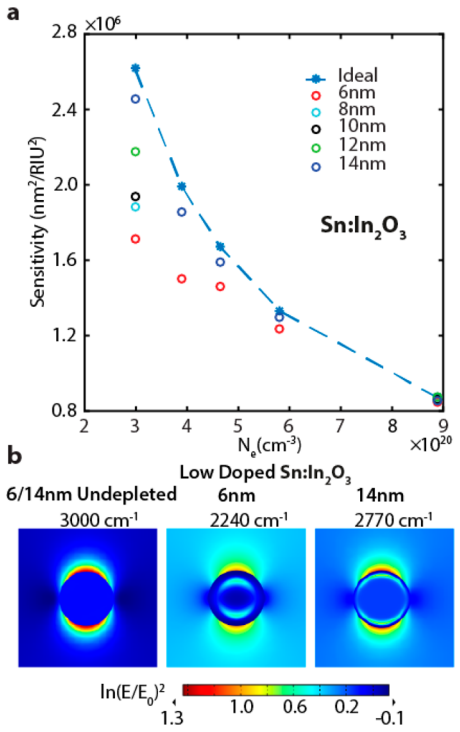

Figure 16. Effect of surface depletion on LSPR sensitivity to the surroundings. (a) Calculated plasmon sensitivity of small and large $Sn:In_2O_3$ NCs with nominal doping concentrations ranging from 1 to 10%. The blue stars indicate the ideal case with the highest sensitivity. The sensitivity factor is calculated based on the LSPR peak position in solvent with refractive indices ranging from 1.30 to 1.55. The presence of a depletion layer near the NC surface partially shields the active LSPR core from the surrounding environment thereby reducing the sensitivity to changes in the surroundings. (b) Calculated NFE maps of a spherical 1% doped $Sn:In_2O_3$ NC showing the effect of surface depletion. NFE is maximum for undepleted ideal NCs but decreases for 6 and 14 nm surface-depleted NCs. NFE decreases substantially for 6 nm NCs as the depletion extends through the core of the NC. Both a and b are adapted with permission from ref 153. Copyright 2017 arXiv.

a 6 nm NC with a 2 nm depletion layer was reduced by 40% compared to the ideal case, while a 14 nm NC with a 2 nm depletion layer had 26% lower NFE than if depletion were absent (Figure 16b). The observation made by Zandi et al.[153] is crucial in correctly estimating the efficacy of plasmonic semiconductor NC for various applications. Furthermore, manipulation or minimization of depletion effects is an attractive target for future development of NCs to maximize NFE and sensitivity. This conceptual framework can be easily extended to other metal oxides as well as other semiconductor NC materials.

2.3.9. Oxidation and Reduction of Metal Oxide LSPR.

Doping control gives semiconductor materials an extra degree of freedom to tune LSPR to a specific energy within a broad infrared spectral window. In addition to synthetic control, semiconductor materials possess unique capability of postsynthetic tuning of LSPR via several different methods such as oxidation/reduction, photochemical, or electrochemical reactions. Each one of the modulation methodologies is discussed later in this review for all the plasmonic semiconductor materials (section 4). Here, we will focus on how free carrier concentration can be controlled by simple exposure oxidative or reductive gaseous environment. Equilibrium oxygen vacancy concentration in a metal oxide depends on the partial pressure of oxygen in the surroundings. This effect, usually limited to the near-surface regime in bulk materials, has been shown to overwhelm the entire volume of small WO_3 NCs, and therefore the LSPR intensity may be greatly diminished under oxidative conditions. In a comprehensive study of $Cs:WO_3$ NCs, Kim et al.[56] tracked the LSPR peak during oxidation via controlled exposure to air and reduction via addition of hydrazine to the NC dispersion. They observed that upon oxidation, the extent of peak shift and the change in peak intensity were not consistent with the hypothesis of uniform decrease of free carrier concentration throughout the NC volume (Figure 17, panels a–i). They suggested an alternative model where oxidation of NCs leads to the formation of a fully depleted shell and a shrinking core with unchanged carrier density (Figure 17, panel a, ii). The simulated evolution of the LSPR spectra based on this redox mechanism was in agreement with the

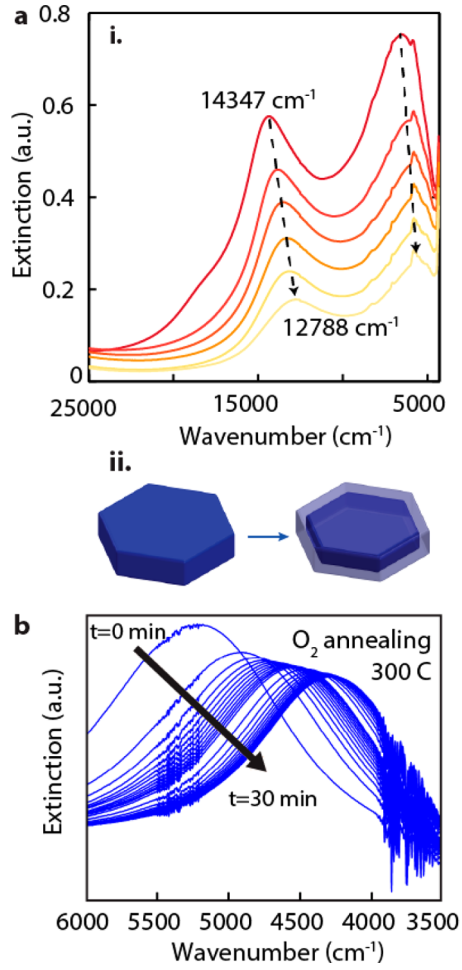

Figure 17. Oxidation of metal oxide NC. (a) (i) Dynamic optical extinction spectra of hexagonal $Cs:WO_3$ platelets undergoing oxidation by exposure to air for up to 24 h. As the oxidation progresses, LSPR intensity weakens and redshifts. (ii) The oxidation process can be modeled assuming oxidation proceeds by the growth of a fully oxidized shell with unchanged carrier density in the core. Reprinted from ref 56. Copyright 2016 American Chemical Society. (b) Absorption spectra of $Sn:In_2O_3$ NCs during annealing at 300 °C under O_2 atmosphere. As the oxidation progresses, due to the formation of Sn–O defect clusters, LSPR shifts toward lower energy. Reprinted from ref 253. Copyright 2017 American Chemical Society.

DOI: 10.1021/acs.chemrev.7b00613
Chem. Rev. 2018, 118, 3121–3207

experimental observations. This study proves that a simplistic way of looking at LSPR modulation through the hypothesis of uniform carrier concentration change throughout the NC volume is not applicable in all scenarios.

Hu et al.[253] performed similar oxidation/reduction experiments with Sn:In_2O_3 NCs where free carriers originate primarily from aliovalent dopants (Sn), and oxygen vacancies are only a minor contributor. In such cases, control over oxygen partial pressure in the surrounding gaseous environment does not substantially fluctuate the free carrier concentration via changes in oxygen vacancy concentration. As discussed earlier (section 2.3.1), in the presence of Sn dopants in the In_2O_3 lattice, the concentration of tin−oxygen ($2Sn_{In}^{\cdot} - O_i''$) complexes depends on the surrounding oxygen concentration. Hu et al.[253] demonstrated that annealing Sn:In_2O_3 at high temperature (250, 300, and 350 °C) under oxygen, red shifts the NC LSPR and lowers its intensity (Figure 17b). This "LSPR bleaching" is reversible, and LSPR can be blue-shifted back to its original position by annealing under N_2 at similar temperatures. The author attributed the reversible LSPR modulation to changes in the concentration of $2Sn_{In}^{\cdot}-O_i''$ clusters inside the NCs, though oxygen interstitials alone may be expected to have a similar effect. Furthermore, via modeling the oxidation and reduction process, the authors demonstrated that the extent of LSPR modulation depends on a combination of surface reaction, interstitial oxygen diffusion, and the formation of ($2Sn_{In}^{\cdot}-O_i''$) complexes.

Later in this review (section 5), we will discuss in detail other modulation studies and various other models proposed to describe LSPR modulation.

2.3.10. Heterostructures. The integration of multiple components into a single NC allows studying the synergistic interactions between materials possessing similar or distinct functional properties. Some of the most common plasmonic heterodimers studied are metal−metal heterodimers (Au−Ag), metal−metal oxide (Au−Fe_2O_3 or Au-TiO_2), and Au-chalcogenide (Au−$Cu_{2-x}E$). Examples of these materials have exhibited enhanced catalytic activity (Au-TiO_2), higher extinction coefficients (Au−$Cu_{2-x}E$), and integration of LSPR and magnetic properties within the same NC (Au−Fe_2O_3). The metal chalcogenide based heterodimers are discussed later in this review (section 2.4.4). With the motivation of creating multifunctional NCs, researchers have synthesized plasmonic metal oxide-metal heterostructures.[173,213,254−256] Ye et al.[213] demonstrated that a variety of metal or metal alloy NCs such as Au, Pt, Pd, and FePt can be used as seeds to grow metal-In doped CdO heterostructures with control over shape and size of the NCs as well as In doping concentration in the CdO lattice (Figure 18). The resultant metal-In:CdO NCs retained the LSPR characteristic of Au in the visible and that of In:CdO in the infrared spectrum. Gordon et al.[255] performed similar work on Au−In_2O_3 heterodimers and showed that using the strategy of dimerization, NCs with LSPR feature in both the visible and IR can be synthesized. To create a multifunctional material, Lou et al.[173] synthesized Pd-WO_3 heterostructures where Pd serves as a catalyst and WO_3 serves as the plasmonic component leading to LSPR-enhanced catalysis of Suzuki coupling reactions (see section 5.3 for more detail).

The designing of heterodimers involving plasmonic metal oxide NCs as one component is a relatively new field. Metal oxide LSPR can be modulated using chemical as well as electrochemical control; in a heterodimer this modulation can conceivably be used to tune the properties of the complementary component due to synergistic coupling between the two systems.

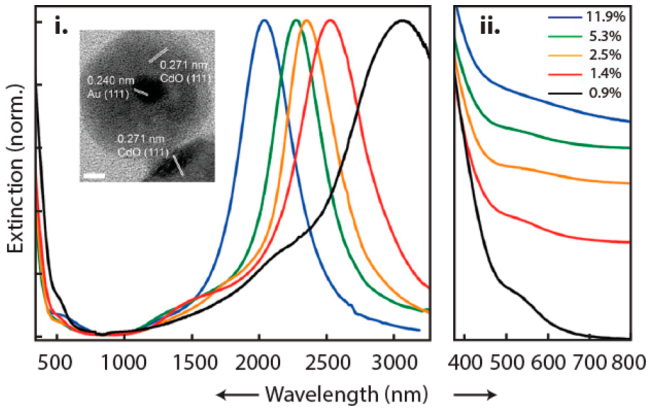

Figure 18. Metal oxide-metal heterostructures. UV−vis−NIR absorption spectra of 5.0 nm Au−In:CdO heterodimers (inset) dispersed in TCE as a function of the In-doping level. (i) Lower energy/longer wavelength spectra show the blue shift of LSPR spectrum originating from In:CdO component with increase in In concentration. (ii) Expanded higher-energy/shorter wavelength spectra show both the bandgap absorption from In:CdO and the LSPR absorption from Au. Reprinted from ref 213. Copyright 2014 American Chemical Society.

2.3.11. Other Oxide Materials. In this review, discussion of LSPR is mostly limited to semiconductor NCs. Here, in this section, we will briefly summarize some of the intrinsically metallic metal oxides such as VO_2 and ReO_3 that show interesting LSPR properties. VO_2 undergoes a semiconductor-metal transition at around 68 °C, accompanying a phase transition from a low-temperature monoclinic to a high-temperature rutile phase.[257,258] In its metallic form, VO_2 displays free carrier absorption characteristics. Several researchers have made efforts to synthesize VO_2 in NC form to study the LSPR absorption properties of this material.[259−264] Several synthetic routes such as solvo-thermal synthesis[263,265] and polymer-assisted deposition[266] have been used to make nanostructured VO_2, though a colloidal route is still lacking. Some researchers have fabricated porous films of VO_2 by rapid thermal annealing of VO_x[261] or V_2O_3[259] NCs. Recently, Ke et al.[267] reported the LSPR properties of periodic arrays of VO_2 spherical NCs showing that the VO_2 LSPR is centered around 1.2 eV (1033 nm). It remains a compelling challenge to prepare well-controlled, solution-dispersible VO_2 NC of uniform shape and size in order to facilitate more detailed study of this material's LSPR properties. Similar to VO_2, ReO_3 is another intrinsically metallic oxide material that displays promising LSPR characteristics. Most of the research on ReO_3 NCs has been focused on synthetic development of the NCs and is covered later in this review (section 3.3.4).

2.4. Metal Chalcogenides

2.4.1. Binary Metal Chalcogenides. Some binary metal chalcogenide compounds such as Cu_2E (see refs 19−21, 95, 98, 98, 99, 112, 112, 161, 170, 198, and 268) and HgE (see refs 230, 269, and 270) (E = S, Se, Te) are intrinsically cation vacancy doped semiconductors that showcase complex phase behavior and vacancy concentration-dependent LSPR properties. Due to high toxicity, mercury chalcogenide NCs have received limited attention with regards to their plasmonic properties and applications. Theoretical and some early experimental works with Cd and Hg chalcogenide NCs have been crucial in building the fundamental understanding of semiconductor plasmonics, especially in the quantum size regime.[230,231] These works were

DOI: 10.1021/acs.chemrev.7b00613
Chem. Rev. 2018, 118, 3121−3207

discussed earlier in this review (section 2.2). This section will focus on nontoxic and widely studied copper chalcogenide NCs. Binary Cu chalcogenides (Cu_2E E = S, Se, Te) exhibit complicated stoichiometry-dependent phase behavior and optical properties. As synthesized, Cu_2E NCs are typically nonstoichiometric, and the extent of Cu deficiency determines the crystal structure of the resultant product.[188,271,272] The vacancy or hole concentration is stoichiometry dependent as it increases with increasing Cu deficiency and is usually on the order of 10^{21} cm^{-3}. Almost all chemical manipulations directed toward hole concentration (thereby, LSPR) tuning lead to changes in the Cu:E (E = S, Se, and Te) stoichiometry and this in turn governs the phase stability, as elucidated for the binary Cu–S system by Chakrabarti et al.[272] The various crystal structures can be classified by either asymmetric hexagonal or symmetric cubic close packing of the sulfur atoms, where the Cu atoms occupy some of the interstices. The complex relationship between the hole concentration and crystal structure (thereby, electronic structure) compounds the detailed analysis of experimental LSPR extinction spectra.

$$Cu_{32}E_{16} \leftrightharpoons Cu_{32-x}E_{16} + xCu^0 \quad (20)$$

Cu_2S is intrinsically unstable under ambient conditions, and it rapidly degrades into a copper-deficient $Cu_{2-x}E$ phase[46] (eq 20). Owing to the low chemical potential of Cu^0, Cu_2S [in the high chalcocite phase with hexagonal close-packed (hcp) sulfur sublattice] instantly reduces to more stable $Cu_{1.94-1.97}S$ (djurleite phase with a monoclinic lattice).[43,146] Depending on the Cu vacancy concentration, $Cu_{2-x}S$ appears in eight different phases (Table 1). Stoichiometric Cu_2S has asymmetric hexagonal closed packing and with increasing Cu vacancy concentration, the sulfur sublattice reorganizes to be face-centered cubic (fcc). Similar phase diversity is observed in $Cu_{2-x}Se$ and $Cu_{2-x}Te$ chalcogenide materials (Tables 2 and 3).

Table 1. Cu–S Phases (Data Extracted from Refs 19, 55, 188, and 272)

name	stoichiometry	crystal structure
low chalcocite (α)	$Cu_{1.991-1.995}S$	monoclinic (stoichiometric)
high chalcocite (β)	$Cu_{2+x}S$	hexagonal (Cu-rich)
djurleite	$Cu_{1.96}S$	monoclinic
digenite	$Cu_{1.8}S$	cubic
roxbyite	$Cu_{1.78-181}S$	triclinic
anilite	$Cu_{1.75}S$	orthorhombic
covellite	CuS	hexagonal

Table 2. Cu–Se Phases (Data Extracted from Ref 271)

name	stoichiometry	crystal structure
bellidoite	Cu_2Se	monoclinic
berzelianite	$Cu_{1.8}Se$	cubic
athabascaite	Cu_5Se_4 or $Cu_{1.25}Se$	orthorhombic
umangite	Cu_3Se_2 or $Cu_{1.5}Se$	tetragonal
klockmannite	CuSe	hexagonal
marcasite	$CuSe_2$ or $Cu_{0.5}Se$	orthorhombic

In contrast to metals or metal oxides, whose LSPRs originate from collective oscillations of free electrons in the conduction band, LSPR optical properties in $Cu_{2-x}E$ (E = S, Se, Te) arise from collective oscillation of free holes in the valence band. Accordingly, stoichiometric Cu_2E does not support LSPR due to the absence of any free holes. As discussed earlier, LSPR shifts toward higher energy with increasing carrier concentration. However, LSPR extinction in $Cu_{2-x}E$ increases and shifts toward higher energy with increasing Cu vacancy concentration. Free hole optical properties have been reported for decades in the thin film literature on related materials.[55,188,273,274] In 2009, Zhao et al.[99] synthesized several phases of $Cu_{2-x}S$ NCs ranging from covellite (CuS) to digenite ($Cu_{1.8}S$) to djurleite ($Cu_{1.97}S$) either by varying the reduction potential (sonoelectrochemical method), adjusting the pH (hydrothermal method), or developing different precursor pretreatments (solvent-less thermolysis) (Figure 19a). They found that $Cu_{1.97}S$ (djurleite) was the most stable NC phase under ambient conditions as expected from the $Cu_{2-x}S$ phase diagram. They were the first to definitely ascribe the origin of infrared absorption in $Cu_{2-x}S$ NCs as free carrier oscillations or LSPR. In earlier thin film literature, most researchers were skeptically describing such infrared extinction features as intraband transitions due to the lack of any comprehensive study on this material.[188] Later, Luther et al.[42] showed both excitonic and LSPR optical features in pseudospherical $Cu_{2-x}S$ NCs of varying sizes (2.4–5.9 nm diameter) thus further advancing the conception of LSPR in metal chalcogenide NCs. Kriegel et al.[112] extended the observation of LSPR to the entire family of $Cu_{2-x}E$ (E = S, Se, Te) chalcogenide NCs. Consistent with the hypothesis of Luther et al.,[42] they demonstrated the rapid in situ conversion of Cu_2S and Cu_2Se into Cu-deficient and more stable $Cu_{1.97}S$ and $Cu_{1.8}Se$ phases, respectively. Moreover, the highly Cu-deficient covellite phase CuS has been shown to be intrinsically metallic rather than being a degenerately doped semiconductor.[275–278]

Table 3. Cu–Te Phases (Data Extracted from Ref 19)

name	stoichiometry	crystal structure
weissite	Cu_2Te	hexagonal
	Cu_7Te_4 or $Cu_{1.75}Te$	trigonal
rickardite	Cu_4Te_3 or $Cu_{1.33}Te$	tetragonal
vulcanite	CuTe	orthorhombic
pyrite	$CuTe_2$ or $Cu_{0.5}Te$	hexagonal

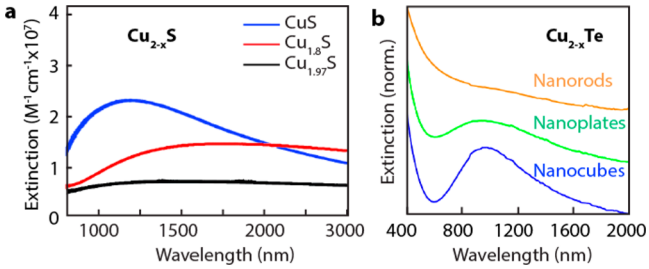

Figure 19. LSPR in metal chalcogenide NCs. (a) Extinction spectra of $Cu_{2-x}S$ NCs: covellite CuS (x = 1), digenite $Cu_{1.8}S$ (x = 0.2), and djurleite $Cu_{1.97}S$ (x = 0.03). LSPR shifts toward higher energy with increasing cation vacancy concentration. Reprinted with permission from ref 99. Copyright 2009 American Chemical Society. (b) Extinction spectra of copper telluride nanocubes, nanoplates, and nanorods. The observed LSPR peak wavelength has very weak dependence on NC shape. For nanoplates and nanocubes, LSPR is pinned at around 900 nm. Reprinted from ref 170. Copyright 2013 American Chemical Society.

As discussed in the metal oxide section, the shape of NCs is critical in determining LSPR and near-field properties. In the case of binary Cu chalcogenides, the effect of shape on LSPR is not

DOI: 10.1021/acs.chemrev.7b00613
Chem. Rev. 2018, 118, 3121–3207

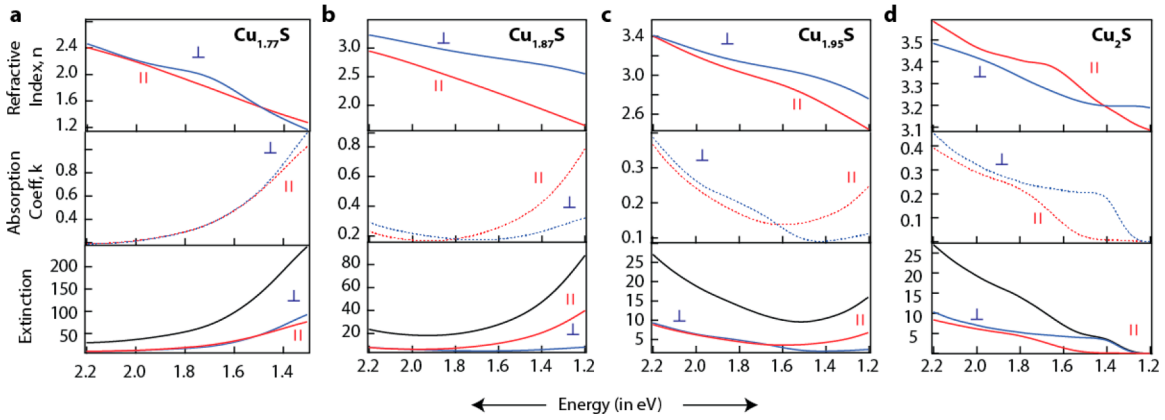

Figure 20. Impact of crystalline anisotropy in metal chalcogenide optical properties. Polarization-dependent refractive index and absorption coefficient of different phases with different cation vacancy concentration. As the free carrier concentration increases from Cu_2S to $Cu_{1.77}S$ (from right to left), free carrier features become stronger. The change in carrier concentration in $Cu_{2-x}S$ is accompanied by a change in crystal structure. The Cu_2S has the asymmetric hcp structure and moving toward higher cation vacancy concentration triggers the transition to symmetric fcc-based structures. Strong influence of the asymmetric crystal structures can be seen on the simulated extinction properties of spherical NCs of 20 nm radius (bottom panel in a–d). The transverse (blue) and longitudinal (red) contributions are shown, along with the overall extinction (black). The top two panels in a–d are adapted with permission from ref 55. Copyright 1972 Wiley-VCH.

clearly understood and is usually convoluted with the anisotropy in crystal structure. Li et al.[170] synthesized tetragonal phase $Cu_{1.25}Te$ nanorods, nanoplates, and nanocubes (Figure 19b). The authors did not observe any distinct LSPR feature in the optical spectra of nanorods, and LSPR was pinned around 900 nm for both nanoplates and nanocubes. In contrast, Kriegel et al.[112] observed a distinct LSPR around 1059 nm for nanorods. However, these nanorods were obtained by postsynthetic cation-exchange,[112] which resulted in the low symmetry weissite crystal structure, while the nanorods from Li et al.[170] exhibited the more symmetric tetragonal crystal structure. Similarly, contradicting reports on the effect of shape on LSPR response in $Cu_{2-x}S$ NCs have been published. Hsu et al.[279−281] synthesized spherical and nanodisk-shaped hexagonal phase $Cu_{2-x}S$ NCs and reported that while spherical NCs show one dipolar resonance mode, for disks, the resonance splits into a higher energy (1600−1900 nm) out-of-plane mode (longitudinal) and a lower-energy (3000−3100 nm) in-plane mode (transverse). In contrast, CuS nanodisks of the intrinsically metallic covellite phase only show an in-plane LSPR mode. In both cases, the layered crystal structures lead to strongly damped out-of-plane modes, thus highlighting the importance of considering crystal phase alongside NC shape to avoid confusion in assigning peaks in LSPR spectra.

$Cu_{2-x}E$ (E = S, Se, or Te) materials exist in several different phases, and depending on how the NCs are synthesized, different crystal structures may result. As discussed earlier (section 2.3.5) for $Cs:WO_{3-x}$, anisotropic crystal structures cause the dielectric function to differ along different crystallographic axes. It is the interplay between the crystalline and shape anisotropy that governs the overall LSPR dependence on carrier concentration and shape. To further expand on this concept, we have simulated the polarization-dependent optical spectra of spherical NCs of different crystal structures of $Cu_{2-x}S$, namely, high chalcocite (Cu_2S), djurleite ($Cu_{1.95}S$), digenite ($Cu_{1.85}S$), and anilite ($Cu_{1.77}S$) (Figure 20, a–d bottom panel). The polarization-dependent dielectric functions were obtained from the seminal work of Mulder in 1973[188] (Figure 20 (panels a–d, top and middle panels). A series of 1970's papers by Mulder are the only accounts of experimentally measured phase and polarization-dependent optical constants of $Cu_{2-x}S$ in literature to date.[55,188,273,274] Simulated optical spectra of spherical particles show a strong dependence on crystalline structure. The offset between the spectral response in transverse and longitudinal directions is maximum for the asymmetric hcp crystal structure, and as we progress toward more symmetric fcc-based structures, the longitudinal mode converges with the transverse mode. We cannot see the peak profile due to the limited energy range over which the dielectric function data were reported. Nonetheless, this simulation clearly illustrates the importance of treating anisotropic crystal structures with an appropriate, orientation-dependent dielectric constant.

2.4.2. Oxidation/Reduction and Phase Transformation of $Cu_{2-x}S$ NCs. LSPR of metal chalcogenide NCs can be tuned over a wide spectral range in a similar manner to metal oxide LSPR modulation by controlled chemical oxidation/reduction and thermal transformation. Cu vacancy concentration can be reversibly tuned via controlled exposure of NCs to oxidizing agents, such as ambient air or cerium(IV) ammonium nitrate, and reducing agents, such as Cu-containing salts. Luther et al.[42] demonstrated that under controlled exposure to air, the LSPR of $Cu_{2-x}S$ NCs shifts toward higher energy as the formation of Cu vacancies gradually increases (Figure 21a). Similarly, Dorfs et al.[43] found that Cu_2Se can be transformed into $Cu_{1.96}Se$, whose IR optical response can be further tuned by incrementally increasing Cu vacancies to yield $Cu_{1.8}Se$. The respective LSPRs shift toward higher energy as a result of increasing the hole carrier concentration (Figure 21b). It is important to note that there was no change in crystal structure during the transformation of $Cu_{2-x}Se$ NCs. In fact, both as-synthesized and oxidized NCs had a cubic berzelianite crystal structure. Furthermore, the authors suggested that during oxidation, Cu^{1+} converts into Cu^{2+}, the latter of which exists in the form of CuO as a separate surrounding domain still bound to the metal chalcogenide NC. Similar transformations between different Cu vacancy states have been achieved via chemical control and are discussed later in this review (section 2.5.1). In some cases, it is desirable to be able to access different phases and tune the NC LSPR across a broad optical range. But in other cases, stability of $Cu_{2-x}S$ in a particular state under ambient conditions remains a topic of active research. Recently, Georgieva et al.[282] showed that by surface functionalization of $Cu_{2-x}S$ NC with MoS_4^{2-}, NC LSPR can be stabilized in the as-synthesized state for a long period of time (Figure 21c).

DOI: 10.1021/acs.chemrev.7b00613
Chem. Rev. 2018, 118, 3121−3207

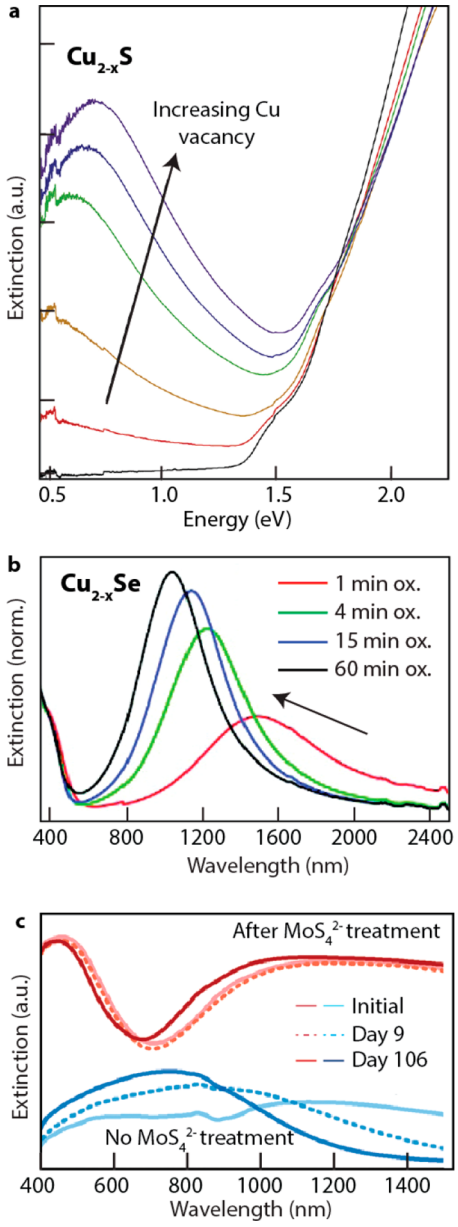

Figure 21. Oxidation and reduction of metal chalcogenide NCs. (a) Extinction spectra of $Cu_{2-x}S$ NCs upon exposure to air. The as-synthesized stoichiometric NCs do not show any LSPR feature (black), but the Cu-deficient counterparts generated under an oxidative environment exhibit higher free hole concentration (red). Increasing the free hole concentration progressively shifts the LSPR feature toward higher energy. Reprinted with permission from ref 42. Copyright 2011 Nature Publishing Group. (b) Extinction spectra of $Cu_{2-x}Se$ NCs dispersed in tetrachloroethylene over time. Under ambient conditions, $Cu_{1.96}Se$ oxidizes to $Cu_{1.81}Se$, thereby shifting the LSPR feature toward higher energy due to an increase in free hole concentration. Reprinted from ref 43. Copyright 2011 American Chemical Society. (c) Upon functionalization of chalcocite $Cu_{1.96}S$ NCs with MoS_4^{2-}, the NC LSPR can be stabilized over long periods of time. Reprinted with permission from ref 282. Copyright 2016 The Royal Society of Chemistry.

The ability to access different crystal phases from a NC of a given shape and size holds great promise for fundamental studies as well as various applications. Xie et al.[198] converted as-synthesized covellite $Cu_{1.1}S$ to Cu_2S via controlled reaction with terakis(acetonitrile)copper(I) hexafluorophosphate ($[Cu(CH_3CN)_4]PF_6$). Through the addition of Cu(I) complex into the system, the LSPR shifted toward lower energy. In fact, the distinct LSPR feature of as-synthesized covellite NCs prominent at 1090 nm shifted to around 1250 nm and significantly decreased in intensity (Figure 22a). Using a combination of

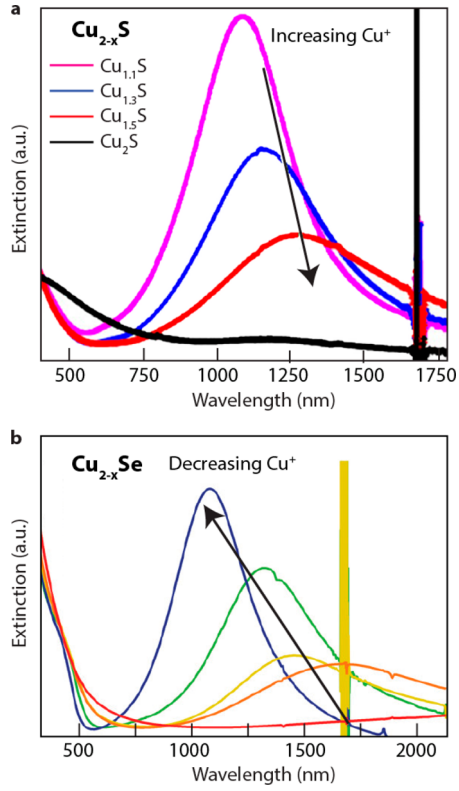

Figure 22. Phase change in metal chalcogenide NCs. (a) Evolution of the extinction spectra from the initial $Cu_{1.1}S$ to Cu_2S NCs. During this process, the stoichiometry is varied by addition of $[Cu(CH_3CN)_4]PF_6$. Optical transition was accompanied by the phase change from covellite CuS to possibly chalcocite Cu_2S phase. Reprinted from ref 198. Copyright 2013 American Chemical Society. (b) Evolution of the extinction spectra of $Cu_{2-x}Se$ from hexagonal phase Cu_2Se (red) to cubic phase $Cu_{1.59}Se$ (blue). Reprinted from ref 197. Copyright 2017 American Chemical Society. In both (a and b), higher energy LSPRs correlate with higher cation vacancy in $Cu_{2-x}S$(e) NCs.

techniques including X-ray photoelectron spectroscopy and electron paramagnetic resonance, the authors also showed that during this transformation, the oxidation state of Cu remained close to +1 while the S valence changed from −1 in covellite to −2 in Cu_2S NCs. Inversely, Liu et al.[283] started with rhombohedral $Cu_{1.8}S$ and transformed it into covellite CuS phase using excess oleic acid in the NC dispersion solution.

Recently, Liu et al.[284] demonstrated the reversible interconversion of covellite CuS into high chalcocite Cu_2S. Unlike the previous study, in this case the transformation is accompanied by a change in shape of the NC; hexagonal disks of CuS are converted into rounded disks of Cu_2S. The authors used 1-dodecanethiol to convert CuS to Cu_2S, while oleic acid-S was used to restore the original shape and composition.

Similar studies have been performed with $Cu_{2-x}Se$ NCs, including the conversion of hexagonal phase Cu_2Se into cubic $Cu_{1.59}Se$ phase under controlled exposure to air reported by Marbella et al.[197] Due to low vacancy concentration in the Cu_2Se phase NCs, the IR absorption of as-synthesized NCs was very weak. Nonetheless, increasing Cu vacancy concentration during

DOI: 10.1021/acs.chemrev.7b00613
Chem. Rev. 2018, 118, 3121−3207

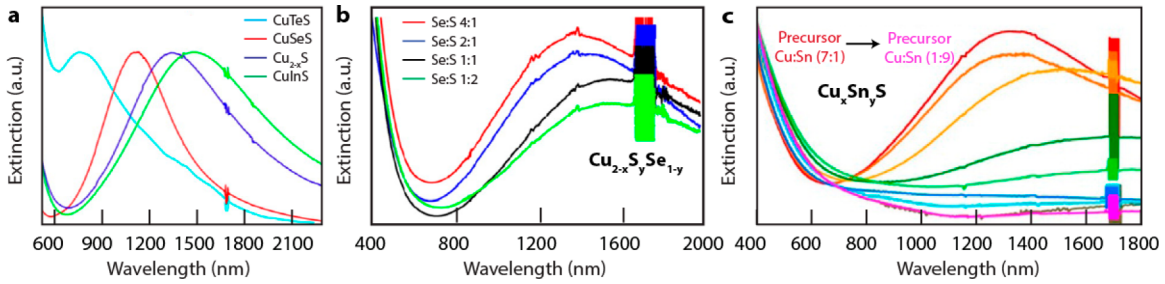

Figure 23. Doping or alloying metal chalcogenides and the impact on NC LSPR. (a) Extinction spectra of $Cu_{2-x}S$ NCs (blue curve) chemically tuned by doping/alloying with different ions (Te, Se, and In). Reprinted from ref 285. Copyright 2016 American Chemical Society. (b) Extinction spectra of $Cu_{2-x}S_{1-y}Se_y$ NCs are more damped when the S content is higher than Se in the NCs. Reprinted from ref 219. Copyright 2013 American Chemical Society. (c) Extinction spectra of $Cu_{2-x}Sn_yS$ NCs weaken in intensity and redshifts as Sn is introduced to the copper sulfide lattice. Reprinted from ref 286. Copyright 2015 American Chemical Society.

the phase transformation to $Cu_{1.59}Se$ NCs progressively strengthened the LSPR band and shifted it toward higher energies (up to 1085 nm, Figure 22b). The authors used novel characterization methods such as powder X-ray diffraction (XRD) and ^{77}Se nuclear magnetic resonance (NMR) to estimate the hole carrier concentration. They estimated the vacancy concentration to increase from less than 3×10^{20} cm^{-3} to 8×10^{21} cm^{-3}.

2.4.3. Ternary Metal Chalcogenide NCs. Doping NCs provides an additional degree of freedom over LSPR tunability and, in the case of aliovalent or interstitial doping, enables control over free carrier concentration as explained earlier for metal oxide NCs (section 2.3.1). Moreover, the influence of dopants on the LSPR relaxation or damping characteristics depends on the interaction between these foreign elements and the host lattice. Although self-or vacancy-doped binary conductive metal chalcogenides have been more extensively studied, a few research articles have focused on understanding the effect of doping or alloying on metal chalcogenide NC LSPR properties.

Ternary alloyed metal chalcogenides include both anion-doped, such as $Cu_{2-x}S_ySe_{1-y}$ [217,217−219,287,288] or $Cu_{2-x}S_yTe_{1-y}$,[285,289] and cation-doped, such as $Cu_{2-x}Sn_yS$/Se[286,290,291] or $Cu_{2-x}In_yS$/Se.[292−294] Dilena et al.[218] synthesized $Cu_{2-x}S_ySe_{1-y}$ NCs with varying S:Se ratio and observed that with increasing Se content, the LSPR peak shifts toward higher energy. Although they did not present any direct evidence, they attributed this effect to increasing Cu vacancy concentration, leading to higher free hole concentration. Liu et al.[219] observed a similar LSPR peak shift trend toward higher energy from 1260 to 1135 nm (Figure 23b) with increasing Se content in NCs. However, in contrast to Dilena et al.'s claim,[218] Liu et al.[219] interpreted this shift progression as a result of Se incorporation in the lattice rather than an increase in Cu vacancy concentration. The authors argued that as Se is substitutionally incorporated into the binary $Cu_{2-x}S$ lattice, the resultant $Cu_{2-x}S_ySe_{1-y}$ has an electronic character closer to binary $Cu_{2-x}Se$. This argument was empirically based on the optical signatures of $Cu_{2-x}Se$ and $Cu_{2-x}S$ for a given x since $Cu_{2-x}Se$ has a more intense and higher energy LSPR compared to $Cu_{2-x}S$. Likewise, Wang et al.[287] argued that blue-shifting of the LSPR with increasing Se content is due to a change in the effective mass of free holes. In particular, Wang et al.[287] suggested that since the effective mass of holes in $Cu_{2-x}Se$ is 0.2−0.25 compared to 0.8 for $Cu_{2-x}S$, it is the decrease in effective mass of holes in the valence band with increasing Se content that leads to LSPR shifting toward higher energy. On the other hand, Guo et al.[285] expanded the alloying system to $Cu_{2-x}S_yTe_{1-y}$ and CuInS and showed that doping can be a useful tool to manipulate the LSPR peak position in metal chalcogenide NCs (Figure 23a).

In addition to anion doping, cation doping of $Cu_{2-x}E$ NCs has been explored. Niezgoda et al.[293] synthesized chalcopyrite phase $Cu_{2-x}In_yS$ NCs with sizes ranging from 4.0 to 5.6 nm. They calculated the carrier density in these NCs to be on the order of 2.6×10^{20} cm^{-3}. The authors also observed that due to quantum size effects, the LSPR shifted toward higher energy as the size decreased with near-constant stoichiometry. Later, Wang et al.[294] systematically studied changes in LSPR behavior as a function of In content by synthesizing larger size NCs (>10 nm) unaffected by quantum confinement. Wang et al.[294] showed that with increasing In incorporation, LSPR intensity weakens and shifts toward lower energy, which was explained as a decrease in the overall free hole concentration. Similar behaviors in terms of LSPR intensity weakening and increased damping were observed in Cu−Sn−S materials (Figure 23c).[286,290] A more detailed DFT study in the future could shed more light on how In or Sn dopants hybridize with the Cu−S electronic structure and how these changes eventually lead to the observed optical effects and possibly a decrease in free hole concentration.

2.4.4. Heterostructures. Similar to metal oxide heterodimers (section 2.3.10), $Cu_{2-x}E$ (E = S, Se, Te)-based heterodimers have been studied for various applications. Early interest in metal chalcogenide heterodimers originated with photothermal therapy and imaging applications. In an effort to maximize the extinction cross section in the infrared window, researchers designed Au−$Cu_{2-x}E$ (E = S, Se) heterodimers that have higher extinction cross sections than the individual components[139,295−297] (Figure 24a). Such heterodimers have shown promising results for photothermal therapy and imaging and are discussed in detail later in this review (section 5.2.1). In addition, the LSPR spectra of Au−$Cu_{2-x}S$ heterodimers has shown enhanced sensitivity.[298] Muhammed et al.[298] observed that the LSPR spectrum of core−shell Au nanorod@Cu_2Se nanoparticles evolved from two peaks into three peaks on exposure to air. In as-synthesized Au nanorod@Cu_2Se core−shell particles, the LSPR spectrum is initially dominated by the metallic character of Au nanorods due to their low copper vacancy concentration. The two apparent LSPR modes correspond to longitudinal and transverse LSPR modes of Au nanorods. When the copper vacancy concentration is increased via air exposure, a third plasmon peak appears, which corresponds to the $Cu_{2-x}Se$ LSPR. Because of the strong hybridization between the different LSPR modes, shifts in both intensity and peak position of the Au modes were observed as the $Cu_{2-x}Se$ LSPR peak intensified and shifted toward the higher-

DOI: 10.1021/acs.chemrev.7b00613
Chem. Rev. 2018, 118, 3121−3207

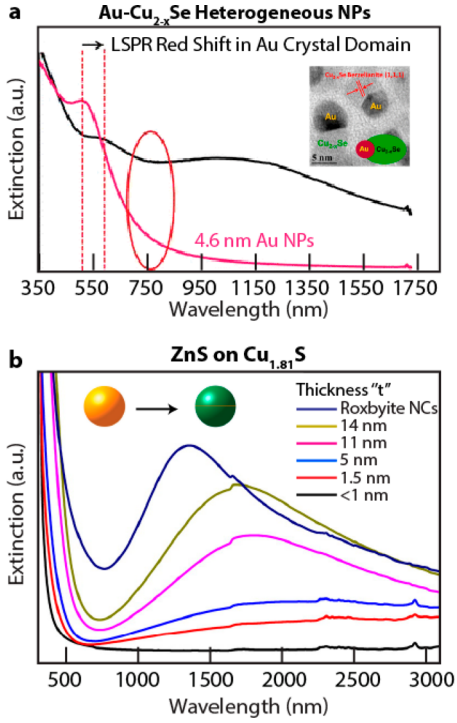

Figure 24. Chalcogenide heterostructures. (a) Extinction of 4.6 nm Au nanoparticles (fuscia) and Au−$Cu_{2-x}Se$ (black) heterostructures shows the increase in extinction in the biological window. Also, due to presence of the $Cu_{2-x}Se$ domain on the surface of Au (inset), the Au LSPR shifts toward lower energy. Reprinted from ref 295. Copyright 2013 American Chemical Society. (b) Cation exchange of Cu with Zn leads to the formation of ZnS-$Cu_{2-x}S$ heterostructures. The initial roxbyite $Cu_{1.81}S$ NCs have a LSPR centered around 1300 nm. As the cation exchange progresses, the copper sulfide domain becomes sandwiched between ZnS domains, and the LSPR spectrum shifts toward lower energy. Reprinted from ref 142. Copyright 2014 American Chemical Society.

energy Au LSPR modes. This type of heterostructure provides an ideal platform to study the hybridization between LSPR originating from different components. Such heterostructures also provide an interesting platform for sensing, photothermal, and other applications. For instance, researchers developed $Cu_{2-x}S$−Pd heterodimers similar to WO_3−Pd heterodimers for enhanced catalysis applications[144] (section 5.3).

The cation-exchange methodology has been used widely in metal chalcogenide NC research to synthesize either $Cu_{2-x}E$ NCs themselves from some other cation-based binary compound (e.g., CuS from CdS) or to perform copper cation exchange in a fraction of a $Cu_{2-x}E$ NC to form phase-separated heterodimers.[142,299−305] Ha et al.[142] synthesized $Cu_{1.81}S$-ZnS heterostructures, in which the $Cu_{1.81}S$ phase was sandwiched between ZnS regions. Control over cation-exchange time allows control over ZnS/$Cu_{1.81}S$ volume fraction. The authors also observed that as cation exchange progresses, the Cu from the ZnS-$Cu_{2-x}S$ interface diffuses into $Cu_{2-x}S$. Because the cation vacancy concentration decreases during this process, the LSPR absorption spectrum shifts toward lower energies (Figure 24b). Using a similar cation-exchange methodology, Xie et al.[208] synthesized $Cu_{2-x}S$-HgS and $Cu_{2-x}S$-CdS heterodimers using covellite CuS NCs as their starting material. These recent developments in the ability to synthesize a diverse variety of heterodimers demands a complementary research effort on the physical properties and applications of such materials, which is so far lacking.

2.5. Other Semiconductor Materials

2.5.1. Si,Ge. Since Group IV elements such as Si and Ge are dominant semiconductors in the microelectronics industry, their optical properties are of great interest for optoelectronics applications. In Group IV elements, intrinsic free carriers occur at very low concentrations, therefore substitutional doping is required to induce plasmonic properties. Unlike metal oxides (n type) or metal chalcogenides (usually p type), these materials can be either n or p type depending on the choice of dopant. Extensive work has been performed on doping bulk and thin films of Group IV elements, but synthesizing colloidally stable doped Si or Ge NCs remained a challenge until recently. Using the synthetic method developed by Pi et al.,[33] Rowe et al.[106] synthesized phosphorus (P)-doped Si NCs using a nonthermal plasma synthesis (more synthetic details are included in section 3.5) and studied the LSPR properties of doped Si NCs. The authors demonstrated that n- and p-type dopants can be controllably incorporated between 0 to 4% doping levels, resulting in LSPR peak energies varying from 600 to 2000 cm^{-1} (Figure 25a). The high propensity of Si to form a native oxide when exposed to air is well-known, but how a native oxide shell affects the NC's LSPR is addressed by Kramer et al.[107] for P- and B-doped Si NCs. Kramer et al.[107] observed as-synthesized P-doped Si NCs rapidly oxidized to form a SiO_2 shell under controlled exposure to air, losing free carriers to trap states at the Si/SiO_2 interface and thereby degrading the LSPR absorption characteristics. In contrast, B-doped Si NCs behaved very differently; as-synthesized B-doped Si NCs had no LSPR absorption, but on air exposure, LSPR emerged and blue-shifted with increasing oxidation. In the case of B:Si NCs, the authors did not see any evidence of formation of a SiO_2 shell even after 57 h of oxidation. The authors hypothesized that B dopants, which are predominantly located near the surface, may be accepting electrons from NC's valence band on oxidation, thus generating free hole carriers and leading to the emergence of LSPR absorption. Overcoming the obstacles to dope B in the bulk of Si NCs, Zhou et al.[306] reported the LSPR properties of B:Si with B doping ranging from 7 to 31%, leading to LSPR energies ranging from 2090 to 3244 cm^{-1}. Expanding on their previous work, Zhou et al.[200] discussed the dependence of LSPR on the B doping level. Similar to their previous study, they showed that with increasing B content, the LSPR blue-shifts (Figure 25b). Additionally, the authors observed that both direct band gap and indirect band gap optical transitions in B:Si NCs red-shifted with increasing B content (Figure 26). This is the opposite of Burstein−Moss shifts typically observed in semiconductor materials, where filling of states near the band edge overwhelms any shrinkage of the electronic band gap, resulting in a blue shift of the optical band gap. By conducting ultraviolet photoelectron spectroscopy (UPS) measurements on B:Si, the authors observed that in addition to the Fermi level moving into the valence band, the original valence band edge also moved to lower energy with increasing B doping concentration. Along with these shifts of the Fermi level and the valence band edge, they also observed that the original conduction band edge moves down in energy even more, resulting in an overall shrinkage of both the electronic and optical band gaps with increasing B doping level (Figure 27a). As discussed for metal oxide NCs (section 2.3), the efficacy of semiconductor materials for applications such as sensing, electro-modulation, and photomodulation depends on band energy alignment in addition to absolute LSPR energy. Accordingly, detailed optical and electronic studies similar to the one by Zhou et al.[200] for B:Si NCs can guide researchers to

DOI: 10.1021/acs.chemrev.7b00613
Chem. Rev. 2018, 118, 3121−3207

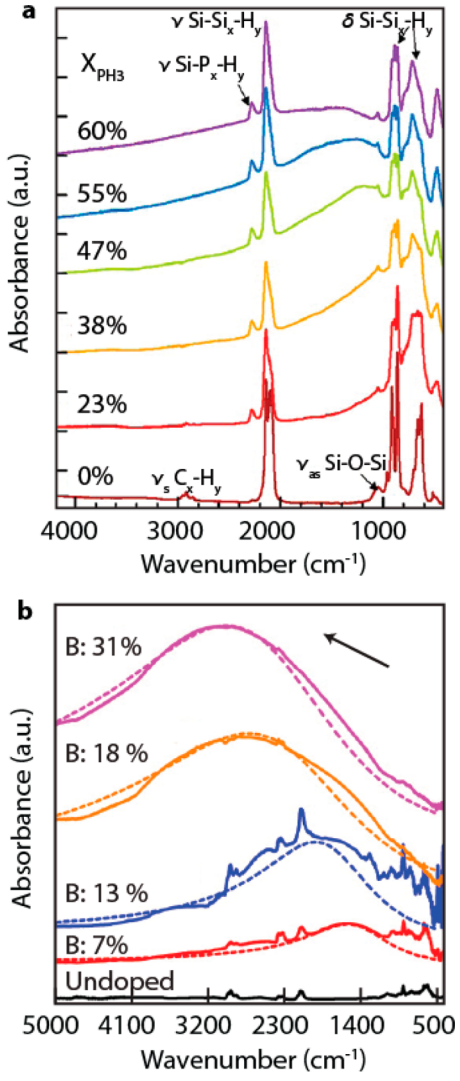

Figure 25. LSPR in doped Si NCs. (a) Absorbance spectra of P-doped Si NCs (n-doped). Incorporation of P dopant increases with increase in PH_3 percentage during nonthermal plasma synthesis. As P dopant percent increases, the free-electron concentration increases and the LSPR spectrum blue shifts. Reprinted from ref 106. Copyright 2013 American Chemical Society. (b) Absorbance spectra of undoped and heavily B-doped Si NCs (p-doped) after HF vapor etching. With increasing B concentration, LSPR blue shifts due to an increase in free hole concentration. The dash lines show the fitting of experimental extinction spectra with the Drude model. B doping levels range from 7% to 31%. Reprinted from ref 200. Copyright 2016 American Chemical Society.

understand the LSPR properties of other semiconductor materials and to design more efficient optical devices.

Both n- and p-type Si have direct as well as indirect interband transitions. Due to the presence of two types of transitions, Zhang et al.[57] argued that both n- and p-type Si NCs can have heavy and light carriers of two different effective masses. The authors used the time-dependent local density approximation approach to calculate the absorption characteristics of NCs simultaneously carrying both light and heavy carriers. Even though there are carriers with two different effective masses, both experimental and modeled spectra showed that LSPR is characterized by a single plasmon resonance. To understand this anomaly, the authors developed a classical hybridization theory based on the incompressible fluid model for a two-component electron fluid system. Here, the authors argued that the interaction between the mode originating from light (ω_1) and heavy electrons (ω_2) results in two hybridized modes: a red-shifted bonding mode (ω_-) and blue-shifted antibonding mode (ω_+). The authors proposed that heavy and light carriers are spatially colocated, so there is strong interaction between the two modes (ω_1 and ω_2). The strong interactions result in shifting the bonding mode, ω_-, to 0 and the antibonding mode, ω_+, to higher energy given by the following correlation,

$$\omega_+ = \sqrt{\frac{4\pi e^2}{3}\left(\frac{n_1}{m_1} + \frac{n_2}{m_2}\right)} \tag{21}$$

The authors further argued that in the quantum plasmon regime, double peak behavior might be observed due to nonlocal effects (Figure 27b). Quantum effects become important both when the carrier density is less than 10^{20} cm^{-3} or in NCs of size smaller than 5 nm. To our knowledge, this was the first report that discussed the correlation between the optical properties and different effective masses in the same crystallographic direction, originating from the band structure. Such treatment could provide further insight on LSPR in other semiconductor materials, especially in materials that display indirect as well as direct band gap transitions, such as cadmium oxide.

Synthesis and study of LSPR in free-standing Si NCs is still a budding field, but there is extensive literature on Si thin films, nanowires, and nanostructures showing promising optical properties.[9,165,190,307−313] With better understanding of Si NC synthesis and assembly, fabricating complex structure from colloidal NCs will be increasingly possible.[314−318] Ge is another promising Group IV elemental semiconductor[205,319−322] that has displayed free carrier optical properties in thin films and in nanostructures, but LSPR in colloidal Ge NCs has not yet been reported.

2.5.2. Nitrides. Metal nitride materials depending on their composition are either intrinsically metallic (TiN, ZrN, TaN), small band gap semiconductors (InN), or wide band gap semiconductor (GaN). All the materials stated here display free carrier optical properties in different frequency ranges. Intrinsically metallic nitrides have been proposed as alternatives to Au or Ag for application concerning LSPR in the visible spectrum for a long time, but there is no report on the preparation of such metal nitrides as NCs through colloidal routes. Similarly, GaN is a wide band gap metal nitride that is also of interest for its free carrier properties in the terahertz frequency range, but again no colloidal synthesis has been reported. Nevertheless, a few reports on InN NC synthesis and subsequent studies of their LSPR characteristics have recently emerged.[199,253,324]

Metal nitride materials exhibit metallic properties at near visible and longer wavelengths. Metal nitrides, such as titanium nitride (TiN), zirconium nitride (ZrN), tantalum nitride (TaN), and hafnium nitrides (HfN) are refractory metals and show high stability as well as hardness in their bulk state.[325,326] Interestingly, metal nitrides exhibit remarkably high carrier concentration, up to 6.6×10^{22} cm^{-3} in TiN,[327,328] resulting in plasmon frequencies near that of Au. These attributes make them potentially suitable alternative plasmonic materials to replace Au or Ag in many applications.[326] In TiN, the bonds are derived from hybridized N 2p and Ti 3d orbitals forming covalent bonds and additional Ti 3d electrons contributing to metallic bonding.[329] When TiN is formed, the N atoms' outer valence shell electrons are engaged in covalent bonding, while the Ti atom, with four valence electrons, contributes three electrons to covalent bonding with N.[330] The

DOI: 10.1021/acs.chemrev.7b00613
Chem. Rev. 2018, 118, 3121−3207

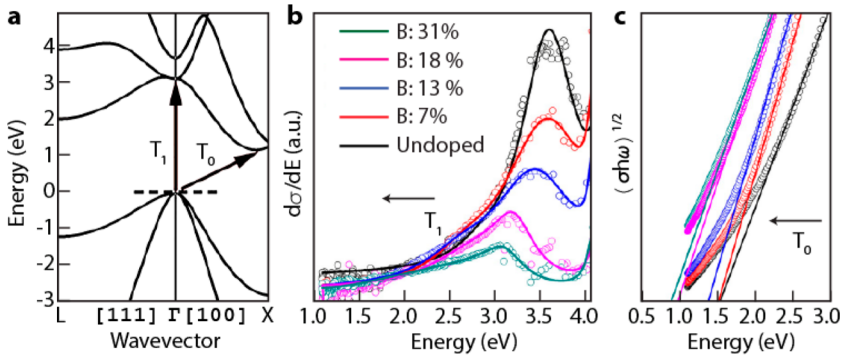

Figure 26. Interband transitions in Si NCs. (a) The band structure of bulk Si in which the indirect phonon-assisted Γ−X transition (T_0) and direct Γ−Γ transition (T_1) are indicated. (b) Derivative absorption spectra and (c) absorption data plotted as $(\sigma\hbar\omega)^{1/2}$ of Cl^- passivated Si NCs (black) and heavily B-doped Si NCs in benzonitrile shows that with increasing B concentration both direct and indirect band transitions shift toward lower energy. Reprinted from ref 200. Copyright 2016 American Chemical Society.

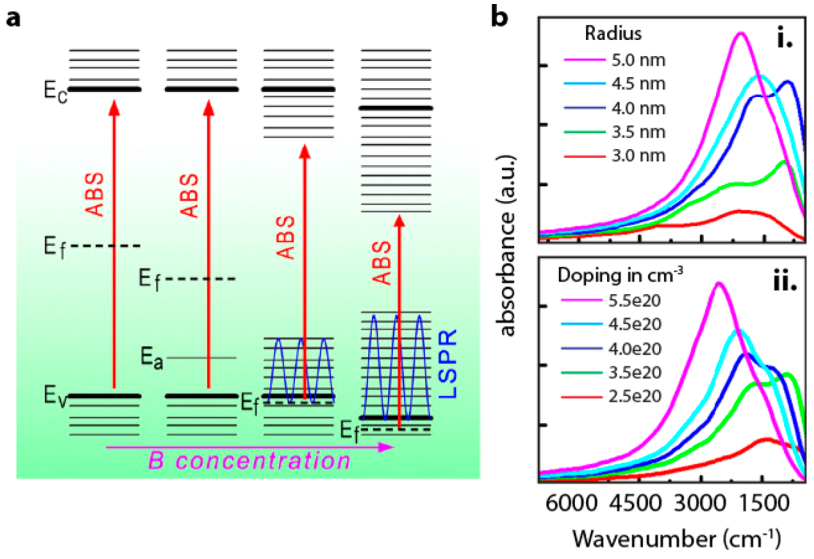

Figure 27. Band structure of doped Si NCs and its impact on LSPR properties. (a) Evolution of B:Si NC band structure with increase in B doping concentration (from left to right). E_c, conduction band edge; E_v, valence band edge; E_f, Fermi energy; and E_a, impurity energy level. Reprinted from ref 200. Copyright 2016 American Chemical Society. (b) Calculated absorbance spectra of (i) B:Si NCs with different radius and doping density fixed at 4.0 × 10^{20} cm^{-3} and (ii) B:Si NCs with different doping density and radius fixed at 8 nm. In both cases, as the NC reaches a quantum confined size or doping regime, the single LSPR peak splits into two distinct LSPR modes due to the presence of light and heavy holes. Reprinted from ref 57. Copyright 2017 American Chemical Society.

remaining Ti electrons are not constrained in covalent bonds[331] and are easily thermally delocalized from Ti atoms to produce shallow donor levels in the TiN bandgap with low activation energy to promote them to the conduction band. This leads to a high free carrier concentration despite this transition metal compound not being a noble metal-type plasmonic material.[329,330]

Due to metal nitrides' high carrier concentrations, their optical properties and those of Ag or Au plasmonic materials exhibit similarities. In metal nitride nanomaterials, the LSPR response has been reported approximately between 800 to 1000 nm wavelength for nonthermal plasma synthesized NCs,[332,333] vapor deposited,[334] and e-beam lithographically fabricated[335,336] TiN nanostructures. In the NIR range, these structures exhibit LSPR optical properties similar to Au and provide advantages in achieving a biocompatible plasmonic optical response in the biological window. Metal nitride dielectric functions derived from thin film spectroscopic ellipsometry measurements reveal exceptionally high permittivity (ε) with a figure of merit performance ($(\varepsilon')^2/\varepsilon''$) more similar to noble metals rather than transparent conductive oxides (Figure 28a).[337,338] A large negative real permittivity (ε') gives rise to reduced field penetration into the material and is typical of metals with high carrier concentration, while a smaller imaginary permittivity (ε'') results in lower electrical field losses. The large real permittivity being a consequence of the high plasma frequency and high carrier concentration, metal nitrides out-perform metal oxides for many established applications of noble metal plasmonic materials and may prove to be an alternative, refractory, cost-effective materials to replace Ag or Au.[326]

As discussed earlier, InN is a small band gap nitride that displays interesting free carrier optical characteristics, but the breakdown of the Drude model in plasmonic nitrides is apparent when considering interband transitions of narrow bandgap nitrides, for which the deviation from bulk carrier effective mass must be considered.[339] Particularly interesting is the investigation of the effects of nonparabolic bands on carrier effective mass in InN that has a narrow direct bandgap of ~0.7 eV for the

DOI: 10.1021/acs.chemrev.7b00613
Chem. Rev. 2018, 118, 3121−3207

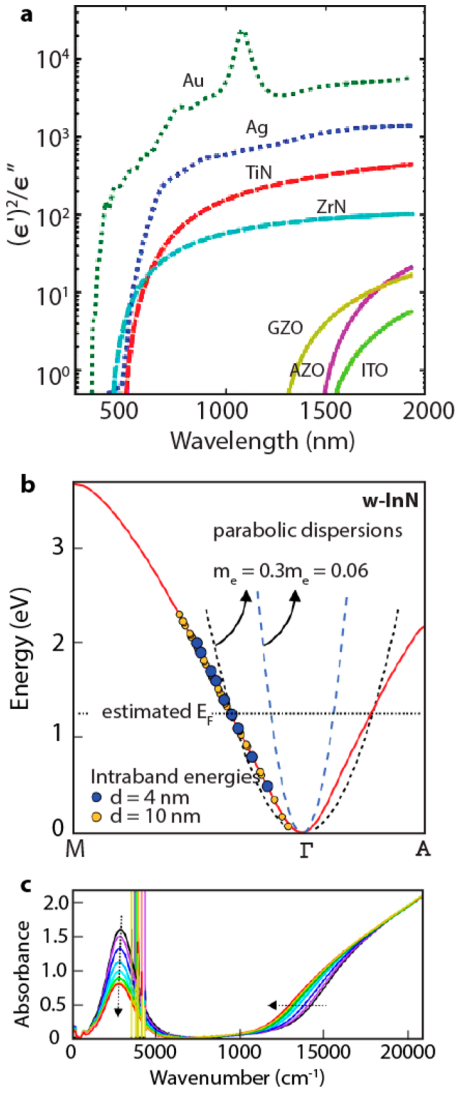

Figure 28. LSPR in metal nitrides. (a) The ratio $(\epsilon')^2/\epsilon''$ is considered as the performance metric for many applications such as plasmonic waveguides or metamaterials. Nitrides (TiN, ZrN) due to high carrier concentration are very similar to conventional plasmonic material such as Au and Ag. Reprinted with permission from ref 9. Copyright 2013 Wiley-VCH. (b) Calculated band structure of wurtzite phase InN which shows the changing band curvature with respect to the energy level. The estimated average Fermi energy (E_F) is also shown, along with calculated particle-in-spherical-box levels for two diameters. (c) Evolution of absorbance spectra of 4.2 nm InN NCs undergoing oxidation with various amounts of $NOBF_4$ oxidant. As the oxidation progresses, LSPR intensity weakens, but no shift was observed. This behavior was attributed to the synergistic effect of decrease in carrier concentration and decrease in effective mass as the oxidation progresses. Reprinted with permission from ref 323. Copyright 2017 American Chemical Society.

bulk material.[340−342] Shifts in interband transition energy were observed by Palomaki et al. in InN NCs undergoing reversible redox reactions.[343] As-synthesized colloidal InN NCs[324,343] had an estimated free electron concentration of 2.89×10^{20} cm^{-3} that led to a Burstein−Moss shift, where the large excess of free electrons moves the Fermi level above the CBM. A blue-shifted interband absorption onset of 1.8 eV was observed, indicating a raised Fermi level in the conduction band. Upon oxidation with nitrosonium tetrafluoroborate ($NOBF_4$), the reduction of the carrier concentration to 2.51×10^{20} cm^{-3} led to an observed shift of the interband absorption edge to ∼1.3 eV, indicating a lower Fermi level within the conduction band.

Liu et al.[339] extended the metal nitride interband studies in colloidally synthesized InN NCs to include effective mass nonparabolicity effects. Remarkably, upon oxidation with nitrosonium salts, the LSPR peak energy was observed to be nearly invariant and unaffected by a carrier density decrease from 7.4×10^{20} cm^{-3} to 3.9×10^{20} cm^{-3} (Figure 28, panels b and c). This invariance was attributed to interband coupling in InN exhibiting a strongly nonparabolic conduction band dispersion at small wavevectors, due to the narrow direct bandgap of ∼0.7 eV. The effective mass is no longer constant as the Fermi level varies and is instead strongly dependent on the carrier wavevector (k), and hence the energetic level within the band.

The high carrier concentration corresponds to a high Fermi energy and large k values so that the effective mass deviates significantly from the reported $m_e = 0.06$ value for bulk InN.[161] The effective mass close to the Fermi energy level E_F can be 1 order of magnitude larger than at the CB minimum Γ at $k = 0$ (Figure 28b).[339,344] By taking into account nonparabolic effects on the carrier effective mass at the Fermi level in InN, the study of Liu et al.[339] achieves agreement with experimental results, which implies the need to consider interband effects arising from low intrinsic bandgap and high free carrier energies.

Another type of metal nitride, the wide band gap semiconductor GaN, has also been shown to exhibit free carrier-related optical properties and has been considered as a promising candidate for terahertz optics. Due to the low carrier concentrations in GaN (10^{18} cm^{-3}), free carrier optical properties overlap with phonon modes.[51,202,345,346] Coupling between plasmon and phonon modes has recently gained attention from researchers interested in enhancing thermal transport. More work toward developing GaN NCs could possibly lead to interesting applications of low-energy GaN NC LSPRs.

2.5.3. Other Materials. Better understanding of LSPR in doped semiconductors and development of improved colloidal synthesis, dispersion, and processing methods are enabling the development of new plasmonic NC materials for various optical applications. Materials such as Cu_3P,[201,204,347] off stoichiometric Ga_2FeO_4,[348] and graphene have recently been colloidally synthesized and shown to display interesting LSPR properties. De Trizio et al.[347] synthesized hexagonal-shaped Cu_3P platelet NCs to be studied as an anode material in Li-ion batteries. Later, Manna et al.[204] studied the optical properties of Cu-deficient $Cu_{3-x}P$ NCs and observed LSPR absorbance features in the 1500−2000 nm wavelength range. Following this work, De Trizio et al.[201] performed DFT calculations that showed that, thermodynamically, formation of Cu vacancies is favorable in Cu_3P, and the resultant free hole carriers give rise to LSPR absorption characteristics.

Urso et al.[348] proposed the study of spinel oxide NCs with an A_2BO_4 general chemical formula. In a defect-free and stoichiometric crystal structure, A^{3+} occupies the lattice site (O_h) with six octahedrally coordinated oxygen atoms and B^{2+} occupies the lattice site (T_d) with four tetrahedrally coordinated oxygen atoms. However, this structure can be disturbed under specific conditions (i.e., at a finite temperature and in equilibrium), which causes cations to switch sites or induces the formation of a nonstoichiometric compound. Control over either of these defect formation mechanisms allows fine-tuning of free carrier concentration. In this study, the authors studied

DOI: 10.1021/acs.chemrev.7b00613
Chem. Rev. 2018, 118, 3121−3207

Ga_2FeO_4 as a model system and showed that by controlling the Ga:Fe precursor ratio, off-stoichiometric (Ga-rich or Fe-rich) spinel oxide NCs can be synthesized. When the oxide was Ga-rich, it behaved as an n-type material, and when it was Fe-rich it behaved like a p-type semiconductor. In both cases, the oxide NCs displayed LSPR absorption properties centered at around 1000 nm wavelength. This study motivates the exploration of other spinel oxides for their novel optical properties.

Another material that has been of interest to many researchers is graphene. In atomic layers of graphene thinner than the penetration depth, the electric fields generated by plasmon waves at the top and bottom surfaces are coupled. This allows much higher light confinement in 2D graphene compared to any 3D structures. Since graphene is a semimetal, its band structure, and thereby its free carrier concentration in the lattice, can also be controlled via chemical doping or electrical gating. Such control over plasmonic properties, especially in the terahertz frequency range, makes graphene a suitable material for a range of emerging applications.[349−352]

Besides the materials discussed in this review so far, there are numerous semiconducting compounds such as InAs, GaAs, InSb, NiSi, and TiSi, whose free carrier properties are well-known in their bulk or thin film forms.[10] Mainly limited by the difficulty in synthesizing NCs, LSPR properties of such materials have not yet been reported. With the development of better synthetic strategies, LSPR properties of the materials listed in this section can be explored for various optical applications.

With the considerable progress made in understanding the fundamentals underlying LSPR in seminconductors, there still remain a number of unanswered questions: (1) Does dopant distribution inside the NC induce spatial dependence to the electronic structure, and if it does, how does this influence LSPR? (2) How can understanding the influence of surface depletion and crystalline anisotropy on LSPR properties of metal oxide NCs be extended to other semiconductor system like metal chalcogenides? (3) Can the idea of hybridization between LSPR based on heavy and light carriers, which was proposed theoretically, be realized experimentally? (4) When integrated architectures, such as metal−insulator−metal stacks, are realized with plasmonic semiconductor NCs, how will the LSPR properties be affected and what unique attributes of semiconductors will need to be considered to fully rationalize the properties observed?

3. SEMICONDUCTOR NC SYNTHESIS

3.1. Introduction

The advancement in the fundamental understanding of LSPR in the doped semiconductor NCs (section 2) and its usage in a wide range of applications (next, section 4) have been propelled by the remarkable progress in wet chemical synthesis techniques over the past three decades. Researchers have developed a variety of NC synthesis techniques that enable us to synthesize NCs of several different geometries and sizes as small as 2 nm with sub-nm uniformity. Furthermore, solution-phase NC synthesis provides chemical control over the dopant type, concentration, and distribution inside the NCs that gives the flexibility to tune the NC LSPR properties widely. Tailored synthesis of NCs can be performed with various available solution−phase chemical methods that include colloidal synthesis, reverse micelle templating, solvothermal synthesis, and coprecipitation in aqueous solvents.[353,354] In particular, the colloidal synthesis methodology has flourished over the years as the most useful in producing homogeneous NC batches, a fact that can be ascribed to the general applicability of this approach to synthesize several different semiconductor NC compositions, including metal oxide and metal chalcogenide NCs. Colloidal synthesis, first described during the 1990's,[355−359] is a versatile technique which produces NCs stabilized by organic surfactants as a colloidal dispersion. Forming a stable NC dispersion allows us to study the LSPR characteristics of isolated NCs, free from aggregation. Furthermore, for large scale applications, colloidally stable NC dispersions provides an added benefit of solution processability that facilitates NC integration (e.g., into thin film architectures or polymer matrices). This versatility in material synthesis and processing is not typical of physical methods like lithography or molecular beam epitaxy, which can produce high quality nanostructures albeit at a high operational cost (due to the requirements of high vacuum and potentially high temperatures).

The geometry and doping characteristics of semiconductor NCs synthesized via colloidal synthesis depends on several factors, namely, NC nucleation, surfactant assisted NC growth, as well as the chemical reactivity of the metal precursors, surfactants, and organic solvent. First, the progress of the NC nucleation and growth processes depending on the reaction conditions and may lead to either thermodynamically favored or kinetically driven NCs of a given shape and size. The quality and geometry of the NCs produced is determined by microscopic factors such as the strength and lability of coordination between the surfactant (ligand) molecules and surface metal sites, as well as control over macroscopic conditions such as temperature and pressure and reaction processes such as hot injection of precursors or heating rate of premixed reagents (sections 3.2.2−3.2.4). Second, the composition of the NCs depends on the reaction mechanism such as alcholysis or aminolysis in case of metal oxides or thiol decomposition in case of metal chalcogenides (section 3.2.5). In addition to the control over reaction conditions, the reaction mechanism is crucial in determining the composition of self-doped semiconductor NCs including oxygen vacancy doped metal oxides (WO_{3-x}, In_2O_{3-x}, etc.) and cation vacancy doped metal chalcogenides ($Cu_{2-x}E$) (section 3.3.3 and 3.3.4). In the case of impurity-doped semiconductor NCs (e.g., Sn:In_2O_3, Al:ZnO, etc.), the relative reactivity of the metal precursors determines the extent of dopant incorporation and the spatial distribution of dopants inside the NCs (sections 3.3.4−3.3.7). Overall, it is the synergistic effects of all the factors such as precursor reactivity, ligand−metal binding strength, reaction parameters and mechanism, and nucleation and growth processes that together determines the size, shape, and composition of the doped semiconductor NCs and thereby their LSPR characteristics. In summary, designing LSPR-active NCs requires thinking in terms of inorganic chemistry, while addressing the interactions between the surfaces of the NCs and ligand molecules necessitates applying the principles of organometallic and coordination chemistry.[360−362]

In the following subsection (section 3.2), we expand on the basic concepts, encompassing chemical synthesis of LSPR-active inorganic NCs. The discussion is focused on providing a general framework for the production of LSPR-active NC with uniform shape, size, and composition. Thereafter, the next section (section 3.3) starts with a generalized introduction of the different doping strategies especially pertaining to synthesis of LSPR-active semiconductor NCs, which then serves as a background for discussing specific cases of doping in subsequent subsections. Chemical synthesis schemes of various categories of

DOI: 10.1021/acs.chemrev.7b00613
Chem. Rev. 2018, 118, 3121−3207

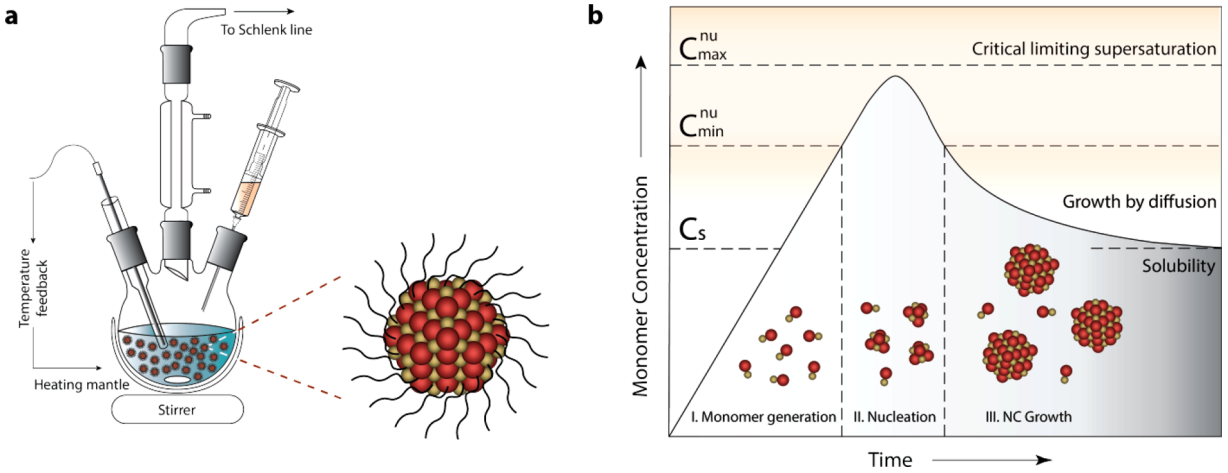

Figure 29. General synthetic apparatus and growth model embodying the colloidal synthetic technique. (a) Schematic showing glassware and peripheral instrumental setup for a typical synthesis of surfactant stabilized NCs, involving hot-injection. (b) LaMer-Dinegar model of colloidal NC formation. The three stages of monomer generation, nucleation, and growth are demarcated in the regions below the growth curve along with cartoons depicting the progression of the synthesis. Adapted from ref 366. Copyright 1950 American Chemical Society.

NCs such as intrinsically metallic, vacancy doped, and interstitially doped NCs are discussed along with representative examples from the literature. This is directly followed by a discussion of synthetic strategies for shape control of LSPR-active NCs (section 3.4). An alternative technique for NC synthesis is discussed next (section 3.5), namely nonthermal plasma synthesis, which despite being outside of the solution chemical synthesis realm, is an attractive route for NCs of more refractory materials and has been successfully employed to prepare LSPR-active NCs beyond metal oxide and chalchogenide compositions. The tools available for characterizing doped NCs and for addressing open questions in this field of research, along with open characterization challenges will constitute the subsequent section (section 3.6) before concluding this chapter of the review (section 3.7).

3.2. Colloidal Synthesis Techniques for Inorganic NCs

The development of chemical synthesis for inorganic nanostructures so far has been most focused on targeting optimized light emission from colloidal semiconductor quantum dots.[363] As a result, a rigorous understanding of the NC nucleation and growth mechanism has been developed over the years, specifically in the context of quantum dot materials. Regarding the choice of model system in these investigations, the ease of synthesis played a major part in the researchers' preference, with II–VI and IV–VI semiconductors (especially Cd and Pb chalcogenides) being dominant choices over their III–V and Group IV counterparts.[364,365]

It is only recently that synthetic efforts have been focused on tailoring chemical protocols and processing schemes aimed at exploring LSPR-active semiconductor nanomaterials, especially after observation and tuning of LSPR in doped semiconductor NCs.[42,84,99] The understanding developed from quantum dot synthesis has formed a general basis toward the mechanistic understanding of LSPR-active NC nucleation and growth (sections 3.2.1–3.2.4), since the underlying chemistry has been essentially the same. However, the bonding in metal oxides and in copper chalcogenides and their precursors differs from that of II–VI and IV–VI compounds. These differences influence synthetic strategies for controlling nucleation and growth including precursor selection, shape control methods, and designing surface chemistry, whose influence on optical properties of LSPR-active NCs has only just begun to be understood and which needs further investigation. The fundamental experimental steps involved in colloidal NC growth are outlined in the following subsection along with descriptions of underlying principles regulating these chemical processes. The basic outline includes general principles for colloidal synthesis (section 3.2.1) and the classical NC nucleation and growth model (section 3.2.2). The delineation of kinetic and thermodynamic products provides a framework for NC shape control (section 3.2.3). A comparison of approaches for combining reagents is made (section 3.2.4), including hot-injection, heat-up, and continuous injection methods, along with hydrothermal methods (section 3.2.6). Chemical precursor (section 3.2.5) and dopant selection (section 3.2.7) is discussed in further detail to consider monomer generation and reactivity balance in LSPR-active NC synthesis.

3.2.1. General Principles. Three major components comprise a typical synthetic system to prepare colloidal NCs: metal precursors, organic surfactants, and solvents, although surfactants can also serve as solvents in many schemes. The generation of reactive chemical species in atomic or molecular form, referred to as monomers hereafter, through chemical conversion of precursors is usually the first step in the synthesis. Identifying suitable precursors then carries substantial importance in the synthetic design, which generally are organometallic compounds or inorganic salts (which are complexed with the surfactants in situ). A more detailed description of the underlying chemistry of monomer generation is included in a subsequent subsection (section 3.2.5), while a schematic depiction of the experimental apparatus typically used for lab-scale colloidal synthesis is shown in Figure 29a. The subsequent growth of NCs from these monomers is significantly influenced by the surfactant molecules present in the reaction mixture. Surfactants possessing large alkyl chains react with metal precursors to form monomers, may participate in decomposition reactions, and eventually coordinate NC surfaces, passivating dangling bonds.

Overall, NC formation through the colloidal route can be divided into two major steps, when it occurs classically: (a) nucleation (of seeds) and (b) growth (of seeds into NCs). The nucleation step is facilitated by the preceding monomer generation step that involves the reaction of the precursors at

DOI: 10.1021/acs.chemrev.7b00613
Chem. Rev. 2018, 118, 3121–3207

moderately high temperatures (typically, 200−350 °C), mandating the need for solvents exhibiting relatively high boiling points. At a critical concentration of the monomers when supersaturation is achieved, a "burst nucleation" of seeds occurs marking the nucleation event. The subsequent growth stage comprises of the assimilation of additional monomers, still present in the reaction mixture, by the growing seeds. In nonclassical growth, NCs may grow larger by fusion of smaller particles. Both classical and nonclassical growth processes can occur in the same class of materials, which for LSPR-active semiconductor NCs remains an open area of study that must be better understand to fully rationalize synthetic design.

3.2.2. Nucleation and Growth of NCs. A general understanding of the basic NC growth mechanism can be attained from the classic work of LaMer and Dinegar in the 1950's, on the formation of sulfur hydrosols from the acid decomposition of thiosulfate ions.[366] The concept of burst nucleation was described in this seminal paper where the formation of many nuclei in a single step and their subsequent growth without the occurrence of additional nucleation events was demonstrated. The principles described therein form the basis of understanding the growth progression of most modern colloidal NC synthesis. The LaMer-Dinegar growth curve, of temporal evolution of monomer concentration, is depicted in (Figure 29b) with the three reaction stages. The initial monomer generation step comprises stage I, wherein the steady rise of the curve signifies the formation of monomers in the reaction mixture and a consequent rise in the concentration. The rate of monomer formation depends on the underlying reaction and also on the temperature of the reaction medium, with a higher rate of generation at higher temperature. However, the monomers do not spontaneously "condense" into nuclei even at the saturation concentration, C_s, due to the considerable energy barrier for nucleation. Above a critical concentration of the monomers, C_{min}^{nu}, burst nucleation commences marking the onset of stage II. The monomers are rapidly consumed at this stage leading to an accelerated growth of the nuclei, partially relieving the supersaturation, and leading to a sudden drop in the monomer concentration (signified by the curve maximum). Additional nucleation events do not occur as the monomer concentration drops below the critical concentration. This marks the onset of stage III, where the nuclei grow by assimilation of monomers, with the monomer concentration dropping progressively toward the saturation concentration or solubility.

The classical LaMer model provides a general framework of nucleation and growth processes that pertains to colloidal NCs, yet the description is not an exhaustive review of the principles that have been described. More complete treatment of nonclassical nucleation can be found in the review by Lee et al.[60] Nonclassical nucleation and growth of nanoparticles allow heterogeneous structures that are not fully explained through classical LaMer model.[60,61] One pathway in nonclassical systems is aggregated nucleation and growth by excess subcritical nuclei binding together at the nucleation stage.[367] Further growth by aggregation allows NCs to merge into networked structures (section 3.4.3). Another pathway is through heterogeneous nucleation when a stable nucleus or NC provides a nucleation site, and further growth occurs on this seed template, allowing synthesis of multicomponent NCs (section 2.3.10).

3.2.3. Thermodynamic and Kinetic Control. Several thermodynamic and kinetic considerations come into play that determine the shape and size of the NCs produced from colloidal synthesis, important in achieving shape-dependent LSPR properties (section 2.3.3). A number of demonstrations have been made by researchers on thermodynamic and kinetic "control" in colloidal NC synthesis (sections 3.4.1 and 3.4.2), mostly referring to the factors determining the shape of NCs but also having relevance for size distributions.[61,65] It is important to be able to discern the differences between growth directed primarily by kinetic versus thermodynamic factors, in order to design a successful synthetic strategy.[65,360] In broad terms, it is generally the relative magnitude of the rate of monomer deposition on the NCs and the rate of surface monomer diffusion that dictates the final morphology of the NCs and also the extent of thermodynamic or kinetic control. Under thermodynamic control, the initially deposited monomers on the NC surface diffuse to lower-energy sites. The diffusion of monomers occurs at a higher rate than their deposition; this is often the case when the monomer concentration is well below the critical concentration needed for nucleation and is approaching the solubility, represented by most of stage III on the LaMer-Dinegar curve (Figure 29b). Kinetically controlled growth conversely entails a higher rate of monomer deposition than diffusion. This can lead to thermodynamically disfavored shapes and usually corresponds to monomer concentrations more significantly above the solubility in the LaMer-Dinegar description.

The equilibrium shape of a NC is that which minimizes its Gibbs free energy and it may be possible to reach this shape at sufficiently long times, should diffusion rate dictate the NC structure to evolve. This thermodynamically controlled product can be achieved by raising the temperature or by running the reaction for a longer time. Now, change (denoted by Δ) in the total Gibbs free energy (G) of a NC is the sum of changes in free energy contributions from the bulk and the surface:

$$\Delta G = \Delta G_{bulk} + \gamma \Delta A \quad (22)$$

Here, γ signifies the surface free energy per unit area while A denotes the surface area. Hence, a minimized total surface free energy (at a fixed volume) will lead to a minimum Gibbs free energy. The surface free energy (γ) varies for different crystallographic planes as a result of differences in atomic arrangement and interactions with bound surfactants, and manipulating it has been central to conceptualizing shape-controlled growth of NCs. Ionic and molecular capping agents (such as organic surfactants) that exhibit selective binding to specific crystal facets play an important role by modifying the relative surface energies of these crystal facets. This leads to altered NC shape due to the maximized expression of the stabilized crystal facets. The chemisorption of surfactants as capping agents also result in hindered monomer deposition on those same crystal facets.[65,368,369] Kinetically, this means that the capping agent also modifies the relative growth rates of different crystal facets, and a slow growth rate of a facet results in greater share of the surface area. Obviously, this implies that thermodynamic considerations can also productively guide the development of shape-controlled NC synthesis taking place in the kinetically controlled regime. From yet another perspective, surface passivation can increase the energy barrier to surface diffusion and hence the final NC shape is determined by the interplay of these various effects.[65,368,369] It is important to note in this regard, that the equilibrium shape of a NC can never be completely spherical as a number of high-index facets with relatively high surface free energies will be needed to form a sphere, albeit NCs are often approximated as spherical for the sake of analysis of optical and electronic properties. Extending

DOI: 10.1021/acs.chemrev.7b00613
Chem. Rev. 2018, 118, 3121−3207

this general principle of thermodynamic and kinetic control over NC products, a section is devoted to NC shape control with exemplary works reported in semiconductor LSPR-active NCs (section 3.4). Approaches to shape control include regulating temperature (section 3.4.1) and introducing chemical complexing agents (section 3.4.2) to determine thermodynamic or kinetic NC shapes. Examples of extrinsic capping agents (section 3.4.3) and cationic dopants (section 3.4.4) used to surface passivate and influence NC shape control will also be covered.

3.2.4. Colloidal Synthesis Approaches. The colloidal synthesis techniques can be divided into several major approaches, that of (a) hot-injection, (b) heat-up method, and (c) continuous injection. The primary difference in the growth progression between these methods lies in the temporal separation of the events of nucleation and growth. In the hot-injection approach, an instantaneous burst nucleation is usually achieved upon injection as a high degree of supersaturation is induced in a very short period of time. The synthesis apparatus is typically similar to that shown schematically in Figure 29a, where two reactant solutions are brought together at a high temperature, one being in the flask and the other in the syringe, or both contained in the syringe with only solvent and surfactant in the flask. For instance, in the cases of II−VI or IV−VI semiconductor metal chalcogenide NC synthesis, a typical hot-injection method encompasses heating the metal precursor in the flask while the chalcogen solution is injected into this flask at a suitable temperature. The aim is to produce a single nucleation event following the injection and a subsequent growth stage which does not overlap with any secondary nucleation. Naturally, a more uniform NC morphology and narrow size distribution can be achieved when this approach succeeds in producing a single nucleation event.

The heat-up approach, on the other hand, entails mixing all the components of the synthesis (precursors, surfactants, and solvents) in a single flask and heating it up to initiate nucleation and subsequent growth.[370] For NCs to nucleate in heat-up synthesis, precursors react to produce and accumulate to monomers eventually reaching the critical concentration for nucleation (Figure 29b). The presence of an energetic barrier to nucleation allows nucleation and growth to be temporally decoupled since the monomer concentration drops suddenly following nucleation, with a portion of the monomer having been consumed. This energetic barrier is also what allows the initial accumulation of monomer, with a delay occurring before nucleation. This barrier is reduced at higher monomer concentrations, ultimately allowing nucleation to take place above the critical value. Meanwhile, the rate of monomer generation is governed by the activation energy required for precursors to disassociate and any other reactions specific to formation of a given monomer.[371] As such, tailoring precursor reactivity helps establish the conditions for temporal separation of nucleation and growth and control over both processes by tuning the temperature profile over the course of the reaction. Due to the continuing monomer generation as a result of sustained heat supply, the nucleation event can last longer than in the hot-injection approach, potentially leading to substantial overlap with the growth stage. This means that additional nucleation events may occur while the initial nuclei are in the growth stage. This overlap can result in a broad size distribution and achieving a high degree of size and shape control is not always possible.

An intermediate approach is the continuous injection method, where precursors are controllably injected into the reaction solution at a slow rate with a syringe pump. A typical hot-injection synthesis supplies precursors in a single event at the start of the reaction, leading to depletion of available monomers during an extended growth time. By continuously injecting precursor solution into the reaction instead, the postnucleation NC growth regime (Figure 29b) can be extended to grow larger NCs, while preventing onset of Ostwald ripening that can broaden the size distribution or degrade kinetically determined shapes toward their thermodynamically favored shape.[372] Sustaining the NC growth stage allows continuous layer-by-layer monomer deposition onto the NC surface, and growth of highly uniform, size-controlled NCs occurs as more precursor is added. Also, a variable composition shell around a NC core can be deposited when a differing reactant solution is injected during the NC growth process.[69]

Each of these approaches have their advantages and disadvantages, and the choice of a suitable approach is largely dependent on the desired end result. For instance, the hot-injection approach is more suited for studies or applications that demand an ensemble of NCs with a tight control over their physical properties which, in turn, are directly related to the NC size and shape distribution. This is particularly more important for light emission from quantum dots as the size quantization effects come into play here. However, this approach is not easily scalable for large scale production due to various factors like (a) heavy reliance on homogeneous reactant mixing at high temperatures in a short period of time in order to achieve a single nucleation nucleation event; rapid mixing becomes infeasible in large batch reactors; (b) cooling rates differ and cooling can become inhomogeneous in larger scale reactors; immediately after the injection, the reaction temperature typically drops, which can assist in separating nucleation from growth since the activation energy is greater for nucleation; (c) larger volumes cannot be injected rapidly, extending the nucleation event and potentially broadening size distributions.[371]

The heat-up approach, on the other hand, can be more easily scaled up and a far higher degree of reproducibility can be achieved due to the absence of the challenges mentioned above. Applications requiring larger batches of NCs are then more disposed to employing heat-up methods. Hence, great attention has been paid and progress made to improve control over nucleation and growth in heat-up reactions, leading to scalable chemistries for some prototypical NC materials.[371,373−375] However, the chemical basis of the synthesis has to be designed in such a way that the nucleation and growth stages are essentially decoupled in order to minimize polydispersity. This means that the interplay of the precursors and surfactants need greater attention in this case, and that generally defines the reaction rates and thereby the duration of the nucleation stage. This is particularly important for NCs containing multiple elements (ternary, quarternary, and multinary compounds, and impurity-doped materials), since these require a good match among the reactivities of the different components.

Continuous injection allows tight control in NC synthesis through predictable layer-by-layer growth. The continuous injection method is versatile for achieving NC size control[68] and controlling spatial dopant distribution in LSPR-active NCs.[121,376] Controlled monomer deposition during NC growth can be utilized for multicomponent core/shell NC synthesis with spatial dopant distribution control.[68,121] Apart from the injection solution containing precursors for the host material, a separate solution containing extrinsic dopant precursors can be sequentially injected at a desired time during NC growth to

DOI: 10.1021/acs.chemrev.7b00613
Chem. Rev. 2018, 118, 3121−3207

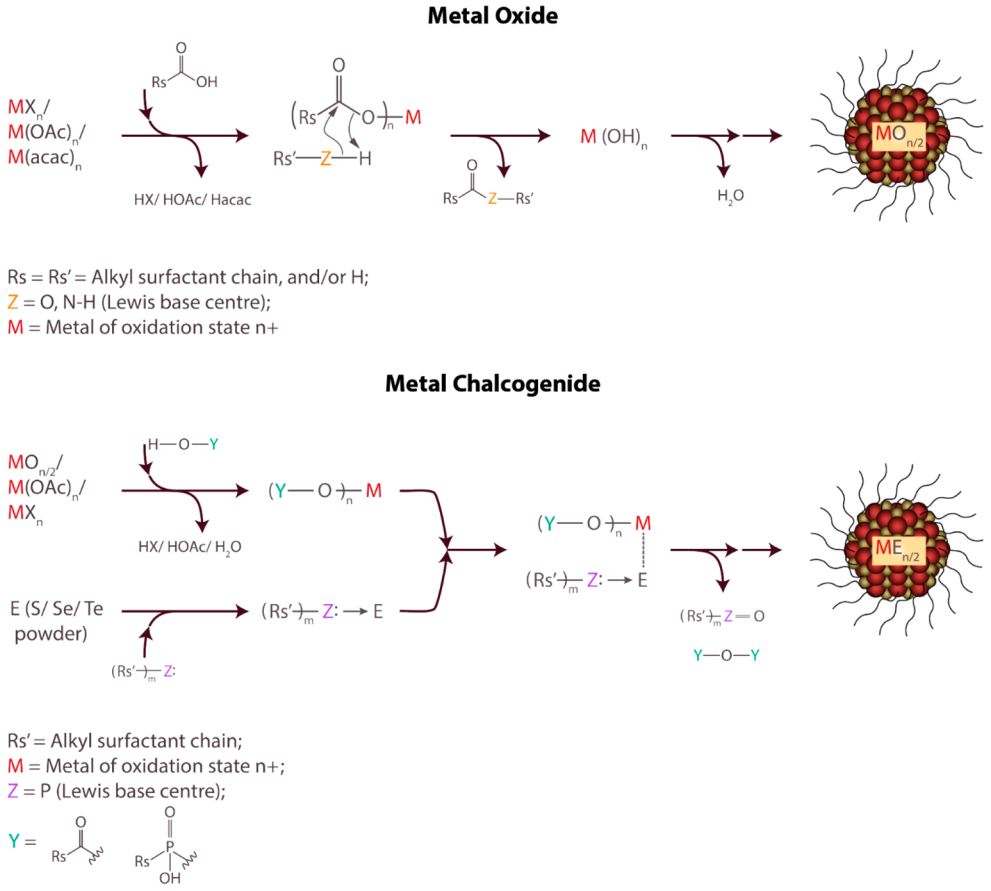

Figure 30. Monomer generation and chemical pathways leading to NC formation. (a) Metal oxide NCs: in situ metal carboxylate formation and subsequent lysis with a suitable protic moiety [e.g., water (hydrolysis), alcohol (alcoholysis), amine (aminolysis) etc.] (b) Metal chalcogenide NCs: organometallic complexes of metals (carboxylates or phosphonates, commonly) and chalcogens (coordinated with phosphines, etc.) reacted together at moderately high temperatures.

grow a shell with a different composition around the NCs. Such sequential layer-by-layer growth is difficult to achieve solely relying on the heat-up synthetic method. The reaction kinetics must be tuned so that the spatially controlled deposition of dopants occurs rapidly enough to avoid significant Ostwald ripening. However, control over the nucleation process in continuous injection requires further investigation as nucleation rates can vary for different NC compositions or reaction conditions,[69] compromising the otherwise excellent control that this method offers. Buidling on the above discussion, the next section (section 3.2.5) will demonstrate the role played by the underlying chemistry of monomer formation on the eventual NC composition. The principles of hard and soft acid−base (HSAB) theory lend qualitative assistance in determining the relative reactivities leading to dopant incorporation, as will be discussed in a later section (section 3.2.7).

3.2.5. Choice of Precursors and Monomer Generation. As mentioned above, the composition of the NC product is heavily dependent on the choice of precursors and the monomer generation chemistry. For instance, pyrolysis of organometallic precursors is the traditional choice for producing NCs of compound semiconductors while hydrolysis of metal salts and subsequent condensation is commonly employed for metal oxide NCs. Then again, a simple reduction of metal ions is used for generating metal NCs. This underlying chemistry of monomer generation plays a crucial role in sustaining the various steps of NC formation and the ligand shell formation, as schematically depicted in Figure 30.

Although generalizing and classifying all the different chemical reactions available for producing NCs of varying compositions is beyond the scope of this review, we discuss here the salient features of two model binary systems: metal oxide and metal chalcogenide NCs. Our choice is based upon the fact that these two categories claim a major share of LSPR-active inorganic NCs reported in the literature and also serve as good examples for demonstrating vastly different chemical pathways employed in colloidal NC growth.[370,377,378] Furthermore, these very principles can be extended to doped or ternary NCs (both oxides and chalcogenides) when additional factors like reactivity balance of different precursors are taken into account. Myriad chemical precursors have been reported in the NC synthesis literature, which are generally inorganic salts or organometallic precursors. However, nonaqueous synthetic techniques commonly involve coordinating the metal salts in situ by their reaction with organic ligands; these coordination complexes then act as the reactive chemical species. The organic ligands play an additional role of imparting dispersibility to the NCs as the surface atoms are also coordinated by these ligands, sterically stabilizing the NCs and preventing their aggregation. A common example of such a coordination is the conversion of metal salts into metal carboxylates through their reaction with long chain carboxylic acid surfactants.

DOI: 10.1021/acs.chemrev.7b00613
Chem. Rev. 2018, 118, 3121−3207

A favored route for formation of metal oxide NCs is through the "lysis" of metal carboxylates (Figure 30), which are usually prepared from the reaction of metal salts with long chain carboxylic acids like oleic acid, stearic acid, etc.[379,380] The lysis can be induced by a suitable nucelophile (e.g., protic moieties like a long chain amine or alcohol or even water), which generates metal hydroxide species that ultimately condense to form the oxide at high temperature accompanied by loss of water. Depending on the lysing agent used, the process is termed aminolysis (for amines),[83,381] alcoholysis (for alcohols),[68,81,382,383] or hydrolysis (for water).[73,382] Employing a long chain amine or alcohol is more appealing as these compounds do not become volatile at the high reaction temperatures; the reaction kinetics can be tuned based on the chain length and molecular structure, and the yields for such reactions are generally higher due to the irreversible nature of the reaction.[382] This is so because esters or amides (Figure 30) that are formed as a result of the lysis are stable and do not exhibit a propensity to react back with the resulting metal hydroxides or oxides. Hydrolysis, on the other hand, can be reversible since it releases carboxylic acids. The long alkyl chains of the surfactants used in these reactants may serve another critical role in constituting the ligand shell of the NCs. Typical metal precursors include metal salts like metal acetate, metal acetylacetonates, and metal halides, which also serve as precursors for extrinsic metal dopants.[370]

Unlike metal oxide NCs, where the component metal and oxygen atoms are often both contributed by the same precursor (e.g., metal carboxylates provide both, Figure 30), metal chalcogenide NC synthesis generally proceeds through a different pathway. As shown in the schematics in Figure 30b, the metal and the chalcogen precursors are prepared separately and then brought into a mutual reaction.[384] The surfactants are chosen to be effective as surface capping agents. This is the general chemical scheme for the most commonplace cadmium and lead chalcogenide NCs, but the principle remains the same for the chalcogenide compositions more relevant to LSPR activity (notably, copper chalcogenide NCs). Since copper ions are softer than cadmium or lead, they are more effectively coordinately by softer bases like alkylamines, instead of alkylcarboxylates. For instance, in the synthesis of copper chalcogenide NCs, copper precursors are coordinated by oleylamine molecules under moderate heating in a reaction flask. A separate stock solution of the chalcogen (S, Se, Te) source is prepared by coordinating with trioctylphosphine (TOP) or oleylamine or through dissolution in the non-coordinating octadecene.[96,146] Swift injection of the chalcogenide stock solution into the metal precursor solution then triggers the formation of metal-chalcogen-bonded monomers (that may be poorly characterized) that eventually lead to NC growth (Figure 30). For metal sulfide NCs, a wide range of sulfur sources have been utilized extending beyond the typical phosphine or oleylamine coordination of elemental sulfur; this includes thiol decomposition.[161,198,268,385−387] The individual sources for metal and chalcogen provide means for synthetic control over stoichiometric ratio to control metal vacancy concentrations and crystal phase, both of which impact LSPR properties as highlighted throughout the metal chalcogenide NC literature.

Naturally, the synthetic considerations in these two widely different classes of materials, with their different chemical approaches, vary and warrant specific consideration to deliberately design controlled NC synthesis reactions. With proper balance in the chemistry, either of these reaction schemes can be suitably tailored to fit a hot-injection or a heat-up approach. In general, these factors become more important when attempting to synthesize multicomponent (ternary, quaternary, or more complex) NC compositions as the number of parameters that influence the synthesis increases. As a natural extension, these factors also pertain to doped compositions, which represent many LSPR-active NCs.

Most of the design considerations for NC synthesis can be connected to the relative reactivities of the metal precursors and their strength of binding with the surfactants present in the reaction mixture. As can be envisaged from the above discussion, NC growth occurs in a rather complex mixture of salts and surfactants, and therefore, it is not always possible to delineate and predict the effect of modifying a reaction parameter (reactant composition, temperature, heating rate, etc.). However, HSAB theory provides a qualitative tool in this regard as a suitable starting point of investigation in rationalizing the outcomes of NC synthesis design and also narrowing the precursor choices.[118−120,388,389] Chemical components, such as metal ions and organic ligands, can be categorized as being hard, borderline, or soft. The definition correlates to the polarizability of the ion (with soft ions being more polarizable) and can be dependent on the ionic radius, charge, and electronegativity.[388,390] The hardness of an ion is roughly related to its charge-to-size ratio, and hence harder ions are those that are highly charged species with relatively small size, and an ion is termed soft when a relatively small charge is accommodated in a large ionic size. Metal ions with high oxidation state (high charge) and smaller ionic radius will lead to a higher charge-to-radius ratio, thus increased hardness.[118−120] Metal ions having lower oxidation state (low charge) and larger radius give low charge-to-radius ratio and are classified as soft. The principles of HSAB theory dictate that a hard (soft) cation will have preferential affinity toward a hard (soft) anion. Hard ions form more ionic bonds, while soft ions bond with more covalent character and hence like pairs exhibit stronger bonding than mismatched hard−soft bonding pairs. From this definition, the harder Cd^{2+} ion with higher oxidation state shows higher affinity to the harder oxygen center of the carboxylate ion with strong localized charge, while a relatively soft Cu^{+} ion with lower oxidation state has the propensity to bind to the softer nitrogen-center of the amine ligand, leading to the differences in the surfactant chemistries employed in Cd and Cu chalcogenide NC synthesis. From the point-of-view of NC synthesis, HSAB theory assists in balancing the metal−ligand interactions. These coordination bonds must be weak enough to facilitate rapid nucleation by precursor decomposition to produce monomers while strong enough to coordinate the NC surface during growth. The bound surfactants form a stabilizing layer that hinders uncontrolled growth and aggregation but permits monomers to precipitate at the NC surface.

3.2.6. Other Solution Based Synthetic Approaches. Although the control offered by colloidal synthesis is undeniable, other solution synthesis methods like sol−gel and solvo(hydro)-thermal techniques have also made significant contributions in nanomaterials research.[76,80,391,392] Solvo(hydro)thermal synthesis are typically conducted in Teflon-lined stainless steel autoclaves in which the precursors and a suitable solvent are sealed and heated at elevated temperatures. The term hydrothermal signifies reaction in water as a solvent, while solvothermal denotes using a solvent other than water, which can be a nonpolar one exhibiting a higher boiling point. The

DOI: 10.1021/acs.chemrev.7b00613
Chem. Rev. 2018, 118, 3121−3207

advantages of this synthesis technique include accessibility of high pressure, which amplifies precursor reactivity and solubility with minimal peripheral instrumental setup. A typical experimental setup employs an autoclave with inner Teflon-lined stainless steel vessel sealed with a stainless steel cap, able to withstand the supercritical temperature (374 °C) and pressure (218 atm) of water.[353] For instance, in hydrothermal synthesis of metal oxide NCs, a large increase in OH^- and H_3O^+ ions occurs under high pressure, favoring hydrolytic reactions leading to metal hydroxide formation.[393] The capability of these autoclaves to withstand high temperature and pressure environments over prolonged periods of time makes them attractive vehicles for achieving enhanced reaction rates (due to increased precursor solubility and reactivity) that are not normally accessible at standard atmospheric pressure. Solvents can also be taken above their atmospheric pressure boiling points, extending the range of accessible temperatures, which can be especially helpful for materials that are difficult to crystallize at lower temperatures.

A number of examples of hydrothermal synthesis of LSPR-active inorganic NCs have been demonstrated such as those of degenerately doped metal oxides like antimony-doped tin dioxide ($Sb:SnO_2$) by Nütz et al.[248] and oxygen-deficient molybdenum oxide (MoO_{3-x}) by Huang et al.[394] Early hydrothermal synthesis of irregularly shaped LSPR-active NCs have been greatly improved by subsequently developed non-hydrolytic colloidal synthesis, providing enhanced uniformity and advancing material diversity. Although the autoclave-based solvo(hydro)thermal synthesis scheme is attractive for reasons introduced above, it does exhibit a few drawbacks. Primary among these is the extreme difficulty in collecting aliquots midsynthesis for following the reaction progress, and also the "black-box" nature of the system makes it difficult to discern any visual changes that are generally afforded by the glassware apparatus of the colloidal technique. These considerations serve as a hindrance toward standardizing synthesis across laboratories or unravelling the mechanisms of NC formation and hence tailoring reactions toward targeted end results, such as realizing a specific optoelectronic property (e.g., LSPR or excitonic frequencies or line widths), is generally difficult. Nevertheless, autoclave-based synthesis have often been the first to access new materials because of the broad range of reaction conditions that can be accessed in a simple laboratory apparatus.

3.2.7. Dopant-Host Reactivity Balance. Doped semiconductor NCs claim a large share of the literature on LSPR-active inorganic NCs since, as already discussed in section 2, essentially any semiconductor NC can sustain LSPR, provided it exhibits appreciable charge carrier concentration.[42] It is, therefore, imperative to take a closer look at the various synthetic strategies that are employed to introduce dopant atoms in a semiconductor NC lattice. Over the past ten years or so, various research groups have developed synthetic strategies that can help establish tight control over the dopant incorporation in semiconductor NCs. The availability of such synthetic methods has fueled the advancement of understanding in this field of research as structure−property correlations allow researchers to elucidate fundamental physical principles across a diverse range of NC compositions.

Incorporating high concentrations of extrinsic aliovalent dopants can induce degeneracy in the dopant energy levels and spatial overlap between carriers associated with individual dopants so that the dopant states form bands. This degenerate doping requires high charge carrier concentrations to create LSPR-active NCs. Effective dopant incorporation requires that the dopants are able to substitute host atoms within the NC core rather than being adsorbed onto the NC surface. Dopant precursor reactivity can determine the success or failure in a NC synthetic methodology as a third atomic dopant component must be added into the single-phase binary compound semiconductor NC host material, such as those of metal oxides or metal chalcogenides. To achieve extrinsic aliovalent substitutional doping, it is critical to carefully balance dopant reaction kinetics with the host NC growth rate by judicious dopant precursor selection.[395,396] Earlier studies deemed NCs as being undopable, citing a self-purification process due to the defect formation energy being higher compared to the bulk materials. Under thermodynamic equilibrium, NCs may be prone to annealing out dopants to minimize the total free energy.[31,397] However, effective NC doping has been realized throughout the literature in solution phase colloidal NC growth at relatively low temperatures (below 400 °C), owing partly to the dominant role of kinetics rather than thermodynamics governing the outcome of NC growth.[395] Kinetic factors can govern dopant incorporation and can be controlled through precursor reactivity balance.

As described above, HSAB theory can be employed in comparing metal−ligand bond strength to fine-tune the reactivity balance in tertiary or doped compound semiconductor NCs. Dopant precursors include metal ions coordinated with a wide range of hard or soft bases such as halides (F^-, Cl^-, Br^-) or organic moieties (acetates, acetylacetonates, 2-ethylhexanoate, stearates).[388,390] Metal ions (Lewis acids) with higher oxidation state and smaller ionic radius are hard, while metal ions with lower oxidation state and larger radius are soft and make bonds with bases that are more covalent in nature[118−120] (Figure 31a).

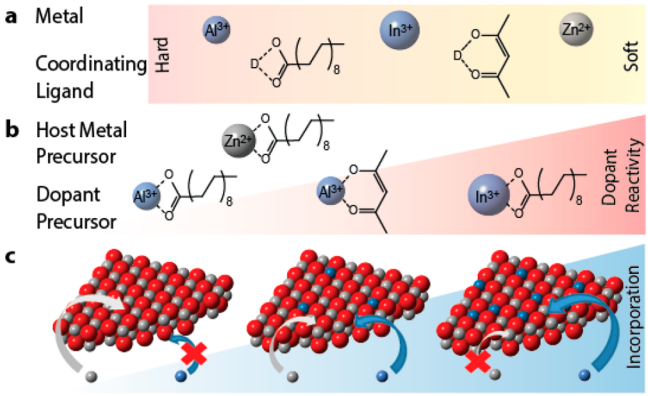

Figure 31. Extrinsic dopant incorporation schematic. (a) Representative examples depicting the relative hardness and softness of metal ions (Al^{3+}, In^{3+}, and Zn^{2+}) and coordinating ligands (stearate, acetylacetonate). (b) Dopant (aluminum(III) stearate, aluminum(III) acetylacetonate, and indium(III) stearate) reactivity relative to host metal precursor (zinc(II) stearate). (c) Dopant incorporation outcome scenarios: dopant incorporation failure due to low dopant precursor reactivity relative to host metal precursor (left); effective incorporation by balanced reactivity with host metal and dopant precursor (center); and phase segregation by excessive dopant reactivity (right).

If the dopant cation is harder than the host cation, the dopant precursor is expected to be less reactive than the host when both cations are coordinated with the same hard ligands. For coordinating ligands (Lewis bases), head groups with larger atomic radius (P, S, Se, Te) or with electron delocalization (as in acetylacetonate) tend to be soft compared to head groups with strongly localized charge ($-COO^-$, $-OH$, $-NH_2$).[388] Hard

DOI: 10.1021/acs.chemrev.7b00613
Chem. Rev. 2018, 118, 3121−3207

acids bind more strongly to hard bases due to the ionic nature of both components and the limitations on orbital overlap to form covalent bonds with hard acids.[389] The same affinity occurs for soft acids and soft bases due to their more covalent nature and high mutual polarizability. A mismatched hard−soft metal−ligand interaction leads to weaker binding, resulting in higher reactivity and high rate of metal−ligand dissociation (Figure 31b).

Careful dopant reactivity balance must be achieved to synthetically incorporate extrinsic dopants into the NC host lattice, similar to the synthetic strategy employed in tertiary NCs to achieve homogeneous compounds or alloys.[19] Host precursors with a weak metal−ligand coordination bond provide a favorable reaction environment for large accumulation of free monomers for facilitating rapid nucleation. Yet, the metal−ligand bonds must be sufficiently strong for both host and dopant precursors during growth phase to both avoid independent homogeneous nucleation and to prevent uncontrolled growth by stabilizing monomer decomposition and promoting layer-by-layer growth of NCs.[371] These trends were demonstrated in doped zinc oxide NC synthesis, where zinc(II) stearate ($Zn(St)_2$) was used as the host precursor for ZnO NCs along with controlled selection of metal−ligand dopant precursors. Buonsanti et al.[84] were able to synthesize colloidal NCs of aluminum-doped zinc oxide (Al:ZnO) by using aluminum(III) acetylacetonate ($Al(acac)_3$) as the dopant precursor to achieve well-balanced reaction with $Zn(St)_2$. Besides HSAB considerations, the coordinating ligands can influence reaction kinetics based on steric effects, where bulkier ligands can slow the rate of conversion from precursors to monomers. Overall, the dopant precursor decomposition rate must be nearly equal to those of host precursor to incorporate dopant atoms uniformly in the NC lattice during growth (Figure 31c, center).

This synthetic example of dopant precursor selection demonstrates the importance of balancing dopant and host precursor reactivity. Excessively stable dopant precursors prevent coordinating ligands from dissociating, resulting in low or inhomogeneous incorporation of dopants in the NCs. If the dopant precursor dissociation is too slow, dopant ions cannot be liberated and fail to be incorporated into the NCs during growth (Figure 31c, left). For example, no dopant incorporation was observed by Buonsanti et al.[84] when aluminum(III) stearate ($Al(St)_3$) replaced $Al(acac)_3$ as the dopant precursor. Al^{3+} is a hard acid and hence binds more strongly with the harder stearate ligand than the comparatively softer and more electron delocalized acetylacetonate ligand. Furthermore, stearate is a bulkier ligand than acetylacetonate. The lower reactivity of $Al(St)_3$ compared to $Zn(St)_2$, the host precursor, resulted in a failure to incorporate dopants in the ZnO NCs. On the other hand, if dopant precursor reactivity is too high, uncontrolled NC products with segregated dopant phases may occur (Figure 31c, right). Studies by Liang et al.[398] have demonstrated that indium(III) stearate ($In(St)_3$) as a dopant precursor was far more reactive than the host zinc(II) stearate ($Zn(St)_2$) precursor and did not lead to a single phase indium-doped zinc oxide (In:ZnO). To improve reactivity balance, replacing the dopant precursor with indium(III) 2-ethylhexanoate ($In(EH)_3$) allowed steric hindrance to slow down the alcoholysis and, hence, reduced the reactivity to closely match that of $Zn(St)_2$.[398,399] Hence, a careful selection of ligand-coordinated precursors for the dopant and host material, guided by the HSAB theory and steric considerations, can determine the success or failure of synthetic designs aimed at producing extrinsically doped LSPR-active semiconductor NCs.

3.3. Doping Schemes for LSPR Active Semiconductor NCs

Elemental metals and binary compound semiconductors were the focus of synthetic developments in the early stages of colloidal synthesis research, partly due to the limited complexity inherent to the chemistry of these syntheses. However, the advent of more elaborate synthesis necessary to make NCs of multinary materials has paved the way for much broader exploration of various physical properties, and LSPR-active NCs, especially those of doped semiconductors, have benefitted immensely from these developments. The preceding section comprised a general discussion of the principles of colloidal synthesis, which provides the basis of understanding necessary for discussing the more specific chemical considerations required for synthesis of LSPR-active NCs. In continuation, this section is devoted to more in-depth assessment of the synthetic considerations for the different core compositions of LSPR-active NCs with particular emphasis on introducing dopant atoms in these NC lattices. A general introduction to the various doping strategies will be given followed by specific examples of the different approaches.

A wide variety of doping strategies is available for compound semiconductors like metal oxides and metal chalcogenides to introduce free charge carriers and induce LSPR optical response. The inorganic chemistry toolbox available for colloidal NC formation already allows the synthesis of a multitude of these nanomaterials. One of the most potent synthetic methods for producing colloidal metal oxide NCs is through the previously mentioned lysis of ligand-coordinated monomers undergoing accumulation and condensation thereafter into NC lattices. Metal chalcogenide NC synthesis primarily employs the strategy of bringing reactive complexes of metals and chalcogens together at high temperature. A rich variety of LSPR-active semiconductor NCs have been reported in the literature, encompassing the doping methods introduced in this section, with their resulting properties further discussed in-depth in respective sections.

Certain metal oxides (e.g., ReO_3, VO_2) and metal chalcogenides (e.g., CuS) are intrinsically metallic in certain crystal phases and hence exhibit LSPR response without requiring extrinsic dopant atoms or intrinsic vacancy doping in order to introduce free charge carriers. For those materials not having an appreciable concentration of free charge carriers, pristine lattices can be perturbed to induce electron or hole compensating defects through intrinsic or extrinsic doping. LSPR-active metal oxide NCs have been almost exclusively doped n type while those of copper chalcogenides have been mostly p-doped. The various doping strategies can be classified through the schematic flowchart shown (Figure 32). In an overall sense, doping strategies can be hierarchically grouped into the following: intrinsic doping, interstitial doping, and substitutional doping.[35]

Intrinsic doping or self-doping can be realized without the need for dopants of a composition different from the atoms found in the stoichiometric material. When either a cation or anion is deficient with respect to the stoichiometric compound, the charge can be completely or partially compensated by free carriers, so the vacancies effectively dope the material. Anion vacancy doping is realized in substoichiometric oxygen vacancy-containing metal oxide NCs (e.g., WO_{3-x},[45] MO_{3-x}[394]). Oxygen vacancies are doubly charged, allowing up to two free electrons to be donated to the conduction band, leading to LSPR in some

DOI: 10.1021/acs.chemrev.7b00613
Chem. Rev. 2018, 118, 3121−3207

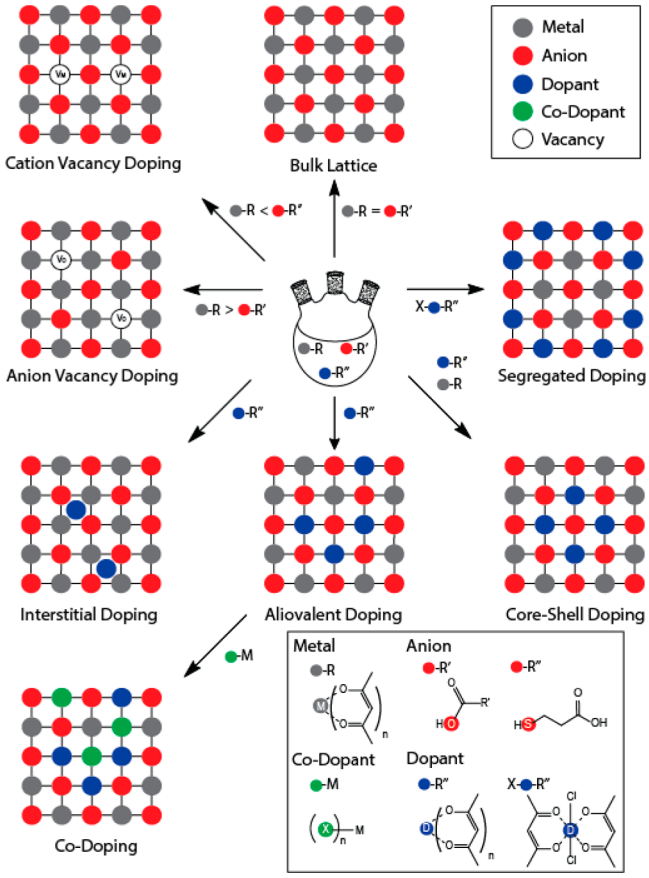

Figure 32. Doping strategies employed in the synthesis of LSPR-active semiconductor NCs. The various modes of doping a NC lattice include cation vacancy doping, anion vacancy doping, interstitial doping, extrinsic aliovalent doping, codoping, core−shell doping, and segregated doping.

anion vacancy doped NCs. In a similar manner, the p-doping in copper chalcogenides, namely the substoichiometric $Cu_{2-x}E$ (E = S, Se, Te) NCs, is also a result of extensive self-doping through the creation of copper vacancies which leads to the generation of a high density of holes in the valence band that can sustain an LSPR response in the NIR.[42,43,99]

On the other hand, interstitial doping is possible in metal oxides with interstitial crystal lattice sites large enough to accommodate an extrinsic dopant without inducing a structural phase change. As exemplified by tungsten bronze materials such as Cs_xWO_3, alkali cations are commonly doped in interstitial lattice sites.[113] Similar attempts at impurity doping of copper chalcogenides have generally led to the formation of multinary chalcogenide phases accompanied by a substantial change in the electronic band structure, so a tunable LSPR response is not always the outcome,[400,401] contrasting with success in metal oxides. Part of the reason for this difference lies in the relatively smaller interstitial sites in copper chalcogenides due to the similarity in the copper and chalcogen ionic radii so that inclusion of a foreign ion cannot be readily accommodated in the original crystal structure, and at meaningful impurity concentrations, doping leads to a complete overhaul of the atomic arrangement.

A wider spectrum of synthetic developments in LSPR-active semiconductor NCs, especially for metal oxides, has been realized with the third type of doping: substitutional doping, by employing a wide selection of extrinsic dopant atoms, precursor reactivity balance, and tuning of growth kinetics. Aliovalent metal ions can substitutionally occupy host cation sites to induce n-doping. In n-doped metal oxide NCs, the higher oxidation state of cationic dopants relative to the host metal cation can be compensated by free electrons when the dopant creates a shallow donor level so that the electron is readily thermalized to the conduction band, leading to LSPR properties in the degenerate limit. LSPR spectral tuning can synthetically be achieved by varying the amount of dopant precursor to change the incorporated doping concentration in NCs.

Within the scope of extrinsic substitutional doping, advanced doping methods allow expansion of LSPR properties in metal oxide NCs while using already available chemical precursors. Co-doping with a secondary dopant atom species precursor allows further LSPR tuning to higher energies in metal oxide NCs (e.g., F,In:CdO[122] and F,Sn:In_2O_3,[89] in which anion doping by F^- accompanies aliovalent cation doping) and opens the possibility of multifunctional LSPR-active magnetic NCs.[402] Control over the spatial distribution of substitutional dopants in NCs can be achieved by utilizing the dopant precursor reactivity difference between the host precursors. A segregated dopant distribution where dopants are distributed near the NC surface minimizes LSPR damping in Sn:In_2O_3.[195] Using a continuous injection method and introducing dopant precursors at a specified stage during the growth of the NCs (section 3.2.4), core−shell-doped Sn:In_2O_3 NCs with controllable radial distribution of Sn have been synthesized.[68] In the following sections, each doping strategy will be discussed in-depth with synthetic procedures and characterization techniques that have been employed to respectively expand and understand plasmonic semiconductor NC development.

3.3.1. Intrinsically Metallic NCs. Few binary semiconductor NCs reported in the literature have metallic properties, yet these examples are interesting as they allow NCs to exhibit LSPR properties without requiring addition of extrinsic dopants. This allows LSPR-active NCs to be synthesized based simply on binary compounds, bypassing the considerations of tertiary dopant reactivity balance in the growth reaction. For instance, rhenium oxide (ReO_3) has remarkable metallic properties for a metal oxide, with high electronic conductivity comparable to copper.[403,404] ReO_3 NCs exhibit LSPR in the visible range similar to that of metallic copper or gold nanoparticles due to free electrons within the conduction band.[403] ReO_3 has one more d electron per Re atom (and so, per formula unit) compared to tungsten (W) atoms in stoichiometric WO_3, which is a semiconductor with an empty conduction band. The extra electron in Re is donated into the conduction band, leading to a partially filled conduction band and metallic properties.[13,405] Biswas et al.[403] performed ReO_3 NC synthesis, realizing LSPR between 490 to 540 nm wavelength using a solvothermal autoclave synthesis by decomposition of presynthesized Re_2O_7-dioxane complex in toluene at 200 °C. Further, core@shell heterostructures with Ag, SiO_2, and TiO_2 were achieved by Ghosh et al.[406] ReO_3@Ag was prepared by shell growth upon reduction of Ag^+ ions, ReO_3@SiO_2 through the Stöber method, and ReO_3@TiO_2 by hydrolyzing titanium precursors. An atmospheric pressure colloidal synthesis has yet to be developed that produces ReO_3 NCs with a higher degree of monodispersity or morphology control, which could reinvigorate investigations into LSPR properties of this material. Another intrinsically LSPR-active NC material is lanthanum hexaboride (LaB_6), which has a fairly high energy LSPR with absorbance around a peak wavelength of 1000 nm, in the NIR region. Similar to ReO_3, LSPR-inducing free carriers in LaB_6 NCs are attributed

DOI: 10.1021/acs.chemrev.7b00613
Chem. Rev. 2018, 118, 3121−3207

to the finite density of state at the Fermi level with free carrier density corresponding to one free electron per formula unit.[407,408] Mattox et al.[407] synthesized colloidal LaB_6 NCs at a modest temperature (360 °C) compared to previously reported methods for synthesizing this refractory material by stirring sodium borohydride ($NaBH_4$) and lanthanum chloride ($LaCl_3$) in a three-neck flask. Prior reports on LaB_6 NC synthesis involved autoclave routes at 400 °C and solid-state reactions under vacuum at 1200 °C.[409,410]

Some insulating metal oxides can undergo phase transitions into intrinsically metallic phases (section 2.3.5), providing inspiration for the idea of phase-modulated LSPR-active nanomaterials. A metal−insulator transition occurs in vanadium dioxide (VO_2) via a thermally induced phase transition without requiring aliovalent dopants or vacancies to introduce free charge carriers, thus opening opportunities for temperature-dependent LSPR control.[260,411] Increasing temperature triggers a structural phase transition from an insulating monoclinic phase to metallic rutile. However, direct colloidal synthesis of VO_2 NCs has proved challenging. Instead, using a heat-up approach, Bergerud et al.[412] developed a colloidal synthesis of metastable bixbyite phase V_2O_3 NCs. Vanadyl acetylacetonate ($VO(acac)_2$) was used as the precursor in squalene, oleic acid, and oleylamine solution with growth temperatures between 310 and 370 °C. The presence of oleylamine to drive aminolysis was likely also responsible for vanadium reduction from 4+ oxidation state as in VO_2 to the 3+ state, resulting in V_2O_3 NCs.[412] Although direct colloidal synthesis of VO_2 has not been reported to this date, a film of metastable V_2O_3 NCs was shown to undergo conversion to VO_2 under controlled oxidative annealing at 375 °C.[259,261] Temperature-dependent NIR transmission modulation by annealed VO_2 phase NC films was observed to reveal the characteristic metal−insulator transition temperature near 70 °C. The high temperature rutile phase of VO_2 is expected to have metallic properties arising from a half-filled 3d-derived outer shell, while in the low temperature monoclinic phase, dimerization of V results in band splitting that opens a bandgap and transforms the material into an insulator.[257,413] EXAFS analysis of postsynthetically annealed VO_2 revealed and verified the temperature-dependent vanadium local bonding environment. Ordered octahedral symmetry characteristic of the metallic rutile phase was observed at high temperature (100 °C), while local distortion was observed in the lower temperature phase (room temperature) indicative of the insulating monoclinic phase due to strained V dimerization.[412]

Covellite (CuS), a stoichiometric member of the rich and diverse phase space of the Cu−S system,[272] is another example of a compound material that exhibits an inherent metallic p-type character arising from a significant density of free holes in its valence band.[276,414−417] The bonding and oxidation states in covellite have been a matter of intense debate, but the general consensus is that it has a layered structure with alternating layers of planar CuS_3 triangles and CuS_4 tetrahedra accompanied by dimerized S−S moieties holding these layers together.[276,418,419] Consequently, the electronic structure of covellite has been modeled differently by different authors, although the p-type conductivity is generally explained by the presence of delocalized holes in the valence band, which is mainly derived from S 3p orbitals.[415,416,418,420] This material is thus capable of sustaining an LSPR response in its nanostructured form, in accordance with its p-type nature. The literature is rife with various reports of general synthetic strategies for producing covellite nanostructures,[94,127,421,422] but the optical characteristics were relatively unexplored until the seminal paper by Zhao et al.[99] in 2009, which prompted more in-depth synthetic and optical studies by Xie et al.[189] in 2013. The synthetic strategy adopted by Xie et al.[189] was the classical hot-injection method where the sulfur source was injected into a copper precursor solution at 180 °C. A subsequent heat-up approach was also demonstrated by Xie et al.[198] in another report that was published around the same time in which the authors demonstrated tunability of the Cu content in the NCs accompanied by a change in the optical response. The Cu content of the NCs was postsynthetically varied by their reaction with a Cu(I) complex ($[Cu(CH_3CN)_4]PF_6$), and the optical response was tuned from the strong LSPR of the covellite NCs to the absence of LSPR in Cu_2S. The authors demonstrated that the oxidation state of Cu remains close to +1, but the average −1 oxidation state of S in covellite gradually progresses to −2 (i.e., sulfur gets progressively reduced due to the cleavage of the S−S dimers).

3.3.2. Cation Vacancy Doped NCs. Cation vacancy doping is the primary mode of self-doping in copper(I) chalcogenide NCs (section 2.4.1) that routinely creates an appreciable density of free holes in the valence band resulting in an LSPR response.[42,43,99,112,146,268] The optical properties of nonstoichiometric $Cu_{2-x}E$ (E = S, Se, Te) NCs can be tuned with considerable control by gradually changing the copper content in these NCs. The Cu vacancies formed by nonstoichiometry are compensated, at least in part, by the creation of holes in the valence band, and the concentration of these holes is often presumed to correlate directly with the copper content. Undoubtedly, increasing the Cu deficiency increases the hole density, which causes the LSPR to shift to higher frequencies. This qualitative relationship between stoichiometry and LSPR frequency has been demonstrated by a number of researchers, starting with Zhao et al.[99] in 2009 with their synthesis of $Cu_{2-x}S$ NCs through sonoelectrochemical, hydrothermal, and solventless thermolysis routes. The Cu:S molar ratio was varied in these NCs from covellite (CuS) to djurleite ($Cu_{1.97}S$) by adopting strategies particular to each synthetic method: reduction potential adjustment in the sonoelectrochemical protocol, pH adjustment for hydrothermal method, and different precursor pretreatments in the solventless thermolysis technique. Later, in 2011, Luther et al.[42] used a hot-injection technique to synthesize Cu_2S NCs of diameters in the range 2.5−6 nm and generated Cu-vacancies in these NCs through exposure to air, leading to the emergence of an LSPR peak that intensified and blue-shifted, due to an increasing concentration of free holes, to an eventual energy of 0.7 eV. Increase in the hole concentration and consequent LSPR frequency tuning upon air exposure was also demonstrated in $Cu_{2-x}S$ and $Cu_{2-x}Se$ NCs by Kriegel et al.[146] These reports point toward the primary difficulty of working with copper chalcogenide NCs, which is their inherent instability in ambient conditions due to the propensity of Cu ions to leach out of the NC lattice upon the slightest exposure to air. Recent work on stabilizing the LSPR response by forming a shell on the LSPR-active NC core like that by Xie et al.[275] has suggested a chemical strategy to pin the LSPR energy through the formation of an alloyed $CuPd_xS$ shell.

Several authors have shown similar LSPR tunability in copper chalcogenide NCs through postsynthetic treatments in mostly air-free conditions in order to exercise a reasonable level of control over the carrier concentration.[43,46,146,423,424] Common oxidants like iodine[46] and ceric ammonium nitrate were shown to generate free holes in the copper chalcogenide NC lattices, while Cu^+ ions were leached out of the lattice in the process of

DOI: 10.1021/acs.chemrev.7b00613
Chem. Rev. 2018, 118, 3121−3207

oxidation.[43] A host of reducing agents have been shown to restore the Cu:E stoichiometry, which include thiols, sodium biphenyl,[46] diisobutylaluminum hydride,[146] lithium triethyl borohydride,[425] methyl viologen radicals,[423] cobaltocene,[424] etc. For instance, Dorfs et al.[43] demonstrated reversible tuning of the LSPR response of $Cu_{2-x}Se$ NCs by creating holes in the NC lattice by Ce^{4+}-based oxidation, which decreased the Cu:Se molar ratio from the ideal 2:1 to a lower limit of 1.6:1 and then restored the stoichiometry by reduction with a Cu(I) complex ($Cu(CH_3CN)_4PF_6$) back to the as-synthesized stoichiometry.[96] Similar reversible tunability through redox pathways has also been demonstrated by other authors.[46,146]

3.3.3. Anion Vacancy Doped NCs. Anionic vacancy doped colloidal metal oxide NCs can be realized by stoichiometric deficiency of oxygen relative to metal atoms (section 2.3.1). Intrinsic doping in metal oxide NCs is achieved when certain metal oxides (WO_3, MO_3) exhibit strong LSPR response due to lattice vacancies.[426,427] This self-doping mechanism does not require extrinsic dopants since oxygen vacancies provide charge balance to free electrons in the conduction band. Oxygen-deficient synthetic conditions can favor the formation of oxygen vacancy point defects in NC lattices, especially when the metals are soft with large atomic radii and diverse stable oxidation states. Under conditions of low partial pressure of oxygen during synthesis, where precursors are degassed prior to nucleation, the metal oxide lattice vacancy equilibrium will be strongly biased toward forming oxygen vacancies and vacancy concentrations can be further adjusted through postsynthetic oxygen exposure.[35,114] An oxygen vacancy can compensate two electrons per defect site according to the Kröger−Vink notation $O_O^{\times} \rightarrow V_O^{\cdot\cdot} + 2e' + \frac{1}{2}O_2$. The oxygen vacancy creates a shallow donor level that easily thermally ionizes to donate two electrons to the conduction band, leaving a dianion point defect $V_O^{\cdot\cdot}$ with a net two electron positive charge. Thus, the donated free electrons enable a LSPR response to occur in stoichiometrically oxygen-deficient WO_{3-x}[45] and MoO_{3-x}NCs.[394,428]

WO_3 can be described as a modified perovskite-type ABO_3 lattice with tungsten occupying the B site and an unoccupied A site.[426] In an oxygen substoichiometric WO_{3-x}, WO_6 octahedron units form distorted hexagonal tunnels due to oxygen vacant WO_{3-x} reduced forms (Figure 33a). XRD patterns of undoped distorted substoichiometric WO_{3-x} phase NCs reveal consistency with the bulk reference pattern of monoclinic $WO_{2.72}$.[113] XPS of $WO_{2.72}$ NCs revealed near-surface tungsten in 6+ and also reduced 5+ and 4+ oxidation states, which can compensate the charge of oxygen vacancies (Figure 33d).[75,429] Various tungsten precursors have been employed in colloidal WO_{3-x} NC synthesis. Lee et al.[78] used tungsten hexacarbonyl ($W(CO)_6$) with oleylamine and trimethylamine *N*-oxide in a slurry to synthesize tungsten oxide nanorods. Manthiram et al.[45] demonstrated colloidal $WO_{2.83}$ NC nanorod synthesis with strong LSPR at 900 nm wavelength by hot injection of tungsten(V) ethoxide in oleic acid and trioctylamine. Mattox et al.[113] further demonstrated heat-up colloidal synthesis of $WO_{2.72}$ NC nanorods by decomposition of WCl_4 in oleylamine and oleic acid solution (Figure 33b). Using $W(CO)_6$ as a precursor, aspect ratio tuning from 30.2 nm long to 84.4 nm long $WO_{2.72}$ NC nanorods was demonstrated by increasing the ratio of trimethylamine *N*-oxide to the tungsten precursor in oleylamine.[75,78]

MoO_{3-x} is another oxygen vacant colloidal LSPR-active NC material reported in the literature within the class of anion vacancy doped NCs. MoO_{3-x} are interesting 2D plasmonic

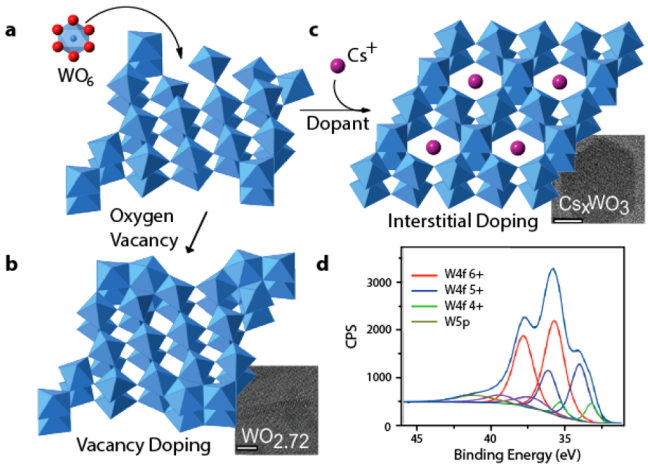

Figure 33. Vacancy doping and interstitial doping. (a) WO_6 octahedron units form perovskite-based structures with hexagonal tunnels. (b) Crystal structure in the polyhedral representation of oxygen substoichiometric $WO_{2.72}$ and high-resolution TEM image (inset, scale bar 5 nm). (c) Interstitially doped Cs_xWO_3 and high-resolution TEM image (inset, scale bar 5 nm). Reprinted with permission from ref 113. Copyright 2014 American Chemical Society. (d) XPS spectrum exhibiting tungsten 6+, 5+, and 4+ oxidation states in $WO_{2.72}$. Reprinted from ref 75. Copyright 2017 American Chemical Society.

materials due to their nanosheet morphology, and XPS studies have been conducted to provide insight into metal oxidation state and valence changes induced by oxygen vacancies (section 2.3.9). Colloidal MoO_{3-x} NCs take a thermodynamically preferred nanosheet morphology based on the orthorhombic α-MoO_3 crystal structure consisting of MoO_6 octahedra sharing four corners to form a plane and two octahedral edges conjoining two planes into a single layered structure.[428] Colloidal oxygen vacancy doped MoO_{3-x} nanosheets were synthesized hydrothermally by Huang et al.[394] with ammonium molybdate as the precursor dissolved in an emulsion of deionized water and hydrochloric acid with oleylamine and cyclohexane in an autoclave at 180 °C. The resulting product was oleylamine surface passivated nanosheets with LSPR absorption peaking at 750 nm wavelength. XPS analysis verified the existence of oxygen vacancy-induced multivalent metals, where Mo(V) valence d^1 and Mo(VI) valence d^0 signals were observed at the XPS $3d_{3/2}$ and $3d_{5/2}$ doublet peak.[430] Postsynthetically after 24 h oxidization in air, the blue MoO_{3-x} nanosheet solution oxidized to nonplasmonic white nanotubes. XPS analysis demonstrated that the oxygen vacancy induced Mo(V) valence 3d peak disappeared and only the Mo(VI) valent 3d peak was observed after oxygen exposure.[430] Postsynthetic LSPR peak tuning in MoO_{3-x} was further demonstrated by Li et al.[431] by manipulating the NCs with reducing agent (section 4.2). Substoichiometric MoO_{3-x} nanodots were synthesized from pristine MoO_3 derived from chemical oxidation of bulk MoS_2. Exposing pristine MoO_3 to a strong reductant sodium borohydride ($NaBH_4$) lead to LSPR-active substoichiometric MoO_{3-x}, and XPS analysis revealed substantial increase of the presence of the Mo(V) valent state. Aqueous MoO_3 exposed to controlled concentrations of the weaker reducing agent ascorbic acid at 60−70 °C resulted in MoO_{3-x} nanodots with further LSPR tunability between 700−1000 nm wavelength. Analogous to $Cu_{2-x}S$ NCs (section 4.2), controlled redshifting of the LSPR was attributed to the decrease of Mo cation vacancy sites existing on the nanodot surface by adding higher concentration of weak organic

DOI: 10.1021/acs.chemrev.7b00613
Chem. Rev. 2018, 118, 3121−3207

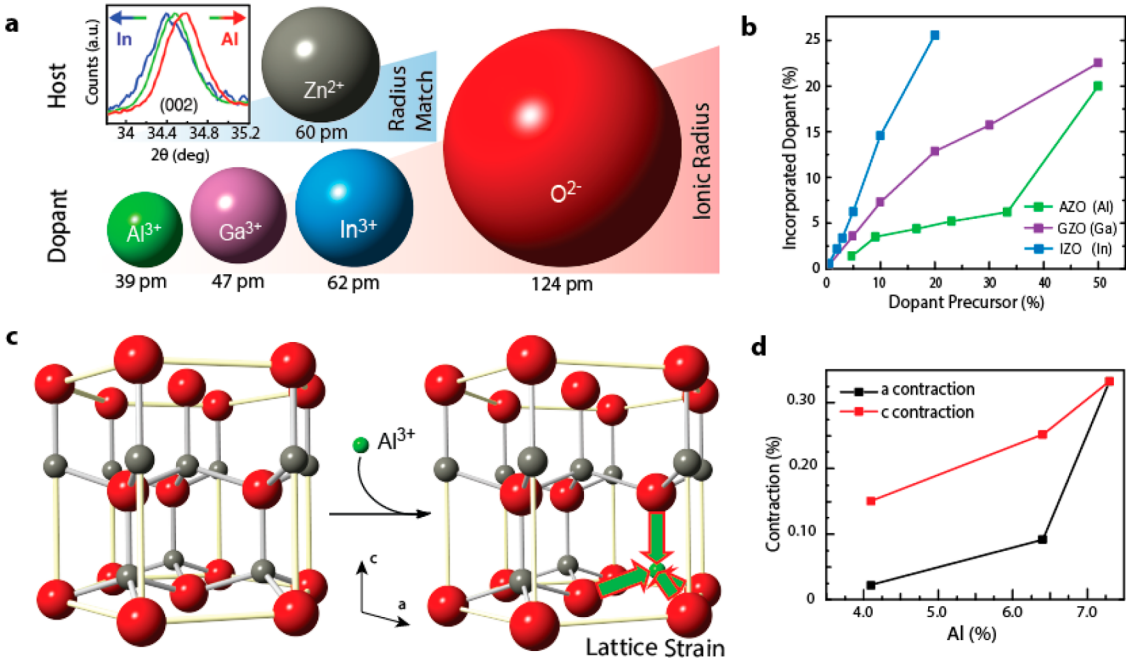

Figure 34. Extrinsic aliovalent substitutional doping. (a) Dopant ionic radius comparison. A difference between the ionic radii of the host metal (Zn^{2+}) and dopant (In^{3+} and Al^{3+}) leads to ZnO NC lattice expansion/contraction observed by analysis of the (002) XRD peak (inset). Reprinted from ref 432. Copyright 2016 American Chemical Society. (b) Al:ZnO, Ga:ZnO, and In:ZnO, dopant incorporation, characterized by ICP-AES, induced lattice mismatch dependent on dopant radius. Data were adapted from refs 84, 70, and 398. (c) Schematic of aluminum dopant induced ZnO lattice straining. (d) Aluminum doping induced *a* and *c* axis lattice contraction in ZnO NCs. Reprinted from ref 84. Copyright 2011 American Chemical Society.

reducing agent, and thus lowering the free electron concentration.[431]

3.3.4. Interstitially Doped NCs. Interstitial doping with extrinsic ions allows introduction of shallow donor states to the band structure of a metal oxide when interstitial lattice sites are sufficiently large to accommodate the dopants (section 2.2.1). Interstitial dopants can contribute electrons to the metal oxide conduction band, leading to LSPR response of free carriers at sufficient concentrations. For instance, theoretical studies of the tungsten bronze $NaWO_3$ suggest that the interstitial sodium alkali atoms donate their 3s electrons to the conduction band.[405]

LSPR has been realized in colloidal tungsten bronze (M_xWO_3) NCs by interstitially doping alkali metal cations in open channels within the WO_3 structure (Figure 33c). Interstitial doping in tungsten bronze NCs was demonstrated by Mattox et al.,[113] where alkali metal chlorides proved to be effective dopant precursors for driving interstitial doping in LSPR-active tungsten bronze NCs. Alkali metal cesium chloride or rubidium chloride precursors were introduced in a heat-up colloidal synthesis. Cs^+ and Rb^+ dopants have large ionic radii of 1.2 and 1.7 Å, respectively, which are compatible with the tunnel-like interstitial pathways in hexagonal WO_3. In Cs_xWO_3, the occupation of interstitial sites stabilizes the hexagonal crystal structure (which is unstable in undoped WO_3) and this structure was observed by XRD of the synthesized NCs, with the presence of Cs^+ ions verified by XPS using the Cs 3d peak. Postsynthetic redox chemistry was used to modulate the LSPR peak by near-surface oxidation or reduction of hexagonal Cs_xWO_3 platelets. Postsynthetic air exposure of 24 h diminished the free electron population resulting in red-shifted LSPR. To reverse the oxidation, hydrazine was added incrementally to act as a reducing agent, which recovered the original LSPR peak energy of the Cs_xWO_3 NCs.[56]

3.3.5. Extrinsic Aliovalent Substitutionally Doped NCs. Extrinsic aliovalent substitutional doping requires synthetically replacing host atoms in a NC lattice structure with impurity atoms. During particle growth, substitutional dopants are added to either metal or oxygen lattice sites, or both, simultaneously with metal oxide precursor decomposition and deposition leading to the growth of as-synthesized doped NCs. Oxidation valence charge imbalance between the host cation or anion and a dopant ion leads to electron or hole compensation per dopant atom.[109] However, the energetic instability of holes in the deep valence band of most metal oxides has meant that metal oxides are almost exclusively electron doped (i.e., n type). A wide range of metal cation precursors can be selected to dope metal oxide NCs. Metal ion dopants with varying valence states are coordinated by various organic or inorganic ligands (e.g., acetate, acetylacetonate, chloride, or 2-ethylhexanoate) to form soluble precursors and to control dopant precursor reactivity during NC growth.

Building on previously established synthesis for metal oxide NCs that can serve as host materials, a wide selection of dopants enables the widest diversity and tunability of LSPR properties by design. In wurtzite phase ZnO NCs, substitutionally doped compositions with aliovalent dopants so far reported are aluminum, (Al:ZnO),[84] gallium, (Ga:ZnO),[433] indium, (In:ZnO),[70,398] and germanium-doped zinc oxide, (Ge:ZnO).[249] In rocksalt phase CdO NCs, indium, (In:CdO),[124] gallium, (Ga:CdO), aluminum, (Al:CdO), and tin-doped cadmium oxide (Sn:CdO) have been reported.[123] Tin, ($Sn:In_2O_3$),[245,434] cerium, ($Ce:In_2O_3$),[59] and titanium-doped indium oxide, ($Ti:In_2O_3$)[242] have been reported based on bixbyite phase In_2O_3 NCs. Titanium oxide NCs have been substitutionally doped with aliovalent niobium ($Nb:TiO_2$).[435] Fluorine is an anionic dopant that has been reported in metal oxide NCs, as in indium-, fluorine- codoped cadmium oxide

DOI: 10.1021/acs.chemrev.7b00613
Chem. Rev. 2018, 118, 3121−3207

(F,In:CdO).[122] The subsequent discussion will focus substantially on single elemental aliovalent substitutional doped ZnO NCs since crystallographic structural studies have been thoroughly conducted in this materials system.

Extrinsic aliovalent substitutionally doped NCs retain their original crystallographic phase at moderate doping concentration. Characteristic XRD peaks are retained in ZnO NCs without appearance of additional phases regardless of dopant choice.[70] Yet, the incorporation of dopants induces strain in the NC lattice where contraction or expansion can be observed by XRD peak shifts. In wurtzite phase ZnO NCs, substitutional tetrahedral coordination of Al^{3+} ion in Zn^{2+} lattice[436] sites causes lattice contraction due to the smaller ionic radius of the dopant (Figure 34c).[437] XRD of doped ZnO NCs reveals that (002) lattice expansion occurs when doping with larger radius In^{3+} (62 pm), while contraction occurs when doping with smaller radius Al^{3+} (39 pm) due to lattice strain (Figure 34d).[432] XRD refinement through Rietveld analysis revealed Al-doped ZnO NCs undergo progressive lattice contraction in both the *a* and *c* crystallographic directions with increasing Al^{3+} dopant ion (39 pm) concentration (Figure 34 d).[84] The consistency of the observed changes in lattice parameter with the relative sizes of the dopant and host material ionic radii is evidence supporting that dopants are incorporated substitutionally, rather than occupying interstitial or surface sites, or being present in a phase-separated portion of the sample.

Progressive increases in the doping level, achieved by the addition of more dopant precursor to the reaction, allow the LSPR peak to be blue-shifted systematically due to increasing free charge carrier concentration. Dopant precursor concentration during synthesis and aliovalent substitutional dopant incorporation in the NC lattice exhibit a monotonic correlation until the lattice fails to accommodate more dopants or a phase change or other major change in the synthetic product occurs (Figure 34b). ICP-AES can be utilized along with EDS, XPS, and Rutherford backscattering spectrometry (RBS)[433] analysis to support dopant quantification. ICP-AES is especially versatile for characterizing low concentration metal dopants by quantifying dopant and host metal spectral signatures in acid-digested NC samples. On the basis of such studies, it is apparent that the efficiency of incorporation of extrinsic dopants differs with composition of the dopant and the coordinating ligands in the dopant precursor. These trends can be influenced by ionic radius differences between dopants and the host material. Della Gaspera et al.[70] demonstrated using metal(III) acetylacetonate dopant precursors that doping efficiency is greater when the ionic radius of the trivalent dopant metal ion [here, In^{3+}, Ga^{3+}, and Al^{3+} (62, 47, and 39 pm, respectively) were considered] closely matches that of tetrahedral coordinated Zn^{2+} (60 pm) in ZnO NCs (Figure 34a). In^{3+} was shown having the most favorable dopant incorporation efficiency due to the similar radius that minimizes lattice strain and the associated free energy cost to forming a substitutional defect on a Zn^{2+} site.

The crystallographic lattice position of dopant atoms in extrinsic aliovalent substitutional-doped NCs is a factor to consider for dopant element selection. At high doping levels, the LSPR frequency may no longer increase and, in some cases, may eventually red-shift due to the formation of defect clusters that create deep, midband gap states. This has been well-studied in $Sn:In_2O_3$, where $2Sn_{In}^{\cdot} - O_i''$ cluster formation at high dopant concentration (section 2.3.1) decreases the free electron concentration.[109] Kelchtermans et al.[436] investigated the crystallographic position of dopants in Al-doped ZnO NCs with XRD crystallographic structure analysis, ICP-AES elemental analysis, and solid state NMR. In wurtzite phase ZnO crystals, substitutional tetrahedral coordination of Al^{3+} ion in Zn^{2+} lattice sites enables free electron donation to the conduction band, while other site occupancy (e.g., interstitial) is not expected to yield this result.[437] Differing coordination preference such as interstitial octahedral or tetrahedral coordination would lead to Al^{3+} ion acting as an acceptor, trapping free electrons. Solid state ^{27}Al-NMR was used in solvothermally synthesized Al-doped ZnO NCs to differentiate Al^{3+} in tetrahedral or octahedral coordination environments, revealing the majority of the dopant ions were located in octahedral sites making them ineffective, or even counterproductive, for charge carrier generation.[436]

Hole doping in metal oxides is challenging to realize owing to typically deep valence bands and the moderate formation energy for oxygen vacancies, which can easily compensate any net negative charge on the crystal lattice. One example of p-type metal oxide NCs has been reported, which is spinel-type gallium iron oxide (Ga_2FeO_4), investigated by Urso et al.[348] Off-stoichiometric precursor ratio control between Ga and Fe allowed either n- or p-type doping (section 2.2.1) to be realized with both producing LSPRs peak down to a wavelength of 1000 nm in the NIR spectral range. The synthesis followed a typical heat-up procedure with gallium(III) acetylacetonate ($Ga(acac)_3$) and ferrous acetylacetonate ($Fe(acac)_2$) precursors in oleic acid, oleylamine, and octadecene solution resulting in Ga_2FeO_4 NCs. The gallium and iron precursor molar ratio was varied between Ga/Fe = 0.7 and 3.3 to induce off-stoichiometric Ga_2FeO_4 in which the NC compositions (determined by ICP-AES) correlate with the compositional ratio of the precursors during the synthesis reactions. First principle DFT calculations by Paudel et al.[438] and experimental X-ray absorption near-edge spectroscopy (XANES) with X-ray emission spectroscopy reported by Shi et al.[439] probed the oxidation states of the cations in bulk spinel oxides suggesting lower formation energy for antisite defects in spinel oxides compared to vacancy or intersititial defects. This low defect formation energy allows charge compensation, at least in part, by valence band holes instead of other point defects, thus enabling the realization of p-type doping in metal oxide NCs. DFT-derived band structures by Urso et al.[348] implied Fe-rich synthetic conditions led to p-type LSPR-active NCs through substitution of Ga^{3+} ions by Fe^{2+} ions (Fe_{Ga}'), resulting in free hole generation with a shallow acceptor level near the CBM. Ga-rich conditions led to n-type doping by conversely replacing Fe^{2+} with Ga^{3+} ions ($Ga_{Fe}^{\cdot}$), producing free electrons and a donor level close to the CBM.[438] Fe^{2+}, not Fe^{3+}, must substitute Ga^{3+} cations to allow effective generation of hole carriers, and thus XPS analysis was conducted to experimentally elucidate the oxidation state of both ions. In off-stoichiometric Fe-rich Ga_2FeO_4 NC samples, the Ga $2p_{3/2}$ XPS peak was consistent with a 3+ oxidation state while Fe 2p peaks suggested 2+ oxidation states down to a ratio of Ga/Fe = 1.6. Although XPS is sensitive only to the near-surface regions, these results implied that Fe-rich NCs have Fe^{2+} that substitutes for Ga^{3+} cations in the lattice, enabling compensation of free holes. To experimentally elucidate the p-type character of carriers in NCs, transient photovoltage (PV) measurements and electrochemical impedance spectroscopy (EIS) were conducted on films of Fe-rich Ga_2FeO_4 NCs. In the PV measurement, the authors observed a potential drop with respect to an Ag/AgCl reference electrode upon exposure to light. The result was attributed to photogenerated hole carriers causing a downward band bending as a consequence of Fermi energy pinning, supported by EIS measurements. Since the band

DOI: 10.1021/acs.chemrev.7b00613
Chem. Rev. 2018, 118, 3121−3207

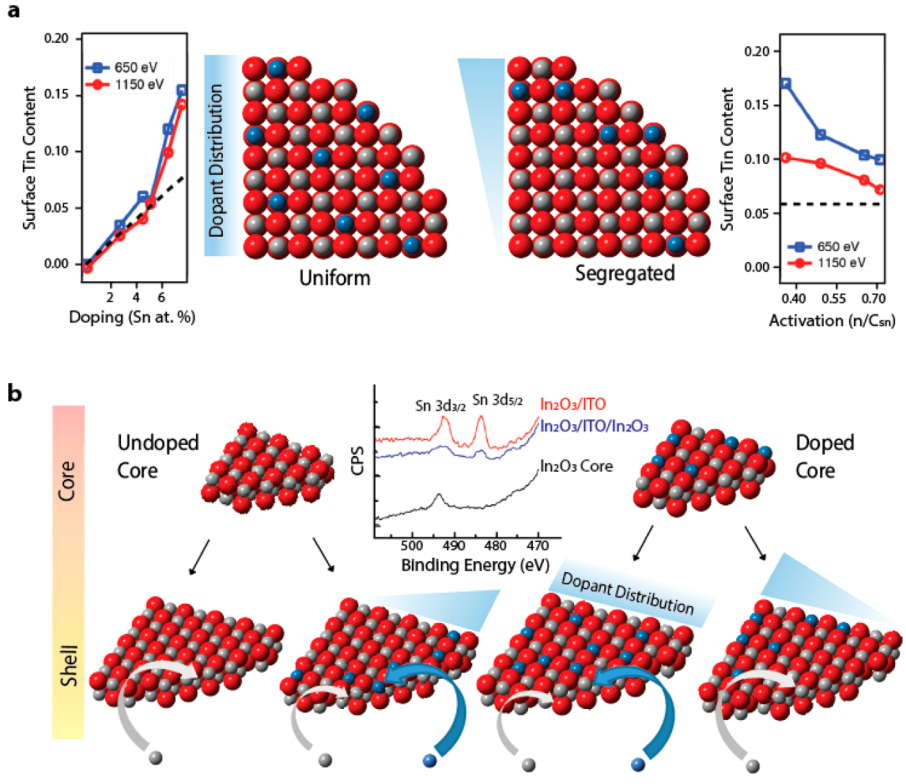

Figure 35. Dopant spatial distribution schematic. (a) Uniformly doped $Sn:In_2O_3$ is shown schematically alongside energy-dependent XPS data (left); surface segregated $Sn:In_2O_3$ is shown with corresponding XPS data (right). Reprinted from ref 195. Copyright 2014 American Chemical Society. (b) Growth-controlled dopant spatial distribution outcomes are shown schematically: undoped In_2O_3 (far left); core/shell $In_2O_3/Sn:In_2O_3$ (center left); doped $Sn:In_2O_3$ (center right); and core/shell $Sn:In_2O_3/In_2O_3$ (far right). A decrease in the XPS Sn 3d peak was seen after undoped shelling in core/shell/shell $In_2O_3/Sn:In_2O_3/In_2O_3$ (inset). Reprinted from ref 68. Copyright 2016 American Chemical Society.

bending behavior was in the opposite direction from what is expected in n-type-doped semiconductors, the data supported the conclusion of achieving p-type doping in LSPR-active metal oxide NCs.

3.3.6. Dopant Spatial Distribution Control. Doping synthetic strategy is not limited to incrementing the level of incorporated dopants in extrinsic aliovalent substitutionally doped NCs (sections 2.2.1 and 2.3.1) but also involves controlling the spatial distribution of the dopants (section 2.3.6) within each NC. One approach to control spatial distribution of dopants is to manipulate the kinetics of dopant incorporation and crystal growth by revisiting the balance of reactivity between precursors for the dopant and host material (e.g., using combinations of organic and halide coordinating ligands). In doped NC growth, the kinetics (rather than thermodynamics) typically govern dopant incorporation since diffusion rates are low, so the dopants remain distributed as they are when initially incorporated.[395] Lounis et al.[195] reported that the spatial distribution of substitutional dopants can strongly impact the LSPR response in metal oxide NCs. Specifically, the authors found that frequency-dependent plasmon damping due to impurity scattering is largely suppressed by distributing substitutional dopants near the surface of $Sn:In_2O_3$ NCs. Previously developed $Sn:In_2O_3$ heat-up colloidal synthetic methods were found to result in either uniform or surface segregated tin-doped NCs. Uniformly doped $Sn:In_2O_3$ NCs were produced using the method of Kanehara et al.[434] that uses indium(III) acetate and tin(II) 2-ethylhexanoate precursors. Surface-segregated $Sn:In_2O_3$ were prepared by the approach of Choi et al.[245] that uses indium(III) acetylacetonate ($In(acac)_3$) and tin(IV) bis(acetylacetonate) dichloride ($Sn(acac)_2Cl_2$) precursors. In $Sn(acac)_2Cl_2$, the halide ligands coordinated with tin are expected to be harder and to bond strongly with Sn^{4+}, diminishing the reactivity of this precursor compared to tin(II) 2-ethylhexanoate. The production of surface-doped $Sn:In_2O_3$ may be due to the reduced reactivity of $Sn(acac)_2Cl_2$ relative to the indium precursor ($In(acac)_3$), though other parameters such as surfactant composition also differed between the two protocols and their potential to influence dopant distribution cannot be ignored. Nonetheless, in general having a dopant precursor with a slower decomposition rate may delay doping until later in the reaction, leading to a spatial gradient of dopants favoring placement near the NC surface rather than being uniformly distributed within the NCs.[195] Further systematic investigation and realization of segregated doping in other compositions of doped NCs would be required to generalize this kinetically controlled strategy for controlling radial distribution of substitutional dopants. Virtual depth profiling by variable energy XPS is an effective tool to assess spatial distribution of dopants that was used in this case to observe the distribution of Sn in $Sn:In_2O_3$ NCs. The escape depth of photoelectrons increases with X-ray energy, so the ratio of signal detected from dopant and host metal ions varies with X-ray energy in case the dopants are not uniformly distributed. Thus, XPS analysis provides general information on dopant distribution without confronting the challenges of TEM-EDS spatial resolution and elemental abundance limits. An expected linear relation (dashed line) in surface tin content compared to overall tin content measured by ICP-AES is observed while using the synthesis method of Kanehara et al.,[434] indicating uniformly distributed tin (Figure

DOI: 10.1021/acs.chemrev.7b00613
Chem. Rev. 2018, 118, 3121−3207

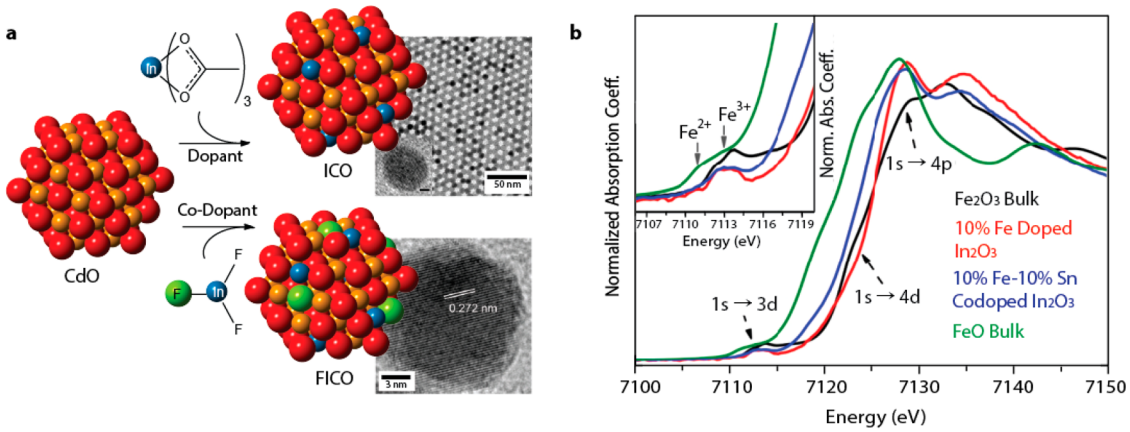

Figure 36. Co-doping oxide NCs. (a) Indium-doped cadmium oxide (In:CdO) synthesis by indium(III) acetate dopant precursor (schematic and TEM image, top). Reprinted from ref 124. Copyright 2013 American Chemical Society. Fluorine and indium-codoped cadmium oxide (F,In:CdO) by indium(III) fluoride dopant precursor (schematic and TEM image, bottom). Reprinted from ref 122. Copyright 2014 American Chemical Society. (b) Sn−Fe codoped In_2O_3 NC X-ray absorption near edge structure (XANES) spectra of Fe dopant. Inset show 1s → 3d peaks characteristic of Fe^{2+} and Fe^{3+}. Reprinted from ref 402. Copyright 2015 American Chemical Society.

35a, left). Meanwhile, the synthesis method of Choi et al.[245] showed higher surface tin content than the overall average doping level (dashed line), indicating surface segregated doping (Figure 35a, right).[195]

Another strategy to control radial dopant distribution is to time the addition of dopant precursors during the NC growth process. To overcome differences in precursor reaction rates, it is helpful to slow the overall reaction, limiting growth by adding reagents continuously and dropwise to facilitate efficient incorporation of dopant atoms without coalescence or ripening.[117] The dopant precursor can then be added at any specified stage of growth, allowing layer-by-layer growth and spatially precise control of composition in the radial direction. Ito et al.[376] synthesized In_2O_3 NCs by slow dropwise injection colloidal synthesis (Figure 35b, far left) and demonstrated that doped metal oxide NCs (specifically $Sn:In_2O_3$) can be synthesized by simultaneously adding host and dopant precursors dropwise into the solution. The indium(III) acetate and tin(IV) acetate precursors mixed in oleic acid contribute to NC growth without unwanted secondary nucleation when injected dropwise into oleyl alcohol at 230 °C (Figure 35b, center right). Jansons et al.[68] further extended this method (section 3.2.4) to achieve control over radial core−shell dopant profiles (section 2.3.6) by timely injection of extrinsic dopant precursor solution during continuous layer-by-layer growth achieved by slow injection colloidal synthesis, allowing precise control over dopant distribution. Continuous injection of a precursor solution containing tin(IV) acetate, indium(III) acetate, and oleic acid into oleyl alcohol heated to 290 °C led to doped $Sn:In_2O_3$ NC nucleation and growth. $Sn:In_2O_3/In_2O_3$ core/shell NCs were synthesized by subsequently injecting a separate undoped indium oleate solution to epitaxially grow In_2O_3 shells around the $Sn:In_2O_3$ cores (Figure 35b, far right). Conversely, Crockett et al.[121] demonstrated $In_2O_3/Sn:In_2O_3$ core/shell synthesis by reversing the order of injection of the Sn-doped and undoped solutions (Figure 35b, center left). $In_2O_3/Sn:In_2O_3/In_2O_3$ core/shell/shell NCs were synthesized by subsequently growing outer In_2O_3 shells through injection of additional indium oleate solution to a reaction mixture containing the $In_2O_3/Sn:In_2O_3$ core/shell NCs.[68] XPS characterization supported that the dopant distributions reflected the order of addition of the precursor solutions in core/shell NCs synthesized by the continuous slow injection method. $In_2O_3/Sn:In_2O_3$ core/shell aliquot XPS spectra show the appearance of Sn 3d peaks characteristic of tin dopants near the NC surface after doped shell growth on undoped cores. Decrease in Sn 3d peak amplitude was observed after subsequent growth of the undoped In_2O_3 shell and ascribed to inelastic scattering caused by the outermost shell, supporting the formation of a $In_2O_3/Sn:In_2O_3/In_2O_3$ core/shell/shell structure (Figure 35b, inset).

3.3.7. Co-Doping in Extrinsic Substitutionally Doped NCs. Further enhancement of charge carrier concentration to push the LSPR toward higher energy can be realized by simultaneously incorporating anion and cation codopants (section 2.3.2). Ye et al.[122] demonstrated that using indium(III) fluoride as a dopant precursor provided a simultaneous source for anionic fluorine and cationic indium cation doping in cadmium oxide NCs (Figure 36a). Cationic and anionic codoping enhances carrier concentration above the limits achievable by single element doping. F- and In-codoped CdO (F,In:CdO) and F- and Sn-codoped In_2O_3 NCs have extended the energy range of achievable LSPR wavelengths in metal oxide NCs down to 1500 nm or more.[122] The ionic radius of F^- anions as a dopant (1.33 Å) is slightly smaller than O^{2-} anions in the host (1.40 Å) in the CdO NC lattice.[122,440] Fluorine atoms can act as electron donors when substituting oxygen atoms in the crystal lattice since the F^- anion has one more valence electron than the host O^{2-} anions. The independence of these defects from cationic substitutions allows for simultaneous doping on anionic and metal cation sites with aliovalent substitutional dopants. Indium(III) fluoride as a codopant precursor was used in a heat-up synthesized CdO NCs with cadmium(II) acetylacetonate, oleic acid, and 1-octadecene reaction mixture. Decoupling of the concentrations of the two dopants is also possible through the combination of an anionic dopant precursor (e.g., LiF, NaF) and a cationic dopant precursor (e.g., indium(III) acetate). Instead of using indium(III) fluoride as a codopant precursor, increasing the amount of LiF or NaF as an anionic dopant precursor allowed additional blue-shifting of the LSPR peak in doped CdO. Fluorine- and tin-codoped indium oxide ($F,Sn:In_2O_3$) was demonstrated through a similar strategy by incorporation of extrinsic F anion and Sn cation dopants.[89] In a heat-up colloidal synthesis approach, tin(IV) fluoride was used as a codopant precursor with indium(III) acetylacetonate in a solution of oleic acid, trioctyl-

DOI: 10.1021/acs.chemrev.7b00613
Chem. Rev. 2018, 118, 3121−3207

amine, and octylamine. Fluorine anions similarly occupy the oxygen lattice site, forming $F_O^{\cdot}$ substitutional defects and contributing free electrons to the In_2O_3 conduction band.

Simultaneous codoping with two different cationic dopants has also been demonstrated in metal oxide NCs, enabling LSPR spectral tunability and further multifunctionality. Ghosh et al.[441] reported Sn and Cd codoping in ZnO NCs by using host metal precursor zinc stearate ($Zn(STA)_2$) and cadmium stearate ($Cd(STA)_2$) and tin myristate ($Sn(MTA)_4$) dopant precursors. Increasing Cd alloying expanded LSPR band spectral tunability from NIR toward the visible spectral range between 890 to 2600 nm wavelength. Tandon et al.[136] reported codoping In_2O_3 NCs with Fe and Sn leading to multifunctional magnetic and plasmonic propeties. A heat-up colloidal synthesis was used with indium(III) acetylacetonate as the metal precursor in oleylamine solution, while tin(IV) bis(acetylacetonate) dichloride and iron(III) acetylacetonate was used as the codopant precursor. Substituting In^{3+} with Sn^{4+} as an aliovalent dopant provides one free electron to the conduction band, while Fe^{3+} ions function as a magnetic dopant with 5 unpaired d-electrons. Substituting In^{3+} with isovalent Fe^{3+} ideally should not affect free electron concentrations, yet a red shift and decrease in LSPR peak intensity was observed upon doping Fe into Sn-doped NCs. Shanker et al.[402] elucidated the origin of the red-shifted LSPR by identifying the dopant oxidation state in Fe- and Sn-codoped In_2O_3 NCs. X-ray absorption near edge structure (XANES) and extended X-ray absorption fine structure (EXAFS) analysis of 10% Fe- 10% Sn-codoped In_2O_3 was conducted in this study. The study attributed lower LSPR energy and intensity damping to Fe^{3+} isovalent iron dopants reducing to Fe^{2+}. XANES results indicated oxygen vacancies, which along with Sn can act as electron donors leading to Fe^{3+} reduction. Due to electron localization at Fe sites, the carrier concentration was diminished and the LSPR red-shifted when doping with Fe^{3+}. Sn K-edge XANES spectra showed no change in the Sn^{4+} oxidation state regardless of the presence of Fe^{3+} codopants in the NCs. However, differences were observed through Fe K-edge XANES spectra supporting the reduction of Fe^{3+} into Fe^{2+}. In the Fe K-edge XANES (Figure 36b), a pre-edge peak at 7113 eV (1s → 3d), a shoulder (1s → 4s), and an edge crest (1s → 4p) showed differences from a reference sample of α-Fe_2O_3 (Fe^{3+} oxidation state) in Fe−Sn codoped In_2O_3. The Fe K XANES edge corresponding to the 1s → 3d transition (Figure 36b, inset) is broadened toward low energy with a similar profile to a reference sample of FeO (Fe^{2+} oxidation state), suggesting a small fraction of Fe^{3+} reduces to Fe^{2+}. EXAFS can be used to assess the local structure around dopants and verify their substitutional position in the crystal lattices. Here, EXAFS revealed a symmetric octahedral coordination environment around the iron center and similar distances to the second nearest neighbors surrounding each type of metal site (Fe, In, and Sn). This structural data supports both Fe^{3+} and Sn^{4+} codopants effectively substituting at the In^{3+} host lattice sites within the NC, rather than occupying surface or interstitial sites.

3.4. NC Shape Control

Shape control of NCs has extensively matured in the noble metal nanoparticle literature[64,368,369] but is still in the early stages of development for LSPR-active semiconductor NCs. Shape control is an attractive synthetic strategy for achieving high NFE around corners of sharply faceted LSPR-active NCs and enabling oriented assemblies in which hot spots arise between NC faces (section 2.3.4). Three interwoven strategies can be applied to influence shape during NC synthesis: exerting control over relative growth kinetics and thermodynamic stability of different facets, capping agent selection, and cation dopant-induced faceting. Kinetic and thermodynamic control influence selective deposition on and surface diffusion along specific NC facets, leading to the preference to eliminate certain facets in favor of others as crystal growth progresses.[64,65] The selection of capping agents can be used to modify the relative kinetic and thermodynamic stability of different crystal facets based on the strength and lability of surfactant bonding with NC surfaces and extrinsic metal dopants also influencing NC shape.[442]

3.4.1. Temperature-Dependent Thermodynamic Shape Control. In thermodynamically controlled NC growth, the shape is ultimately dictated by the Wulff construction, which minimizes the overall surface energy by exposing a combination of stable facets. The surface energy (γ) varies by crystal facet, based, in part, on the extent to which orbitals available for bonding are satisfied by bonding to the crystal lattices (section 3.2.3, eq 22). A NC of a fixed volume achieves a global minimum in Gibbs free energy (ΔG) by minimizing $\Delta G = \Sigma \gamma_i A_i$, which is the sum of contributions from each facet, considering their specific surface energy (γ_i) and area (A_i).[443−445] The presence of high surface energy facets is energetically unfavorable, leading to preferential formation of low-energy facets in NCs. Although the relative energies of different facets depends on their chemical termination (see below); in the absence of specific binding it is generally agreed that the relative surface energies for low-index facets in a face centered cubic (FCC) crystals is on the order of $\gamma_{(111)} < \gamma_{(100)} < \gamma_{(110)} < \gamma_{(\text{higher index})}$.[64,446] Although this structure is too simple to represent LSPR-active semiconductor NCs, it is common for plasmonic metals and consideration of factors governing shape control of these can inform understanding of shape control in more complex material systems. Taking a simple broken bond approximation, where the presence or absence (due to crystal truncation at the surface) of bonding interactions with nearest neighbors is considered, the surface free energy of a crystallographic plane can be represented as $\gamma_i = 1/2 N_B \varepsilon \rho_a$, where N_B is number of broken atomic bonds per surface unit cell, ε is bond strength, and ρ_a is the number of surface atoms per unit area.[447,448] In an FCC structure with a_0 as the lattice constant, the number of broken bonds per surface unit cell N_B is 3, 4, 5 for each respective (111), (100), and (110) planes, leading to $\gamma_{(111)} = 3.46\left(\frac{\varepsilon}{a_0^2}\right)$, $\gamma_{(100)} = 4\left(\frac{\varepsilon}{a_0^2}\right)$, and $\gamma_{(110)} = 4.24\left(\frac{\varepsilon}{a_0^2}\right)$ when ρ_a is considered for each facet.[65] The broken bond approximation provides a simple and reasonable way to predict the relative energetics of different crystallographic facets, although computational models based on density functional theory (DFT) can provide more accurate values in which the surface can be allowed to structurally relax before assessing the energetic cost of truncating the crystal.[446,449−451]

NCs, however, are not generally equilibrium products and kinetic effects can either amplify or oppose the thermodynamic tendencies to dominate the resultant NC shape, as demonstrated in metal, metal oxide, and metal chalcogenide NCs.[452−455] The conceptual framework for this approach to NC shape control is that competing growth pathways occur at each exposed facet during NC growth, where growth involves two physiochemical processes, the first being deposition (V_{dep}) on crystallographic facets favoring those with high surface energy, which are most reactive, and the second being surface diffusion (V_{diff}) to minimize the total surface energy of the NC by exposing the lowest-energy crystallographic planes (Figure 37).[65,368,369] At

DOI: 10.1021/acs.chemrev.7b00613
Chem. Rev. 2018, 118, 3121−3207

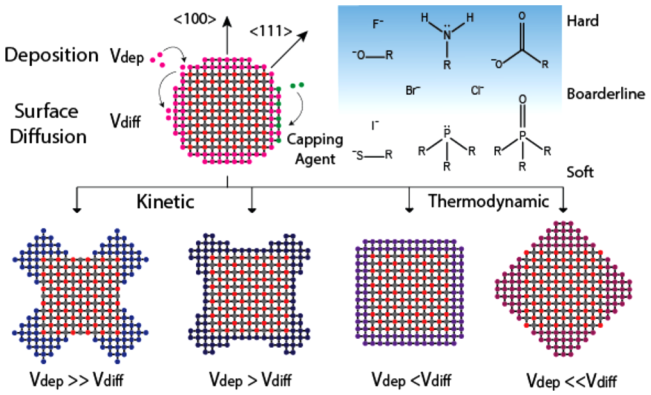

Figure 37. Shape control in NC synthesis. Kinetic and thermodynamic effects on shape control are governed by the relative rates of deposition (V_{dep}) and diffusion (V_{diff}) and by hard–soft acid–base (HSAB) considerations of capping agent-metal ion coordination bonding. Adapted from ref 368. Copyright 2016 American Chemical Society.

slow growth rates, thermodynamic considerations can be expected to reasonably explain NC shape since surface diffusion rates can be significantly faster than the deposition rate of additional monomer ($V_{dep} \ll V_{diff}$) (Figure 37, far right).[369] Xia et al.[369] demonstrated in Pd nanocubes that slow adatom deposition led to effective surface diffusion of adatoms to (100) facets despite those facets being passivated by Br^-, so the thermodynamically favored shape resulted, favoring (111) facets based on minimization of surface energy. Diverging from Wulff theory,[445] kinetically determined NC products deviate from thermodynamically advantageous surface energy minimized shapes. Overall, the kinetically determined shapes may have a higher total energy compared to those predicted based strictly on thermodynamic considerations, even including the presentation of high index facets, which typically have high specific surface energy. However, under kinetically driven conditions where the deposition rate is greater than the surface diffusion rate ($V_{dep} \gg V_{diff}$), adatoms site-selectively deposit on high-energy facets and are retained there, leading to continuous overgrowth and propagation of these high-energy surfaces (Figure 37, far left).[369] For instance, in FCC structured metals deposition leads to energetically disadvantageous <111> directional growth and results in growth of protrusions and formation of unconventional high index facets.[369]

Reaction temperature offers one option for control in regulating the importance of thermodynamic versus kinetic effects since deposition and diffusion, having different activation energies, will generally respond with differential sensitivity to changes in temperature. For example, at a higher reaction temperature, Diroll et al.[123] observed LSPR-active Sn:In_2O_3 NCs with spherical shape at high (320 °C) and octahedral facets at lower (300 °C) temperature. A heat-up colloidal synthesis with indium(III) acetate and tin(IV) acetate precursor in oleic acid and 1-octadecene solution under prolonged 1 h reaction at elevated temperature, either at 320 or 300 °C, allowed thermally induced decomposition of accumulated metal carboxylates. At the lower 300 °C temperature, larger-sized thermodynamically predictable octahedral NCs were observed due to the generation of fewer nuclei, indicative of a slower reaction rate. The slower production of monomers from precursors may also have allowed thermodynamically controlled conditions to occur where the rate of V_{diff} exceeds the deposition rate, (V_{dep}). Monomers may have diffused to the (100) crystallographic planes in the cubic bixbyite structure In_2O_3,[449] with growth in the corresponding direction ultimately leading to the neat elimination of those planes and resulting in an octahedral shape with the most stable low surface energy (111) facets exposed. The resulting octahedrally shaped Sn:In_2O_3 NCs are consistent with the DFT-derived Wulff construction, where the calculated relaxed surface energy $\gamma_{(111)}$ = 0.891 J/m^2 is energetically preferred over oxygen terminated $\gamma_{(100)}$ = 1.759 J/m^2. At a higher reaction temperature of 320 °C, synthesized spherical-shaped Sn:In_2O_3 NCs may have deviated away from the expected Wulff construction octahedral shape product, due to a higher deposition rate and a diffusion rate that did not increase as substantially, presumably due to lower activation energy for diffusion. The high precursor decomposition rates possible at such high reaction temperatures may have accelerated deposition on all facets to the extent that monomer deposition leading to growth is not facet-selective and spherical NC shapes result. Similar observation were made in

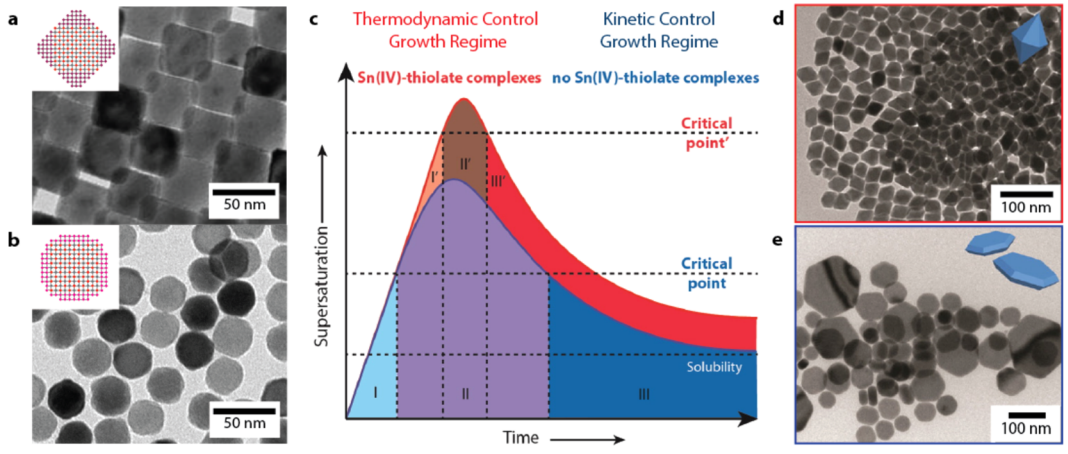

Figure 38. Thermodynamic and kinetic shape control in NC synthesis. (a) TEM image of octahedral-shaped NCs synthesized at lower 300 °C reaction temperature and (b) spherical shaped In:CdO NC synthesized at 320 °C. Reprinted from ref 124. Copyright 2013 American Chemical Society. (c) Critical supersaturation point of $Cu_{2-x}S$ NC influenced by presence of Sn(IV) thiolate complex. Sn(IV) complex inhibits nucleation and raises the critical point favoring thermodynamic growth over kinetically controlled growth. (d) Bipyramid-shaped $Cu_{2-x}S$ NC resulting from thermodynamic growth synthesized at a Cu:Sn ratio of 2:1, and (e) nanoplatelet-shaped $Cu_{2-x}S$ NC, resulting from kinetic growth without Sn. Reprinted from ref 455. Copyright 2016 American Chemical Society.

DOI: 10.1021/acs.chemrev.7b00613
Chem. Rev. 2018, 118, 3121–3207

indium-doped cadmium oxide NCs (In:CdO). Octahedral-shaped In:CdO NCs were synthesized by Gordon et al.[124] by extending a previous shape-controlled cadmium oxide synthesis procedure that had produced octahedral NCs.[456] Extrinsic aliovalent doping of indium in CdO allowed a LSPR response centered around 3900 nm with a shape-dependent multimodal peak shape. Heat-up colloidal synthesis at higher and lower reaction temperatures with cadmium(II) acetylacetonate as the host precursor and indium(III) acetate as the dopant source in oleic acid and 1-octadecene solution allowed different-shaped In:CdO NCs to be realized. Synthesis at a reaction temperature of 300 °C led to octahedral NCs, yielding larger particles due to the smaller number of initial nuclei with a slower reaction (Figure 38a, top). Growth at 320 °C, under reflux, led to spherical In:CdO NCs (Figure 38a, bottom),[124] also possibly due to NC shape product deviating away from the thermodynamically faceted NCs under favorably high thermal condition. Despite prominent synthetic examples in metal and metal oxide NC developments, there remains a significant opportunity in LSPR-active semiconducting NCs to controllably synthesize complex shapes and to demonstrate how kinetic and thermodynamic shape control can be leveraged to create high index facets and especially high curvature regions that can produce maximal NFE under resonant excitation by far field radiation.

3.4.2. Complexing Agent Thermodynamic and Kinetic Shape Control. Changing the nucleation rate through chemical intermediates can provide an additional mode of control in achieving thermodynamic or kinetically induced NC shapes. Thermodynamic and kinetic shape control by tuning the nucleation rate in copper chalcogenide NCs was realized by employing inorganic complexing agents. Chen et al.[457] demonstrated shape control in djulerite phase nanodisk-shaped $Cu_{2-x}S$ NCs by adding tin(IV) chloride pentahydrate to the reaction, which led to elongated tetradecahedra-shaped NCs. The introduction of foreign metal cations influenced the morphology of the $Cu_{2-x}S$ NCs, yet the mechanism was unclear. $Cu_{2-x}S$ NCs treated with Sn (IV) failed to incorporate Sn above the detection limit of EDS, hinting at a mechanism other than adsorption of dopant cations on specific crystal planes.[457]

Further studies by van der Stam et al.[455] suggested that Sn (IV) additives are complexing agents with thiols that can dramatically change NC products from kinetic to thermodynamically controlled shapes based on their sequestering of the thiols. The inclusion of a Sn(IV) complexing agent can substantially raise the $Cu_{2-x}S$ NCs supersaturation critical point, facilitating depletion of monomers available for NC growth after nucleation. $Cu_{2-x}S$ NCs synthesized through a heat-up colloidal method with CuCl precursor in 1-dodecanethiol and oleylamine led to polydisperse nanoplatelet shaped NCs (Figure 38e). The 1-dodecanethiol coordinates with the Cu(I) leading to an accumulation of copper(I) thiolate single-source precursors, and then the thermally induced cleavage of C−S bond to yield [Cu−S] monomers becomes the rate-limiting step in $Cu_{2-x}S$ NC nucleation and growth. Solution and solid state[119] Sn NMR spectroscopy elucidated that the addition of $SnBr_4$ in the thiol solution leads to bromide replacement by thiol molecules and formation of Sn-thiolate complexes ($Sn(DDT)_xBr_y$). A mechanism was proposed where $Sn(DDT)_xBr_y$ imposes an additional nucleation barrier by interacting with [Cu−S] monomers, where Sn(IV)−Cu(I) thiolate complexes were observed through NMR.[458,459] The presence of Sn(IV) complexes significantly increases the activation energy for nucleation and allows a higher concentration of monomers to accumulate (Figure 38c), so that a higher nucleation rate ultimately occurs, leading to the observed monodisperse and smaller hexagonal bipyramid shaped NC product (Figure 38d).

The morphology of the $Cu_{2-x}S$ NCs was further rationalized by the concepts of kinetic and thermodynamic control over NC growth. $Cu_{2-x}S$ NCs synthesized with pristine Cu-DDT complexes resulted in NC shapes that were consistent with kinetic considerations, where the high surface energy facets, specifically (010) and (001) rapidly added material, leading to the hexagonal nanoplatelet morphology as typically observed in previous $Cu_{2-x}S$ NC synthesis.[460−462] The presence of Sn-$(DDT)_xBr_y$ induces a high nucleation rate as mentioned before, leading to a high concentration of nuclei and a rapid depletion of monomers available for growth. The result is slower NC growth, allowing growth to occur in the thermodynamic regime where the monomers are deposited and diffuse across the dynamic surface of the growing NC so that the total NC surface energy is minimized resulting in a [100] directionally elongated hexagonal bipyramid equilibrium shape.[386,457]

3.4.3. Capping Agent Shape Control. Surface ligand groups can be employed in engineering shape control within the context of the above-described thermodynamic and kinetic concepts for controlling NC shapes leading, in some cases, to highly faceted shapes, even exhibiting high index facets.[463,464] As described above, the energetic ordering in an elemental metal with the FCC structure is $\gamma_{(111)} < \gamma_{(100)} < \gamma_{(110)}$, and the relative surface energies can be reasonably estimated using the broken bond approximation.[64,446] However, unlike noble metal LSPR-active NCs, diatomic metal oxide NC facets have energetics that are influenced substantially by their termination with either oxygen or metal or mixed atomic layers, leading to differing degrees of polarity. Highly polar surfaces tend to have high energy in vacuum, but these energetics can be drastically modified by passivation with organic surfactants.[465,466] As thoroughly investigated in the literature regarding CdSe NC synthesis, the surfactants used in synthesis (e.g., oleic acid, oleylamine, alkyl-thiols, trialkyllphosphines, and phosphonic acids, etc.) can induce inversions in the crystallographic plane energies due to their binding affinity and specificity for different crystalline facets.[467] Surfactants thus play a central role in tailoring shape control in NCs, including the LSPR-active semiconductor NCs. Specificity refers to the difference in binding strength between crystallographic planes due to the varying presence of dangling bonds at metal and oxygen sites that may be coordinated by the surfactant. To some extent, the importance of surface bonding in modifying surface energy (sections 3.2.3 and 3.4.1) and the ligand affinity for different facets can be rationalized by the HSAB principle (sections 3.2.7 and 3.2.5), where strong binding affinity can suppress growth in a specific crystallographic direction, resulting in the prevalence of the corresponding facets in the realized NC shape.[468] The surfactant head groups are generally Lewis bases across the spectrum from hard to soft, and metal atom sites on the terminated NC surface facets serve as Lewis acids with varying degree of hardness. Hard Lewis bases commonly employed in synthesis include alkyl carboxylates ($R\text{-}COO^-$), fluoride (F^-), and chloride (Cl^-), which energetically prefer electrostatic interactions with hard Lewis acid metals (e.g., In^{3+}, Al^{3+}, Ti^{4+}, and Sn^{4+}). Soft Lewis bases include trialkylphosphines (R_3−P:), trioctylphosphine oxide (R_3−P═O), and thiolates ($R-S^-$) which bind more strongly to soft Lewis acid metals (Cu^+, Au^+, Ag^+, Hg^+, and Cd^{2+}) (Figure 37, inset).[19,71,450] Alkylamines ($R-NH_2$), which are commonly used, have intermediate hardness

DOI: 10.1021/acs.chemrev.7b00613
Chem. Rev. 2018, 118, 3121−3207

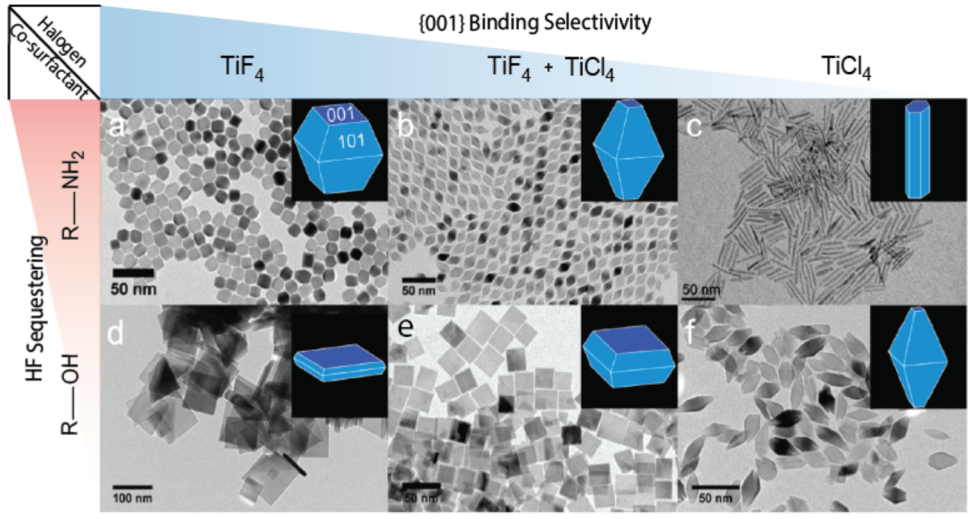

Figure 39. Halogen capping agent shape control. Increasing fluorine enables selective {001} facet passivation in anatase phase TiO_2 NC (right to left). Amine head groups in surfactants cause an HF sequestering effect (top) that is absent for alcohols (bottom), leading to less pronounced {001} surface passivation. Adapted from ref 128. Copyright 2012 American Chemical Society.

and have frequently been reported to effect significant changes in NC shape as a result.

Anionic halogen capping agents (F^-, Cl^-, Br^-, and I^-) can provide effective selective facet passivation in LSPR-active semiconductor NCs due to their chemical stability, electronegativity, and wide range of hardness. The resulting faceted NCs can enable studies of shape-dependent LSPR modes and associated properties. Among plasmonic metal oxide NCs, shape control induced by anionic halogen capping agents along with surfactants oleylamine or 1-octadecanol was demonstrated in anatase phase titanium dioxide (TiO_2) NCs by Gordon et al.[128] In situ release of hydrofluoric acid (HF) in the reaction solution leads to favorable selective binding of F^- at {001} facets resulting in a platelet morphology.[129] First-principle calculations supported the role of F as a selective modifier of surface energies; the surface energy of a fluorine-terminated {001} facet in anatase TiO_2 was found to be lower than that of fluorine-terminated {101} facets,[469] which have been observed to be dominant in the absence of F^-. Synthetic control over the extent of fluorine capping was affected by varying the ratio of F^- to Cl^- by changing the TiF_4 to $TiCl_4$ precursor ratio. Pronounced exposure of {001} facets was observed as more TiF_4 was used (Figure 39, panels a and d), while using more of the chloride precursor led to reduced exposure of {001} facets (Figure 39, panels c and f). Chemical interaction between HF and oleylamine, included in this case as a surfactant and nucleophile to drive the reaction, was described as playing a role in shape control. Amines may sequester in situ generated HF by forming alkyl ammonium fluoride salts ($RNH_3^+F^-$) and reducing the availability of F− to passivate {001} facets. The use of 1-octadecanol instead of oleylamine prevented HF sequestration and led to enhanced {001} facet formation, resulting in platelet-shaped NCs (Figure 39d). Use of oleylamine led to less pronounced {001} facets and resulted in truncated tetragonal bipyramidal shaped NCs (Figure 39, panels a and b). Pure $TiCl_4$ precursor in oleylamine led to NCs exhibiting a rodlike morphology, in which {001} facets were minimally present (Figure 39c).

Anionic capping agents have also been employed to realize shape control in LSPR-active metal chalcogenide NCs, although softer halide anions (typically, I^-) show effective passivation due to the softer acid Cu^+, contrasting with the harder halogen preference (F^-) in metal oxide NCs. The synthesis of various $Cu_{2-x}S$ or $Cu_{2-x}Se$ NCs with hexagonal nanoplatelet morphologies with LSPR response in the NIR has been demonstrated.[189,268,294,460,470] Hsu et al.[385] further investigated shape control in (001) faceted triangular prism morphology CuS NCs by comparing binding interactions between various halide anions (Cl^-, Br^-, and I^-). To controllably induce shape selective growth of covellite phase CuS, a two-phase colloidal synthesis was conducted involving a top layer of octadecene and oleylamine with dissolved elemental S and a bottom layer of 1,5-pentanediol with $Cu(NO_3)_2$ and sodium halide (NaX) salt. CuS nucleation occurs at the two-phase interface along with halide passivation, and the NCs diffuse toward the nonpolar top solution, so they experience minimal halide exposure after growth. The low-index facets were stabilized similarly in anion shape directed growth of anisotropic Au nanoprisms.[471] Only in the presence of Cl^-, Br^-, or I^- halide capping agents were triangular prism morphologies of CuS NCs realized, while the absence of halogens lead to spherical NCs.[385,460] It was observed that I^- capping led to the most monodisperse triangular NC product with the order of $Cl^- < Br^- < I^-$, ascribed to stronger affinity to the CuS surface for the softer halides.[472] Both size and shape were well-controlled in this study, demonstrating the potential for strongly surface-interacting halide ions to direct NC growth.

Organic ligand capping agents influence morphology of doped LSPR-active NCs and provide an avenue for shape control; combining their selective binding with concepts of kinetic growth allows the realization of anisotropic NC morphologies with high aspect ratios. Among interstitially doped metal oxide NCs, Mattox et al.[113] induced shape control in Cs_xWO_3 by varying the ratio between oleylamine and oleic acid capping agents, observing strongly faceted shapes when the oleic acid concentration was high. Cs_xWO_3 NCs with hexagonal prism shapes resulted when an oleic acid:oleylamine ratio of 12.5−31 was used, truncated cubes were seen for ratios of 5.2−12.5, and pseudospheres resulted from ratios of 2.1−5.2.[113] Among LSPR-active metal chalcogenide NCs, Kriegel et al.[112] synthesized anisotropic rod and tetrapod shaped $Cu_{2-x}Te$ NCs using surfactants to control the morphology of CdTe NCs[130,132] as a template then conducting cation exchange from Cd^{2+} to Cu^+

DOI: 10.1021/acs.chemrev.7b00613
Chem. Rev. 2018, 118, 3121−3207

ions. Among aliovalent substitutionally doped LSPR-active NCs, Ghosh et al.[85] explored surfactant-induced shape control in tin-doped cadmium oxide (Sn:CdO) NCs. Sn:CdO NC synthesis was conducted with oleylamine, oleic acid, 1-octadecene, trioctylphosphine (TOP), and trioctylphosphine oxide (TOPO) surfactants and resulted in a wide variety of anisotropic morphologies. CdO was selected as a model material, since the relative growth rates of {111} and {100} facets in the cubic rock salt phase can be controlled by the choice and ratio of surfactant capping agents. Octahedral Sn:CdO NCs were synthesized with cadmium(II) acetate ($Cd(acac)_2$) and tin(IV) myristate ($Sn(MTA)_4$) precursors using a heat-up colloidal synthesis in myristic acid and oleylamine solution at 240 °C (Figure 40a).

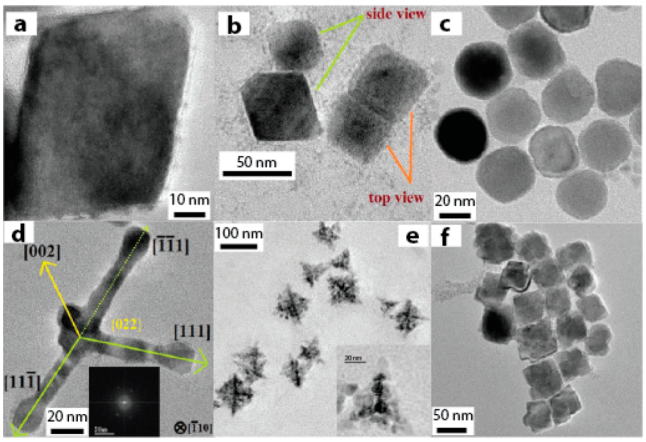

Figure 40. Organic ligand capping agent shape control. TEM images of tin-doped cadmium oxide (Sn:CdO) NCs with morphology controlled by surfactants. (a) Octahedral NC with oleylamine surfactant. (b) Truncated octahedral NCs synthesized with oleic acid and oleylamine. (c) Irregular spheres synthesized with oleic acid at high temperature. (d) Anisotropically branched NC synthesized with 1-octadecanol and oleylamine. (e) Dendritic NCs synthesized with 1-octadecanol and TOP. (f) Rhombohedra synthesized with oleylamine and TOPO. Reprinted with permission from ref 85. Copyright 2017 John Wiley & Sons, Inc.

The polar {111} facets of the cubic rock-salt CdO structure consists of alternating stacks of Cd and O atomic layers. Capping this facet with polar $-NH_2$ head groups, the surface energy of the polar {111} planes can be diminished to such a significant extent that they dominate the surface of the resulting NCs, leading to an octahedral shape. By introducing oleic acid surfactant as a capping agent into the reaction, the oleic acid acted as a selective stabilizer for the neutral {001} facets, leading to a truncated octahedron NC morphology (Figure 40b). It was observed that increasing the ratio of oleic acid to oleylamine led to greater {001} facet stabilization, resulting in progression of the NC morphology from octahedral, to truncated octahedral, to cuboctahedral supporting the role of oleic acid as a selective facet capping agent in CdO. However, it must be recognized that organic ligands are typically weakly bound at high temperatures typical of NC growth, especially at nonpolar facets. Indeed, dynamic, labile coordination is a prerequisite to facilitate NC growth at all. The implications of weakening coordination at higher temperature for NC shape control was revealed, for example, by the failure of oleic acid to selectively passivate the neutral {001} facets of CdO at the high temperature of 300 °C, leading to irregular spherical Sn:CdO NCs without any apparent faceting (Figure 40c).[85]

A combination of kinetic shape control and capping agents allowed synthesis of highly anisotropic plasmonic Sn:CdO NCs with complex shapes.[85] Highly anisotropic branched Sn:CdO NCs were observed with arm lengths up to 55 nm long and 10 nm wide when synthesized using an oleylamine and 1-octadecanol surfactant mixture (Figure 40d). During a relatively short growth time (15 min) ascribed to kinetic control, the [111] direction growth was more pronounced due to the highly polar {111} facets that alternate in Cd and O termination. This was attributed to the polar {111} facets being stabilized by oleylamine, while the neutral {200} facets were stabilized by 1-octadecanol. Employing TOP and TOPO surfactants resulted in Sn:CdO NCs with interesting complex shapes due to coalescence and aggregation of smaller particles. Using TOP alone as a capping agent in 1-octadecanol resulted in dendritic structured Sn:CdO NCs (Figure 40e), and TOPO with oleylamine resulted in distorted rhombohedral NCs (Figure 40f).[85]

3.4.4. Cationic Dopant Shape Control. Cationic substitutional dopants can also direct faceting during NC growth since ionic impurities can influence phase and shape in metal oxides and metal chalcogenides under high doping conditions, resulting in shapes differing from those expected based solely on the host material.[442] Joo et al.[88] carried out aspect ratio control covering 4 orders of magnitude (height/diameter ratio: 0.1−100) in hydrothermally grown ZnO nanowires ranging from platelet to needle morphology through selective addition of bivalent or trivalent cations. The basis for systematic shape control was rationalized as facet selective electrostatic interactions between charged crystal surfaces and metal ions during growth. Cations form unreactive complexes that can localize at oppositely charged crystal surfaces in hydrothermal synthesis. Their accumulation would competitively limit the access of the reactive zinc intermediates and inhibit growth in a facet specific manner. Facet selective electrostatic interaction in wurtzite phase ZnO

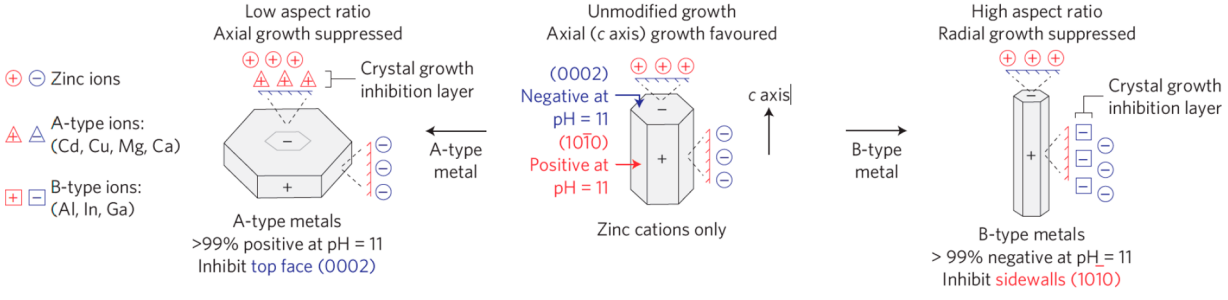

Figure 41. Dopants influence NC shape. Cation doping influences ZnO NC shape. Bivalent cations inhibited (0002) facet growth (left) while trivalent cations inhibited (10$\bar{1}$0) facet growth (right). Reprinted with permission from ref 88. Copyright 2011 Macmillan Publishers Limited.

DOI: 10.1021/acs.chemrev.7b00613
Chem. Rev. 2018, 118, 3121−3207

can influence either (0002) or (10$\bar{1}$0) facet growth depending on the cationic species.[88] Trivalent cations such as Al^{3+}, In^{3+}, and Ga^{3+} can lead to negatively charged complex ions advantageous for passivating positively charged (10$\bar{1}$0) sidewall facets, leading to needlelike shapes. Bivalent cations including Cd^{2+}, Cu^{2+}, Mg^{2+}, and Ca^{2+} can form positively charged complexes that block negatively charged (0002) top surface plane growth (Figure 41) and lead to platelet morphologies.

However, thorough studies of the influence of cationic dopants on NC are scarce in the LSPR-active NC literature, and this topic could benefit from further synthetic investigations in the future. The translation of observations made regarding dopant-induced shape control in hydrothermal synthesis to a systematic understanding of such effects in colloidally synthesized LSPR-active metal oxide NCs is uncertain. Understanding the influence of cationic dopants on NC shape involves decoupling thermodynamic and kinetic effects along with the role of surfactants as capping agents, all of which impose significant challenges as the effects are convoluted and influenced by one another. Dopant-influenced shape control is an interesting avenue for investigation that remains insufficiently distinguished from other synthetic strategies affecting shape. Indeed, cationic dopants influencing the shape and crystal phase have been noted throughout the LSPR-active semiconductor NC literature. In colloidal niobium-doped titanium oxide (Nb:TiO_2) NCs, increasing Nb^{5+} doping induced a transition from TiO_2 tetragonal platelets to peanut-shaped nanorods when a Nb precursor concentration of 14% was reached. It was attributed to systematic elongation of the anatase structure along the longitudinal *c* axis, while the *ab* plane lattice parameter was reduced.[435,442] Among metal oxides exhibiting phase transitions, Gao et al.[473] observed cation dopants influencing phase stability in VO_2. Hydrothermally synthesized VO_2 without dopants resulted in large micron-sized rods in the tetragonal VO_2 (A) (*I*4/*m*) phase, based on selected area electron diffraction (SAED). Upon the addition of antimony (Sb^{3+}) as a dopant, however, 8−30 nm sized monoclinic rutile-type, VO_2 (M) (P21/c) phase Sb:VO_2 NCs were formed. This dramatic change in synthetic outcome was attributed partially to substituting the larger radius Sb^{3+} cation for the smaller V^{4+} ion in the host lattice, which would distort the lattice and change the interatomic coupling effects that influence phase stability in this class of materials.[474] Among metal chalcogenide NCs, Al^{3+} ions were used to direct usually spherical Cu_xSe NCs into monodisperse cube shaped NCs. It was hypothesized that the Al^{3+} blocks the binding of hexadecylamine (HDA) to the {111} facet early in the synthesis. During ripening to evolve the NC shape, HDA-capped {100} facets are stable toward Cu and Se dissolution and are preserved, while {111} facets are subject to fast exchange of Cu and Se ions and disappear as the reaction proceeds.[425]

Shape influence from aliovalent substitutional dopants in LSPR-active indium- or aluminum-doped ZnO (In:ZnO, Al:ZnO) was investigated by Mehra et al.[475] using slow injection synthesis. Nanorods with branches and rough surface morphology were prevalent when In^{3+} or Al^{3+} dopants were introduced. This observation was ascribed to lattice strain due to the larger In^{3+} metal cation (94 pm) compared to Zn^{2+} (86 pm). Through Rietveld refinement of the nanorod XRD, lattice expansion was observed in In-doped nanorods and lattice contraction in Al-doped, due to the smaller ionic radius of Al^{3+}. The nanorod shapes were more regular when the dopant precursors were introduced during the latter stages of growth when the shape was already well-established by the growth of pure ZnO. Morphological irregularities due to lattice strain might be expected to be more severe when dopants are incorporated within the NC core.

3.5. Mechanism of Nonthermal Plasma Synthesis

More refractory materials can be difficult to crystallize at the moderate temperatures necessarily employed for colloidal synthesis. Limitations due to the boiling point or thermal decomposition of solvents can be overcome using the nonthermal plasma method. Metal pnictides (TiN, InN) and doped silicon (B-doped Si, P-doped Si) have high melting temperatures, and nonthermal plasma synthesis has been well-applied to synthesize NCs of these compositions. NCs are heated intensely by highly exothermic surface reactions occurring stochastically on NC surfaces under plasma flux allowing crystallization of high melting point materials.[476,477] Nonthermal plasma offers some further advantages over liquid phase colloidal synthesis in metal oxide NCs. Chemical precursors in a nonthermal plasma undergo extensive electron collisions and produce highly reactive host material and dopant precursors that drive NC growth far away from chemical equilibrium. This provides significant advantage in doped metal oxide and silicon NCs, where high reactivity allows greater loading of dopants into the NCs compared to their colloidally synthesized counterparts.[102]

NC growth in nonthermal plasma synthesis involves fundamentally different chemical reactions and kinetics compared to liquid phase colloidal synthesis. The initial elementary process in plasma synthesis requires applying sufficiently high electric field to ionize the carrier gas (A) and, to create an electron avalanche ($A + e_{fast} \rightarrow A^+ + 2e_{slow}$), a process referred to as breakdown (Figure 42a).[100] High-energy free electrons collide with atom or molecule A and ionize additional

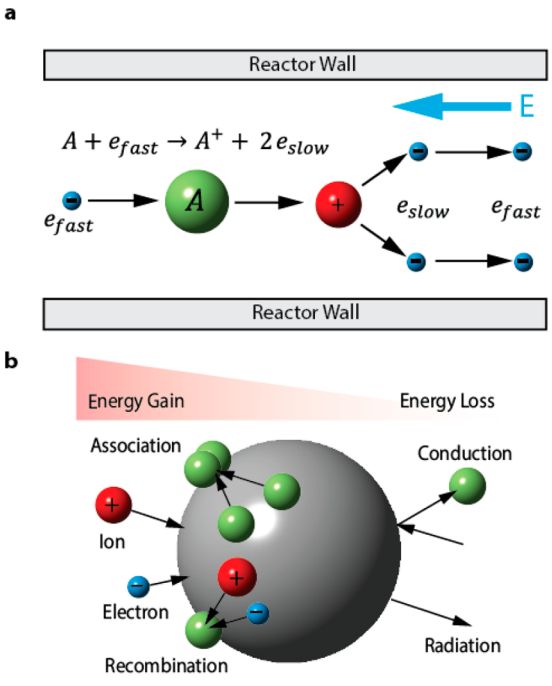

Figure 42. Nonthermal plasma synthesis schematic. (a) Electron avalanche scheme: fast electrons ionize precursors and additional, slow electrons are generated. The electromagnetic field in the plasma chamber accelerates electrons that further ionize precursors. (b) NCs gain energy by association, ion collision, electron collision, and recombination. Under low pressure, energy loss through conduction and radiation become negligible in nonthermal plasma synthesis. Adapted from ref 100. Copyright 2016 American Chemical Society.

DOI: 10.1021/acs.chemrev.7b00613
Chem. Rev. 2018, 118, 3121−3207

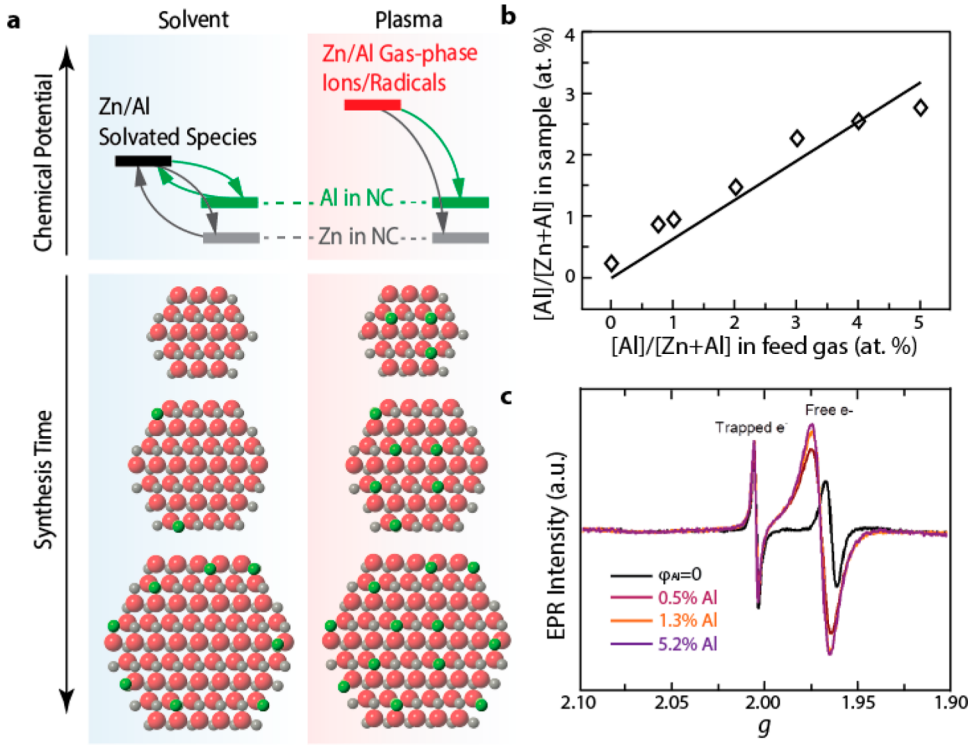

Figure 43. Metal oxide NC nonthermal plasma synthesis. (a) Comparison between colloidal synthesis (left) and nonthermal plasma synthesis (right) in terms of chemical potential (top) and dopant incorporation during growth (bottom). (b) Dopant feed and incorporation in NCs in nonthermal plasma synthesized Al:ZnO are linearly correlated (fit, black line). (c) EPR spectra of nonthermal plasma synthesized Al:ZnO NCs with quantified free/trapped electron ratio (inset). Adapted from ref 102. Copyright 2015 American Chemical Society.

electrons that are subsequently accelerated by the plasma electric field, resulting in exponential creation of ions and electrons. Under low pressure synthetic conditions, conduction and radiative transfer is negligible and electron−ion recombination is the main source of energy driving NC growth.[478] Thus, nonthermal plasma can achieve extraordinary temperatures hundreds of Kelvin higher than liquid phase synthesis, with free electrons at 11000−55000 K and ion species at 300−1200 K.[100] Energy is added to a plasma suspended NC when electrons and ions recombine on the NC surface, while energy loss occurs through radiation and heat conduction, though these loss processes are minimized under low-pressure conditions (Figure 42b). NC growth takes place via a three-step process as proposed by Boufendi et al.[479] First, nucleation occurs by formation of a cluster with neutral or singly negatively charge at high concentration. The second stage involves cluster and NC agglomeration, where initial neutral clusters merge until acquiring a negative charge that prevents further aggregation owing to electrostatic repulsion. In the third stage, NCs grow further as surface reactions consume precursors and add material to the growing NCs. Longer retention time within the plasma leads to larger-sized NCs as precursors are consumed. The NCs in the plasma are primarily negatively charged, preventing agglomeration during growth and enabling production of fairly uniform NCs.

An experimental apparatus for plasma synthesis of LSPR-active NCs employs a continuous-flow nonthermal plasma system, as demonstrated by Greenberg et al.[102] for aluminum-doped zinc oxide (Al:ZnO) and Alvarez Barragan et al.[101] for titanium nitride NCs. This continuous flow method is attractive for producing significant quantities of NC product for study. The absence of organic surfactants allows pristine, ligand-free NC surfaces, which enables study of LSPR-active NCs in the absence of complicating effects due to surfactants. Liquid chemical precursors are placed in a bubbler and delivered to the plasma reactor by vapor via a carrier gas, typically argon. To sustain the plasma, 13.56 MHz radio frequency (RF) power is supplied through copper ring electrodes encircling the low-pressure gas flow reaction chamber. Synthesized NCs are collected downstream on any desired substrate.

3.5.1. Doped Metal Oxide/Metal Chalcogenide (Group 16) NC Synthesis. Using nonthermal plasma synthesis, Greenberg et al.[102] observed unique dopant kinetics diverging from colloidal synthesis in extrinsic aliovalent substitutionally doped Al:ZnO. The host precursor diethylzinc (DEZ) and the dopant source trimethylaluminum (TMA) were injected in an Ar/O_2 aerosol plasma. Organometallics such as DEZ and TMA are suitable precursors for nonthermal plasma synthesis due to their high aerosol vapor pressure and limited carbon content, especially compared to the sterically bulky precursors (e.g., metal oleates) used in colloidal synthesis. It is proposed that active host and dopant species become highly reactive ions with high chemical potential in the plasma, rendering irrelevant any differences in reactivity between dopant and host precursors (Figure 43a, top right). In colloidal synthesis, the far lower chemical potential of solvated precursor species makes such reactivity differences more impactful in determining the synthetic outcome (Figure 43a, top left). Furthermore, surface deposition during colloidal synthesis can be reversible during NC growth, which is not the case for plasma synthesis thus obviating Oswald ripening that can lead to size polydispersity in colloidal NCs. Depending on the energetics of dopant incorporation, this dynamic equilibrium between NC and solution can also result in dopant segregation or lower dopant incorporation efficiency

DOI: 10.1021/acs.chemrev.7b00613
Chem. Rev. 2018, 118, 3121−3207

(Figure 43a, bottom left). For example, in the colloidal synthesis of Al:ZnO NCs, the core is predominantly undoped zinc oxide and less Al is incorporated compared to plasma-synthesized Al:ZnO NCs, which were reported to have a uniform dopant distribution.

Nonthermal plasma NC synthesis allows high dopant incorporation (Figure 43a, bottom right) with dopant concentration in NCs nearly matching the composition of the precursor feed (Figure 43b). XRD analysis of plasma synthesized Al:ZnO NC with Al dopant incorporation ranging from 0 to 3.2% revealed lattice expansion, in contrast with the lattice contraction seen in colloidally synthesized Al:ZnO NCs by Buonsanti et al.[84] It is proposed that in plasma synthesis $Al_2^{3+}O_i^{2-}$ defects are responsible for lattice expansion, with two adjacent substitutional Al cations complexed with an interstitial O anion. Electron paramagnetic resonance (EPR) was used to verify the presence of free electrons that result in LSPR (Figure 43c). The concentration of free electrons in the conduction band increased as more dopant was incorporated into Al:ZnO as was observed and quantified through EPR. The g = 2.0 resonance signal was assigned to electrons trapped on oxygen vacancy sites,[480,481] and a resonance at g = 1.96 (undoped) and g = 1.97 (doped) was attributed to free conduction band electrons with the shift ascribed to the blue-shifted bandgap in doped Al:ZnO.[39,482,483]

Nonthermal plasma synthesis methods can be usefully employed to synthesize metal chalcogenide NCs, and researchers have succeeded in tuning the stoichiometric ratio between metal to chalcogen to influence LSPR properties. Copper chalcogenides occur in a wide variety of crystal phases depending on the concentration of metal vacancies, which diminishes upon progressing from covellite (CuS), digenite ($Cu_{1.8}S$), djulerite ($Cu_{1.94}S$), to chalcocite (Cu_2S). To vary the stoichiometry, the ratio of copper and sulfur precursors in the feed is controlled. Thimsen et al.[104,484] demonstrated nonthermal plasma synthesis of copper sulfide NCs using hexafluoroacetylacetonate Cu(I) vinyltrimethylsilane and elemental sulfur vapor in an argon gas flow. Controlling the composition of the precursor feed allowed crystallographic phase tuning in the resulting copper sulfide NCs. XRD was used to identify the crystal structures of the NCs. Under a low copper molar fractional ratio feed rate into the plasma reactor ($Cu/(S+Cu) = F_{Cu} = 0.1$), CuS was synthesized. With higher Cu feed rate ($F_{Cu} = 0.6$), the cubic α-Cu_2S phase was observed, while at even higher feed rate ($F_{Cu} = 0.85$) elemental Cu NCs were produced.[484] Surface oxidation of Cu_2S NCs upon air exposure led to LSPR NIR absorption as Cu^+ vacancies formed, resulting in free valence band holes.

3.5.2. Metal Pnictide (Group 15) NC Synthesis. Nonthermal plasma methods allow controlled synthesis of high melting temperature nitride NCs (section 2.5.2) that were previously synthesized through direct nitration[485] or laser ablation[486] methods that resulted in polydisperse NC products. While nitridation of precursor powder would typically require reaction at 800 °C or more due to the highly covalent bonding character, free-standing NCs of these materials can be controllably synthesized by plasma synthesis. Alvarez Barragan et al.[101] developed a plasma synthesis route for plasmonic TiN NCs (Figure 44a, d) using titanium tetrachloride ($TiCl_4$) as the metal precursor and ammonia (NH_3) as the nitrogen source (Figure 44b). Ar gas was used to deliver $TiCl_4$ precursor from a bubbler. Size control was achieved, tuning from ~4 nm to ~8 nm by varying the NH_3 flow rate from 6 to 1.5 sccm, respectively. The LSPR response also shifted when the NH_3 flow rate was changed, blue-shifting from 1000 to 800 nm wavelength when

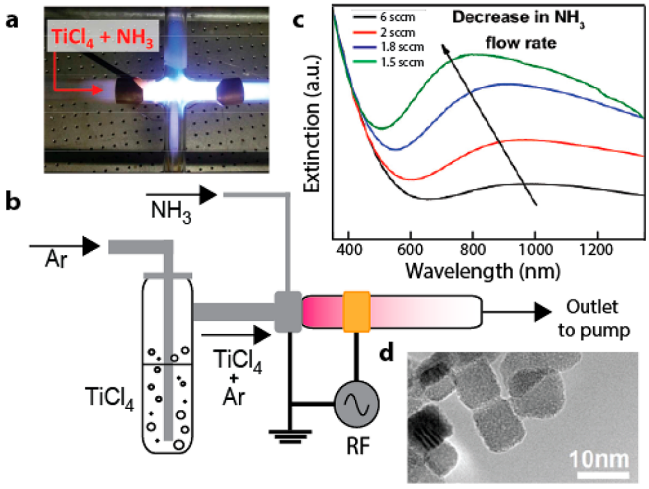

Figure 44. Nitride NC nonthermal plasma synthesis. (a) Photograph of a nonthermal plasma during titanium nitride (TiN) NC synthesis. (b) Schematic of the apparatus for TiN nonthermal plasma synthesis. (c) TiN NC LSPR frequency is tuned by varying the NH_3 flow rate in plasma synthesis. (d) TEM image of nonthermal plasma synthesized TiN NCs. Adapted from ref 101. Copyright 2017 American Chemical Society.

the flow rate was reduced from 6 to 1.5 sccm. This observation contradicts the qualitative trends expected from simple Mie theory, which predicts a small red-shift as NC size increases (Figure 44c). Evidently, LSPR red-shifting was due to an increased extent of oxidation under high NH_3 flow. The Ti 2p peak in XPS showed increased intensity in a shoulder assigned to TiO_2 for the smaller TiN NCs synthesized under high NH_3 flow rate. EDS measurement show a higher N to Ti molar ratio in the larger TiN NCs with blue-shifted LSPR, supporting that oxidation is responsible for LSPR red-shifting. Postsynthetic LSPR tuning toward lower energy was also demonstrated by annealing TiN NCs at 150 or 250 °C for 1 h in air due to partial oxidation.

Indium nitride (InN) is another nitride material for which NCs have been shown to exhibit LSPR,[199,323,487] in this case tunable through postsynthetic surface redox treatment. Nonthermal plasma colloidal synthesis has not yet been demonstrated but Palomaki et al.[199] reported a solvothermal route to colloidal InN NCs. In_2S_3 and $NaNH_2$ precursors in octadecene were reacted solvothermally at 100 °C followed by extensive workup. XRD revealed purified InN phase product after acid sonication to remove the metallic indium metal byproduct and capping InN with oleylamine. Followed by ligand removal treatment with triethyloxonium tetrafluoroborate (Et_3OBF_4) Meerwein's salt, reversible oxidation, and reduction of InN allowed postsynthetic LSPR tuning. Surface-oxidized InN treated with nitrosonium tetrafluoroborate ($NOBF_4$) exhibited a red-shifted LSPR peak at 3545 nm. The corresponding free electron density was estimated to decrease by about ~4 electrons per NC. The red shift could be reversed by a reducing treatment using Bu_3NBF_4, after which the LSPR peak returned to 3303 nm, comparable to the LSPR wavelength of the original oleylamine-capped NCs (2996 nm).

3.5.3. Doped Silicon (Group 14) Plasma Synthesis. Extrinsic aliovalent doping can be achieved in silicon (Si) NCs by incorporating either n-type or p-type dopants (section 2.5.1), leading to an LSPR response.[488] Despite there being established solution phase colloidal[489,490] and thermal decomposition

DOI: 10.1021/acs.chemrev.7b00613
Chem. Rev. 2018, 118, 3121−3207

methods for Si NCs,[491−494] extending these methods to dope Si NCs with conventional n-type group 15 elements such as phosphorus (P) or p-type dopants from group 13 such as boron (B) has proved challenging. Reaction conditions for Si NCs require high temperatures of 1000−1200 °C that may anneal kinetically trapped dopants out of NCs.[488,490] Solution phase colloidal synthesis using highly reactive silicon precursors may also make it infeasible to balance reactivity between dopant and host precursors.[492] Solution-phase colloidal synthesis of 6% P-doped Si NC was reported by a coreduction of silicon tetrachloride ($SiCl_4$) and phosphorus trichloride (PCl_3) with finely divided magnesium (Mg) in 1,2-dimethoxyethane, although no plasmonic response was reported in that study.[495] Thermal decomposition of silane (SiH_4) had earlier enabled the gas phase synthesis of Si NCs,[496−498] and further advancement using continuous nonthermal plasma synthesis enabled effective dopant incorporation into Si NCs and realization of LSPR. Synthesis for both p-type and n-type-doped Si NCs were successfully developed by Pi et al.[33] and Zhou et al.[306] using nonthermal plasma methods. Rowe et al.[106] investigated LSPR properties in n-type P:Si NCs prepared using SiH_4 with phosphine (PH_3) gas as precursors, while Kramer et al.[107] and Zhou et al.[200] demonstrated LSPR response in p-type-doped B:Si NCs synthesized with diborane (B_2H_6). Similarly, P-doped Ge NCs have been successfully synthesized with GeH_4 and PH_3 gas as precursors, although LSPR properties were not reported in that study.[499]

In P-doped Si NCs synthesized by nonthermal plasma as investigated by Rowe et al.,[106] it was shown that dopants in the NC core actively contributed to LSPR while surface-segregated dopants did not. Smaller NCs reach higher temperature allowing Si atoms to rearrange, forming crystalline cores.[476] However, as Si NC size increases, Si and P atoms attach randomly to the NC surface, which can be disordered as a result, suppressing free carrier ionization from dopants.[106] Using a stoichiometrically controlled silane/phosphine (SiH_4/PH_3) mixture, the overall composition of the NCs was tuned, closely reflecting that of the precursor mixture.[33] A fractional flow rate $X_{PH3} = [PH_3]/([PH_3]+[SiH_4]) \times 100\%$ was thus defined and used to describe the NC composition. Despite P:Si NCs being produced successfully at $X_{PH3} = 50\%$, the majority of the P dopants were deposited near the NC surface where the associated carriers could be trapped in defect states. This was supported by TEM images in which an amorphous shell was seen around both lightly and heavily doped P-doped Si NCs, along with the strong presence of surface Si−P_x-H_y vibrational peaks around 2300 cm^{-1} in the FTIR spectrum.[106] Postsynthetically etching the P:Si NC surface with hydrofluoric acid vapor removed the amorphous shell and allowed investigation of the pristine P-doped core for which a modified dopant incorporation measure $X_P = [P]/([P]+[Si]) \times 100\%$ was assigned based on SEM-EDS analysis. The P:Si NCs produced at $X_{PH3} = 50\%$ actually had only $X_P = 5\%$ in the crystalline core.

LSPR has been investigated by Kramer et al. in nonthermal plasma synthesized B-doped Si NCs, which show contrasting doping behavior compared to P-doped Si NCs.[107] The nominal dopant incorporation of B was approximately ten times lower than P when analyzed by ICP-AES,[33] which can be rationalized based on the formation energy of substitutional B defect sites that are larger than that for P doping of Si.[500] Contrary to P-doped Si NCs, B-doped Si NCs initially do not exhibit LSPR, but LSPR emerges when the NCs are oxidized. By contrast, when P-doped Si NCs were exposed to air for 4 h, the LSPR response vanished. Oxidation of these n-type Si NCs, evinced by the appearance of a strong Si−O−Si bridging vibration peak at 1050 cm^{-1}, drastically reduced the free electron concentration. However, B-doped Si NCs exhibited stable LSPR only after 57 h of air exposure, and then it was stable even after a year. Oxidation was considered stabilized in B-doped Si NCs based on FTIR and XPS analysis, where no significant changes in Si−O related features were observed after initial oxidation. EPR measurement also supported the long-term stability against further oxidation in B-doped Si NCs where little EPR signal change occurred.[501]

3.6. Characterizing LSPR Active NCs

Recent advances in developing tailored synthetic methodologies for LSPR-active NCs have immensely facilitated addressing the fundamental questions in this field of research. Developing new materials that break various performance ceilings is and will always be an attractive driver for research, and making a close inspection of these emerging materials can reap significant benefits in the form of improved understanding, which in turn enables future development. However, all these synthetic advancements require characterization of the NCs during and after their growth to obtain detailed information regarding local structure of the as-synthesized NCs and to assess the implications of structure for the optoelectronic properties. Furthermore, following the nucleation and growth of NCs provides important perspective about growth mechanisms, which in turn enables new levels of control over size, shape, and composition. As evident from the discussion so far, extrinsically doped NCs are well-represented among LSPR-active NCs and correlating the optical responses of these NCs with their internal structure entails careful characterization. Determining the location of dopant atoms, whether located at substitutional or interstitial crystallographic sites or merely acting as surface-adsorbed species, is not a trivial task and mandates the sophisticated application of a multitude of analytical tools to paint a complete picture.

Determining elemental composition is central to find the extrinsic dopant concentration in a NC and also essential for self-doped LSPR-active NCs where stoichiometry determines the concentration of charged defects. ICP-AES is useful for obtaining the global elemental composition of NCs,[70,84,123] while more local elemental analysis can be performed in an electron microscope, by techniques like energy dispersive X-ray spectroscopy (EDS). EDS of individual NCs can, in fact, be used to quantify the variation in dopant concentration between NCs in an ensemble.[126] However, ascertaining phase purity is also important, and XRD provides useful information especially when Rietveld refinement of the pattern is performed. Since dopant incorporation often perturbs the host lattice, XRD signatures are important in understanding structural aspects of doping;[84,502] most directly, peak shifts occur due to lattice contraction or expansion. Strain, and the corresponding peak shifts, are more pronounced for dopants that differ significantly in size compared to the host cation. Structural information can be correlated with the electronic structure of the NCs, about which indirect information is obtained by optical absorption spectroscopy[59] or EPR.[102] Dopant incorporation induces electronic structure modifications such as creating localized trap states or leads to degenerate defect bands (when in high concentration) and can also lead to changes in the band structure as dopants hybridize with bands of the host material. The valence electronic structure is also evidenced in X-ray absorption near-edge structure (XANES),[402] and chemically specific local structure information

DOI: 10.1021/acs.chemrev.7b00613
Chem. Rev. 2018, 118, 3121−3207

can be probed using extended X-ray absorption fine structure spectroscopy (EXAFS).[154,402] Unlike XRD, which provides information about the long-range periodic structure, the short-range structure is highlighted by EXAFS. EXAFS is thus particularly useful in cases where (portions of) the sample do not exhibit a high level of crystallinity or information about the local coordination structure around an ion is sought.

Recent endeavors in understanding the structure of the organic ligand shell, that enables solution processability and interrogation of NC properties absent aggregation, has brought a whole host of other characterization techniques to the table.[67] FTIR and NMR spectroscopies are now routinely used to gather basic information about the organic molecules tethered to the NC surface, and this information can be used to strategize further surface manipulation of these NCs (e.g., ligand exchange to make them dispersible in another preferred solvent). Probably the most broadly applied technique for analysis of the inorganic components at the NC surface is XPS. XPS is particularly relevant in the case of doped NCs as it provides information for the spatial distribution of the dopants in the NCs, as described in section 3.3.6. Although it has been applied widely to determine oxidation states of metal ions in NCs, it is essential to remember that XPS is intrinsically surface-sensitive, so the information gleaned may not represent the core of the NCs being interrogated.

3.7. Synthetic Outlook

While much progress has been made in the synthetic development of LSPR-active semiconductor NCs, there are now more opportunities and questions to address than before due to the level of compositional and structural complexity that has been made possible. One of the fundamental questions that has recently started to catch researchers' attention is the spatial distribution of the dopants in the NCs.[68,121] Synthetic methodologies enabling sophisticated control of the dopant distribution and dopant activation are actively under development. Changes in electronic band structure brought about by doping or alloying, especially with deliberately varied spatial distribution of the dopants, need deeper interrogation, and combined experimental and theoretical examinations on a variety of NCs will be required to fully explore this topic. In the case of colloidal NCs, this type of investigation will also require a thorough understanding of the surface as well and material synthesis should be aimed at making materials with well-defined surface chemistry that can facilitate such studies. The LSPR response of NCs is influenced by a number of factors, including anisotropy in the crystal structure and the morphology. While we recently established the interplay of shape and crystalline anisotropy in determining LSPR properties of one type of NC,[56] demonstrating the effect of such anisotropy in NCs exhibiting varied compositions will require synthesis of systematically varied NCs, aimed at understanding these trends. Then again, the chemistry of doping require attention and systematic pursuit, particularly as most doping methods do not lead to full activation.

With the vast number of LSPR-active NC materials rapidly being developed, practical considerations such as cost, safety, stability, and compatibility should be weighed for practical applications. In large scale production, where cost may be traded off against performance, using Earth-abundant materials such as doped ZnO NC may be preferred over doped In_2O_3 NCs or Ag or Au nanoparticles. In complying with consumer safety regulations,[503] safer In_2O_3 based NCs may be preferable over toxic and heavily regulated cadmium-containing doped CdO NCs. In consideration of environmental stability, metal nitride NCs or B-doped Si NCs may be more advantageous than oxygen vacancy doped WO_{3-x} or MoO_{3-x} NCs. For biocompatibility related to biomedical applications, toxicity of metal, anion, and organic components must be assessed.

With the rapid synthetic advancement in semiconductor LSPR-active NCs, full control over doping and crystal growth chemistries that can fulfill the need for detailed structure–property correlations is still emerging. Future research questions on synthetic control of LSPR-active semiconductor NCs include the following. (1) How can synthetic methods be advanced to create highly uniform dopant distributions between NCs in the ensemble and to exercise precise control over dopant distribution within NCs? (2) In self-doped NC materials, how can the active defect site concentration be experimentally quantified? (3) How can the influence of dopants on NC size and shape be deconvoluted from thermodynamic and surfactant-related effects?

4. DYNAMIC LSPR MODULATION

4.1. Introduction

Owing to the semiconducting nature of the host materials, LSPR of degenerately doped NCs can be dynamically modulated through tuning their carrier concentration. Dynamic and external control over LSPR has led to promising applications in IR electrochromic smart windows, redox sensors, and electro-optical modulators. Dynamic LSPR tuning is demonstrated using four different approaches: (1) chemical redox reaction, based on electron transfer to and from NCs when exposed to reducing or oxidizing agents. (2) Photochemical charging, usually achieved through illumination with above band gap energy light under anaerobic conditions and in the presence of a hole scavenger to stabilize free electrons in the NC CB. (3) Photocharging under ambient condition for ultrafast modulators. (4) Electrochemical charging/discharging, where the Fermi level (thus the concentration of CB electrons) is shifted by applying an electrochemical potential, usually to samples in the form of films or assemblies.

Such reversible modulation of free carriers not only underlines the versatility of LSPR absorbance in semiconductor NCs but also allows systematic probing and control over the electro-optics of these materials in ways not achievable with static measurements. Each of these approaches have benefited from the rich chemistry of nanoscale electron transfer leading to the development of more efficient and robust LSPR modulation strategies. In the following sections, we elaborate on previous findings and discuss further opportunities.

We note that attempts have been made to modulate LSPR of metal nanostructures, such as electrochemical charging of Au and Ag nanostructures.[504,505] Metals, however, exhibited a very small optical modulation (about 10 nm shift in LSPR peak wavelength) due to an intrinsically high carrier concentration. Larger modulation can be achieved indirectly by inducing chemical and electrochemical changes in the nanostructure environment (e.g., altering the dielectric environment of the Au nanorods embedded in a conductive polymeric host). Such an approach, however, leaves the plasmonic material as a passive indicator, limiting their applicability and versatility. Contrary to metals, semiconductor NCs allow substantially greater LSPR modulation (over 1300 nm change in peak wavelength) when carriers

DOI: 10.1021/acs.chemrev.7b00613
Chem. Rev. 2018, 118, 3121–3207

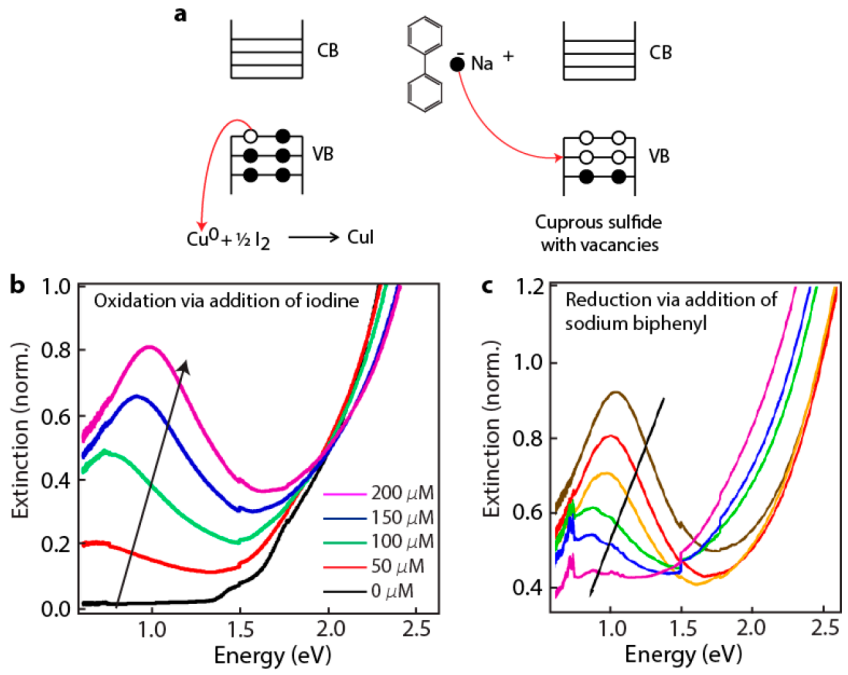

Figure 45. Chemical control of metal chalcogenide NC LSPR. (a) Copper vacancy concentration in $Cu_{2-x}S$ can be reversibly tuned by adding oxidant such as iodine or reductant such as sodium biphenyl. (b) With the increasing amount of iodine added, copper vacancy concentration increases shifting the LSPR toward higher energy. (c) Reductant such as sodium biphenyl donated electron to the NC, effectively reducing the free hole concentration and shifting the LSPR to lower energy. Reprinted from ref 46. Copyright 2013 American Chemical Society.

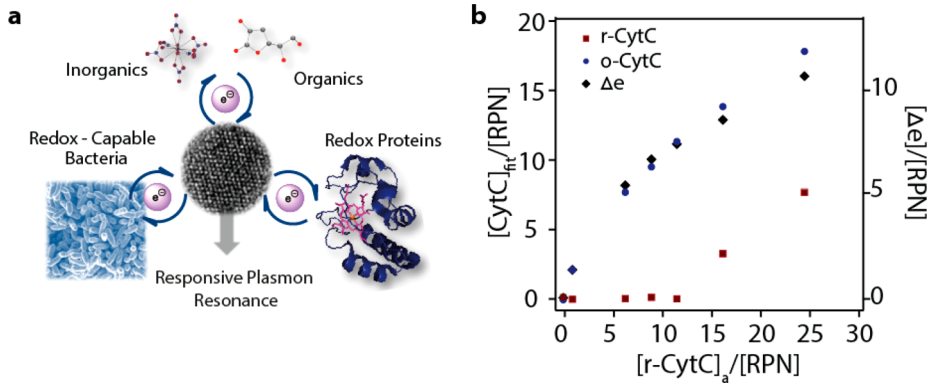

Figure 46. Chemical control of metal oxide NC LSPR. (a and b) LSPR modulation in metal oxide via addition or removal of electron from the conduction is used as the redox sensor. Extent of oxidation of cytochrome C (CytC) to reductase (r-CytC) is tracked using buffered $Sn:In_2O_3$ NCs as remote nanoelectrometers (RPN). The electron concentration extracted via quantitative modeling of absorption spectra shows that the number of transferred electrons follows the amount of r-CytC converted to CytC oxidase (o-CytC), with [r-CytC]a being the concentration of r-CytC added and $[CytC]_{fit}$ being the optically determined concentration of either form of CytC. Reprinted with permission from ref 145. Copyright 2015 John Wiley & Sons, Inc.

are added to or removed from their conduction band owing to significantly lower carrier concentration.

4.2. LSPR Modulation via Chemical Redox

Sensitivity of LSPR peak energy to changes in the surrounding dielectric environment or interparticle coupling is the basis of the well-established field of plasmonic sensing with metal nanostructures. In such systems, the plasmonic particles are passive indicators which do not participate in the chemical processes happening in the medium. Therefore, detectable changes in dielectric properties of the surrounding are necessary to induce a measurable LSPR change.[1,506−509] Semiconductor NCs offer a unique additional characteristic of behaving as redox reagents where they can mediate electron transfer reactions through accepting or donating their conduction or valence band electrons (see refs 43, 46, 145, 146, 148, 150, 483, and 510−513). As the LSPR of semiconductor NCs is extremely sensitive to addition or subtraction of a small number of charge carriers, this approach provides a robust method to track electron transfer events in complex media. Optical detection can be sensitive to changes as low as 1 e^- per NC. Further, such processes involve distinct optical signatures. Addition of electrons to NCs not only alters the LSPR intensity and peak frequency but also causes a detectable bleach of the interband excitonic transition due to filling the conduction band edge energy levels, effectively increasing the optical band gap, a phenomenon known as the Burstein−Moss shift.[34,510,513] Reversible electron transfer to NCs was first demonstrated for CdSe and ZnO NCs when exposed to sodium biphenyl or metallic sodium as reducing

DOI: 10.1021/acs.chemrev.7b00613
Chem. Rev. 2018, 118, 3121−3207

agents. In both cases, upon electron transfer, a broad IR band appeared concomitant with bleach of the lowest energy excitonic transition.[510]

Dorfs et al.[43] demonstrated reversible tunability of LSPR in $Cu_{2-x}Se$ enabled by redox tuning of the Cu stoichiometry. Nonstoichiometric $Cu_{2-x}Se$ exhibits a plasmonic response around 0.5−1.0 eV due to an excess concentration of holes in the valence band. It was shown that upon addition of oxidizing Ce(IV) to stoichiometric Cu_2Se that the LSPR absorption wavelength can be modulated by 400 nm and can be reverted by exposure to reducing agents such as Cu(I) complexes. Jain et al.[46] built upon this work to demonstrate reversible LSPR modulation in copper sulfide NCs in contact with reducing or oxidizing species (Figure 45a). Addition of oxidants such as I_2 led to oxidation and creation of Cu vacancies, which manifests as increasing the LSPR energy and intensity of $Cu_{2-x}S$ NCs (Figure 45b). Addition of a reducing agent such as sodium biphenyl results in filing of the valence band holes, thus diminishing the LSPR intensity (Figure 45c). Additionally, it was demonstrated that the LSPR of $Cu_{2-x}S$ NCs is sensitive to the nature of the capping ligands, suggesting that this approach can be used to detect bonding depending on the electron-withdrawing or -donating nature of ligands.[46,268]

The redox-sensitive LSPR properties of semiconductor NCs were further leveraged and applied to detect redox reactions in aqueous and biological media. Mendelsberg et al.[145] demonstrated that polymer-capped $Sn:In_2O_3$ NCs exhibit large, fast, and reversible changes in LSPR when exposed to oxidizing cerium(IV) nitrate (E^0 = 1.72 V vs SHE) and reducing sodium ascorbate (E^0 = 0.39 V vs SHE) molecules. Moreover, $Sn:In_2O_3$ NCs mediated as well as monitored the electron transfer during chemical conversion of CytC oxidase (o-CytC) to CytC reductase (r-CytC). Optical modeling of the LSPR was used to quantify the number of transferred electrons (Figure 46). Further, Sn:In2O3 LSPR was shown to be sensitive to electrons transferred to the NCs from bacteria. This approach thus provides an electrode-less probe to monitor electroactive biological processes in complex media.

Plasmonic metal oxide NCs are well-suited to monitor redox events involving small electron transfer events due to the fact that a change as low as 1 e^- per NC has a substantial impact on carrier concentration in NCs with low dopant densities. This provides a compelling outlook for sensing applications as well as systematic fundamental studies of electron transfer at the nanoscale. Indeed, the field is still young and demands further fundamental understanding of such heterogeneous electron transfer reactions. Methods need to be developed to stably disperse NCs in various media, with simple and robust surface modifications. Moreover, plasmonic NCs can also be utilized in thin films and assemblies for integration into solid state devices and chemosensors. Changes in the sensor chemical environments can be detected both optically (from the LSPR response) and electrically (from changes in resistance). Sturaro et al.[514] demonstrated an example by employing a thin film of Ga:ZnO NCs to detect ppm levels of NO_2 and H_2 gases.

4.3. Photochemical Charging

Photochemical charging (also known as photodoping) has emerged as a universal method to dynamically tune electron density, thus the LSPR of semiconductor NCs (see refs 39, 39, 79, 79, 148, 149, 196, 214, 246, 248, and 515−517). Photochemical charging was first demonstrated by Haase et al.[214] on ZnO NCs. Upon UV illumination, electrons were excited to the conduction band and stabilized by using EtOH as a hole scavenger. A strong bleach of band gap absorption occurred associated with the filling of the lowest conduction band states. The process was shown to be reversible by exposure to O_2 as an electron scavenger. Similar observations were later made for CdSe and ZnO quantum dots by the Guyot-Sionnest group.[510,518,519] Upon exposure of a solution of ZnO NCs to UV light, a strong IR peak appeared concomitant with extensive bleach of the interband transition and complete quenching of photoluminescence[247] (Figure 47). Since these early studies, ZnO has been extensively studied as a model system for photodoping and the concept has been extended to other oxide and chalcogenide materials.

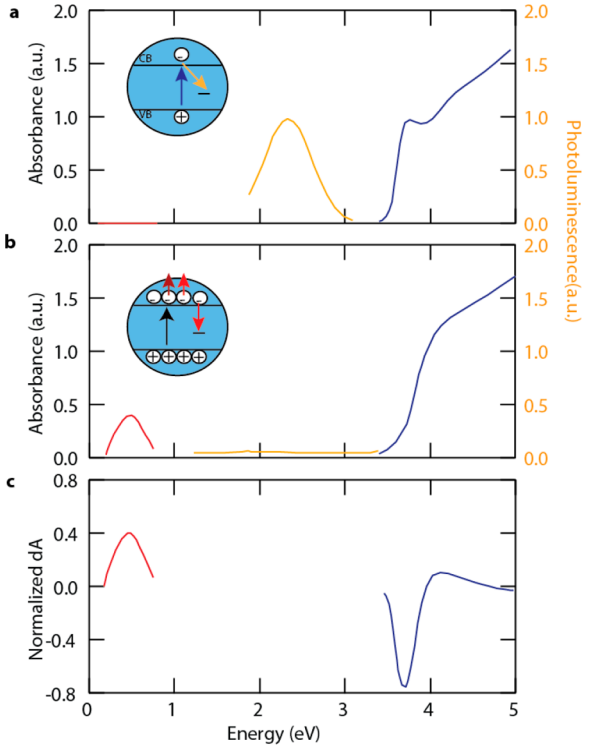

Figure 47. Photoexcitaton of metal oxide NCs. Addition of electrons in TOPO-capped ZnO NCs (3.1 nm size) via charge-donating sodium biphenyl reductant lead to changes in three distinct optical features: (a) as synthesized ZnO, (b) charged ZnO, and (c) differential plot. Charged NCs display distinct infrared absorption in the IR spectrum arising from free carrier excitation that is absent in ZnO NCs (red in a and b). In addition, due to the addition of electrons in the conduction band, visible absorption shows a Burstien-Moss shift toward higher energy (blue curve). Moreover, ZnO PL gets quenched due to enhanced Auger recombination (yellow curve). Reprinted from ref 247. Copyright 2001 American Chemical Society.

Addition of electrons to the conduction band of NCs results in three universal optical signatures (Figure 47): (1) appearance of an IR absorption band commonly attributed to intraband transitions within the conduction band, (2) significant bleach of the interband transition due to the Burstein−Moss effect, and (3) extensive quench of photoluminescence attributed to enhanced Auger recombination.[79,247] The IR absorption band in charged NCs has usually been assigned to direct single electron transitions between the discrete states of the conduction band. In the majority of reported cases, however, the IR absorption has not been quantified. By careful quantification of the absorption

DOI: 10.1021/acs.chemrev.7b00613
Chem. Rev. 2018, 118, 3121−3207

behavior upon increasing charging (prolonged illumination), one can distinguish single electron excitations from an LSPR mode. For a single electron transition, the IR peak energy is expected to red shift as the NCs are increasingly charged since electronic levels are more closely packed at higher energies and transitions between these contribute to the spectrum for more highly charged NCs. In contrast, an LSPR peak is expected to blue shift with increasing concentration of free carriers according to the Drude model.[196] Faucheaux et al.[196] analyzed the dynamics of conduction band electrons in photocharged ZnO NCs where they attributed the IR band to collective oscillation of a plasma of degenerate electrons based on the following observations. First, the peak of the IR band shifted to higher energy upon further charging, consistent with LSPR behavior. Second, the IR band was shown to redshift upon increased electromagnetic coupling in a film of NCs as compared to a NC dispersion. Third, the carrier density of charged NCs, estimated from the LSPR peak frequency, was in agreement with the reported literature values obtained by chemical titration. Such quantifications allow one to draw conclusions as to the dynamics of excess conduction band electrons and the nature of their optical signature. As explained earlier in this review (section 2.2.3.2), there is a close connection between single-carrier transitions and LSPR. In fact, at high enough carrier density, single carrier transitions converge to an LSPR mode. Determining factors relevant to this convergence are the NCs size and Mott carrier density. For example, for small ZnO NCs, even a single e- per NC, produces carrier densities that exceed the Mott limit (for ZnO this limit is 6×10^{18} cm^{-3}). Examples of LSPR in semiconductor NCs have been demonstrated with a handful of electrons (e.g., in ZnO NCs), as little as 4 e^- per NC.[196,520] Small (3−7 nm) photocharged ZnO NCs exhibited delocalized conduction band electrons as confirmed by temperature-independent g* values in EPR measurements.[482,521]

These observations indicate that the traditional notion of associating plasmonic response with a high density of electrons, as in metals, needs to be scrutinized. As we discussed earlier in this review (section 2.2.3.2), recent theoretical work[196,231] showed that a crossover from single-electron excitation to plasma absorption is determined by the size of NCs, density of electrons, and electronic band structure. As carriers are progressively added to the NCs, single carrier excitation evolves into and coexists with few carrier collective excitations that ultimately converge to purely collective plasmon resonance. At high enough carrier densities, carrier dynamics are purely determined by the Coulombic repulsion between carriers rather than confinement. The degree of localization (i.e., the effective mass) plays an important role in determining the transition from single carrier to collective excitation. Finally, there is the size effect; in smaller NC, high confinement energy induces fully quantum mechanical transitions. As the size increases, the collective oscillation can be fully rationalized by the classical Drude model.[230,231]

In order to stably introduce free carriers, Gamelin and co-workers (see refs 34, 39, 40, 79, 148−150, 482, and 522) and Mayer and co-workers (see refs 511 and 523−525) used EtOH as a hole scavenger. Effective hole collection by EtOH produces stable conduction band electrons under vigorously anaerobic conditions. This approach was further rationalized as a proton coupled electron transfer event (PCET). Protons (a product of EtOH oxidation) serve to stabilize the conduction band electrons through surface adsorption and intercalation. Stabilization of photodoped electrons allowed for the quantification of the excess conduction band electrons in ZnO by titration against a chemical oxidant such as $FeCp_2^{*+}$ or $CoCp_2^{*+}$.[148,150] This allowed Schimpf et al.[40] to systematically investigate effects of NC size, kinetics of the hole scavenger, and the type of charge compensating cations on the extent and dynamics of photodoping (Figure 48a). A maximum number of electrons per NC, $<n_{max}>$, was found that scales with the volume of the NCs, giving a constant maximum electron density ($<N_{max}>$) for a given hole scavenger (Figure 48b). These results were initially rationalized as a kinetic competition between hole collection and multicarrier

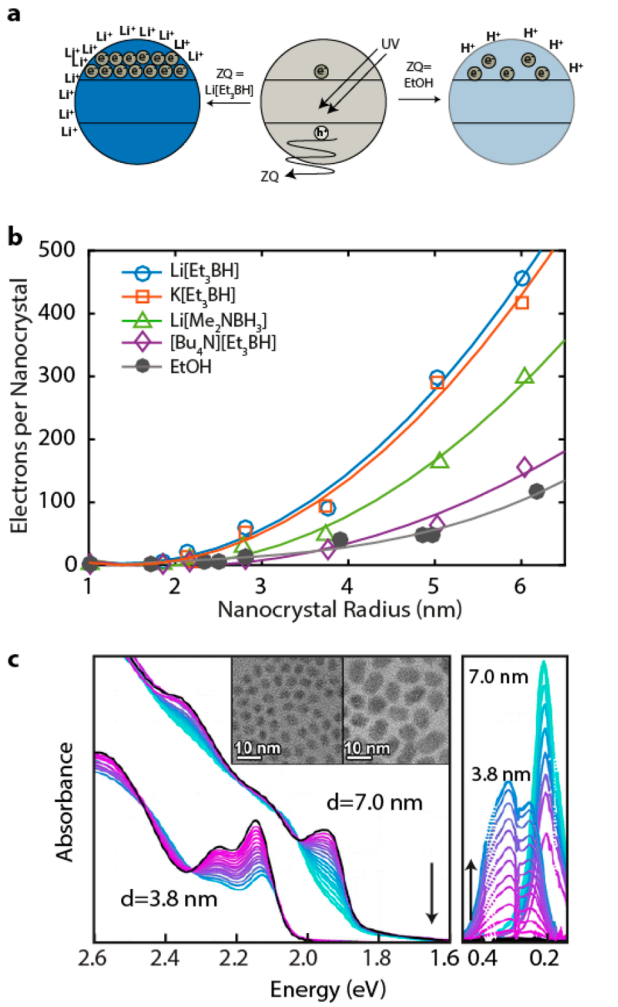

Figure 48. Photochemical control of semiconductor NC LSPR. (a) Schematic shows the dependence of photo-induced electron concentration on the nature of the hole quencher (ZQ). Due to the photon coupled electron transfer process, electrons accumulate in the conduction band and charge compensating cations (Z^+) concentrate in a charged double layer on the NC surface. Depending on the redox potential of ZQ and relative steric bulk of both cations (Z^+) and anions (Q^-), different degrees of photocharging can be accumulated in the conduction band. (b) Irrespective of hole quencher, the maximum number of photodoped electrons scales with the volume of the NCs. Solid lines are cubic polynomial fits. Panels a and b reprinted from ref 40. Copyright 2013 American Chemical Society. (c) In CdSe, photogenerated holes (h^+) are quenched by the electron donated by the $Li[Et_3BH]$ reducing agent. This leads to the accumulation of free electrons in conduction band that give rise to infrared intraband absorption spectra (right) and bleaching of visible absorption (left). Panel c reprinted from ref 38. Copyright 2013 American Chemical Society.

DOI: 10.1021/acs.chemrev.7b00613
Chem. Rev. 2018, 118, 3121−3207

Auger recombination.[40] Using borohydride hole scavengers allowed up to 3 times higher e^- densities compared to EtOH, owing to faster kinetics of hydride oxidation. Among hydrides, $Li[Et_3BH]$ produced higher electron density than $[Bu_4N][Et_3BH]$. It was argued that Li^+ more effectively stabilizes the CB electrons in a similar manner as H^+. Later it was found that the maximum photodoping is controlled by thermodynamics rather than kinetic limitations (i.e., the energetic alignment of the NC Fermi level with the chemical oxidants or the products of hole scavenger oxidation redox potentials determines the maximum carrier injection in the NCs).[148,511] In the case of EtOH, it was shown that $< n >_{max}$ is limited by the aldehyde reduction potential, that being the product of EtOH oxidation[148] similar to photodoping, NCs can be alternatively charged using ground state charge transfer from reducing agents as discussed in the previous section. Valdez et al.[150] demonstrated that electron transfer from $CoCp_2^{*+}$ to ZnO NCs in aprotic solvents is strongly coupled to the availability of protons that are required to stabilize the CB electrons. Additionally, protons shift the band energies, and thus driving force for charger transfer, by changing the local pH at the NC surface.

Photodoping in the presence of a chemical hole scavenger was extended to metal chalcogenides where CdSe and CdTe NCs were n-doped photochemically using $Li[Et_3BH]$ as the hole quencher[38] (Figure 48c). The photodoped NCs exhibited the key spectroscopic signatures of filling conduction band states including bleaching of interband absorption, appearance of an IR absorption band, and quenching of the photoluminescence. Recently, Alam et al.[423] demonstrated LSPR modulation in $Cu_{2-x}S$ NCs through photochemically generated methyl viologen ($MV^{+\bullet}$) radicals. Titration of the added electrons demonstrated reversible electron transfer, analogous to the case of ZnO, indicating the generality and versatility of this approach.

In addition to modulating free electron concentration in intrinsic and vacancy-doped semiconductors, photocharging can also introduce additional carriers in aliovalent-doped semiconductors. Using $Sn:In_2O_3$ as a model system, Schimpf et al.[149] investigated the impact of the presence of Sn on the extent of photocharging possible in doped indium oxide. The authors found that even though Sn^{4+} doping causes In_2O_3 to have an LSPR and free charge carriers, the addition of photoinduced carrier density (N_{photo}) is minimally impacted by the presence of Sn, such that doped and undoped In_2O_3 could be photodoped to a similar concentration of additional electrons (Figure 49, panels a and b). The authors hypothesized that in contrast to aliovalent doping, where there is a change in band structure with every dopant introduced to the lattice, the maximum extent of photodoping is mainly determined by the thermodynamic factors relating to the hole quencher and surface chemistry of protons and not by kinetic effects, such as competitive Auger recombination dynamics in effect during the photodoping process (Figure 49, panels a and b). This is an important distinction as it indicates that the electron concentration of a material can be modulated with only small changes to the thermodynamic equilibrium potential at the interface between the NC and its surroundings. Recently, Zandi et al.[153] performed a detailed study on the impact of surface potential on the carrier concentration as well carrier distribution inside doped NCs and thereby on NC LSPR, which is discussed in detail in a later section (section 4.5).

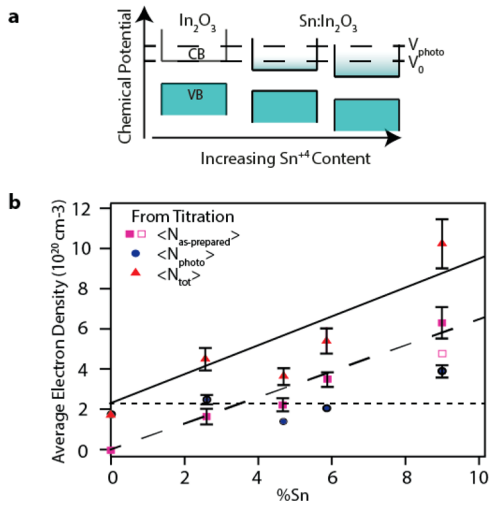

Figure 49. Simultaneous impurity doping and photodoping of metal oxide NCs. (a) The schematic shows that irrespective of Sn dopant concentration in $Sn:In_2O_3$ NCs, the maximum number of photoelectrons remains the same and is determined thermodynamically. (b) The difference between the total density of free electrons (red ▲) and impurity doping induced free carriers (pink ■) equals the photoelectron concentration (blue ●), and this value remains constant irrespective of dopant concentration (dashed line). Reprinted from ref 149. Copyright 2015 American Chemical Society.

4.4. Ultrafast LSPR Modulation

All optical excitation possesses a characteristic lifetime during which the material undergoes relaxation to the initial state. The relaxation dynamics of a particular optical process are determined by both the intrinsic (electronic structure) and the extrinsic (shape, size, and surrounding) characteristics of the NCs. As it is determined by the electronic structure of the NC, the study of relaxation dynamics frequently becomes the probe to study the former. Doped semiconductor NCs display different characteristic lifetimes for different optical transitions. The relaxation dynamics of two optical transitions (relevant to this review) that are of interest to the semiconductor LSPR research community are (1) the radiative and nonradiative relaxation dynamics of NC LSPR excitations and (2) the e-h recombination dynamics corresponding to different interband transitions. The photoexcitation of interband transitions in semiconductor NCs transiently increases the free-electron concentration in the conduction band thereby blue-shifting the LSPR for the short time interval before e-h recombination occurs. The LSPR dynamics during the relaxation of the photoexcited interband transitions provide useful insight into the material properties and are also of interest for applications such as ultrafast optical modulators. Moreover, the study of relaxation of LSPR via direct excitation of the LSPR yields information about the extent of local heating and hot electron generation that is critical for photothermal and catalysis applications. In semiconductor NCs, the interband and LSPR transitions are typically well-separated, the latter being far lower in energy. In this section, we will first focus our discussion on ultrafast LSPR modulation via interband excitation and later describe the relaxation dynamics of NC LSPR.

Semiconductors are interesting for ultrafast optical modulation as direct excitation of interband transition can lead to large changes in LSPR absorption on the femtosecond time scale. When light of sufficiently high energy is used to excite an electron across the band gap, the charge carrier concentration increases

DOI: 10.1021/acs.chemrev.7b00613
Chem. Rev. 2018, 118, 3121−3207

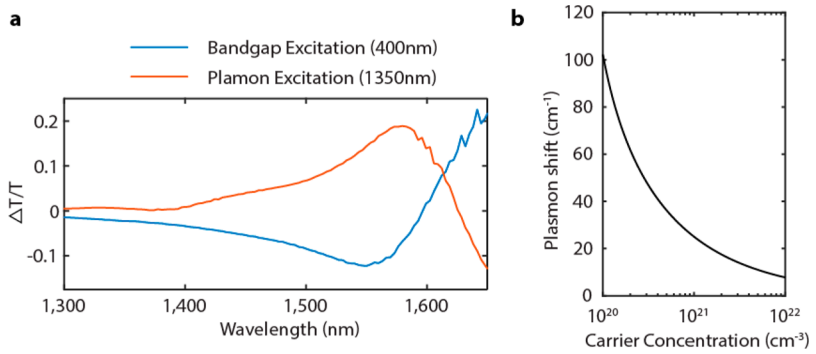

Figure 50. Ultrafast modulation of semiconductor NCs. (a) Pumping the band gap (blue) and the LSPR (orange) of F,In codoped CdO NCs shows blue and red shift of the LSPR, respectively, in the transient absorption spectra. Reprinted from ref 147. Copyright 2016 American Chemical Society. (b) The theoretical modulation of a 6 nm Sn:In_2O_3 sample upon excitation of 1 exciton across a wide range of carrier concentrations shows that the LSPR energy of NCs with an initially lower carrier concentration is impacted more strongly per photon.

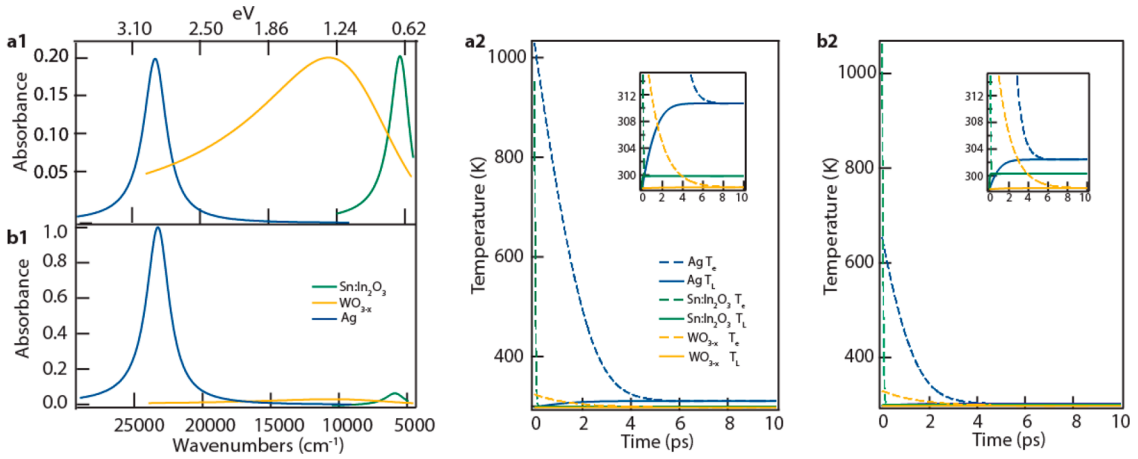

Figure 51. Temperature of hot electrons. (a1) Normalized LSPR spectra of three materials and (a2) the corresponding theoretical temporal progression of temperature of the electrons and the lattice. (b1) Fixed volume fraction spectra of same materials and (b2) the corresponding theoretical temporal progression of temperature of the electrons and the lattice. In the normalized case, silver appears to be hotter because there is less material needed to reach the same optical density as for the lower carrier concentration samples. Reprinted with permission from ref 526. Copyright 2017 The Royal Society of Chemistry.

during the lifetime of the electron−hole pair manifesting in a transient blue shift of the LSPR. Pumping the bandgap to modulate carrier concentration is far more effective at lower carrier concentrations where the optically excited carriers cause a significant deviation from the steady state (Figure 50a). In Figure 50b, the effect of exciting 1 electron−hole pair on the resonance energy of the LSPR of a 6 nm diameter Sn:In_2O_3 NC is shown over a wide range of baseline carrier concentrations. Adding one electron more drastically changes the plasma frequency of a lower carrier concentration NC than a higher one. These relatively modest shifts indicate that to achieve significant signal modulation, pump intensities will need to excite several electron−hole pairs simultaneously, which can complicate modeling these changes with standard dielectric function models.

Another important property of semiconductor LSPR materials that influence optical modulation is the degree to which optical density changes with carrier concentration.[526] In most ultrafast transient absorption experiments samples are made with similar optical densities at the pump wavelength, but when comparing samples with drastically different carrier concentrations and resonant frequencies, this can result in comparing samples that have very different material concentrations in solution. This is illustrated in Figure 51, where (a) samples are prepared to have the same optical density, by allowing the volume fractions to differ compared to (b), in which the relative optical density of the three samples are shown by comparing what the spectra would look like for three samples with identical volume fractions. When one considers the effects of excitation in these systems, it is clear that the ratio of light absorbed to amount of sample will impact how energy is partitioned within the system.

The same plasmonic materials that were studied for LSPR modulation through interband excitation can also undergo LSPR modulation through direct energy pumping near the LSPR frequency. Once excited, an LSPR will create a resonant local near field for only a short period of time, on the order of a few femtoseconds. The dephasing of the NC LSPR can occur through radiative and nonradiative damping mechanisms. For small-sized NC (in the quasistatic regime), nonradiative decay is the primary relaxation route following coherent LSPR excitation. The dephasing of LSPR transfers energy into the conduction band electron. The excited carriers quickly equilibrate (within 100 fs) via electron−electron scattering to form a hot electron distribution.[147,285,515,527−531] Eventually, if the hot electrons do not undergo charge transfer reaction, the energy from the hot electrons transfers to the lattice via electron−phonon scattering. The dynamics of energy distribution first creating a hot electron distribution then transferring energy to the lattice and eventually dissipating energy as heat to the surroundings are usually

DOI: 10.1021/acs.chemrev.7b00613
Chem. Rev. 2018, 118, 3121−3207

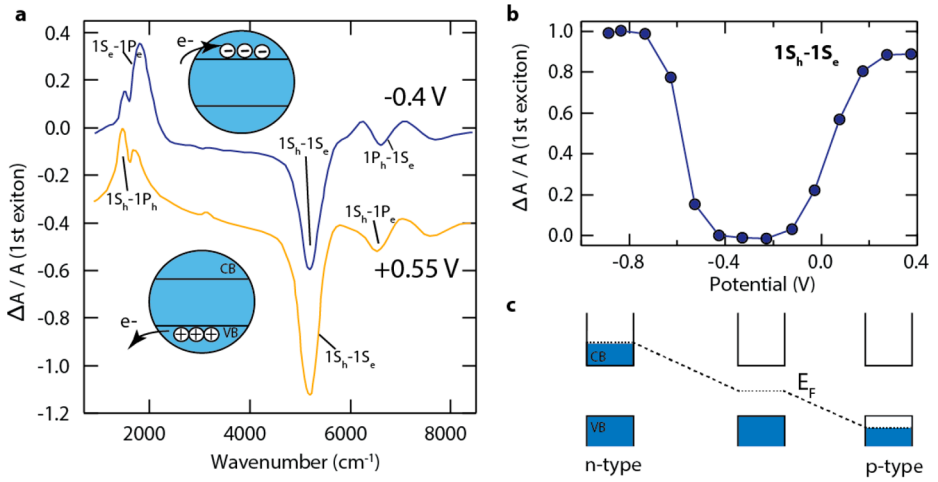

Figure 52. Electrochemical control of the optical characteristic of semiconductor NCs. (a) Electrochemical charging of PbSe quantum dots in between −0.4 V (injecting electrons into the conduction band) and 0.55 V (extracting electrons or injecting holes into the valence band). Relative to an uncharged film, applying reducing or oxidizing potential changes both interband absorption in the high-energy spectrum and intraband absorption in the low-energy spectrum. At −0.4 V, filling of electrons in the $1S_e$ state within the conduction band bleaches the $1S_h \rightarrow 1S_e$ and $1S_h \rightarrow 1S_e$ transitions and gives rise to a $1S_e \rightarrow 1P_e$ intraband transition in the IR. Similarly, at 0.55 V, filling of holes in the $1S_h$ state bleaches the $1S_h \rightarrow 1S_e$ and $1S_h \rightarrow 1P_e$ transitions but gives rise to a $1S_h \rightarrow 1P_h$ intraband transition in the IR. (b) The normalized bleach of the first exciton, $1S_h \rightarrow 1S_e$, is plotted as a function of applied potential. Panels a and b are reprinted from ref 549. Copyright 2003 American Chemical Society. (c) Schematic shows the shifting of electrochemical applied potential dependent Fermi level from well within the valence band to within the conduction band. This transforms the material from n type to p type.

expressed using the two temperature model, with one temperature describing the electrons and one the lattice.[532−535] Researchers have been studying these effects in metals for a very long time,[532−535] but more recently, studies have been performed on plasmonic semiconductor NCs.[147,285,515,526−531] It is of interest to understand both the extent of hot electron excitation and the eventual local heat generation.

Direct excitation of the LSPR leads to hot electrons, which results in a red shift of the LSPR[147] (Figure 50a). Typically, the energy following optical excitation of an LSPR is initially distributed to a population of hot electrons. This energy, over time, equilibrates with phonons in the crystal leading to an increase in the lattice temperature. This process has been studied thoroughly in classical metal nanoparticles and indeed plasmonic systems can be made to generate significant local heat.[161,536,537] As researchers continue to investigate the ultrafast relaxation in LSPR-active semiconductor NCs with variable carrier concentrations, it is important to keep in mind the ratio of optical density to volume fraction as shown in Figure 51. Samples prepared at the same optical density (a) will not experience the same temperature progression that would be comparatively expected on a per material basis and (b) not accounting for these effects could lead to misleading conclusions, for example that coinage metals are drastically better at generating heat than semiconductor systems, when in fact these differences on a per material basis are more modest. Further, lower carrier concentration systems, depending on their electron heat capacity, may actually produce hotter electrons transiently than coinage metals, which would not be apparent when comparing samples prepared at the same optical density rather than material density. The potential of semiconductor NC LSPR excitations to produce hotter electrons than classical metals is particularly striking when considering the low energy, IR light that these semiconductors harvest. The potential to employ these hot electrons in further photochemical processes is compelling indeed. The study of ultrafast modulation of semiconductor NC is still at a preliminary stage but has already shown promising results for optical modulation, photothermal heating, and catalysis applications. There are several unanswered questions that need to be addressed to develop better understanding of LSPR modulation and decay dynamics in semiconductor NCs: (1) Is it possible to modulate the LSPR by dynamically controlling the extent of dopant activation in doped semiconductor NC? (2) How does the dopant concentration affect the electron−electron and electron−lattice scattering parameters, thereby determining the decay lifetime? (3) Is it possible to harness the hot electrons in materials with a low baseline carrier concentration for charge transfer reactions at NC surfaces?

4.5. Electrochemical LSPR Modulation

Free carrier concentration in semiconductor materials can be modulated through the application of an external voltage leading to accumulation or depletion of charge carriers near their surfaces and interfaces. This approach has been employed to modulate the optical properties of semiconductor NCs to achieve electrochromism either based on electronic charging in a capacitor device or on electrochemical charging in a battery-type cell (see refs 36, 37, 41, 74, 75, 151, 152, 154, 223, and 538−544). Electrochemical control of the Fermi level offers a robust approach to disrupt the equilibrium carrier concentration in a film of semiconductor NCs, thus achieving on-demand tuning of their optical properties. For a given reducing potential, the extent of carrier modulation is determined by the NC size, surface chemistry, and the nature of charge compensating ions in the electrolyte.

Electrochemical carrier modulation in nanocrystalline systems was first demonstrated using a transparent film of ZnO NCs[545] as well as on NC dispersions in electrolyte.[546] A strong bleach of the interband absorption was observed upon application of the negative bias and attributed to the Burstein−Moss effect. Later, Wang et al.[547] demonstrated electron injection into the quantum confined states of CdSe[548,549] NCs characterized by the key signatures of accumulating excess electrons in the conduction band: the appearance of a MIR absorption band concomitant

DOI: 10.1021/acs.chemrev.7b00613
Chem. Rev. 2018, 118, 3121−3207

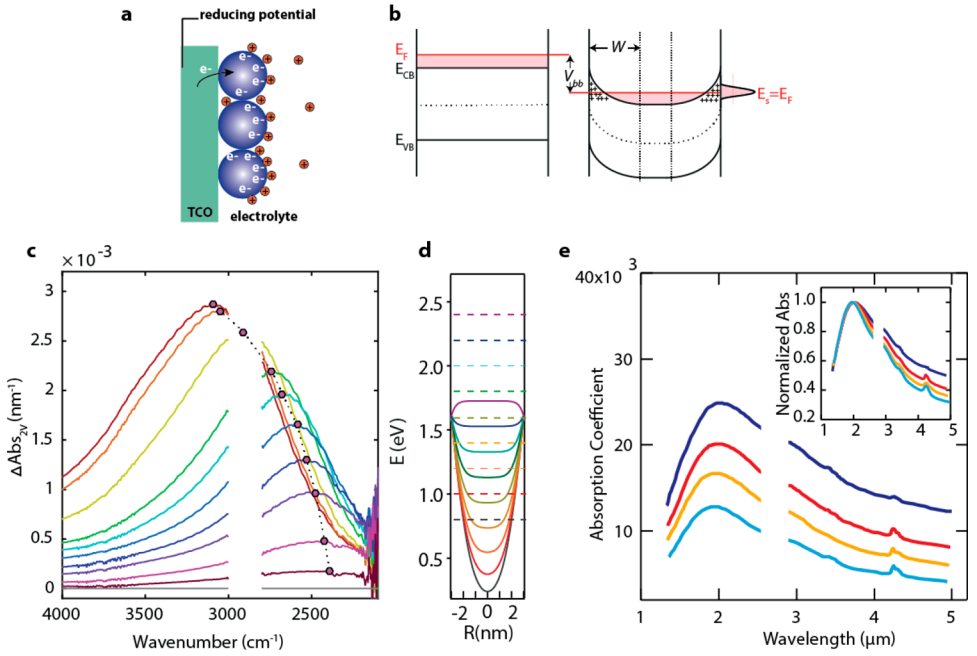

Figure 53. Electrochemical control of metal oxide NC LSPR. (a) Schematic showing the capacitive charging of NCs deposited on a conductive substrate. As a reducing potential is applied to the NC film, electrons injected into the NCs modify their LSPR characteristics. (b) Schematic representing the band energetics of a NC under flat band (left) and band bending (right) conditions where E_S represents the surface state potential, E_{vb} is the VBM, E_{CB} is the CBM, and E_f is the Fermi level. (c and d) In situ FTIR SEC spectra of a film of NCs collected at various applied potentials for 1%-doped, 7.4 nm diameter Sn:In_2O_3 NCs. Calculated conduction band profiles for a low (1%) doped, 6 nm diameter NC at different surface potentials shows that at oxidizing potentials the depletion region extends throughout the NC, depleting it of free carriers. Depletion of free carriers changes the plasma frequency of the NC, resulting in changes in LSPR peak frequency. Reprinted with permission from ref 153. Copyright 2017 arXiv. (e) NIR electrochromic response of Sb-doped tin oxide NC films. Optical response was measured as a function of applied potential vs Ag/AgCl. In contrast to (c), changes in surface potential only changed the LSPR optical density but did not change the LSPR energy. Reprinted from ref 540. Copyright 2000 American Chemical Society.

with the bleach of the visible interband excitation and quenching of PL. In the case of small band gap PbSe and HgTe NCs, both electron and hole injection (i.e., p-type and n-type doping) were achieved electrochemically, indicating the versatility of this approach to dynamically tune the electronic properties of NCs[549,550] (Figure 52). Boehme et al.[551] employed similar ideology to determine the absolute energy level of CdSe quantum dots by electrochemical charge injection.

Electrochemical modulation of LSPR in metal oxide NCs has particularly received attention due to promising optoelectronic properties for use in IR electrochromic smart windows.[36,37] Degenerately doped wide band gap oxides (e.g., Sn:In_2O_3 (ITO), Sb:SnO_2, Al:ZnO, and WO_{3-x}) are transparent in the visible while exhibiting LSPR in the NIR to mid-IR. Electrochemically tunable LSPR in these materials has been leveraged to develop smart windows where one can modulate the NIR solar transmission by inducing large shifts and amplitude changes in the LSPR absorption (as high as 80% change in NIR transmittance). Combining plasmonic NCs with traditional visible electrochromic materials such as NbO_x, researchers have developed composite materials that allow voltage-selective control over visible and NIR transmittance offering dual-band electrochromism for smart windows.[152,552] The approach holds a tremendous potential for energy savings in buildings by regulating light and heat transmission through windows.[553,554] Such battery-type electrochromic devices consist of an active electrochromic electrode layer, a counter electrode, an electrolyte separating the two electrodes, and two transparent conducting oxide coated supporting substrates, which serve as electrical contacts. Injected electrons are stabilized by electrolyte cations through Faradaic (intercalation of cations such as Li^+ or H^+) or capacitive processes (Figure 53a). Effective charge injection requires a conductive network of NCs (i.e., the native ligands need to be removed from the NCs). Moreover, the film of NCs must be porous enough to allow fast charging/discharging kinetics and migration of charge compensating ions. Future work on this front will need to focus on color neutrality, switching speeds, and methods of precharging NC films.

Although numerous examples of electrochemical LSPR modulation have been demonstrated, less is known about the fundamental relationship between carrier modulation and the optical properties. Plasmonic semiconductor NCs are often treated as metallic particles and their optical physics described by the classic Drude model. Semiconductor properties such as band structure modification upon doping and surface chemistry, however, strongly impact the extent and the nature of LSPR modulation.[153] For example, the Fermi level of semiconductor NCs at the surface is defined by the surface redox potential (e.g., fixed by a redox couple in the environment or by the presence of surface states). Surface states energetically located below the Fermi level would induce surface depletion, the extent of which will depend on factors such as NC size, doping density, and energy difference between the Fermi level and the surface states (Figure 53b). zum Felde et al.[540] were the first to observe anomalous LSPR modulation behavior deviating from the Drude model upon application of reducing potential to Sb:SnO_2 NC films. They observed an increase in the LSPR intensity but no LSPR frequency change, contrary to the expected blue shift as the electron density increases (Figure 53e). This behavior was rationalized by considering NC surface depletion effects; in

DOI: 10.1021/acs.chemrev.7b00613
Chem. Rev. 2018, 118, 3121−3207

depleted NCs, the injected electrons are consumed in the depletion layer thus resulting in a constant electron density in the plasmonic core. The volume of the charged core however increases as the absolute number of electrons goes up, which results in a net increase in the LSPR intensity. These results, though discussed qualitatively, were revealing as to the role of surface chemistry and surface depletion on LSPR properties. In order to fully understand the effect of surface depletion, Zandi et al.[153] studied Sn:In_2O_3 NCs as a model system in which size and doping level could independently be well-controlled. Synthesizing monodisperse NCs with various sizes and doping levels allowed systematic analysis of depletion effects. A combination of in situ FTIR spectroelectrochemical measurements, charge distribution calculations, and optical modeling allowed them to establish a fundamental framework for controlling electrochemical modulation of LSPR intensity and frequency. Briefly, in the case of low-doped and smaller NCs, the depletion width occupies nearly the entire NC volume. Charging such NC films results in an increase in the electron density, thus modulation of both LSPR frequency and intensity (Figure 53, panels c and d). In contrast, in the case of highly doped NCs (similar to the work by zum Felde et al.[540]), the depletion layer occupies less than 20% of the NC volume. Charging in this case only expands the undepleted core while maintaining a constant carrier density. The result is little frequency change while the intensity is still strongly modulated.

The effects of surface depletion extend beyond the impact on LSPR modulation. As we discussed earlier in this review (section 2.3.8), the existence of a shell of depleted material strongly reduces the LSPR's sensitivity to dielectric changes in the surrounding medium. Further work is needed to fully understand the effects surface chemistry, especially in dispersed NC systems and by systematically changing the surface chemistry. Further work needs to be done to fully understand depletion and accumulation conditions in plasmonic NCs, the latter of which seems to be difficult to achieve in conventional electrolytes. Additionally, in electro-optical and sensing devices, it is necessary to use larger NCs to achieve high NFE. In such large NCs, the carrier concentration modulation is limited to a shell of a few nanometers thickness on the surface and the majority of the core remains unchanged with variable applied bias. Understanding of LSPR modulation in larger, highly doped NCs in needed to fully exploit the dynamic advantage of this class of plasmonic materials.

Analogous to studies of metal oxide NCs, recent studies[555,556] with metal chalcogenide NCs have explored electrochemical modulation of the optical properties of NC films. Llorente et al.[555] demonstrated the capacitive charging/discharging of $Cu_{2-x}Se$ accompanied by the switching of optical properties from absorbing to transparent in the NIR. The authors used an electrolyte solution containing tetrabutylammonium hexafluorophosphate (TBAHFP) in dichloromethane (DCM) in their experiment. The electrochemical charging mechanism is purely capacitive due to large ionic radius of the cation, TBA^+, which prevents any intercalation into the $Cu_{2-x}Se$ crystal lattice. Here, during reduction, filling of the valence band leads to a decrease in free hole concentration, which results in the complete suppression of LSPR absorption. Absorption is reversibly recovered during oxidative charging (Figure 54a). The authors also studied the optical modulation of CuS NC films, but due to the intrinsically metallic properties of the CuS, very little optical modulation was observed during capacitive charging. Following up on this work, van der Stam et al.[556] used electrolytes

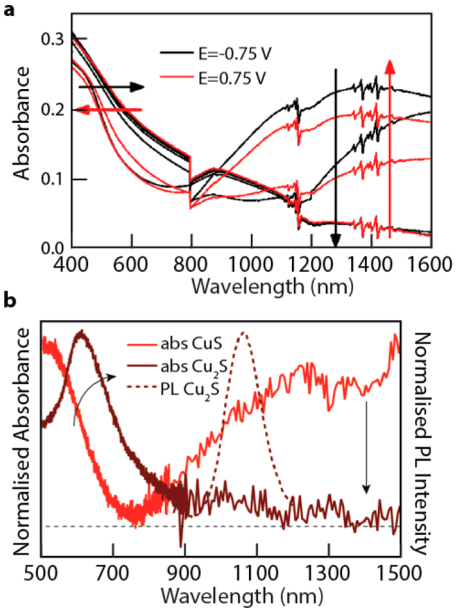

Figure 54. Electrochemical control of metal chalcogenide NCs LSPR. (a) Dynamic tuning of absorption spectra of $Cu_{2-x}Se$ NCs in Nafion between an LSPR bleached state at −0.75 V and an LSPR-active state at 0.75 V. Addition of electrons during charging of the NC film reduced the free hole concentration that results in bleaching of the LSPR absorption. In the UV−vis part of the absorption spectrum, the decrease in free hole concentration leads to a shift in interband absorption to lower energy. Reprinted from ref 555. Copyright 2017 American Chemical Society. (b) Electrochemical intercalation of Cu^+ ions in a covelite CuS NC film irreversibly forms low chalcocite Cu_2S phase. Addition of Cu to the NCs reduces the free hole concentration that bleaches the LSPR absorption. The electrochemically charged Cu_2S NC film also exhibited photoluminescence. Reprinted from ref 556. Copyright 2017 American Chemical Society.

containing cations with smaller ionic radii such as Li^+ and Cu^+, allowing intercalation in CuS metallic NC films and observed a corresponding optical change. The authors argued that since CuS has a layered hcp-based crystal structure, it can easily accommodate Li^+ or Cu^+ inside the lattice. They observed that during Li^+ intercalation, the NCs changed from the hcp CuS phase to a low chalcocite CuLiS phase. This phase change was accompanied by an optical change: LSPR absorption intensity weakened and red shifted with phase transformation toward the low chalcocite phase. The phase change was reversible allowing full recovery of the original LSPR spectrum. The authors also performed the same experiment with a Cu^+ cation containing electrolyte, and similar to the previous case, during the Cu^+ intercalation process, the NC phase transformed from hcp CuS to low chalcocite Cu_2S phase. But with Cu^+ cations, the phase change was irreversible. The authors argued that stoichiometric as-synthesized low chalcocite Cu_2S NCs are usually very unstable under ambient conditions and have been shown to transform quickly to the $Cu_{1.96}S$ djurlite phase. But the low chalcocite Cu_2S NCs prepared through electrochemical reduction were surprisingly very stable. The electrochemically synthesized Cu_2S NCs also display unique PL characteristics not typically seen in as-synthesized Cu_2S NCs, though the precise origin of the light emission remains uncertain (Figure 54b).

LSPR modulation through a variety of techniques described in this section allows probing a material to gain fundamental understanding of the electronic and optical nature of the material in NC form. The photocharging experiments allow probing

DOI: 10.1021/acs.chemrev.7b00613
Chem. Rev. 2018, 118, 3121−3207

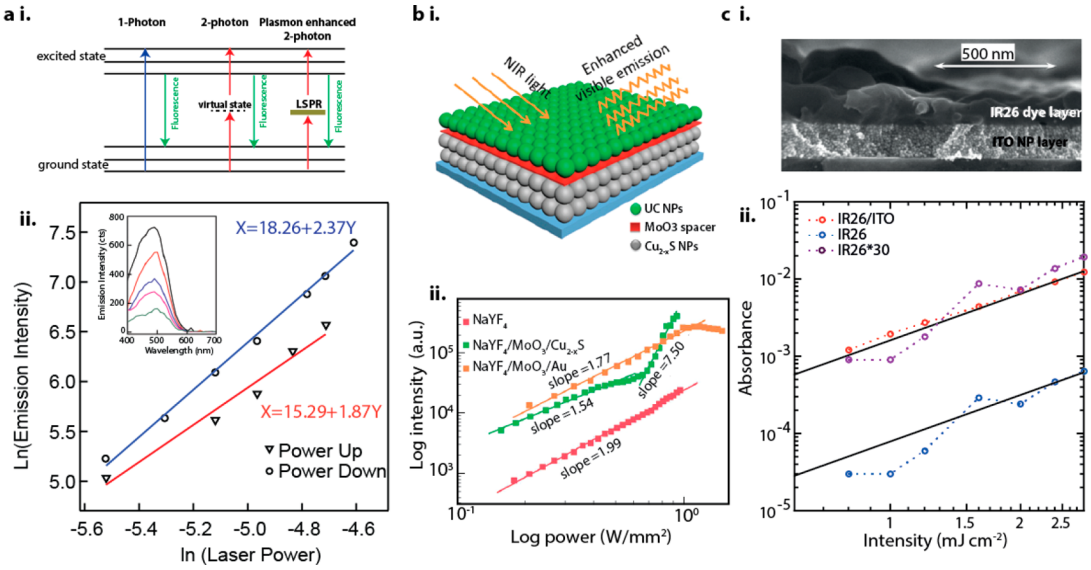

Figure 55. LSPR coupling with electronic transitions. (a) (i) Process of self-upconversion. If the LSPR frequency is at half the energy of an exciton transition, at high power density, CuS undergoes two photon upconversion. (ii) log−log plot showing the power-square dependence of emission. Nonlinear correlation between emission and incident power and slope of 2 on a log−log scale suggests the possibility of 2 photon upconversion. Reprinted from ref 567. Copyright 2016 American Chemical Society. (b) (i) Schematic illustrating the $Cu_{2-x}S$-MoO_3−$NaYF_4$ hybrid structure. $NaYF_4$ is doped with other rare earth ions to act as an upconverter (UCNP) in the scheme. (ii) Power density dependence of integral up conversion luminescence intensity of $NaYF_4$:Yb^{3+},Er^{3+}, Au-MoO_3−$NaYF_4$:Yb^{3+},Er^{3+}, and $Cu_{2-x}S$-MoO_3−$NaYF_4$:Yb^{3+},Er^{3+} ($^4S_{3/2}/^2H_{11/2}$−$^4I_{15/2}$ transitions). At low power density, Au enhances slightly more than $Cu_{2-x}S$ NCs. But at high power, due to direct hole transfer from $Cu_{2-x}S$ to the UCNPs, there is a steep surge in luminescence intensity. Reprinted from ref 169. Copyright 2016 American Chemical Society. (c) (i) SEM cross-sectional image of IR dye (IR26) on a layer of Sn:In_2O_3 NCs. (ii) This system showed 30-fold enhancement in two-photon absorption of the dye in the presence of a Sn:In_2O_3 layer. This increase could be attributed to plasmon-induced near-field enhancement at the dye−NC film interface. Reprinted with permission from ref 168. Copyright 2012 Wiley-VCH.

quantum size effects on optical response, electrochemical charging gives insight into how depletion in semiconductor NCs changes their optical properties and how the electrochemically driven phase changes in WO_3, Nb:TiO_2, or CuS affects optical properties. Research on optical modulation of semiconductor NCs can also lead to the development of interesting technologies such as redox probes, sensors, and smart windows. The work done to date demonstrates the immense promise that plasmonic semiconductor NCs hold, while there remain several open questions that need to be answered to best direct the field and potential future applications. Some of them are as follows. (1) How does the dopant distribution inside the NC affect the modulation characteristics? (2) How do the phase changes in metal chalcogenide or metal oxide materials modify the band structure and thereby properties like plasma frequency and effective mass of the free carriers? (3) How do the electrochemically induced phases in NCs differ from their bulk counterparts?

With these open questions in mind, the next section will focus on several interesting applications that have, at least preliminarily, been demonstrated with plasmonic semiconductor NCs.

5. APPLICATION OF PLASMONIC SEMICONDUCTOR NCS

5.1. Coupling with Other Resonant Processes

High NFE around metallic nanoparticles has been used as a high power excitation source to excite other weak optical transitions such as molecular vibration modes,[205,557−562] Raman modes,[563−565] and electronic transitions.[166,168,566−568] The efficacy of coupling depends on the spectral overlap between NC LSPR and other optical processes. LSPR energies of metallic nanoparticles of size less than 50 nm and of simple geometries such as spheres or faceted shapes like cubes and octahedra are limited to the visible spectrum. This limits the potential for LSPR coupling to other optical processes that occur in the IR spectral range. As we better understand LSPR of semiconductor NCs, improving the optical efficiency of low-energy processes using plasmonic semiconductor NCs holds great promise.

The potential for plasmonic semiconductor NCs to enhance two photon absorption and upconversion, which occur more efficiently within strong electromagnetic fields, has been explored. Increasing the cross section for these processes has the potential to improve the efficiency of light harvesting. Furube et al.[168] studied the transient absorption of a dye coated on a Sn:In_2O_3 NC film. The NIR-absorbing laser dye IR26 was coated on the top of the 100−150 nm thick NC film, which has a LSPR maximum wavelength around 2140 nm. By pumping with a laser of wavelength 2200 nm, a strong transient bleach in the dye absorption occurred in the presence of the NCs compared to no signal from a film of only IR26 (Figure 55c). This observation suggests the NFE of the NCs supported a two photon absorption in the dye that nonplasmon enhanced light of the same power did not induce. On the basis of the pump power dependence of bleaching amplitude, the authors quantified a NFE factor of around 6. Matsui et al.[167] showed similar enhancement of light emission from Er:ZnO by Sn:In_2O_3 NC films.

Recently, Zhou et al.[169] performed studies exploring luminescence upconversion enhancement of $NaYF_4$:Yb^{3+},Er^{3+} upconverting nanoparticles (UCNPs) induced by $Cu_{2-x}S$ NCs. A three-layer structure containing plasmonic $Cu_{2-x}S$ NCs at the bottom, MoO_3 as a separator layer in the middle, and a top layer of UCNPs was fabricated to study the power dependence of red, green, and blue emission from the UCNPs. The authors also compared the performance of $Cu_{2-x}S$ NCs with Au NCs. For

DOI: 10.1021/acs.chemrev.7b00613
Chem. Rev. 2018, 118, 3121−3207

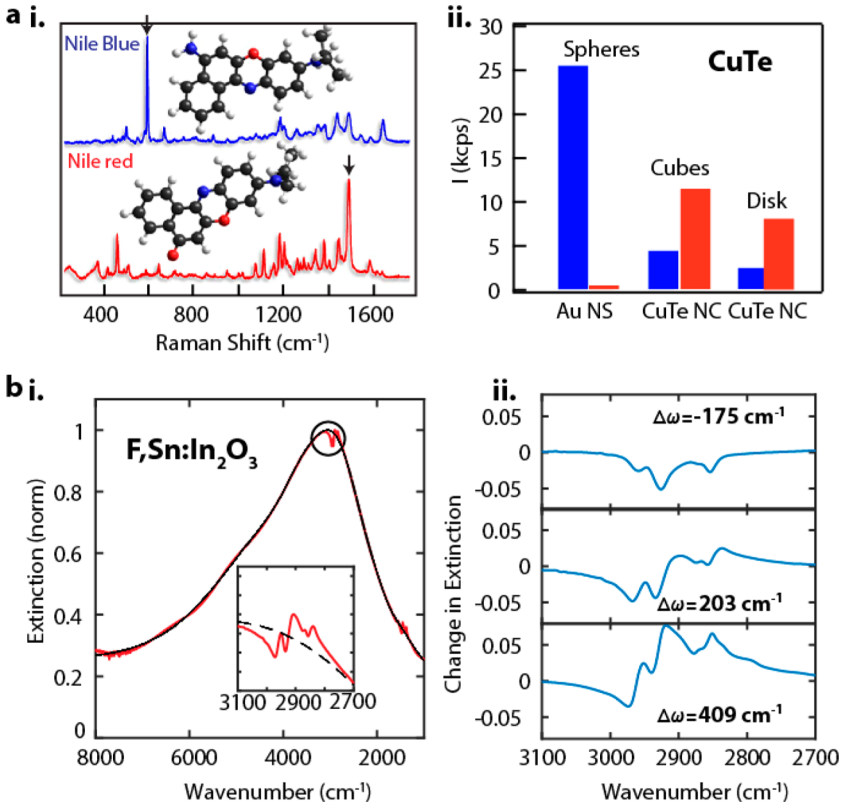

Figure 56. LSPR coupling with molecular vibrational resonances. (a) (i) SERS spectra of Nile blue and Nile red. (ii) The Maximal Nile blue signal enhancement was found to be on Au nanospheres, while the maximal Nile red enhacement was on CuTe nanocubes. Reprinted from ref 170. Copyright 2013 American Chemical Society. (b) (i) A Fano-shaped oleic acid C−H vibration signal superimposed on broader Sn,F codoped In_2O_3 LSPR spectrum is present in the extinction spectrum of a film of 20 nm ligand capped NCs. (ii) The background-subtracted vibrational signal changes from plasmon induced transparency to Fano interference with increase in detuning of the frequencies between the LSPR of the film of 20 nm nanocubes and the oleic acid C−H vibrational resonances. Reprinted from ref 89. Copyright 2017 American Chemical Society.

both Au and $Cu_{2-x}S$, the slope n of log−log plots of emission intensity versus excitation power were around 2 in the low power regime (Figure 55b), indicative of two photon up conversion. In this power regime, Au NPs had higher enhancement compared to $Cu_{2-x}S$ NCs. In contrast, at high power density (>0.7 W/mm^2), the slope for $Cu_{2-x}S$ NCs dramatically increases to 7.0, whereas for Au NPs, the enhancement factor saturated and then started decaying slightly, which was ascribed to detrimental local heating. In the case of $Cu_{2-x}S$, the authors argued that at high power density, the enhancement is not solely driven by LSPR, rather the electrons from valence band of $Cu_{2-x}S$ NPs are excited into the direct conduction band of $Cu_{2-x}S$ through a two-photon process. This excitation passes through the MoO_3 layer to the $NaYF_4$:Yb^{3+},Er^{3+} layer by diffusion. Due to precise energy matching between the band gap of $Cu_{2-x}S$ and the green emission transitions in the $NaYF_4$:Yb^{3+},Er^{3+} layer, the energy is captured by Er^{3+} ions. This process leads to stronger green than red emission and to very different power-dependence of emission in the two spectral bands. Furthermore, the authors supported the occurrence of electron diffusion from the $Cu_{2-x}S$ layer to the $NaYF_4$:Yb^{3+},Er^{3+} layer by investigating the PL decay dynamics of the $Cu_{2-x}S$ film and the $Cu_{2-x}S$-MoO_3−$NaYF_4$:Yb^{3+},Er^{3+} multilayer film. In the multilayer film, the decay time constant of the $Cu_{2-x}S$ decreased from 10.20 to 2.21 ps, which is indicative of nonradiative energy migration from $Cu_{2-x}S$ to the $NaYF_4$:Yb^{3+},Er^{3+} layer. Marin et al.[567] performed a similar study utilizing the unique band structure of covellite phase CuS NCs for plasmon-enhanced 2-photon upconversion. The authors demonstrated that due to the alignment of the CuS band gap at twice the LSPR energy, the CuS displays self-enhanced luminescence (Figure 55a). The upconversion properties associated uniquely with the LSPR and band structure of this copper sulfide material motivate system-specific upconversion studies, despite the fact that the NFE in such materials is lower than that of metallic materials. Moreover, with development of NCs of metal oxides and nitrides capable of stronger NFE, improved luminescent enhancement in coupled systems can be expected.

Surface-enhanced Raman spectroscopy (SERS) is a technique where the scattering cross section of vibrational or rotational transitions of molecules is enhanced due to the presence of metallic objects around the molecules. The signal enhancement originates from chemical pathways as well as electromagnetic field localization around the metallic object. Gold is the most common substrate used for SERS applications.[564] Li et al.[170] explored CuTe as a substrate to detect molecules that cannot be effectively analyzed with Au nanostructures due to poor affinity of certain molecules like ketones toward the metal surface. The authors observed that a ketone-containing molecule, here, Nile red, has much higher signal strength on CuTe NCs compared to Au nanostructures (Figure 56a). However, a molecule containing a positively charged amino group, here Nile blue, which has high affinity toward negatively charged Au nanostructures compared to CuTe NCs, was far more easily detected using Au compared to CuTe NCs. This study showed that in addition to near field strength, specific binding properties of the molecules under

DOI: 10.1021/acs.chemrev.7b00613
Chem. Rev. 2018, 118, 3121−3207

consideration plays an important role in determining the SERS signal strength. In this sense, plasmonic semiconductor NCs offer to complement conventional SERS substrates like Au since the surface chemical bonding with analytes is quite distinct for metal oxides, metal chalcogenides, and classical metals.

Another optical process, mid-IR absorption by molecular vibrational modes, has a low cross section and its coupling to the near field around plasmonic NCs is desirable for enhanced signal detection. The interaction between a molecular vibrational transition and an LSPR is essentially the interference of two oscillating electric dipoles.[559,569] The electromagnetic interference between the plasmonic near field and a molecular bond resonance leads to a Fano resonance, which can be observed in absorption spectra as a molecular vibration lineshapes on top of the broader plasmon feature. The strength and nature of the interaction depends upon the difference between the LSPR and vibrational frequencies, the extent of NFE, and the ratio of LSPR scattering to absorption of the NC material under study.[89,559] Due to better overlap between molecular vibrations and LSPR of semiconductors, especially metal oxides with mid-IR LSPR, higher vibrational signal enhancement is expected compared to Au nanoparticles. Abb et al.[557] studied the effect on the C═O molecular vibration of coupling to LSPR of lithographically patterned Sn:In_2O_3 nanorods with controlled inter-rod spacing and rod length by coating the patterned nanorods with PMMA. The authors observed that the Fano resonance line shape strongly depends on the size and resonance frequency of the nanorods. Recently, Agrawal et al.[89] studied the coupling between C−H stretches of native oleate ligands and the LSPR of NC films of F- and Sn- codoped In_2O_3. The authors systematically varied the dopant density and size of the NCs to study the nature of the molecular vibration signal observed in FTIR transmission spectra as a function of size of the cubic NCs. The results were analyzed with the help of computational modeling by considering the relative optical decay rate through different pathways (i.e., reflection, transmission, and absorption). The energetic offset between the NC LSPR and the molecular vibrational modes was identified as a key parameter controlling coupling. The findings suggested that the pathway for decay of the LSPR energy plays a crucial role in determining the transmission line shape of the coupled system (Figure 56b). This more nuanced interpretation highlights the importance of considerations beyond the NFE and optical detuning, which have usually been considered the sole dominant factors governing the coupling strength and spectroscopic signature of LSPR-coupled molecular vibrations. These foundational works considering coupling of molecular vibrations with LSPR of nanostructured metal oxides show the promise of these materials but leave much to be explored. The effect of dopant distribution, dopant activation, and the spatial orientation of molecular vibrations relative to the NC surface on coupling is largely unknown. Also, the fabrication of optical structures incorporating NCs and utilizing a metal−insulator−metal resonator, as has been done in vapor deposited thin film structures, will be able to offer more sensitive detection capabilities and may enable the direction of energy into specific molecular bonds via near field coupling.[215]

5.2. Photothermal Applications

Localization of intense electromagnetic field inside and around the plasmonic NCs leads strong absorption of far field illumination. The absorbed light is dissipated to the surroundings in the form of heat establishing NCs as local heat sources. The high absorption cross section of plasmonic materials makes them promising candidates for photoacoustic imaging,[158,163,570,571,571−574] photothermal therapy and imaging,[157−159,163,238,537,573−583] perfect IR absorbers,[584] waste heat recovery,[164,585,586] and more.

5.2.1. Biological Applications. LSPR-induced heat-based therapy and imaging have generated much interest, especially for tumor detection and noninvasive treatment. Au or Ag nanoparticles have been used to demonstrate the potential of LSPR-based methodology on the lab scale. Even though Au has high absorption cross section, the use of metallic materials in the human body poses several challenges. Choi et al.[578] argued that gold has an X-ray attenuation coefficient 150-fold higher than bone and can interfere with accurate computed tomographic (CT) scanning in organs such as the liver where nanoparticles eventually accumulate. In order to avoid such accumulation and to promote efficient renal clearance, it has been shown that plasmonic NCs smaller than 5.5 nm are optimal.[578] In this size regime, gold invariably has a plasmon in the visible spectrum, which is outside the first biological transparency window (wavelength from 700 to 950 nm).[587] Semiconductor NCs such as $Cu_{2-x}X$ (X = S, Se, Te), WO_{3-x}, and MoO_{3-x} can all be made at small sizes with an LSPR in the biological transparency window in the NIR. Even though these material have extinction in the appropriate spectral range, due to high electron damping they all have low absorption cross section at their LSPR peak. The low absorption cross section and small NC size less than 5 nm leads to laser power requirement as high as 16−24 W/cm^2, which is 48−72 times higher than the laser intensity limit (0.33 W/cm^2) for human skin exposure.[588] To overcome the limitation of low permissible laser intensity, some researchers[589−591] are developing materials whose absorption is centered in the second NIR window (1000−1350 nm), where the maximum permissible exposure is 1 W/cm^2. As a result, most of the research in recent years is focused on LSPR materials with the following guiding design principles. (1) The absorption cross section in one of the IR biological transparency windows (750−950 nm or 1000−1350 nm) should be maximized. (2) The size of the NCs should be smaller than 5 nm for easy renal clearance. (3) The material should be nontoxic and nonreactive in the human body.

With these guiding principles, some of the semiconductor materials that come close to meeting practical requirements are $Cu_{2-x}S$ NCs with high Cu vacancy concentrations, metal chalcogenide heterostructures, and ultrasmall tungsten oxide NCs. Ding et al.[589] synthesized Au−$Cu_{1.8}S$ core/shell structures that have high extinction in the second NIR window and exhibit 50% higher extinction at 1064 nm compared to the individual components. The heterostructured NCs showed high photothermal transduction efficiency at 37%, large tissue penetration depth and low cytotoxicity. Recently, Zhu et al.[592] used such heterostructures for photothermal therapy and demonstrated that, with the nanoparticles under NIR irradiation (808 nm, 1.5 W/cm^2), tumor volume decreased by 50% in 22 days. The same tumor increased by 2−3 times in absence of NCs. But the use of high power, above therapeutically permissible values, limits the impact of the study for any practical application. Additionally, in all these studies, the size of the heterostructured NCs exceeded 20 nm. Overcoming these limits to a certain extent, Wang et al.[593] worked with 6.5 nm $Cu_{2-x}S$ NCs with LSPR centered at 1300 nm, with which they demonstrated high photothermal therapy efficiency using an 808 nm wavelength laser with power intensity of 0.6 W/cm^2 (Figure 57, panels c and d). Work to further optimize copper sulfide materials for this application are still underway, while at the same time some researchers are exploring

DOI: 10.1021/acs.chemrev.7b00613
Chem. Rev. 2018, 118, 3121−3207

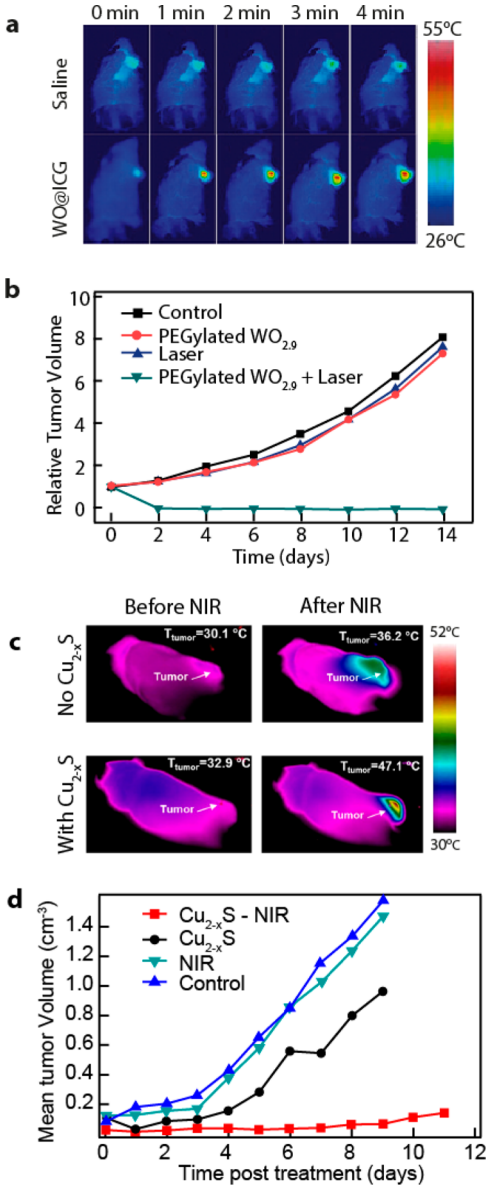

Figure 57. Photothermal therapy and imaging. (a) Photothermal imaging shown with the infrared heat map taken before and after the injection of WO_{3-x} NCs around the tumor site. The time dependence of temperature increase shows the sharp rise in local temperature after the injection of NCs. Reprinted with permission from ref 159. Copyright 2015 JohnWiley & Sons, Inc. (b) The high local heat effectively kills the infected tumor (green), while tumors untreated by NCs under laser illumination continue to grow over a 14 day period. Reprinted with permission from ref 577. Copyright 2015 Nature Publishing Group. (c) Photothermal imaging before and after the injection of $Cu_{2-x}S$ NCs displays the clear difference in local temperature rise after the laser illumination. (d) This temperature rise suppresses tumor growth (red curve) during a 10 day treatment period. Panels c and d are reprinted from ref 593. Copyright 2015 American Chemical Society.

metal oxides like tungsten oxide and molybdenum oxide NCs for such applications.

As the plasmon energy of metal oxide NCs does not depend strongly on size, they can be made at small sizes with an LSPR in the biological transparency window in the IR. Doped tungsten oxide[45,113,577,585] and molybdenum oxide[576] exhibit plasmonic absorption between 500 and 1000 nm wavelength, and thus are promising for such applications. Zhou et al.,[577] Deng et al.,[159] and Wen et al.[594] have recently demonstrated that PEGylated WO_{3-x} rods act as a multifunctionality materials; simultaneously functioning as a CT imaging agent, a photothermal imaging agent, as well as for photothermal therapy purposes. Wen et al.[594] demonstrated that photothermal therapeutic tungsten oxide nanodots (<2 nm) responding to 808 nm light with intensity of 0.75 W/cm^2 can lead to an incremental temperature change of up to 25 °C within 10 min, which induces apoptosis in tumor cells, killing them. Zhou et al.[577] additionally imaged xenografted HeLa tumors in a mouse with a dosage of 20 mg/kg of body weight; the tumor signal was enhanced 60 times in the presence of WO_{3-x} NCs (Figure 57a). Tumor cell viability tests showed a promising decrease in viable cancer cells by more than 80% at moderately low laser power (Figure 57b).[159] Studies also found WO_3 to be nontoxic in the short term, though the long-term implications and lifetime inside the human body are still unknown.

Along with photothermal therapy and imaging, plasmonic materials are also explored as contrast agents for photoacoustic imaging. Photoacoustic imaging is based on the detection of thermoelastic expansion and ultrasonic signals caused by photothermal expansion of light absorbing tissue.[595] The technique combines the molecular specificity of optical imaging with the depth and spatiotemporal resolution of sonography.[595] Gold nanostructures are the most widely used contrast agents for enhancement of photoacoustic imaging. However, gold nanostructures face the same hurdle in this context as they do for photothermal therapy, including low rate of renal clearance for particles sufficiently large to exhibit NIR response, restricting their use as contrast agents for photoacoustic imaging. Ku et al.[596] demonstrated the use of 11 nm CuS NCs with LSPR centered around 950 nm for photoacoustic imaging. The authors used a 1064 nm laser, well within the second IR biological window, to conduct the photoacoustic imaging experiment. In the study, agarose gel containing CuS NCs embedded in chicken breast at a depth of ~5 cm could be imaged with a high in-plane resolution of ~800 μm and a sensitivity of ~0.7 nmol per imaging voxel. These results indicated that it should be possible to image lesions in the human breast at a depth of up to 40 mm with imaging resolution and sensitivity similar to that obtained with CuS NPs in chicken breast muscles. Zha et al.[573] demostrated the change in photoacoustic image sensitivity as a function of depth. The authors acquired tomographic images of an agar gel with embedded CuS NCs in vitro under pieces of chicken breast muscle. The NIR intensity was weakened as the depth of chicken breast muscles increased; however, the five agar objects containing CuS were still clearly visible, retaining on average 14% more photoacoustic signal amplitude over the agar gel background at the maximum depth of 3.2 cm (Figure 58a). Several researchers have demonstrated similar results with CuS NCs.[571,573,574,595−597] Recently, Mou et al.[163] used CuS NCs less than 5 nm in size (below the renal clearance limit) for imaging and therapy applications. Simlar to $Cu_{2-x}S$, WO_{3-x},[594,598] and MoO_{3-x}[158,238,599] NCs with NIR LSPR have also been explored for photoacoustic imaging. Bao et al.[158] observed significant enhancement in ultrasound signal intensity in photoacoustic imaging when PEG-MoO_{3-x} NCs were injected intratumorally (i.t.) (Figure 58b). Recent advances, promise, and drawbacks of semiconductor NCs for biological applications are covered in greater detail in various reviews published in recent years.[588,595,600,601]

5.2.2. Near Field Radiative Heat Transfer. Semiconductor NCs with high absorption cross section in the mid-IR range are

DOI: 10.1021/acs.chemrev.7b00613
Chem. Rev. 2018, 118, 3121−3207

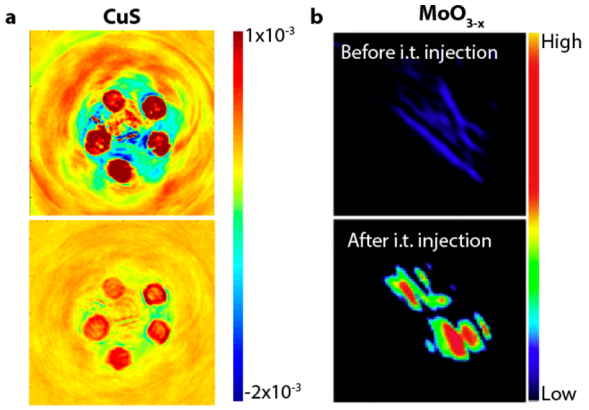

Figure 58. Photoacoustic (PAT) imaging. (a) In vitro PAT images of CuS@Gel−DOX nanoparticles embedded in an agar phantom that was placed under chicken breast muscle at a depth of 0 cm (top) and 1.1 cm (bottom). Reprinted with permission from ref 573. Copyright 2013 Royal Society of Chemistry. (b) In vivo PAT images of tumor sites before and after intratumorally injecting PEG-MoO_{3-x} NCs. High intensity and improved contrast after injection (bottom) is apparent by comparison to the images taken before injection (top). Reprinted with permission from ref 158. Copyright 2016 Elsevier.

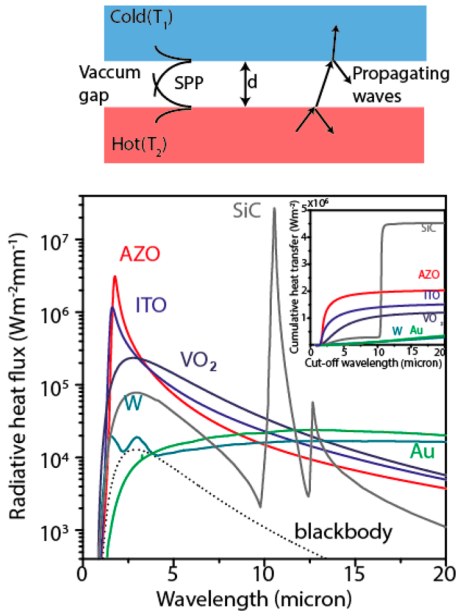

Figure 59. Near field heat transfer. Heat transfer between a hot and a cold body via surface plasmon polariton evanescent wave coupling originating from two surfaces (top). The calculated wavelength-dependent heat flux spectra are shown (bottom) between two bodies with temperatures of 1000 and 360 K and separated by 20 nm gap. The heat flux spectra show that heat flux encompassing the blackbody radiation is higher for metal oxide plasmonic materials compared with Au. Integrated spectra (inset) show that metal oxides might have the highest cumulative heat transfer in the blackbody radiation spectral range. Reprinted with permission from ref 585. Copyright 2015 MDPI AG.

not useful for biological applications, but researchers have been exploring them for waste heat management. Various researchers have proposed enhancing radiative heat transfer between a hot and a cold surface by decreasing the separation between them to less than the wavelength of thermal radiation.[164,585,602] Bringing them closer allows near field heat transfer mediated by surface phonon polaritons or surfaces plasmon polaritons (SPP) to take place; this could substantially increase the heat flux between the hot and cold bodies, which may benefit applications such as waste heat management or thermal photovoltaics. The Chen group,[164,585] spearheading research on this topic, has shown via both modeling and experiments that SPR-meditated heat transfer using metal oxide plasmonic materials such as Al:ZnO or $Sn:In_2O_3$ significantly outperforms conventional plasmonic metals like Au or Ag. The main reason is the significant overlap of metal oxide SPP modes with the thermal radiation from the hot body at 1000 K. By Wein's displacement law, peak thermal radiation from the body at 1000 K is at a wavelength of 2900 nm, in the IR region and far from the energetic range of the Au or Ag SPR edges in the UV or visible region. The thermal radiation excites SPP waves, making possible energy exchange between two surfaces via evanescent coupled SPP waves (Figure 59). For an optimized design for maximum radiative heat flux, significant overlap between the SPP-mediated radiation spectrum and blackbody radiation is desirable. Owing to this consideration, broader plasmons in metal oxides (Al:ZnO, $Sn:In_2O_3$, VO_2), had higher cumulative heat transfer than more conventional surface phonon mediated materials, such as SiC, in the blackbody radiation spectrum range (Figure 59). In addition, using ultrathin films reduces metal oxide dissipation losses, thereby enhancing the efficiency of the heat transfer process. The Chen group further proposed that the use of photonic structures such as a hyperbolic layer stack structures or nanomaterials for enhanced local field and low angular dependence should be studied in detail to improve heat transfer performance. Such devices could enable efficient energy-conversion processes, by creating nonequilibrium between electron and phonon energy distributions in cold films for thermoelectric power conversion.

5.3. Catalysis

Over the past decade, plasmon-enhanced catalysis using Au and Ag nanoparticles has been demonstrated for a wide range of chemical reactions such as water splitting, reduction of CO_2 to form hydrocarbon fuel, or enhancing the rate of reaction of various organic reactions.[171,172,603−605] In general, there are two proposed mechanisms for plasmonic enhancement of photocatalysis: (1) local electric field enhancement or (2) charge transfer due to the generation of hot carriers. With Au NCs that act as both catalyst and LSPR component, the validity of both mechanisms is widely debated and is still under intense investigation. There are only a few studies showing the potential of plasmonic semiconductor NCs for photocatalytic applications. In most studies, metal−semiconductor heterostructures were used by researchers for photocatalysis experiments where metals such as Pd or Pt serve as the catalytic center and semiconductors such as $Cu_{2-x}S$ or WO_{3-x} act as the LSPR component. Cui et al.[144] used $Cu_{1.75}S$−Pd heterostructures to enhance the conversion efficiency of a number of chemical reactions such as the Suzuki coupling reaction between iodobenzene and phenylboronic acid, oxidation of benzyl alcohol, as well as hydrogenation of nitrobenzene. The LSPR spectra of the $Cu_{1.75}S$−Pd heterostructures were centered around 1500 nm. The authors observed that for all three reaction systems, the maximum conversion was observed under 1500 nm laser illumination. For Suzuki reactions, in 30 min, 1500 nm irradiation gave 97% conversion while 808 and 980 nm irradiation gave 45% and 50% conversion, respectively. The authors also performed a series of other control experiments, where direct illumination was eliminated but in all cases

DOI: 10.1021/acs.chemrev.7b00613
Chem. Rev. 2018, 118, 3121−3207

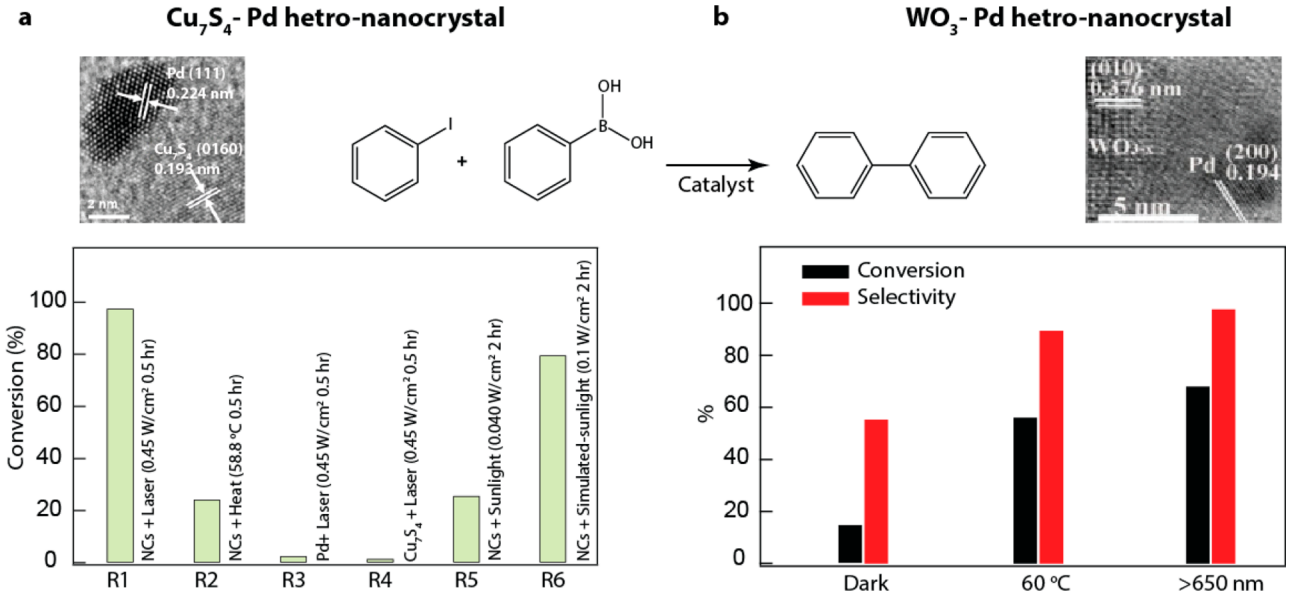

Figure 60. Enhanced photocatalytic activity. Photocatalytic activity of Cu_7S_4–Pd (a) and WO_3–Pd hetero-NCs for the Suzuki coupling reaction of iodobenzene with phenylboronic acid. (a) Conversion using the heterostructure as a catalyst under illumination (both under laser power and simulated sunlight) gave much higher conversion compared with different control catalysts under various catalytic conditions. Reprinted from ref 144. Copyright 2015 American Chemical Society. (b) With the WO_3–Pd heterostructure, conversion is higher under illumination compared to the dark. With WO_3–Pd, higher conversion is attributed to thermal effects since the conversion is similar to that under direct heat. Reprinted with permission from ref 173. Copyright 2016 Elsevier.

conversion efficiency was much lower (Figure 60a). The authors hypothesized that under 1500 nm illumination, high LSPR absorption leads to the formation of hot holes in $Cu_{1.75}S$ NCs that possess enough energy to overcome the Schottky barrier at the $Cu_{1.75}S$–Pd junction and so accumulate in the Pd domain. Accumulation of holes in Pd makes the Pd surface electron deficient, making it positively charged and more conducive for catalytic reaction. In the Suzuki coupling reaction, a positively charged surface promotes and accelerates the rate-limiting oxidation of aryl halides on a Pd surface. Similar to this study, Lou et al.[173] used WO_{3-x}-Pd heterostructures to perform the same Suzuki reaction (Figure 60b). Here, the authors used a broad band light source (wavelength > 650 nm) to drive the reaction. In the presence of WO_{3-x}-Pd heterostructures, the conversion efficiency almost tripled under illumination compared to the reaction performed in the dark. In contrast to the rationale for enhancement provided by Cui et al.,[144] Lou et al.[173] argued that enhanced conversion during LSPR catalysis was purely due to thermal effects. In another study, Manzi et al.[301] showed that under broad band illumination, $Cu_{2-x}S$ nanorods decorated with Pt on their tips serve as a highly selective photocatalyst for reducing CO_2 to CO as the major product and methane as the byproduct, preferentially favored over hydrogen production. Even though the studies discussed here report LSPR-induced catalytic enhancement, the mechanisms behind the observed enhancements are still unknown. With the development of new semiconductor NCs and semiconductor-metal heterostructures, more comprehensive investigation of LSPR-enhanced catalysis could work toward answering following questions. (1) How efficient can low-energy semiconductor LSPR materials be in generating hot carriers that can be useful for photocatalysis? (2) Is it possible to selectively pump energy into specific bonds using resonant, mid-IR LSPR NCs to drive a particular reaction to enhance turnover or to enhance product selectivity? (3) How are "hot hole" materials different from "hot electron" materials in terms of their role in influencing catalytic mechanisms?

5.4. Other Promising Applications

Semiconductor NCs showcasing tunable plasmonics, enhanced near field properties in the IR, high absorption cross section, and the ability to assemble complex nanostructures can open doors to niche applications that are currently limited by the availability of cheap and scalable materials or material processing methods. Dynamic control over the effective refractive index of the NCs film could lead to interesting developments in the field of tunable photonics. Some recent work on metal oxide and silicon thin films suggests the promise of these materials. Introducing metal oxide thin films as the modulator layer has led to the development of tunable nanophotonic modulators and perfect absorber modulators. Lee et al.[606] designed and experimentally demonstrated a plasmonic slot waveguide field effect modulator dubbed a "PlasMOStor." A PlasMOStor is an electrically driven optical modulator, in which the semiconductor (in this case a $Sn:In_2O_3$ waveguide) optical response is modulated by an applied voltage. This voltage leads to the accumulation or depletion of electron concentration near the conducting core-insulating clad interface and results in the modulation of the dielectric function near the interface of the metal oxide layer. This modulation changes the overall energy loss of the waveguide, allowing the output light intensity of the waveguide to be actively controlled. Further improving the modulation speed from the gigahertz to terahertz range, Kinsey et al.[530] used fast recombination dynamics to design an ultrafast epsilon near zero (ENZ) Al:ZnO-based absorption modulator. Moreover, Park et al.[607] designed highly absorbing metal insulator metal (MIM) structures using $Sn:In_2O_3$ as the intermediate active layer. Changing $Sn:In_2O_3$ from dielectric to metallic leads to reflection modulation of up to 15%. The other promising property of semiconductor plasmonics that has generated great interest among researchers is the presence of ENZ modes in

DOI: 10.1021/acs.chemrev.7b00613
Chem. Rev. 2018, 118, 3121–3207

ultrathin nanostructures. Runnerstrom et al.[608] demonstrated the presence of ENZ modes in F:CdO thin films. Earlier, Campione et al.[609−611] developed the theoretical framework explaining ENZ phenomena in ultrathin films.

Considering the promising results produced with semiconductor plasmonic materials in the thin film literature relevant to various telecommunication and photonics applications, future research on applications employing semiconductor plasmonic NCs can be guided by answering the following questions. (1) How does the difference in electromagnetic wave transport in SPR- versus LSPR-based systems affect the applicability of NCs for photonic or telecommunication applications? (2) How will the LSPR mode(s) interact with other possible ENZ or SPR modes if semiconductor films are embedded inside a plasmonic matrix or otherwise integrated? (3) How can the exceptional dynamic tunability properties of semiconductor materials be used to design tunable photonics?

6. CONCLUSION

LSPR in semiconductor NCs has been used to demonstrate the feasibility of a wide range of applications, ranging from photothermal therapy, bioimaging, SERS, SEIRA, enhanced catalysis, metamaterials, redox sensors, ultrafast modulators, and smart windows. The suitability and efficacy of a given LSPR-active semiconductor NC material for any one of these applications, or others not yet imagined, depends on several different factors, starting with the nature of the defects responsible for balancing the charge of the free carriers in the conduction or valence band. LSPR in semiconductors can be tuned based on the chemical principles governing colloidal synthesis by an array of different chemical control strategies involving factors such as dopant choice, reactivity tuning, ligand−NC interactions for surface passivation, ligand−metal interactions in solution, and different synthetic routes used to manipulate reaction and crystallization kinetics. Each one of these control parameters influences the LSPR properties by determining how the dopants interact with the host lattice, the equilibrium free carrier concentration and free carrier spatial distribution in the NC, and morphology of the NC. LSPR of semiconductor NCs is distinguished from LSPR in classical metals in that it can also be strongly modulated post synthetically using chemical, photochemical, and electrochemical control. Although there has been substantial progress made in understanding LSPR in colloidal NCs and its relevance for applications, there remain a number of answered questions relating to each aspect of NC synthesis, physics, modulation, and applications. To conclude this review and provide an outlook on the field, we pose a series of questions that illustrate the potential for interwoven advances in the future.

(i) How does NC surface reconstruction, both the relaxation of atomic positions and bonding with ligands, change the NC LSPR characteristics? What characterization techniques can be used to assess the structure and chemistry of the surface and to quantify the impact of surface reconstruction on band structure thereby on LSPR properties?

(ii) Directly mapping dopant distributions and the local crystallographic environments of dopants in LSPR-active NCs is challenging due to the limited spatial resolution of analytical electron microscopy compounded by the low concentration of dopants. The task may be further challenged for light elements with small cross sections for electron scattering and correspondingly weak X-ray emission and atomic contrast signatures. Further difficulty is found for metal chalcogenide NCs since the metals (most often copper) are highly mobile in the NCs, so the samples are prone to electron beam damage during analysis. How can characterization methods be refined to map dopant and defect distributions so that the impact on LSPR properties can be rigorously understood?

(iii) Related to the characterization challenge highlighted above, the concentration and spatial profile of dopants in LSPR-active NCs may be correlated with the far- and near-field spectral response. How can the dopant type, concentration, and spatial distribution within the NC be utilized to design materials to optimize specific near field and far field optical properties?

(iv) Within a single batch of colloidally synthesized NCs, individual NCs can have more or less subtly varied shape, size, dopant concentration, and dopant distribution. This physiochemical heterogeneity implies that the collective LSPR behavior may likely differ from the properties of each single NC. Given the inevitable heterogeneity, how can we robustly correlate LSPR properties with the structure and chemistry of individual NCs?

(v) Understanding the dominant sources of heterogeneity that impact LSPR properties in colloidally synthesized NCs through advanced characterization may suggest avenues to improve the uniformity of LSPR properties across NCs in the ensemble so that properties can be more rationally understood and tuned. Which NC attributes (e.g., shape, size, dopant concentration, and dopant spatial distribution) dominate the spectral heterogeneity among individual NCs and how can synthetic methods be refined so that particle-to-particle variability of these attributes is minimized?

(vi) Synthesis of LSPR-active NCs on large scale to meet application demands may require innovations in manufacturing techniques to retain quality control. How can industrial scale synthetic and post-treatment strategies be developed while keeping tight control over shape, size, and doping for various large scale applications?

(vii) The surface chemistry of interaction between surfactant ligands and the surface of LSPR-active semiconductor NCs is not well-studied. Surface ligands may influence LSPR behavior, where surface effects can confound interpretation of differences in properties when comparing isolated, dispersed NCs to properties evident in assemblies and thin films of NCs. How do NC surfaces and interfacial chemistries affect the optical and electronic properties of NC assemblies?

(viii) With the recent availability of LSPR-active NCs, how can colloidally synthesized NCs be incorporated into more complex architectures displaying unique optical behavior based on coupling of plasmonic and photonic properties? Opportunities to combine plasmonic semiconductor NCs with other functional NCs that have plasmonic, photoluminescent, magnetic, or upconverting properties have only begun to be explored. How can LSPR-active NCs couple and interact with other classes of NCs, molecules, or other optical components in multicomponent assemblies to give rise to tunable, potentially dynamic optical behavior?

(ix) Practical considerations such as cost, safety, stability, and biocompatibility must be explored in detail for any possible large-scale or biomedical applications. Moreover, a comparative study considering both performance and practicality metrics needs be performed across a wide selection of materials (metal oxides, metal chalcogenides, metal nitrides, silicon, etc.) whose synthesis is achievable by applying the still-developing chemical tool box, so that optimal matches can be made between candidate materials and potential applications.

DOI: 10.1021/acs.chemrev.7b00613
Chem. Rev. 2018, 118, 3121−3207

(x) The band structures and crystal structures of LSPR-active NCs may, with careful study be correlated with their LSPR properties. However, as these materials undergo chemical and electrochemical reactions postsynthetically to modulate their LSPR, how is their physical and electronic structure modified and what are the implications of these changes for understanding their dynamic LSPR response?

The exploration of different types of semiconductor NCs has built a vast library of materials displaying unique LSPR properties. With the rapid pace of advances in the field of semiconductor NC LSPR, in the near future it should be feasible to synthetically construct an optimal semiconductor NC for a given application by choice of dopant, dopant distribution, ligand−NC interaction, shape, and size of the NC. The fundamental understanding of LSPR on the intrinsic, single NC scale will guide the design of large scale tunable photonic, optoelectronic, sensing, and spectroscopy applications.

AUTHOR INFORMATION

Corresponding Author

*E-mail: milliron@che.utexas.edu.

ORCID

Ankit Agrawal: 0000-0001-7311-7873
Sandeep Ghosh: 0000-0002-1149-9199
Delia J. Milliron: 0000-0002-8737-451X

Notes

The authors declare the following competing financial interest(s): DJM has a financial interest in Heliotrope Technologies, a company pursuing commercial development of electrochromic devices.

Biographies

Ankit Agrawal received his Ph.D. in Chemical Engineering at The University of Texas at Austin where he worked on understanding the phenomenon of localized surface plasmon resonance in metal oxide nanocrystals under the supervision of Dr. Delia Milliron. Earlier, he received a Bachelor of Technology and a Master of technology (2008) in Chemical Engineering and a minor in Mathematics and Computing at the Indian Institute of Technology, Kharagpur, India, working under the supervision of Dr. Saikat Chakraborty. He is currently pursuing postdoctoral research under Dr. John B. Goodenough at The University of Texas at Austin, working on developing cathode and electrolyte materials for solid state batteries.

Shin Hum Cho received his B.S. (2015) in Chemical and Biomolecular Engineering and Chemistry at the Korea Advanced Institute of Science and Technology (KAIST), working under the supervision of Dr. Doh Chang Lee in photoemissive quantum dot synthesis. He is a Ph.D. candidate in Chemical Engineering at The University of Texas at Austin, with the guidance of Dr. Delia Milliron under the Fulbright Foreign Student Program (2015−2016). His research focuses on synthetic development of doped plasmonic semiconductor nanocrystals.

Omid Zandi received his Ph.D. in Chemistry from Michigan State University in 2015, where he worked on thin film metal oxide semiconductors for photoelectrochemical water splitting under the advisement of Prof. Thomas W. Hamann. He then joined Prof. Delia J. Milliron's group at the University of Texas at Austin as a Postdoctoral Fellow, where he worked on dynamic electrochemical modulation of LSPR in plasmonic semiconductor nanocrystals for tunable optoelectronics. He is currently employed as a Research Scientist at Tokyo Electron US Technology Development Center in Austin, Texas.

Sandeep Ghosh is a postdoctoral researcher in Delia Milliron's group in the McKetta Department of Chemical Engineering in the University of Texas (UT) at Austin since February 2017. He has a BSc (2004) in Chemistry from Jadavpur University, Kolkata, and received his M.S. (2007) and Ph.D. (2011) in Chemistry from Indian Institute of Science, Bangalore, India. A one year internship stint in 2009 with Izumi Ichinose in the National Institute for Material Science (NIMS), Tsukuba, Japan, comprises part of his Ph.D. studies, where his research was focused on ultrathin polymeric membranes for water filtration. Prior to joining UT, he was a postdoctoral researcher in Istituto Italiano di Tecnologia Genoa, Italy, from 2012−2016 under the mentorship of Liberato Manna, where he researched colloidal inorganic nanocrystals, their growth, transformation, and surface characteristics. His research interests include exploring colloidal semiconductor nanocrystals with regard to the correlation between their internal structure and their optoelectronic properties, with the goal of tweaking the underlying chemistry to arrive at smart functional nanomaterials.

Robert W. Johns received a B.S. in chemistry from the University of Washington, and his Ph.D. in physical chemistry from the University of California, Berkeley. During his graduate work, he was a fellow at the Advanced Light Source at Lawrence Berkeley National Laboratory and focused on developing experimental methods for optical characterization of doped metal oxide nanocrystals using infrared light. He has traveled to do research at the University of Wisconsin, Madison, Université de Genève, Politecnico di Milano, and the University of Texas at Austin. He is continuing to pursue his passion for the growth and analysis of nanoscale semiconductor structures in the Portland Technology Development group at Intel.

Delia J. Milliron is a Professor in the McKetta Department of Chemical Engineering at the University of Texas at Austin. She also serves as an Associate Editor for the journal, *Nano Letters*. Dr. Milliron received her Ph.D. in Chemistry from the University of California, Berkeley, in 2004. From 2004 to 2008 she worked for IBM's research division, initially as a postdoctoral researcher and subsequently as a member of the research staff. In 2008, she joined the research staff at the Molecular Foundry, Lawrence Berkeley National Lab, where she served as the Director of the Inorganic Nanostructures Facility and later as the Deputy Director. Dr. Milliron's awards include a Sloan Research Fellowship, a DOE Early Career award, a Resonate Award from Caltech's Resnick Institute, a Norman Hackerman Award from the Welch Foundation, and the Edith and Peter O'Donnell Award in Engineering from The Academy of Medicine, Engineering & Science of Texas. Her research is motivated by the potential for nanomaterials to introduce new functionality to and reduce manufacturing costs of electrochemical, optical, and electronic materials. Her group's activities span from the fundamental chemistry and assembly pathways of nanomaterials to device integration and characterization.

ACKNOWLEDGMENTS

This research was supported by the National Science Foundation (NSF, CHE-1609656, NASCENT, EEC-1160494, and MRSEC, DMR-1720595) and the Welch Foundation (F-1848). The authors thank Gary K. Ong, Camila A. Saez Cabezas, Lauren J. Reimnitz, Corey M. Staller, Stephen L. Gibbs and Manuel N. Dominguez for help with proof-reading the text and figures.

ABBREVIATIONS

BCC	body-centered cubic
CBM	conduction band minimum
DFT	density functional theory
EDOS	energy density of states
EDS	energy-dispersive X-ray spectroscopy

DOI: 10.1021/acs.chemrev.7b00613
Chem. Rev. 2018, 118, 3121−3207

EIS	electrochemical impedance spectroscopy
ENZ	epsilon near zero
EPR	electron paramagnetic resonance
EXAFS	extended X-ray absorption fine structure
FCC	face-centered cubic
FIR	far infrared
FTIR	Fourier transform infrared
fwhm	full-width half-maximum
HCP	hexagonal close-packed
HSAB	hard and soft acid−base
ICP-AES	inductively coupled plasma-atomic emission spectroscopy
IR	infrared
LSPR	localized surface plasmon resonance
MIR	mid infrared
NC(s)	nanocrystal(s)
NFE	near field enhancement
NIR	near infrared
NMR	nuclear magnetic resonance
PCET	proton coupled electron transfer
PEDOS	partial energy density of states
RBS	Rutherford backscattering spectrometry
SAED	selected area electron diffraction
SEIRA	surface-enhanced infrared absorption
SEM	scanning electron microscopy
SERS	surface-enhanced Raman scattering
SINS	synchrotron infrared nanospectroscopy
SPR	surface plasmon resonance
TEM	transmission electron microscopy
VBM	valence band maximum
XANES	X-ray absorption near edge structure
XAS	X-ray absorption spectroscopy
XPS	X-ray photoelectron spectroscopy
XRD	X-ray diffraction

REFERENCES

(1) Anker, J. N.; Hall, W. P.; Lyandres, O.; Shah, N. C.; Zhao, J.; Van Duyne, R. P. Biosensing with Plasmonic Nanosensors. *Nat. Mater.* **2008**, *7*, 442−453.

(2) Willets, K. A.; Van Duyne, R. P. Localized Surface Plasmon Resonance Spectroscopy and Sensing. *Annu. Rev. Phys. Chem.* **2007**, *58*, 267−297.

(3) Hu, M.; Chen, J.; Li, Z.-Y.; Au, L.; Hartland, G. V.; Li, X.; Marquez, M.; Xia, Y. Gold Nanostructures: Engineering Their Plasmonic Properties for Biomedical Applications. *Chem. Soc. Rev.* **2006**, *35*, 1084.

(4) Giannini, V.; Fernández-Domínguez, A. I.; Heck, S. C.; Maier, S. A. Plasmonic Nanoantennas: Fundamentals and Their Use in Controlling the Radiative Properties of Nanoemitters. *Chem. Rev.* **2011**, *111*, 3888−3912.

(5) Maier, S. A. *Plasmonics: Fundamentals and Applications*; Springer: Boston, MA, 2007.

(6) Trügler, A. *Optical Properties of Metallic Nanoparticles*; Springer International Publishing, 2016.

(7) Cooper, B. R.; Ehrenreich, H.; Philipp, H. R. Optical Properties of Noble Metals. II. *Phys. Rev.* **1965**, *138*, A494−A507.

(8) Naik, G.; Boltasseva, A. Plasmonics and Metamaterials: Looking beyond Gold and Silver. *SPIE Newsroom*, **2012**.10.1117/2.1201201.004077

(9) Naik, G. V.; Shalaev, V. M.; Boltasseva, A. Alternative Plasmonic Materials: Beyond Gold and Silver. *Adv. Mater.* **2013**, *25*, 3264−3294.

(10) Zhong, Y.; Malagari, S. D.; Hamilton, T.; Wasserman, D. M. Review of Mid-Infrared Plasmonic Materials. *J. Nanophotonics* **2015**, *9*, 093791.

(11) Agrawal, A.; Johns, R. W.; Milliron, D. Control of Localized Surface Plasmon Resonances in Metal Oxide Nanocrystals. *Annu. Rev. Mater. Res.* **2017**, *47*, 1−31.

(12) Kriegel, I.; Scotognella, F.; Manna, L. Plasmonic Doped Semiconductor Nanocrystals: Properties, Fabrication, Applications and Perspectives. *Phys. Rep.* **2017**, *674*, 1−52.

(13) Comin, A.; Manna, L. New Materials for Tunable Plasmonic Colloidal Nanocrystals. *Chem. Soc. Rev.* **2014**, *43*, 3957−3975.

(14) Buonsanti, R.; Milliron, D. J. Chemistry of Doped Colloidal Nanocrystals. *Chem. Mater.* **2013**, *25*, 1305−1317.

(15) Owen, J. The Coordination Chemistry of Nanocrystal Surfaces. *Science* **2015**, *347*, 615−616.

(16) Rabenau, A. The Role of Hydrothermal Synthesis in Preparative Chemistry. *Angew. Chem., Int. Ed. Engl.* **1985**, *24*, 1026−1040.

(17) Ho, T.-L. Hard Soft Acids Bases (HSAB) Principle and Organic Chemistry. *Chem. Rev.* **1975**, *75*, 1−20.

(18) Kortshagen, U. R.; Sankaran, R. M.; Pereira, R. N.; Girshick, S. L.; Wu, J. J.; Aydil, E. S. Nonthermal Plasma Synthesis of Nanocrystals: Fundamental Principles, Materials, and Applications. *Chem. Rev.* **2016**, *116*, 11061−11127.

(19) Coughlan, C.; Ibáñez, M.; Dobrozhan, O.; Singh, A.; Cabot, A.; Ryan, K. M. Compound Copper Chalcogenide Nanocrystals. *Chem. Rev.* **2017**, *117*, 5865−6109.

(20) Mattox, T. M.; Ye, X.; Manthiram, K.; Schuck, P. J.; Alivisatos, A. P.; Urban, J. J. Chemical Control of Plasmons in Metal Chalcogenide and Metal Oxide Nanostructures. *Adv. Mater.* **2015**, *27*, 5830−5837.

(21) van der Stam, W.; Berends, A. C.; de Mello Donega, C. Prospects of Colloidal Copper Chalcogenide Nanocrystals. *ChemPhysChem* **2016**, *17*, 559−581.

(22) Guler, U.; Shalaev, V. M.; Boltasseva, A. Nanoparticle Plasmonics: Going Practical with Transition Metal Nitrides. *Mater. Today* **2015**, *18*, 227−237.

(23) Auguié, B.; Barnes, W. L. Collective Resonances in Gold Nanoparticle Arrays. *Phys. Rev. Lett.* **2008**, *101*, 143902.

(24) Genç, A.; Patarroyo, J.; Sancho-Parramon, J.; Arenal, R.; Duchamp, M.; Gonzalez, E. E.; Henrard, L.; Bastús, N. G.; Dunin-Borkowski, R. E.; Puntes, V. F.; et al. Tuning the Plasmonic Response up: Hollow Cuboid Metal Nanostructures. *ACS Photonics* **2016**, *3*, 770−779.

(25) Yang, H. U.; D'Archangel, J.; Sundheimer, M. L.; Tucker, E.; Boreman, G. D.; Raschke, M. B. Optical Dielectric Function of Silver. *Phys. Rev. B: Condens. Matter Mater. Phys.* **2015**, *91*, 235137.

(26) Olmon, R. L.; Slovick, B.; Johnson, T. W.; Shelton, D.; Oh, S.-H.; Boreman, G. D.; Raschke, M. B. Optical Dielectric Function of Gold. *Phys. Rev. B: Condens. Matter Mater. Phys.* **2012**, *86*, 235147.

(27) Shen, Y.; Zhou, J.; Liu, T.; Tao, Y.; Jiang, R.; Liu, M.; Xiao, G.; Zhu, J.; Zhou, Z.-K.; Wang, X.; et al. Plasmonic Gold Mushroom Arrays with Refractive Index Sensing Figures of Merit Approaching the Theoretical Limit. *Nat. Commun.* **2013**, *4*, 2381.

(28) Noguez, C. Surface Plasmons on Metal Nanoparticles: The Influence of Shape and Physical Environment. *J. Phys. Chem. C* **2007**, *111*, 3806−3819.

(29) Kabashin, A. V.; Evans, P.; Pastkovsky, S.; Hendren, W.; Wurtz, G. A.; Atkinson, R.; Pollard, R.; Podolskiy, V. A.; Zayats, A. V. Plasmonic Nanorod Metamaterials for Biosensing. *Nat. Mater.* **2009**, *8*, 867−871.

(30) Wu, C.; Khanikaev, A. B.; Adato, R.; Arju, N.; Yanik, A. A.; Altug, H.; Shvets, G. Fano-Resonant Asymmetric Metamaterials for Ultrasensitive Spectroscopy and Identification of Molecular Monolayers. *Nat. Mater.* **2012**, *11*, 69−75.

(31) Erwin, S. C.; Zu, L.; Haftel, M. I.; Efros, A. L.; Kennedy, T. A.; Norris, D. J. Doping Semiconductor Nanocrystals. *Nature* **2005**, *436*, 91−94.

(32) Liu, Y.; Liu, M.; Swihart, M. T. Plasmonic Copper Sulfide-Based Materials: A Brief Introduction to Their Synthesis, Doping, Alloying, and Applications. *J. Phys. Chem. C* **2017**, *121*, 13435−13447.

(33) Pi, X. D.; Gresback, R.; Liptak, R. W.; Campbell, S. A.; Kortshagen, U. Doping Efficiency, Dopant Location, and Oxidation of Si Nanocrystals. *Appl. Phys. Lett.* **2008**, *92*, 123102.

DOI: 10.1021/acs.chemrev.7b00613
Chem. Rev. 2018, 118, 3121−3207

(34) Schimpf, A. M.; Knowles, K. E.; Carroll, G. M.; Gamelin, D. R. Electronic Doping and Redox-Potential Tuning in Colloidal Semiconductor Nanocrystals. *Acc. Chem. Res.* **2015**, *48*, 1929−1937.
(35) Lounis, S. D.; Runnerstrom, E. L.; Llordés, A.; Milliron, D. J. Defect Chemistry and Plasmon Physics of Colloidal Metal Oxide Nanocrystals. *J. Phys. Chem. Lett.* **2014**, *5*, 1564−1574.
(36) Wang, Y.; Runnerstrom, E. L.; Milliron, D. J. Switchable Materials for Smart Windows. *Annu. Rev. Chem. Biomol. Eng.* **2016**, *7*, 283−304.
(37) Runnerstrom, E. L.; Llordés, A.; Lounis, S. D.; Milliron, D. J. Nanostructured Electrochromic Smart Windows: Traditional Materials and NIR-Selective Plasmonic Nanocrystals. *Chem. Commun.* **2014**, *50*, 10555−10572.
(38) Rinehart, J. D.; Schimpf, A. M.; Weaver, A. L.; Cohn, A. W.; Gamelin, D. R. Photochemical Electronic Doping of Colloidal CdSe Nanocrystals. *J. Am. Chem. Soc.* **2013**, *135* (50), 18782−18785.
(39) Schimpf, A. M.; Ochsenbein, S. T.; Buonsanti, R.; Milliron, D. J.; Gamelin, D. R. Comparison of Extra Electrons in Colloidal n-Type Al^{3+}-Doped and Photochemically Reduced ZnO Nanocrystals. *Chem. Commun.* **2012**, *48*, 9352−9354.
(40) Schimpf, A. M.; Gunthardt, C. E.; Rinehart, J. D.; Mayer, J. M.; Gamelin, D. R. Controlling Carrier Densities in Photochemically Reduced Colloidal ZnO Nanocrystals: Size Dependence and Role of the Hole Quencher. *J. Am. Chem. Soc.* **2013**, *135*, 16569−16577.
(41) Garcia, G.; Buonsanti, R.; Llordes, A.; Runnerstrom, E. L.; Bergerud, A.; Milliron, D. J. Near-Infrared Spectrally Selective Plasmonic Electrochromic Thin Films. *Adv. Opt. Mater.* **2013**, *1*, 215−220.
(42) Luther, J. M.; Jain, P. K.; Ewers, T.; Alivisatos, A. P. Localized Surface Plasmon Resonances Arising from Free Carriers in Doped Quantum Dots. *Nat. Mater.* **2011**, *10*, 361−366.
(43) Dorfs, D.; Härtling, T.; Miszta, K.; Bigall, N. C.; Kim, M. R.; Genovese, A.; Falqui, A.; Povia, M.; Manna, L. Reversible Tunability of the Near-Infrared Valence Band Plasmon Resonance in $Cu_{2-x}Se$ Nanocrystals. *J. Am. Chem. Soc.* **2011**, *133*, 11175−11180.
(44) Kalusniak, S.; Sadofev, S.; Henneberger, F. ZnO as a Tunable Metal: New Types of Surface Plasmon Polaritons. *Phys. Rev. Lett.* **2014**, *112*, 137401.
(45) Manthiram, K.; Alivisatos, A. P. Tunable Localized Surface Plasmon Resonances in Tungsten Oxide Nanocrystals. *J. Am. Chem. Soc.* **2012**, *134*, 3995−3998.
(46) Jain, P. K.; Manthiram, K.; Engel, J. H.; White, S. L.; Faucheaux, J. A.; Alivisatos, A. P. Doped Nanocrystals as Plasmonic Probes of Redox Chemistry. *Angew. Chem., Int. Ed.* **2013**, *52*, 13671−13675.
(47) Bohren, C. F.; Huffman *Absorption and Scattering of Light by Small Particles*; Wiley-VCH, 2007.
(48) Jackson, J. D. *Classical Electrodynamics*, 3rd ed.; Wiley, 2007.
(49) Sihvola, A. H. *Electromagnetic Mixing Formulas and Applications*; IET, 1999.
(50) Mendelsberg, R. J.; Garcia, G.; Milliron, D. J. Extracting Reliable Electronic Properties from Transmission Spectra of Indium Tin Oxide Thin Films and Nanocrystal Films by Careful Application of the Drude Theory. *J. Appl. Phys.* **2012**, *111*, 063515.
(51) Kasic, A.; Schubert, M.; Einfeldt, S.; Hommel, D.; Tiwald, T. E. Free-Carrier and Phonon Properties of n- and p-Type Hexagonal GaN Films Measured by Infrared Ellipsometry. *Phys. Rev. B: Condens. Matter Mater. Phys.* **2000**, *62*, 7365−7377.
(52) Jung, J.; Pedersen, T. G. Analysis of Plasmonic Properties of Heavily Doped Semiconductors Using Full Band Structure Calculations. *J. Appl. Phys.* **2013**, *113*, 114904.
(53) Berggren, K.-F.; Sernelius, B. E.; Engström, L.; Hamberg, I.; Granqvist, C. G. Bandgap Widening in Heavily Sn-Doped In_2O_3. In *Proceedings of the 17th International Conference on the Physics of Semiconductors*; Chadi, J. D., Harrison, W. A., Eds.; Springer: New York, 1985; pp 1051−1054.
(54) Goings, J. J.; Schimpf, A. M.; May, J. W.; Johns, R. W.; Gamelin, D. R.; Li, X. Theoretical Characterization of Conduction-Band Electrons in Photodoped and Aluminum-Doped Zinc Oxide (AZO) Quantum Dots. *J. Phys. Chem. C* **2014**, *118*, 26584−26590.
(55) Mulder, B. J. Optical Properties of Crystals of Cuprous Sulphides (Chalcosite, Djurleite, $Cu_{1.9}S$, and Digenite). *Phys. Status Solidi A* **1972**, *13*, 79−88.
(56) Kim, J.; Agrawal, A.; Krieg, F.; Bergerud, A.; Milliron, D. J. The Interplay of Shape and Crystalline Anisotropies in Plasmonic Semiconductor Nanocrystals. *Nano Lett.* **2016**, *16*, 3879−3884.
(57) Zhang, H.; Zhang, R.; Schramke, K. S.; Bedford, N. M.; Hunter, K.; Kortshagen, U. R.; Nordlander, P. Doped Silicon Nanocrystal Plasmonics. *ACS Photonics* **2017**, *4*, 963−970.
(58) Sachet, E.; Shelton, C. T.; Harris, J. S.; Gaddy, B. E.; Irving, D. L.; Curtarolo, S.; Donovan, B. F.; Hopkins, P. E.; Sharma, P. A.; Sharma, A. L.; et al. Dysprosium-Doped Cadmium Oxide as a Gateway Material for Mid-Infrared Plasmonics. *Nat. Mater.* **2015**, *14*, 414−420.
(59) Runnerstrom, E. L.; Bergerud, A.; Agrawal, A.; Johns, R. W.; Dahlman, C. J.; Singh, A.; Selbach, S. M.; Milliron, D. J. Defect Engineering in Plasmonic Metal Oxide Nanocrystals. *Nano Lett.* **2016**, *16*, 3390−3398.
(60) Lee, J.; Yang, J.; Kwon, S. G.; Hyeon, T. Nonclassical Nucleation and Growth of Inorganic Nanoparticles. *Nat. Rev. Mater.* **2016**, *1*, 16034.
(61) Thanh, N. T. K.; Maclean, N.; Mahiddine, S. Mechanisms of Nucleation and Growth of Nanoparticles in Solution. *Chem. Rev.* **2014**, *114*, 7610−7630.
(62) Chang, J.; Waclawik, E. R. Colloidal Semiconductor Nanocrystals: Controlled Synthesis and Surface Chemistry in Organic Media. *RSC Adv.* **2014**, *4*, 23505−23527.
(63) Fichthorn, K. A. Atomic-Scale Theory and Simulations for Colloidal Metal Nanocrystal Growth. *J. Chem. Eng. Data* **2014**, *59*, 3113−3119.
(64) Wang, Y.; He, J.; Liu, C.; Chong, W. H.; Chen, H. Thermodynamics versus Kinetics in Nanosynthesis. *Angew. Chem., Int. Ed.* **2015**, *54*, 2022−2051.
(65) Xia, Y.; Xia, X.; Peng, H.-C. Shape-Controlled Synthesis of Colloidal Metal Nanocrystals: Thermodynamic versus Kinetic Products. *J. Am. Chem. Soc.* **2015**, *137*, 7947−7966.
(66) Sluydts, M.; De Nolf, K.; Van Speybroeck, V.; Cottenier, S.; Hens, Z. Ligand Addition Energies and the Stoichiometry of Colloidal Nanocrystals. *ACS Nano* **2016**, *10*, 1462−1474.
(67) Morris-Cohen, A. J.; Malicki, M.; Peterson, M. D.; Slavin, J. W. J.; Weiss, E. A. Chemical, Structural, and Quantitative Analysis of the Ligand Shells of Colloidal Quantum Dots. *Chem. Mater.* **2013**, *25*, 1155−1165.
(68) Jansons, A. W.; Hutchison, J. E. Continuous Growth of Metal Oxide Nanocrystals: Enhanced Control of Nanocrystal Size and Radial Dopant Distribution. *ACS Nano* **2016**, *10*, 6942−6951.
(69) Jansons, A. W.; Plummer, L. K.; Hutchison, J. E. Living Nanocrystals. *Chem. Mater.* **2017**, *29*, 5415−5425.
(70) Della Gaspera, E.; Chesman, A. S. R.; van Embden, J.; Jasieniak, J. J. Non-Injection Synthesis of Doped Zinc Oxide Plasmonic Nanocrystals. *ACS Nano* **2014**, *8*, 9154−9163.
(71) Boles, M. A.; Ling, D.; Hyeon, T.; Talapin, D. V. The Surface Science of Nanocrystals. *Nat. Mater.* **2016**, *15*, 141−153.
(72) De Roo, J.; Van den Broeck, F.; De Keukeleere, K.; Martins, J. C.; Van Driessche, I.; Hens, Z. Unravelling the Surface Chemistry of Metal Oxide Nanocrystals, the Role of Acids and Bases. *J. Am. Chem. Soc.* **2014**, *136*, 9650−9657.
(73) Deshmukh, R.; Niederberger, M. Mechanistic Aspects in the Formation, Growth and Surface Functionalization of Metal Oxide Nanoparticles in Organic Solvents. *Chem. - Eur. J.* **2017**, *23*, 8542−8570.
(74) Kim, J.; Ong, G. K.; Wang, Y.; LeBlanc, G.; Williams, T. E.; Mattox, T. M.; Helms, B. A.; Milliron, D. J. Nanocomposite Architecture for Rapid, Spectrally-Selective Electrochromic Modulation of Solar Transmittance. *Nano Lett.* **2015**, *15*, 5574−5579.
(75) Heo, S.; Kim, J.; Ong, G. K.; Milliron, D. J. Template-Free Mesoporous Electrochromic Films on Flexible Substrates from Tungsten Oxide Nanorods. *Nano Lett.* **2017**, *17*, 5756−5761.
(76) Li, J.; Wu, Q.; Wu, J. Synthesis of Nanoparticles via Solvothermal and Hydrothermal Methods. In *Handbook of Nanoparticles*; Aliofkhazraei, M., Ed.; Springer International Publishing, 2016; pp 295−328.

DOI: 10.1021/acs.chemrev.7b00613
Chem. Rev. 2018, 118, 3121−3207

(77) Hodges, J. M.; Morse, J. R.; Fenton, J. L.; Ackerman, J. D.; Alameda, L. T.; Schaak, R. E. Insights into the Seeded-Growth Synthesis of Colloidal Hybrid Nanoparticles. *Chem. Mater.* **2017**, *29*, 106−119.
(78) Lee, K.; Seo, W. S.; Park, J. T. Synthesis and Optical Properties of Colloidal Tungsten Oxide Nanorods. *J. Am. Chem. Soc.* **2003**, *125*, 3408−3409.
(79) Cohn, A. W.; Janßen, N.; Mayer, J. M.; Gamelin, D. R. Photocharging ZnO Nanocrystals: Picosecond Hole Capture, Electron Accumulation, and Auger Recombination. *J. Phys. Chem. C* **2012**, *116*, 20633−20642.
(80) Blanchard, J.; In, M.; Schaudel, B.; Sanchez, C. Hydrolysis and Condensation Reactions of Transition Metal Alkoxides: Calorimetric Study and Evaluation of the Extent of Reaction. *Eur. J. Inorg. Chem.* **1998**, *1998*, 1115−1127.
(81) Zhong, X.; Feng, Y.; Zhang, Y.; Lieberwirth, I.; Knoll, W. Nonhydrolytic Alcoholysis Route to Morphology-Controlled ZnO Nanocrystals. *Small* **2007**, *3*, 1194−1199.
(82) De Roo, J.; Coucke, S.; Rijckaert, H.; De Keukeleere, K.; Sinnaeve, D.; Hens, Z.; Martins, J. C.; Van Driessche, I. Amino Acid-Based Stabilization of Oxide Nanocrystals in Polar Media: From Insight in Ligand Exchange to Solution ^{1}H NMR Probing of Short-Chained Adsorbates. *Langmuir* **2016**, *32*, 1962−1970.
(83) Zhang, Z.; Zhong, X.; Liu, S.; Li, D.; Han, M. Aminolysis Route to Monodisperse Titania Nanorods with Tunable Aspect Ratio. *Angew. Chem., Int. Ed.* **2005**, *44*, 3466−3470.
(84) Buonsanti, R.; Llordes, A.; Aloni, S.; Helms, B. A.; Milliron, D. J. Tunable Infrared Absorption and Visible Transparency of Colloidal Aluminum-Doped Zinc Oxide Nanocrystals. *Nano Lett.* **2011**, *11*, 4706−4710.
(85) Ghosh, S.; Saha, M.; Paul, S.; De, S. K. Shape Controlled Plasmonic Sn Doped CdO Colloidal Nanocrystals: A Synthetic Route to Maximize the Figure of Merit of Transparent Conducting Oxide. *Small* **2017**, *13*, 1602469.
(86) Yang, Y.; Jin, Y.; He, H.; Wang, Q.; Tu, Y.; Lu, H.; Ye, Z. Dopant-Induced Shape Evolution of Colloidal Nanocrystals: The Case of Zinc Oxide. *J. Am. Chem. Soc.* **2010**, *132*, 13381−13394.
(87) Bühler, G.; Thölmann, D.; Feldmann, C. One-Pot Synthesis of Highly Conductive Indium Tin Oxide Nanocrystals. *Adv. Mater.* **2007**, *19*, 2224−2227.
(88) Joo, J.; Chow, B. Y.; Prakash, M.; Boyden, E. S.; Jacobson, J. M. Face-Selective Electrostatic Control of Hydrothermal Zinc Oxide Nanowire Synthesis. *Nat. Mater.* **2011**, *10*, 596−601.
(89) Agrawal, A.; Singh, A.; Yazdi, S.; Singh, A.; Ong, G. K.; Bustillo, K.; Johns, R. W.; Ringe, E.; Milliron, D. J. Resonant Coupling between Molecular Vibrations and Localized Surface Plasmon Resonance of Faceted Metal Oxide Nanocrystals. *Nano Lett.* **2017**, *17*, 2611−2620.
(90) De Roo, J.; Justo, Y.; De Keukeleere, K.; Van den Broeck, F.; Martins, J. C.; Van Driessche, I.; Hens, Z. Carboxylic-Acid-Passivated Metal Oxide Nanocrystals: Ligand Exchange Characteristics of a New Binding Motif. *Angew. Chem.* **2015**, *127*, 6588−6591.
(91) Anderson, N. C.; Hendricks, M. P.; Choi, J. J.; Owen, J. S. Ligand Exchange and the Stoichiometry of Metal Chalcogenide Nanocrystals: Spectroscopic Observation of Facile Metal-Carboxylate Displacement and Binding. *J. Am. Chem. Soc.* **2013**, *135*, 18536−18548.
(92) Gao, M. R.; Xu, Y. F.; Jiang, J.; Yu, S. H. Nanostructured Metal Chalcogenides: Synthesis, Modification, and Applications in Energy Conversion and Storage Devices. *Chem. Soc. Rev.* **2013**, *42*, 2986−3017.
(93) Kershaw, S. V.; Susha, A. S.; Rogach, A. L. Narrow Bandgap Colloidal Metal Chalcogenide Quantum Dots: Synthetic Methods, Heterostructures, Assemblies, Electronic and Infrared Optical Properties. *Chem. Soc. Rev.* **2013**, *42*, 3033−3087.
(94) Ghezelbash, A.; Korgel, B. A. Nickel Sulfide and Copper Sulfide Nanocrystal Synthesis and Polymorphism. *Langmuir* **2005**, *21*, 9451−9456.
(95) Wang, F.; Li, Q.; Lin, L.; Peng, H.; Liu, Z.; Xu, D. Monodisperse Copper Chalcogenide Nanocrystals: Controllable Synthesis and the Pinning of Plasmonic Resonance Absorption. *J. Am. Chem. Soc.* **2015**, *137*, 12006−12012.
(96) Deka, S.; Genovese, A.; Zhang, Y.; Miszta, K.; Bertoni, G.; Krahne, R.; Giannini, C.; Manna, L. Phosphine-Free Synthesis of p-Type Copper(I) Selenide Nanocrystals in Hot Coordinating Solvents. *J. Am. Chem. Soc.* **2010**, *132*, 8912−8914.
(97) Elimelech, O.; Liu, J.; Plonka, A. M.; Frenkel, A. I.; Banin, U. Size Dependence of Doping by a Vacancy Formation Reaction in Copper Sulfide Nanocrystals. *Angew. Chem.* **2017**, *129*, 10471−10476.
(98) Lie, S. Q.; Wang, D. M.; Gao, M. X.; Huang, C. Z. Controllable Copper Deficiency in $Cu_{2-x}Se$ Nanocrystals with Tunable Localized Surface Plasmon Resonance and Enhanced Chemiluminescence. *Nanoscale* **2014**, *6*, 10289−10296.
(99) Zhao, Y.; Pan, H.; Lou, Y.; Qiu, X.; Zhu, J.; Burda, C. Plasmonic $Cu_{2-x}S$ Nanocrystals: Optical and Structural Properties of Copper-Deficient Copper(I) Sulfides. *J. Am. Chem. Soc.* **2009**, *131*, 4253−4261.
(100) Kortshagen, U. R.; Sankaran, R. M.; Pereira, R. N.; Girshick, S. L.; Wu, J. J.; Aydil, E. S. Nonthermal Plasma Synthesis of Nanocrystals: Fundamental Principles, Materials, and Applications. *Chem. Rev.* **2016**, *116*, 11061−11127.
(101) Alvarez Barragan, A.; Ilawe, N. V.; Zhong, L.; Wong, B. M.; Mangolini, L. A Non-Thermal Plasma Route to Plasmonic TiN Nanoparticles. *J. Phys. Chem. C* **2017**, *121*, 2316−2322.
(102) Greenberg, B. L.; Ganguly, S.; Held, J. T.; Kramer, N. J.; Mkhoyan, K. A.; Aydil, E. S.; Kortshagen, U. R. Nonequilibrium-Plasma-Synthesized ZnO Nanocrystals with Plasmon Resonance Tunable via Al Doping and Quantum Confinement. *Nano Lett.* **2015**, *15*, 8162−8169.
(103) Mangolini, L.; Thimsen, E.; Kortshagen, U. High-Yield Plasma Synthesis of Luminescent Silicon Nanocrystals. *Nano Lett.* **2005**, *5*, 655−659.
(104) Thimsen, E.; Kortshagen, U. R.; Aydil, E. S. Plasma Synthesis of Stoichiometric Cu_2S Nanocrystals Stabilized by Oleylamine. *Chem. Commun.* **2014**, *50*, 8346−8349.
(105) Yuan, T. H.; Pi, X. D.; Yang, D. Nonthermal Plasma Synthesized Boron-Doped Germanium Nanocrystals. *IEEE J. Sel. Top. Quantum Electron.* **2017**, *23*, 1−5.
(106) Rowe, D. J.; Jeong, J. S.; Mkhoyan, K. A.; Kortshagen, U. R. Phosphorus-Doped Silicon Nanocrystals Exhibiting Mid-Infrared Localized Surface Plasmon Resonance. *Nano Lett.* **2013**, *13*, 1317−1322.
(107) Kramer, N. J.; Schramke, K. S.; Kortshagen, U. R. Plasmonic Properties of Silicon Nanocrystals Doped with Boron and Phosphorus. *Nano Lett.* **2015**, *15*, 5597−5603.
(108) Ágoston, P.; Erhart, P.; Klein, A.; Albe, K. Geometry, Electronic Structure and Thermodynamic Stability of Intrinsic Point Defects in Indium Oxide. *J. Phys.: Condens. Matter* **2009**, *21*, 455801.
(109) Frank, G.; Köstlin, H. Electrical Properties and Defect Model of Tin-Doped Indium Oxide Layers. *Appl. Phys. A: Solids Surf.* **1982**, *27*, 197−206.
(110) Bhachu, D. S.; Scanlon, D. O.; Sankar, G.; Veal, T. D.; Egdell, R. G.; Cibin, G.; Dent, A. J.; Knapp, C. E.; Carmalt, C. J.; Parkin, I. P. Origin of High Mobility in Molybdenum-Doped Indium Oxide. *Chem. Mater.* **2015**, *27*, 2788−2796.
(111) Donovan, B. F.; Sachet, E.; Maria, J.-P.; Hopkins, P. E. Interplay between Mass-Impurity and Vacancy Phonon Scattering Effects on the Thermal Conductivity of Doped Cadmium Oxide. *Appl. Phys. Lett.* **2016**, *108*, 021901.
(112) Kriegel, I.; Rodríguez-Fernández, J.; Wisnet, A.; Zhang, H.; Waurisch, C.; Eychmüller, A.; Dubavik, A.; Govorov, A. O.; Feldmann, J. Shedding Light on Vacancy-Doped Copper Chalcogenides: Shape-Controlled Synthesis, Optical Properties, and Modeling of Copper Telluride Nanocrystals with Near-Infrared Plasmon Resonances. *ACS Nano* **2013**, *7*, 4367−4377.
(113) Mattox, T. M.; Bergerud, A.; Agrawal, A.; Milliron, D. J. Influence of Shape on the Surface Plasmon Resonance of Tungsten Bronze Nanocrystals. *Chem. Mater.* **2014**, *26*, 1779−1784.
(114) Hwang, J. Point Defects and Electrical Properties of Sn-Doped In-Based Transparent Conducting Oxides. *Solid State Ionics* **2000**, *129*, 135−144.
(115) Taha, M. K. H.; Boisron, O.; Canut, B.; Melinon, P.; Penuelas, J.; Gendry, M.; Masenelli, B. Control of the Compensating Defects in Al-

DOI: 10.1021/acs.chemrev.7b00613
Chem. Rev. 2018, 118, 3121−3207

Doped and Ga-Doped ZnO Nanocrystals for MIR Plasmonics. *RSC Adv.* **2017**, *7*, 28677−28683.
(116) Robertson, J.; Clark, S. J. Limits to Doping in Oxides. *Phys. Rev. B: Condens. Matter Mater. Phys.* **2011**, *83*, 075205.
(117) Jansons, A. W.; Koskela, K. M.; Crockett, B. M.; Hutchison, J. E. Transition Metal-Doped Metal Oxide Nanocrystals: Efficient Substitutional Doping Through a Continuous Growth Process. *Chem. Mater.* **2017**, *29*, 8167−8176.
(118) Pearson, R. G. Hard and Soft Acids and Bases, HSAB, Part II: Underlying Theories. *J. Chem. Educ.* **1968**, *45*, 643.
(119) Pearson, R. G. Recent Advances in the Concept of Hard and Soft Acids and Bases. *J. Chem. Educ.* **1987**, *64*, 561.
(120) Pearson, R. G. Hard and Soft Acids and Bases, HSAB, Part 1: Fundamental Principles. *J. Chem. Educ.* **1968**, *45*, 581.
(121) Crockett, B. M.; Jansons, A. W.; Koskela, K. M.; Johnson, D. W.; Hutchison, J. E. Radial Dopant Placement for Tuning Plasmonic Properties in Metal Oxide Nanocrystals. *ACS Nano* **2017**, *11*, 7719−7728.
(122) Ye, X.; Fei, J.; Diroll, B. T.; Paik, T.; Murray, C. B. Expanding the Spectral Tunability of Plasmonic Resonances in Doped Metal-Oxide Nanocrystals through Cooperative Cation−Anion Codoping. *J. Am. Chem. Soc.* **2014**, *136*, 11680−11686.
(123) Diroll, B. T.; Gordon, T. R.; Gaulding, E. A.; Klein, D. R.; Paik, T.; Yun, H. J.; Goodwin, E. D.; Damodhar, D.; Kagan, C. R.; Murray, C. B. Synthesis of n-Type Plasmonic Oxide Nanocrystals and the Optical and Electrical Characterization of Their Transparent Conducting Films. *Chem. Mater.* **2014**, *26*, 4579−4588.
(124) Gordon, T. R.; Paik, T.; Klein, D. R.; Naik, G. V.; Caglayan, H.; Boltasseva, A.; Murray, C. B. Shape-Dependent Plasmonic Response and Directed Self-Assembly in a New Semiconductor Building Block, Indium-Doped Cadmium Oxide (ICO). *Nano Lett.* **2013**, *13*, 2857−2863.
(125) Gerlach, E. Carrier Scattering and Transport in Semiconductors Treated by the Energy-Loss Method. *J. Phys. C: Solid State Phys.* **1986**, *19*, 4585.
(126) Johns, R. W.; Bechtel, H. A.; Runnerstrom, E. L.; Agrawal, A.; Lounis, S. D.; Milliron, D. J. Direct Observation of Narrow Mid-Infrared Plasmon Linewidths of Single Metal Oxide Nanocrystals. *Nat. Commun.* **2016**, *7*, 11583.
(127) Du, W.; Qian, X.; Ma, X.; Gong, Q.; Cao, H.; Yin, J. Shape-Controlled Synthesis and Self-Assembly of Hexagonal Covellite (CuS) Nanoplatelets. *Chem. - Eur. J.* **2007**, *13*, 3241−3247.
(128) Gordon, T. R.; Cargnello, M.; Paik, T.; Mangolini, F.; Weber, R. T.; Fornasiero, P.; Murray, C. B. Nonaqueous Synthesis of TiO_2 Nanocrystals Using TiF_4 to Engineer Morphology, Oxygen Vacancy Concentration, and Photocatalytic Activity. *J. Am. Chem. Soc.* **2012**, *134*, 6751−6761.
(129) Liu, G.; Yang, H. G.; Pan, J.; Yang, Y. Q.; Lu, G. Q.; Cheng, H.-M. Titanium Dioxide Crystals with Tailored Facets. *Chem. Rev.* **2014**, *114*, 9559−9612.
(130) Shieh, F.; Saunders, A. E.; Korgel, B. A. General Shape Control of Colloidal CdS, CdSe, CdTe Quantum Rods and Quantum Rod Heterostructures. *J. Phys. Chem. B* **2005**, *109*, 8538−8542.
(131) Chang, J.; Waclawik, E. R. Experimental and Theoretical Investigation of Ligand Effects on the Synthesis of ZnO Nanoparticles. *J. Nanopart. Res.* **2012**, *14*, 1012.
(132) Yu, W. W.; Wang, Y. A.; Peng, X. Formation and Stability of Size-, Shape-, and Structure-Controlled CdTe Nanocrystals: Ligand Effects on Monomers and Nanocrystals. *Chem. Mater.* **2003**, *15*, 4300−4308.
(133) Ahmed, I.; Khoo, E. H.; Kurniawan, O.; Li, E. P. Modeling and Simulation of Active Plasmonics with the FDTD Method by Using Solid State and Lorentz−Drude Dispersive Model. *J. Opt. Soc. Am. B* **2011**, *28*, 352−359.
(134) Colas des Francs, G.; Derom, S.; Vincent, R.; Bouhelier, A.; Dereux, A. Mie Plasmons: Modes Volumes, Quality Factors, and Coupling Strengths (Purcell Factor) to a Dipolar Emitter. *Int. J. Opt.* **2012**, *2012*, No. e175162.
(135) Agrawal, A.; Kriegel, I.; Milliron, D. J. Shape-Dependent Field Enhancement and Plasmon Resonance of Oxide Nanocrystals. *J. Phys. Chem. C* **2015**, *119*, 6227−6238.
(136) Tandon, B.; Shanker, G. S.; Nag, A. Multifunctional Sn- and Fe-Codoped In_2O_3 Colloidal Nanocrystals: Plasmonics and Magnetism. *J. Phys. Chem. Lett.* **2014**, *5*, 2306−2311.
(137) Tandon, B.; Yadav, A.; Nag, A. Delocalized Electrons Mediated Magnetic Coupling in Mn−Sn Codoped In_2O_3 Nanocrystals: Plasmonics Shows the Way. *Chem. Mater.* **2016**, *28*, 3620−3624.
(138) Wang, Y.; Chen, Z.; Shen, R.; Cao, X.; Chen, Y.; Chen, C.; Wang, D.; Peng, Q.; Li, Y. Pd-Dispersed CuS Hetero-Nanoplates for Selective Hydrogenation of Phenylacetylene. *Nano Res.* **2016**, *9*, 1209−1219.
(139) Ding, X.; Zou, Y.; Jiang, J. Au−Cu_2S Heterodimer Formation via Oxidization of AuCu Alloy Nanoparticles and in Situ Formed Copper Thiolate. *J. Mater. Chem.* **2012**, *22*, 23169−23174.
(140) Wu, H.; Chen, O.; Zhuang, J.; Lynch, J.; LaMontagne, D.; Nagaoka, Y.; Cao, Y. C. Formation of Heterodimer Nanocrystals: UO_2/In_2O_3 and FePt/In_2O_3. *J. Am. Chem. Soc.* **2011**, *133*, 14327−14337.
(141) Ding, X.; Zou, Y.; Ye, F.; Yang, J.; Jiang, J. Pt−CuS Heterodimers by Sulfidation of CuPt Alloy Nanoparticles and Their Selective Catalytic Activity toward Methanol Oxidation. *J. Mater. Chem. A* **2013**, *1*, 11880−11886.
(142) Ha, D.-H.; Caldwell, A. H.; Ward, M. J.; Honrao, S.; Mathew, K.; Hovden, R.; Koker, M. K. A.; Muller, D. A.; Hennig, R. G.; Robinson, R. D. Solid−Solid Phase Transformations Induced through Cation Exchange and Strain in 2D Heterostructured Copper Sulfide Nanocrystals. *Nano Lett.* **2014**, *14*, 7090−7099.
(143) Kumar, D. R.; Manoj, D.; Santhanalakshmi, J. Au−ZnO Bullet-like Heterodimer Nanoparticles: Synthesis and Use for Enhanced Nonenzymatic Electrochemical Determination of Glucose. *RSC Adv.* **2014**, *4*, 8943−8952.
(144) Cui, J.; Li, Y.; Liu, L.; Chen, L.; Xu, J.; Ma, J.; Fang, G.; Zhu, E.; Wu, H.; Zhao, L.; et al. Near-Infrared Plasmonic-Enhanced Solar Energy Harvest for Highly Efficient Photocatalytic Reactions. *Nano Lett.* **2015**, *15*, 6295−6301.
(145) Mendelsberg, R. J.; McBride, P. M.; Duong, J. T.; Bailey, M. J.; Llordes, A.; Milliron, D. J.; Helms, B. A. Dispersible Plasmonic Doped Metal Oxide Nanocrystal Sensors That Optically Track Redox Reactions in Aqueous Media with Single-Electron Sensitivity. *Adv. Opt. Mater.* **2015**, *3*, 1293−1300.
(146) Kriegel, I.; Jiang, C.; Rodríguez-Fernández, J.; Schaller, R. D.; Talapin, D. V.; da Como, E.; Feldmann, J. Tuning the Excitonic and Plasmonic Properties of Copper Chalcogenide Nanocrystals. *J. Am. Chem. Soc.* **2012**, *134*, 1583−1590.
(147) Kriegel, I.; Urso, C.; Viola, D.; De Trizio, L.; Scotognella, F.; Cerullo, G.; Manna, L. Ultrafast Photodoping and Plasmon Dynamics in Fluorine−Indium Codoped Cadmium Oxide Nanocrystals for All-Optical Signal Manipulation at Optical Communication Wavelengths. *J. Phys. Chem. Lett.* **2016**, *7*, 3873−3881.
(148) Carroll, G. M.; Schimpf, A. M.; Tsui, E. Y.; Gamelin, D. R. Redox Potentials of Colloidal n-Type ZnO Nanocrystals: Effects of Confinement, Electron Density, and Fermi-Level Pinning by Aldehyde Hydrogenation. *J. Am. Chem. Soc.* **2015**, *137*, 11163−11169.
(149) Schimpf, A. M.; Lounis, S. D.; Runnerstrom, E. L.; Milliron, D. J.; Gamelin, D. R. Redox Chemistries and Plasmon Energies of Photodoped In_2O_3 and Sn-Doped In_2O_3 (ITO) Nanocrystals. *J. Am. Chem. Soc.* **2015**, *137*, 518−524.
(150) Valdez, C. N.; Braten, M.; Soria, A.; Gamelin, D. R.; Mayer, J. M. Effect of Protons on the Redox Chemistry of Colloidal Zinc Oxide Nanocrystals. *J. Am. Chem. Soc.* **2013**, *135*, 8492−8495.
(151) Garcia, G.; Buonsanti, R.; Runnerstrom, E. L.; Mendelsberg, R. J.; Llordes, A.; Anders, A.; Richardson, T. J.; Milliron, D. J. Dynamically Modulating the Surface Plasmon Resonance of Doped Semiconductor Nanocrystals. *Nano Lett.* **2011**, *11*, 4415−4420.
(152) Llordés, A.; Garcia, G.; Gazquez, J.; Milliron, D. J. Tunable Near-Infrared and Visible-Light Transmittance in Nanocrystal-in-Glass Composites. *Nature* **2013**, *500*, 323−326.
(153) Zandi, O.; Agrawal, A.; Shearer, A. B.; Gilbert, L. C.; Dahlman, C. J.; Staller, C. M.; Milliron, D. J. Impacts of Surface Depletion on the

DOI: 10.1021/acs.chemrev.7b00613
Chem. Rev. 2018, 118, 3121−3207

Plasmonic Properties of Doped Semiconductor Nanocrystals. arXiv:1709.07136v2, 2017.
(154) Dahlman, C. J.; Tan, Y.; Marcus, M. A.; Milliron, D. J. Spectroelectrochemical Signatures of Capacitive Charging and Ion Insertion in Doped Anatase Titania Nanocrystals. *J. Am. Chem. Soc.* **2015**, *137*, 9160−9166.
(155) Babicheva, V. E.; Boltasseva, A.; Lavrinenko, A. V. Transparent Conducting Oxides for Electro-Optical Plasmonic Modulators. *Nanophotonics* **2015**, *4*, 165−185.
(156) Kinsey, N.; Ferrera, M.; Shalaev, V. M.; Boltasseva, A. Examining Nanophotonics for Integrated Hybrid Systems: A Review of Plasmonic Interconnects and Modulators Using Traditional and Alternative Materials. *J. Opt. Soc. Am. B* **2015**, *32*, 121.
(157) Wu, D.; Duan, J.; Zhang, C.; Guo, K.; Zhu, H. Sacrificial Template Synthesis and Photothermal Conversion Enhancements of Hierarchical and Hollow $CuInS_2$ Microspheres. *J. Phys. Chem. C* **2013**, *117*, 9121−9128.
(158) Bao, T.; Yin, W.; Zheng, X.; Zhang, X.; Yu, J.; Dong, X.; Yong, Y.; Gao, F.; Yan, L.; Gu, Z.; et al. One-Pot Synthesis of PEGylated Plasmonic MoO_{3-x} Hollow Nanospheres for Photoacoustic Imaging Guided Chemo-Photothermal Combinational Therapy of Cancer. *Biomaterials* **2016**, *76*, 11−24.
(159) Deng, K.; Hou, Z.; Deng, X.; Yang, P.; Li, C.; Lin, J. Enhanced Antitumor Efficacy by 808 nm Laser-Induced Synergistic Photothermal and Photodynamic Therapy Based on a Indocyanine-Green-Attached $W_{18}O_{49}$ Nanostructure. *Adv. Funct. Mater.* **2015**, *25*, 7280−7290.
(160) Dou, K.; Zhu, W.; Zou, Y.; Gu, Y.; Li, J.; Zhang, S.; Liu, Z.; Zeng, H. Metallic Oxide Nanocrystals with Near-Infrared Plasmon Resonance for Efficient, Stable and Biocompatible Photothermal Cancer Therapy. *J. Mater. Chem. B* **2017**, *5*, 7393−7402.
(161) Hessel, C. M.; Pattani, V. P.; Rasch, M.; Panthani, M. G.; Koo, B.; Tunnell, J. W.; Korgel, B. A. Copper Selenide Nanocrystals for Photothermal Therapy. *Nano Lett.* **2011**, *11*, 2560−2566.
(162) Li, Y.; Lu, W.; Huang, Q.; Li, C.; Chen, W. Copper Sulfide Nanoparticles for Photothermal Ablation of Tumor Cells. *Nanomedicine* **2010**, *5*, 1161−1171.
(163) Mou, J.; Li, P.; Liu, C.; Xu, H.; Song, L.; Wang, J.; Zhang, K.; Chen, Y.; Shi, J.; Chen, H. Ultrasmall $Cu_{2-X}S$ Nanodots for Highly Efficient Photoacoustic Imaging-Guided Photothermal Therapy. *Small* **2015**, *11*, 2275−2283.
(164) Boriskina, S. V.; Ghasemi, H.; Chen, G. Plasmonic Materials for Energy: From Physics to Applications. *Mater. Today* **2013**, *16*, 375−386.
(165) Boyuk, D. S.; Chou, L.-W.; Filler, M. A. Strong Near-Field Coupling of Plasmonic Resonators Embedded in Si Nanowires. *ACS Photonics* **2016**, *3*, 184−189.
(166) Fofang, N. T.; Park, T.-H.; Neumann, O.; Mirin, N. A.; Nordlander, P.; Halas, N. J. Plexcitonic Nanoparticles: Plasmon−Exciton Coupling in Nanoshell−J-Aggregate Complexes. *Nano Lett.* **2008**, *8*, 3481−3487.
(167) Matsui, H.; Badalawa, W.; Hasebe, T.; Furuta, S.; Nomura, W.; Yatsui, T.; Ohtsu, M.; Tabata, H. Coupling of Er Light Emissions to Plasmon Modes on In_2O_3: Sn Nanoparticle Sheets in the near-Infrared Range. *Appl. Phys. Lett.* **2014**, *105*, 041903.
(168) Furube, A.; Yoshinaga, T.; Kanehara, M.; Eguchi, M.; Teranishi, T. Electric-Field Enhancement Inducing Near-Infrared Two-Photon Absorption in an Indium−Tin Oxide Nanoparticle Film. *Angew. Chem., Int. Ed.* **2012**, *51*, 2640−2642.
(169) Zhou, D.; Liu, D.; Xu, W.; Yin, Z.; Chen, X.; Zhou, P.; Cui, S.; Chen, Z.; Song, H. Observation of Considerable Upconversion Enhancement Induced by $Cu_{2-x}S$ Plasmon Nanoparticles. *ACS Nano* **2016**, *10*, 5169−5179.
(170) Li, W.; Zamani, R.; Rivera Gil, P.; Pelaz, B.; Ibáñez, M.; Cadavid, D.; Shavel, A.; Alvarez-Puebla, R. A.; Parak, W. J.; Arbiol, J.; et al. CuTe Nanocrystals: Shape and Size Control, Plasmonic Properties, and Use as SERS Probes and Photothermal Agents. *J. Am. Chem. Soc.* **2013**, *135*, 7098−7101.
(171) Hou, W.; Cronin, S. B. A Review of Surface Plasmon Resonance-Enhanced Photocatalysis. *Adv. Funct. Mater.* **2013**, *23*, 1612−1619.
(172) Kim, S. M.; Lee, S. W.; Moon, S. Y.; Park, J. Y. The Effect of Hot Electrons and Surface Plasmons on Heterogeneous Catalysis. *J. Phys.: Condens. Matter* **2016**, *28*, 254002.
(173) Lou, Z.; Gu, Q.; Liao, Y.; Yu, S.; Xue, C. Promoting Pd-Catalyzed Suzuki Coupling Reactions through near-Infrared Plasmon Excitation of WO_{3-x} Nanowires. *Appl. Catal., B* **2016**, *184*, 258−263.
(174) Draine, B. T.; Flatau, P. J. Discrete-Dipole Approximation For Scattering Calculations. *J. Opt. Soc. Am. A* **1994**, *11*, 1491−1499.
(175) Yurkin, M. A.; Hoekstra, A. G. The Discrete Dipole Approximation: An Overview and Recent Developments. *J. Quant. Spectrosc. Radiat. Transfer* **2007**, *106*, 558−589.
(176) Burger, S.; Zschiedrich, L.; Pomplun, J.; Schmidt, F. Finite Element Method for Accurate 3D Simulation of Plasmonic Waveguides. *Proc. SPIE* **2010**, *7604*, 76040.
(177) Khoury, C. G.; Norton, S. J.; Vo-Dinh, T. Plasmonics of 3-D Nanoshell Dimers Using Multipole Expansion and Finite Element Method. *ACS Nano* **2009**, *3*, 2776−2788.
(178) Musa, M. S. *Computational Nanophotonics: Modeling and Applications*; CRC Press, 2017.
(179) Waxenegger, J.; Trügler, A.; Hohenester, U. Plasmonics Simulations with the MNPBEM Toolbox: Consideration of Substrates and Layer Structures. *Comput. Phys. Commun.* **2015**, *193*, 138−150.
(180) Hao, E.; Schatz, G. C. Electromagnetic Fields around Silver Nanoparticles and Dimers. *J. Chem. Phys.* **2004**, *120*, 357.
(181) Wiley, B. J.; Chen, Y.; McLellan, J. M.; Xiong, Y.; Li, Z.-Y.; Ginger, D.; Xia, Y. Synthesis and Optical Properties of Silver Nanobars and Nanorice. *Nano Lett.* **2007**, *7*, 1032−1036.
(182) Myroshnychenko, V.; Rodríguez-Fernández, J.; Pastoriza-Santos, I.; Funston, A. M.; Novo, C.; Mulvaney, P.; Liz-Marzán, L. M.; García de Abajo, F. J. Modelling the Optical Response of Gold Nanoparticles. *Chem. Soc. Rev.* **2008**, *37*, 1792.
(183) Hamberg, I.; Granqvist, C. G. Evaporated Sn-doped In_2O_3 Films: Basic Optical Properties and Applications to Energy-efficient Windows. *J. Appl. Phys.* **1986**, *60*, R123−R160.
(184) Li, S. Q.; Guo, P.; Zhang, L.; Zhou, W.; Odom, T. W.; Seideman, T.; Ketterson, J. B.; Chang, R. P. H. Infrared Plasmonics with Indium−Tin-Oxide Nanorod Arrays. *ACS Nano* **2011**, *5*, 9161−9170.
(185) Brewer, S. H.; Franzen, S. Calculation of the Electronic and Optical Properties of Indium Tin Oxide by Density Functional Theory. *Chem. Phys.* **2004**, *300*, 285−293.
(186) Zhu, Y.; Mendelsberg, R. J.; Zhu, J.; Han, J.; Anders, A. Structural, Optical, and Electrical Properties of Indium-Doped Cadmium Oxide Films Prepared by Pulsed Filtered Cathodic Arc Deposition. *J. Mater. Sci.* **2013**, *48*, 3789−3797.
(187) Mendelsberg, R. J.; Zhu, Y.; Anders, A. Determining the Nonparabolicity Factor of the CdO Conduction Band Using Indium Doping and the Drude Theory. *J. Phys. D: Appl. Phys.* **2012**, *45*, 425302.
(188) Mulder, B. J. Optical Properties and Energy Band Scheme of Cuprous Sulphides with Ordered and Disordered Copper Ions. *Phys. Status Solidi A* **1973**, *18*, 633−638.
(189) Xie, Y.; Carbone, L.; Nobile, C.; Grillo, V.; D'Agostino, S.; Della Sala, F.; Giannini, C.; Altamura, D.; Oelsner, C.; Kryschi, C.; et al. Metallic-like Stoichiometric Copper Sulfide Nanocrystals: Phase- and Shape-Selective Synthesis, Near-Infrared Surface Plasmon Resonance Properties, and Their Modeling. *ACS Nano* **2013**, *7*, 7352−7369.
(190) Chou, L.-W.; Filler, M. A. Engineering Multimodal Localized Surface Plasmon Resonances in Silicon Nanowires. *Angew. Chem.* **2013**, *125*, 8237−8241.
(191) Rycenga, M.; Cobley, C. M.; Zeng, J.; Li, W.; Moran, C. H.; Zhang, Q.; Qin, D.; Xia, Y. Controlling the Synthesis and Assembly of Silver Nanostructures for Plasmonic Applications. *Chem. Rev.* **2011**, *111*, 3669−3712.
(192) Mulvihill, M. J.; Ling, X. Y.; Henzie, J.; Yang, P. Anisotropic Etching of Silver Nanoparticles for Plasmonic Structures Capable of Single-Particle SERS. *J. Am. Chem. Soc.* **2010**, *132*, 268−274.
(193) Gansel, J. K.; Thiel, M.; Rill, M. S.; Decker, M.; Bade, K.; Saile, V.; von Freymann, G.; Linden, S.; Wegener, M. Gold Helix Photonic Metamaterial as Broadband Circular Polarizer. *Science* **2009**, *325*, 1513−1515.

DOI: 10.1021/acs.chemrev.7b00613
Chem. Rev. 2018, 118, 3121−3207

(194) Pors, A.; Willatzen, M.; Albrektsen, O.; Bozhevolnyi, S. I. From Plasmonic Nanoantennas to Split-Ring Resonators: Tuning Scattering Strength. *J. Opt. Soc. Am. B* **2010**, *27*, 1680−1687.
(195) Lounis, S. D.; Runnerstrom, E. L.; Bergerud, A.; Nordlund, D.; Milliron, D. J. Influence of Dopant Distribution on the Plasmonic Properties of Indium Tin Oxide Nanocrystals. *J. Am. Chem. Soc.* **2014**, *136*, 7110−7116.
(196) Faucheaux, J. A.; Jain, P. K. Plasmons in Photocharged ZnO Nanocrystals Revealing the Nature of Charge Dynamics. *J. Phys. Chem. Lett.* **2013**, *4*, 3024−3030.
(197) Marbella, L. E.; Gan, X. Y.; Kaseman, D. C.; Millstone, J. E. Correlating Carrier Density and Emergent Plasmonic Features in $Cu_{2-x}Se$ Nanoparticles. *Nano Lett.* **2017**, *17*, 2414−2419.
(198) Xie, Y.; Riedinger, A.; Prato, M.; Casu, A.; Genovese, A.; Guardia, P.; Sottini, S.; Sangregorio, C.; Miszta, K.; Ghosh, S.; et al. Copper Sulfide Nanocrystals with Tunable Composition by Reduction of Covellite Nanocrystals with Cu^+ Ions. *J. Am. Chem. Soc.* **2013**, *135*, 17630−17637.
(199) Palomaki, P. K. B.; Miller, E. M.; Neale, N. R. Control of Plasmonic and Interband Transitions in Colloidal Indium Nitride Nanocrystals. *J. Am. Chem. Soc.* **2013**, *135*, 14142−14150.
(200) Zhou, S.; Ni, Z.; Ding, Y.; Sugaya, M.; Pi, X.; Nozaki, T. Ligand-Free, Colloidal, and Plasmonic Silicon Nanocrystals Heavily Doped with Boron. *ACS Photonics* **2016**, *3*, 415−422.
(201) De Trizio, L.; Gaspari, R.; Bertoni, G.; Kriegel, I.; Moretti, L.; Scotognella, F.; Maserati, L.; Zhang, Y.; Messina, G. C.; Prato, M.; et al. $Cu_{3-X}P$ Nanocrystals as a Material Platform for Near-Infrared Plasmonics and Cation Exchange Reactions. *Chem. Mater.* **2015**, *27*, 1120−1128.
(202) Kozawa, T.; Kachi, T.; Kano, H.; Taga, Y.; Hashimoto, M.; Koide, N.; Manabe, K. Raman Scattering from LO Phonon-plasmon Coupled Modes in Gallium Nitride. *J. Appl. Phys.* **1994**, *75*, 1098−1101.
(203) Brown, A. M.; Sundararaman, R.; Narang, P.; Goddard, W. A.; Atwater, H. A. Nonradiative Plasmon Decay and Hot Carrier Dynamics: Effects of Phonons, Surfaces, and Geometry. *ACS Nano* **2016**, *10*, 957−966.
(204) Manna, G.; Bose, R.; Pradhan, N. Semiconducting and Plasmonic Copper Phosphide Platelets. *Angew. Chem., Int. Ed.* **2013**, *52*, 6762−6766.
(205) Baldassarre, L.; Sakat, E.; Frigerio, J.; Samarelli, A.; Gallacher, K.; Calandrini, E.; Isella, G.; Paul, D. J.; Ortolani, M.; Biagioni, P. Midinfrared Plasmon-Enhanced Spectroscopy with Germanium Antennas on Silicon Substrates. *Nano Lett.* **2015**, *15*, 7225−7231.
(206) Chandradass, J.; Bae, D. S.; Kim, K. H. A Simple Method to Prepare Indium Oxide Nanoparticles: Structural, Microstructural and Magnetic Properties. *Adv. Powder Technol.* **2011**, *22*, 370−374.
(207) Sachet, E.; Losego, M. D.; Guske, J.; Franzen, S.; Maria, J.-P. Mid-Infrared Surface Plasmon Resonance in Zinc Oxide Semiconductor Thin Films. *Appl. Phys. Lett.* **2013**, *102*, 051111.
(208) Xie, Y.; Bertoni, G.; Riedinger, A.; Sathya, A.; Prato, M.; Marras, S.; Tu, R.; Pellegrino, T.; Manna, L. Nanoscale Transformations in Covellite (CuS) Nanocrystals in the Presence of Divalent Metal Cations in a Mild Reducing Environment. *Chem. Mater.* **2015**, *27*, 7531−7537.
(209) Wang, T.; Radovanovic, P. V. Free Electron Concentration in Colloidal Indium Tin Oxide Nanocrystals Determined by Their Size and Structure. *J. Phys. Chem. C* **2011**, *115*, 406−413.
(210) Franzen, S. Surface Plasmon Polaritons and Screened Plasma Absorption in Indium Tin Oxide Compared to Silver and Gold. *J. Phys. Chem. C* **2008**, *112*, 6027−6032.
(211) Gilstrap, R. A., Jr.; Capozzi, C. J.; Carson, C. G.; Gerhardt, R. A.; Summers, C. J. Synthesis of a Nonagglomerated Indium Tin Oxide Nanoparticle Dispersion. *Adv. Mater.* **2008**, *20*, 4163−4166.
(212) Kang, M. S.; Losego, M.; Sachet, E.; Maria, J.-P.; Franzen, S. Near-Infrared Optical Extinction of Indium Tin Oxide Structures Prepared by Nanosphere Lithography. *ACS Photonics* **2016**, *3*, 1993−1999.
(213) Ye, X.; Reifsnyder Hickey, D.; Fei, J.; Diroll, B. T.; Paik, T.; Chen, J.; Murray, C. B. Seeded Growth of Metal-Doped Plasmonic Oxide Heterodimer Nanocrystals and Their Chemical Transformation. *J. Am. Chem. Soc.* **2014**, *136*, 5106−5115.
(214) Haase, M.; Weller, H.; Henglein, A. Photochemistry and Radiation Chemistry of Colloidal Semiconductors. 23. Electron Storage on Zinc Oxide Particles and Size Quantization. *J. Phys. Chem.* **1988**, *92*, 482−487.
(215) Kim, J.; Dutta, A.; Memarzadeh, B.; Kildishev, A. V.; Mosallaei, H.; Boltasseva, A. Zinc Oxide Based Plasmonic Multilayer Resonator: Localized and Gap Surface Plasmon in the Infrared. *ACS Photonics* **2015**, *2*, 1224−1230.
(216) Ni, Z.; Pi, X.; Zhou, S.; Nozaki, T.; Grandidier, B.; Yang, D. Size-Dependent Structures and Optical Absorption of Boron-Hyperdoped Silicon Nanocrystals. *Adv. Opt. Mater.* **2016**, *4*, 700−707.
(217) Xu, J.; Yang, X.; Yang, Q.-D.; Huang, X.; Tang, Y.; Zhang, W.; Lee, C.-S. Controllable Synthesis of Bandgap-Tunable CuS_xSe_{1-x} Nanoplate Alloys. *Chem. - Asian J.* **2015**, *10*, 1490−1495.
(218) Dilena, E.; Dorfs, D.; George, C.; Miszta, K.; Povia, M.; Genovese, A.; Casu, A.; Prato, M.; Manna, L. Colloidal $Cu_{2-x}(S_ySe_{1-y})$ Alloy Nanocrystals with Controllable Crystal Phase: Synthesis, Plasmonic Properties, Cation Exchange and Electrochemical Lithiation. *J. Mater. Chem.* **2012**, *22*, 13023−13031.
(219) Liu, X.; Wang, X.; Swihart, M. T. $Cu_{2-x}S_{1-y}Se_y$ Alloy Nanocrystals with Broadly Tunable Near-Infrared Localized Surface Plasmon Resonance. *Chem. Mater.* **2013**, *25*, 4402−4408.
(220) Deb, S. K. Optical and Photoelectric Properties and Colour Centres in Thin Films of Tungsten Oxide. *Philos. Mag.* **1973**, *27*, 801−822.
(221) Hussain, A.; Gruehn, R.; Rüscher, C. H. Crystal Growth of Alkali Metal Tungsten Brozes M_xWO_3 (M = K, Rb, Cs), and Their Optical Properties. *J. Alloys Compd.* **1997**, *246*, 51−61.
(222) Ingham, B.; Hendy, S. C.; Chong, S. V.; Tallon, J. L. Density-Functional Studies of Tungsten Trioxide, Tungsten Bronzes, and Related Systems. *Phys. Rev. B: Condens. Matter Mater. Phys.* **2005**, *72*, 075109.
(223) Deepa, M.; Srivastava, A. K.; Sood, K. N.; Agnihotry, S. A. Nanostructured Mesoporous Tungsten Oxide Films with Fast Kinetics for Electrochromic Smart Windows. *Nanotechnology* **2006**, *17*, 2625−2630.
(224) Yang, C.; Chen, J.-F.; Zeng, X.; Cheng, D.; Huang, H.; Cao, D. Enhanced Near-Infrared Shielding Ability of (Li,K)-Codoped WO_3 for Smart Windows: DFT Prediction Validated by Experiment. *Nanotechnology* **2016**, *27*, 075203.
(225) Hutfluss, L. N.; Radovanovic, P. V. Controlling the Mechanism of Phase Transformation of Colloidal In_2O_3 Nanocrystals. *J. Am. Chem. Soc.* **2015**, *137*, 1101−1108.
(226) Chattopadhyay, D.; Queisser, H. J. Electron Scattering by Ionized Impurities in Semiconductors. *Rev. Mod. Phys.* **1981**, *53*, 745−768.
(227) Kittel, C. *Introduction to Solid State Physics*, 8th ed.; Wiley, 2004.
(228) Monreal, R. C.; Antosiewicz, T. J.; Apell, S. P. Diffuse Surface Scattering and Quantum Size Effects in the Surface Plasmon Resonances of Low-Carrier-Density Nanocrystals. *J. Phys. Chem. C* **2016**, *120*, 5074−5082.
(229) Monreal, R. C.; Antosiewicz, T. J.; Apell, S. P. Diffuse Surface Scattering in the Plasmonic Resonances of Ultralow Electron Density Nanospheres. *J. Phys. Chem. Lett.* **2015**, *6*, 1847−1853.
(230) Shen, G.; Guyot-Sionnest, P. HgS and HgS/CdS Colloidal Quantum Dots with Infrared Intraband Transitions and Emergence of a Surface Plasmon. *J. Phys. Chem. C* **2016**, *120*, 11744−11753.
(231) Zhang, H.; Kulkarni, V.; Prodan, E.; Nordlander, P.; Govorov, A. O. Theory of Quantum Plasmon Resonances in Doped Semiconductor Nanocrystals. *J. Phys. Chem. C* **2014**, *118*, 16035−16042.
(232) Maack, J. R.; Mortensen, N. A.; Wubs, M. Size-Dependent Nonlocal Effects in Plasmonic Semiconductor Particles. *EPL Europhys. Lett.* **2017**, *119*, 17003.
(233) Jain, P. K. Plasmon-in-a-Box: On the Physical Nature of Few-Carrier Plasmon Resonances. *J. Phys. Chem. Lett.* **2014**, *5*, 3112−3119.
(234) Monreal, R. C.; Apell, S. P.; Antosiewicz, T. J. Infrared Absorption and Hot Electron Production in Low-Electron-Density

DOI: 10.1021/acs.chemrev.7b00613
Chem. Rev. 2018, 118, 3121−3207

Nanospheres: A Look at Real Systems. *J. Phys. Chem. Lett.* **2017**, *8*, 524−530.
(235) Fan, X.; Zheng, W.; Singh, D. J. Light Scattering and Surface Plasmons on Small Spherical Particles. *Light: Sci. Appl.* **2014**, *3*, e179.
(236) Jin, D.; Hu, Q.; Neuhauser, D.; von Cube, F.; Yang, Y.; Sachan, R.; Luk, T. S.; Bell, D. C.; Fang, N. X. Quantum-Spillover-Enhanced Surface-Plasmonic Absorption at the Interface of Silver and High-Index Dielectrics. *Phys. Rev. Lett.* **2015**, *115*, 193901.
(237) Burbano, M.; Scanlon, D. O.; Watson, G. W. Sources of Conductivity and Doping Limits in CdO from Hybrid Density Functional Theory. *J. Am. Chem. Soc.* **2011**, *133*, 15065−15072.
(238) Liu, Q.; Sun, C.; He, Q.; Liu, D.; Khalil, A.; Xiang, T.; Wu, Z.; Wang, J.; Song, L. Ultrathin Carbon Layer Coated MoO_2 Nanoparticles for High-Performance near-Infrared Photothermal Cancer Therapy. *Chem. Commun.* **2015**, *51*, 10054−10057.
(239) Chen, A.; Zhu, K.; Zhong, H.; Shao, Q.; Ge, G. A New Investigation of Oxygen Flow Influence on ITO Thin Films by Magnetron Sputtering. *Sol. Energy Mater. Sol. Cells* **2014**, *120*, 157−162.
(240) Hu, H.; Ji, H.-F.; Sun, Y. The Effect of Oxygen Vacancies on Water Wettability of a ZnO Surface. *Phys. Chem. Chem. Phys.* **2013**, *15*, 16557−16565.
(241) Kim, J.; Naik, G. V.; Gavrilenko, A. V.; Dondapati, K.; Gavrilenko, V. I.; Prokes, S. M.; Glembocki, O. J.; Shalaev, V. M.; Boltasseva, A. Optical Properties of Gallium-Doped Zinc Oxide: A Low-Loss Plasmonic Material: First-Principles Theory and Experiment. *Phys. Rev. X* **2013**, *3*, 041037.
(242) Fang, H.; Hegde, M.; Yin, P.; Radovanovic, P. V. Tuning Plasmon Resonance of In_2O_3 Nanocrystals throughout the Mid-Infrared Region by Competition between Electron Activation and Trapping. *Chem. Mater.* **2017**, *29*, 4970−4979.
(243) Demchenko, D. O.; Earles, B.; Liu, H. Y.; Avrutin, V.; Izyumskaya, N.; Özgür, Ü.; Morkoç, H. Impurity Complexes and Conductivity of Ga-Doped ZnO. *Phys. Rev. B: Condens. Matter Mater. Phys.* **2011**, *84*, 075201.
(244) Smyth, D. M. The Effects of Dopants on the Properties of Metal Oxides. *Solid State Ionics* **2000**, *129*, 5−12.
(245) Choi, S.-I.; Nam, K. M.; Park, B. K.; Seo, W. S.; Park, J. T. Preparation and Optical Properties of Colloidal, Monodisperse, and Highly Crystalline ITO Nanoparticles. *Chem. Mater.* **2008**, *20*, 2609−2611.
(246) Zhou, D.; Kittilstved, K. R. Electron Trapping on Fe^{3+} Sites in Photodoped ZnO Colloidal Nanocrystals. *Chem. Commun.* **2016**, *52*, 9101−9104.
(247) Shim, M.; Guyot-Sionnest, P. Organic-Capped ZnO Nanocrystals: Synthesis and n-Type Character. *J. Am. Chem. Soc.* **2001**, *123*, 11651−11654.
(248) Nütz, T.; zum Felde, U.; Haase, M. Wet-Chemical Synthesis of Doped Nanoparticles: Blue-Colored Colloids of n-Doped SnO_2:Sb. *J. Chem. Phys.* **1999**, *110*, 12142−12150.
(249) Della Gaspera, E.; Duffy, N. W.; van Embden, J.; Waddington, L.; Bourgeois, L.; Jasieniak, J. J.; Chesman, A. S. R. Plasmonic Ge-Doped ZnO Nanocrystals. *Chem. Commun.* **2015**, *51*, 12369−12372.
(250) Collins, S. M.; Ringe, E.; Duchamp, M.; Saghi, Z.; Dunin-Borkowski, R. E.; Midgley, P. A. Eigenmode Tomography of Surface Charge Oscillations of Plasmonic Nanoparticles by Electron Energy Loss Spectroscopy. *ACS Photonics* **2015**, *2*, 1628−1635.
(251) Barrow, S. J.; Collins, S. M.; Rossouw, D.; Funston, A. M.; Botton, G. A.; Midgley, P. A.; Mulvaney, P. Electron Energy Loss Spectroscopy Investigation into Symmetry in Gold Trimer and Tetramer Plasmonic Nanoparticle Structures. *ACS Nano* **2016**, *10*, 8552−8563.
(252) Kuznetsov, A. S. Effect of Proximity in Arrays of Plasmonic Nanoantennas on Hot Spots Density: Degenerate Semiconductors vs. Conventional Metals. *Plasmonics* **2016**, *11*, 1487−1493.
(253) Hu, W.; Guo, S.; Gaul, J. P.; Boebinger, M. G.; McDowell, M. T.; Filler, M. A. Reversible Tuning of the Surface Plasmon Resonance of Indium Tin Oxide Nanocrystals by Gas-Phase Oxidation and Reduction. *J. Phys. Chem. C* **2017**, *121*, 15970−15976.
(254) Chen, Y.; Zeng, D.; Zhang, K.; Lu, A.; Wang, L.; Peng, D.-L. Au−ZnO Hybrid Nanoflowers, Nanomultipods and Nanopyramids: One-Pot Reaction Synthesis and Photocatalytic Properties. *Nanoscale* **2014**, *6*, 874−881.
(255) Gordon, T. R.; Schaak, R. E. Synthesis of Hybrid Au-In_2O_3 Nanoparticles Exhibiting Dual Plasmonic Resonance. *Chem. Mater.* **2014**, *26*, 5900−5904.
(256) Li, P.; Wei, Z.; Wu, T.; Peng, Q.; Li, Y. Au−ZnO Hybrid Nanopyramids and Their Photocatalytic Properties. *J. Am. Chem. Soc.* **2011**, *133*, 5660−5663.
(257) Goodenough, J. B. Anomalous Properties of the Vanadium Oxides. *Annu. Rev. Mater. Sci.* **1971**, *1*, 101−138.
(258) Goodenough, J. B. The Two Components of the Crystallographic Transition in VO_2. *J. Solid State Chem.* **1971**, *3*, 490−500.
(259) Dahlman, C. J.; LeBlanc, G.; Bergerud, A.; Staller, C.; Adair, J.; Milliron, D. J. Electrochemically Induced Transformations of Vanadium Dioxide Nanocrystals. *Nano Lett.* **2016**, *16*, 6021−6027.
(260) Niklasson, G. A.; Li, S.-Y.; Granqvist, C. G. Thermochromic Vanadium Oxide Thin Films: Electronic and Optical Properties. *J. Phys. Conf. Ser.* **2014**, *559*, 012001.
(261) Paik, T.; Hong, S.-H.; Gaulding, E. A.; Caglayan, H.; Gordon, T. R.; Engheta, N.; Kagan, C. R.; Murray, C. B. Solution-Processed Phase-Change VO_2 Metamaterials from Colloidal Vanadium Oxide (VO_x) Nanocrystals. *ACS Nano* **2014**, *8*, 797−806.
(262) Holsteen, A.; Kim, I. S.; Lauhon, L. J. Extraordinary Dynamic Mechanical Response of Vanadium Dioxide Nanowires around the Insulator to Metal Phase Transition. *Nano Lett.* **2014**, *14*, 1898−1902.
(263) Son, J.-H.; Wei, J.; Cobden, D.; Cao, G.; Xia, Y. Hydrothermal Synthesis of Monoclinic VO_2 Micro- and Nanocrystals in One Step and Their Use in Fabricating Inverse Opals. *Chem. Mater.* **2010**, *22*, 3043−3050.
(264) Sun, Y.; Jiang, S.; Bi, W.; Long, R.; Tan, X.; Wu, C.; Wei, S.; Xie, Y. New Aspects of Size-Dependent Metal-Insulator Transition in Synthetic Single-Domain Monoclinic Vanadium Dioxide Nanocrystals. *Nanoscale* **2011**, *3*, 4394−4401.
(265) Whittaker, L.; Jaye, C.; Fu, Z.; Fischer, D. A.; Banerjee, S. Depressed Phase Transition in Solution-Grown VO_2 Nanostructures. *J. Am. Chem. Soc.* **2009**, *131*, 8884−8894.
(266) Kang, L.; Gao, Y.; Luo, H.; Chen, Z.; Du, J.; Zhang, Z. Nanoporous Thermochromic VO_2 Films with Low Optical Constants, Enhanced Luminous Transmittance and Thermochromic Properties. *ACS Appl. Mater. Interfaces* **2011**, *3*, 135−138.
(267) Ke, Y.; Wen, X.; Zhao, D.; Che, R.; Xiong, Q.; Long, Y. Controllable Fabrication of Two-Dimensional Patterned VO_2 Nanoparticle, Nanodome, and Nanonet Arrays with Tunable Temperature-Dependent Localized Surface Plasmon Resonance. *ACS Nano* **2017**, *11*, 7542−7551.
(268) Liu, X.; Wang, X.; Zhou, B.; Law, W.-C.; Cartwright, A. N.; Swihart, M. T. Size-Controlled Synthesis of $Cu_{2-X}E$ (E = S, Se) Nanocrystals with Strong Tunable Near-Infrared Localized Surface Plasmon Resonance and High Conductivity in Thin Films. *Adv. Funct. Mater.* **2013**, *23*, 1256−1264.
(269) Chen, M.; Guyot-Sionnest, P. Reversible Electrochemistry of Mercury Chalcogenide Colloidal Quantum Dot Films. *ACS Nano* **2017**, *11*, 4165−4173.
(270) Zhang, H.; Xia, Y. Ratiometry, Wavelength, and Intensity: Triple Signal Readout for Colorimetric Sensing of Mercury Ions by Plasmonic $Cu_{2-X}Se$ Nanoparticles. *ACS Sens.* **2016**, *1*, 384−391.
(271) Chakrabarti, D. J.; Laughlin, D. E. The Cu−Se (Copper-Selenium) System. *Bull. Alloy Phase Diagrams* **1981**, *2*, 305−315.
(272) Chakrabarti, D. J.; Laughlin, D. E. The Cu-S (Copper-Sulfur) System. *Bull. Alloy Phase Diagrams* **1983**, *4*, 254.
(273) Mulder, B. J. Optical Properties of an Unusual Form of Thin Chalcosite (Cu_2S) Crystals. *Phys. Status Solidi A* **1973**, *15*, 409−413.
(274) Mulder, B. J. Proto-Djurleite, a Metastable Form of Cuprous Sulphide. *Krist. Tech.* **1973**, *8* (7), 825−832.
(275) Xie, Y.; Chen, W.; Bertoni, G.; Kriegel, I.; Xiong, M.; Li, N.; Prato, M.; Riedinger, A.; Sathya, A.; Manna, L. Tuning and Locking the

DOI: 10.1021/acs.chemrev.7b00613
Chem. Rev. 2018, 118, 3121−3207

Localized Surface Plasmon Resonances of CuS (Covellite) Nanocrystals by an Amorphous $CuPd_xS$ Shell. *Chem. Mater.* **2017**, *29*, 1716−1723.
(276) Liang, W.; Whangbo, M.-H. Conductivity Anisotropy and Structural Phase Transition in Covellite CuS. *Solid State Commun.* **1993**, *85*, 405−408.
(277) Xiao, L.; Wu, J.; Ran, J.; Liu, Y.; Qiu, W.; Lu, F.; Shao, F.; Tang, D.; Peng, P. Near-Infrared Radiation Absorption Properties of Covellite (CuS) Using First-Principles Calculations. *AIP Adv.* **2016**, *6*, 085122.
(278) Conejeros, S.; de P. R. Moreira, I.; Alemany, P.; Canadell, E. Nature of Holes, Oxidation States, and Hypervalency in Covellite (CuS). *Inorg. Chem.* **2014**, *53*, 12402−12406.
(279) Hsu, S.-W.; On, K.; Tao, A. R. Localized Surface Plasmon Resonances of Anisotropic Semiconductor Nanocrystals. *J. Am. Chem. Soc.* **2011**, *133*, 19072−19075.
(280) Hsu, S.-W.; Bryks, W.; Tao, A. R. Effects of Carrier Density and Shape on the Localized Surface Plasmon Resonances of $Cu_{2-x}S$ Nanodisks. *Chem. Mater.* **2012**, *24*, 3765−3771.
(281) Hsu, S.-W.; Ngo, C.; Tao, A. R. Tunable and Directional Plasmonic Coupling within Semiconductor Nanodisk Assemblies. *Nano Lett.* **2014**, *14*, 2372−2380.
(282) Georgieva, Z. N.; Tomat, M. A.; Kim, C.; Plass, K. E. Stabilization of Plasmon Resonance in $Cu_{2-x}S$ Semiconductor Nanoparticles. *Chem. Commun.* **2016**, *52*, 9082−9085.
(283) Liu, L.; Zhong, H.; Bai, Z.; Zhang, T.; Fu, W.; Shi, L.; Xie, H.; Deng, L.; Zou, B. Controllable Transformation from Rhombohedral $Cu_{1.8}S$ Nanocrystals to Hexagonal CuS Clusters: Phase- and Composition-Dependent Plasmonic Properties. *Chem. Mater.* **2013**, *25*, 4828−4834.
(284) Liu, Y.; Liu, M.; Swihart, M. T. Reversible Crystal Phase Interconversion between Covellite CuS and High Chalcocite Cu_2S Nanocrystals. *Chem. Mater.* **2017**, *29*, 4783−4791.
(285) Guo, Q.; Yao, Y.; Luo, Z.-C.; Qin, Z.; Xie, G.; Liu, M.; Kang, J.; Zhang, S.; Bi, G.; Liu, X.; et al. Universal Near-Infrared and Mid-Infrared Optical Modulation for Ultrafast Pulse Generation Enabled by Colloidal Plasmonic Semiconductor Nanocrystals. *ACS Nano* **2016**, *10*, 9463−9469.
(286) Liu, X.; Wang, X.; Swihart, M. T. Composition-Dependent Crystal Phase, Optical Properties, and Self-Assembly of Cu−Sn−S Colloidal Nanocrystals. *Chem. Mater.* **2015**, *27*, 1342−1348.
(287) Wang, J.-J.; Xue, D.-J.; Guo, Y.-G.; Hu, J.-S.; Wan, L.-J. Bandgap Engineering of Monodispersed $Cu_{2-x}S_ySe_{1-y}$ Nanocrystals through Chalcogen Ratio and Crystal Structure. *J. Am. Chem. Soc.* **2011**, *133*, 18558−18561.
(288) Xu, J.; Yang, X.; Yang, Q.; Zhang, W.; Lee, C.-S. Phase Conversion from Hexagonal CuS_ySe_{1-y} to Cubic $Cu_{2-x}S_ySe_{1-y}$: Composition Variation, Morphology Evolution, Optical Tuning, and Solar Cell Applications. *ACS Appl. Mater. Interfaces* **2014**, *6*, 16352−16359.
(289) Saldanha, P. L.; Brescia, R.; Prato, M.; Li, H.; Povia, M.; Manna, L.; Lesnyak, V. Generalized One-Pot Synthesis of Copper Sulfide, Selenide-Sulfide, and Telluride-Sulfide Nanoparticles. *Chem. Mater.* **2014**, *26*, 1442−1449.
(290) De Trizio, L.; Li, H.; Casu, A.; Genovese, A.; Sathya, A.; Messina, G. C.; Manna, L. Sn Cation Valency Dependence in Cation Exchange Reactions Involving $Cu_{2-X}Se$ Nanocrystals. *J. Am. Chem. Soc.* **2014**, *136*, 16277−16284.
(291) Lesnyak, V.; Brescia, R.; Messina, G. C.; Manna, L. Cu Vacancies Boost Cation Exchange Reactions in Copper Selenide Nanocrystals. *J. Am. Chem. Soc.* **2015**, *137*, 9315−9323.
(292) Leach, A. D. P.; Macdonald, J. E. Optoelectronic Properties of $CuInS_2$ Nanocrystals and Their Origin. *J. Phys. Chem. Lett.* **2016**, *7*, 572−583.
(293) Niezgoda, J. S.; Yap, E.; Keene, J. D.; McBride, J. R.; Rosenthal, S. J. Plasmonic $Cu_xIn_yS_2$ Quantum Dots Make Better Photovoltaics Than Their Nonplasmonic Counterparts. *Nano Lett.* **2014**, *14*, 3262−3269.
(294) Wang, X.; Swihart, M. T. Controlling the Size, Shape, Phase, Band Gap, and Localized Surface Plasmon Resonance of $Cu_{2-x}S$ and Cu_xIn_yS Nanocrystals. *Chem. Mater.* **2015**, *27*, 1786−1791.
(295) Liu, X.; Lee, C.; Law, W.-C.; Zhu, D.; Liu, M.; Jeon, M.; Kim, J.; Prasad, P. N.; Kim, C.; Swihart, M. T. Au−$Cu_{2-x}Se$ Heterodimer Nanoparticles with Broad Localized Surface Plasmon Resonance as Contrast Agents for Deep Tissue Imaging. *Nano Lett.* **2013**, *13*, 4333−4339.
(296) Nelson, A.; Ha, D.-H.; Robinson, R. D. Selective Etching of Copper Sulfide Nanoparticles and Heterostructures through Sulfur Abstraction: Phase Transformations and Optical Properties. *Chem. Mater.* **2016**, *28*, 8530−8541.
(297) Zhu, D.; Liu, M.; Liu, X.; Liu, Y.; Prasad, P. N.; Swihart, M. T. Au−$Cu_{2-x}Se$ Heterogeneous Nanocrystals for Efficient Photothermal Heating for Cancer Therapy. *J. Mater. Chem. B* **2017**, *5*, 4934−4942.
(298) Muhammed, M. A. H.; Döblinger, M.; Rodríguez-Fernández, J. Switching Plasmons: Gold Nanorod−Copper Chalcogenide Core−Shell Nanoparticle Clusters with Selectable Metal/Semiconductor NIR Plasmon Resonances. *J. Am. Chem. Soc.* **2015**, *137*, 11666−11677.
(299) De Trizio, L.; Manna, L. Forging Colloidal Nanostructures via Cation Exchange Reactions. *Chem. Rev.* **2016**, *116*, 10852−10887.
(300) Rivest, J. B.; Jain, P. K. Cation Exchange on the Nanoscale: An Emerging Technique for New Material Synthesis, Device Fabrication, and Chemical Sensing. *Chem. Soc. Rev.* **2013**, *42*, 89−96.
(301) Manzi, A.; Simon, T.; Sonnleitner, C.; Döblinger, M.; Wyrwich, R.; Stern, O.; Stolarczyk, J. K.; Feldmann, J. Light-Induced Cation Exchange for Copper Sulfide Based CO_2 Reduction. *J. Am. Chem. Soc.* **2015**, *137*, 14007−14010.
(302) Lubeck, C. R.; Han, T. Y.-J.; Gash, A. E.; Satcher, J. H.; Doyle, F. M. Synthesis of Mesostructured Copper Sulfide by Cation Exchange and Liquid-Crystal Templating. *Adv. Mater.* **2006**, *18*, 781−784.
(303) Cook, W. R.; Shiozawa, L.; Augustine, F. Relationship of Copper Sulfide and Cadmium Sulfide Phases. *J. Appl. Phys.* **1970**, *41*, 3058−3063.
(304) Sadtler, B.; Demchenko, D. O.; Zheng, H.; Hughes, S. M.; Merkle, M. G.; Dahmen, U.; Wang, L.-W.; Alivisatos, A. P. Selective Facet Reactivity during Cation Exchange in Cadmium Sulfide Nanorods. *J. Am. Chem. Soc.* **2009**, *131*, 5285−5293.
(305) Luther, J. M.; Zheng, H.; Sadtler, B.; Alivisatos, A. P. Synthesis of PbS Nanorods and Other Ionic Nanocrystals of Complex Morphology by Sequential Cation Exchange Reactions. *J. Am. Chem. Soc.* **2009**, *131*, 16851−16857.
(306) Zhou, S.; Pi, X.; Ni, Z.; Ding, Y.; Jiang, Y.; Jin, C.; Delerue, C.; Yang, D.; Nozaki, T. Comparative Study on the Localized Surface Plasmon Resonance of Boron- and Phosphorus-Doped Silicon Nanocrystals. *ACS Nano* **2015**, *9*, 378−386.
(307) Ginn, J. C.; Jarecki, R. L.; Shaner, E. A.; Davids, P. S. Infrared Plasmons on Heavily-Doped Silicon. *J. Appl. Phys.* **2011**, *110*, 043110.
(308) Cleary, J. W.; Peale, R. E.; Shelton, D. J.; Boreman, G. D.; Smith, C. W.; Ishigami, M.; Soref, R.; Drehman, A.; Buchwald, W. R. IR Permittivities for Silicides and Doped Silicon. *J. Opt. Soc. Am. B* **2010**, *27*, 730−734.
(309) Soref, R. Mid-Infrared Photonics in Silicon and Germanium. *Nat. Photonics* **2010**, *4*, 495−497.
(310) Hryciw, A.; Jun, Y. C.; Brongersma, M. L. Plasmonics: Electrifying Plasmonics on Silicon. *Nat. Mater.* **2010**, *9*, 3−4.
(311) Dionne, J. A.; Sweatlock, L. A.; Sheldon, M. T.; Alivisatos, A. P.; Atwater, H. A. Silicon-Based Plasmonics for On-Chip Photonics. *IEEE J. Sel. Top. Quantum Electron.* **2010**, *16*, 295−306.
(312) Chou, L. W.; Shin, N.; Sivaram, S. V.; Filler, M. A. Tunable Mid-Infrared Localized Surface Plasmon Resonances in Silicon Nanowires. *J. Am. Chem. Soc.* **2012**, *134*, 16155−16158.
(313) Chou, L.-W.; Boyuk, D. S.; Filler, M. A. Optically Abrupt Localized Surface Plasmon Resonances in Si Nanowires by Mitigation of Carrier Density Gradients. *ACS Nano* **2015**, *9*, 1250−1256.
(314) Yu, Y.; Bosoy, C. A.; Hessel, C. M.; Smilgies, D.-M.; Korgel, B. A. Silicon Nanocrystal Superlattices. *ChemPhysChem* **2013**, *14*, 84−87.
(315) Yu, Y.; Lu, X.; Guillaussier, A.; Voggu, V. R.; Pineros, W.; de la Mata, M.; Arbiol, J.; Smilgies, D.-M.; Truskett, T. M.; Korgel, B. A. Orientationally Ordered Silicon Nanocrystal Cuboctahedra in Superlattices. *Nano Lett.* **2016**, *16*, 7814−7821.

DOI: 10.1021/acs.chemrev.7b00613
Chem. Rev. 2018, 118, 3121−3207

(316) Yu, Y.; Bosoy, C. A.; Smilgies, D.-M.; Korgel, B. A. Self-Assembly and Thermal Stability of Binary Superlattices of Gold and Silicon Nanocrystals. *J. Phys. Chem. Lett.* **2013**, *4*, 3677−3682.
(317) Constantinou, M.; Rigas, G. P.; Castro, F. A.; Stolojan, V.; Hoettges, K. F.; Hughes, M. P.; Adkins, E.; Korgel, B. A.; Shkunov, M. Simultaneous Tunable Selection and Self-Assembly of Si Nanowires from Heterogeneous Feedstock. *ACS Nano* **2016**, *10*, 4384−4394.
(318) Korgel, B. A. Nanocrystal Superlattices: Assembly at Liquid Interfaces. *Nat. Mater.* **2010**, *9*, 701−703.
(319) Baldassarre, L.; Sakat, E.; Bollani, M.; Samarelli, A.; Gallacher, K.; Frigerio, J.; Pellegrini, G.; Giliberti, V.; Ballabio, A.; Fischer, M. P.; et al. Mid-Infrared Plasmonic Platform Based on n-Doped Ge-on-Si: Molecular Sensing with Germanium Nano-Antennas on Si. *41st International Conference on Infrared, Millimeter, and Terahertz waves (IRMMW-THz)* **2016**, 1−2.
(320) Fischer, M. P.; Riede, A.; Grupp, A.; Gallacher, K.; Frigerio, J.; Ortolani, M.; Paul, D. J.; Isella, G.; Leitenstorfer, A.; Biagioni, P.; et al. Germanium Plasmonic Nanoantennas for Third-Harmonic Generation in the Mid Infrared. *41st International Conference on Infrared, Millimeter, and Terahertz waves (IRMMW-THz)* **2016**, 1−2.
(321) Frigerio, J.; Ballabio, A.; Isella, G.; Sakat, E.; Pellegrini, G.; Biagioni, P.; Bollani, M.; Napolitani, E.; Manganelli, C.; Virgilio, M.; et al. Tunability of the Dielectric Function of Heavily Doped Germanium Thin Films for Mid-Infrared Plasmonics. *Phys. Rev. B: Condens. Matter Mater. Phys.* **2016**, *94*, 085202.
(322) Prucnal, S.; Liu, F.; Voelskow, M.; Vines, L.; Rebohle, L.; Lang, D.; Berencén, Y.; Andric, S.; Boettger, R.; Helm, M.; et al. Ultra-Doped *n*-Type Germanium Thin Films for Sensing in the Mid-Infrared. *Sci. Rep.* **2016**, *6*, 27643.
(323) Liu, Z.; Beaulac, R. Nature of the Infrared Transition of Colloidal Indium Nitride Nanocrystals: Nonparabolicity Effects on the Plasmonic Behavior of Doped Semiconductor Nanomaterials. *Chem. Mater.* **2017**, *29*, 7507−7514.
(324) Chen, Z.; Li, Y.; Cao, C.; Zhao, S.; Fathololoumi, S.; Mi, Z.; Xu, X. Large-Scale Cubic InN Nanocrystals by a Combined Solution- and Vapor-Phase Method under Silica Confinement. *J. Am. Chem. Soc.* **2012**, *134*, 780−783.
(325) Guler, U.; Shalaev, V. M.; Boltasseva, A. Nanoparticle Plasmonics: Going Practical with Transition Metal Nitrides. *Mater. Today* **2015**, *18*, 227−237.
(326) Naik, G. V.; Shalaev, V. M.; Boltasseva, A. Alternative Plasmonic Materials: Beyond Gold and Silver. *Adv. Mater.* **2013**, *25*, 3264−3294.
(327) Patsalas, P.; Logothetidis, S. Interface Properties and Structural Evolution of TiN/Si and TiN/GaN Heterostructures. *J. Appl. Phys.* **2003**, *93*, 989−998.
(328) Walker, C. G. H.; Matthew, J. A. D.; Anderson, C. A.; Brown, N. M. D. An Estimate of the Electron Effective Mass in Titanium Nitride Using UPS and EELS. *Surf. Sci.* **1998**, *412*−*413*, 405−414.
(329) Chen, N. C.; Lien, W. C.; Liu, C. R.; Huang, Y. L.; Lin, Y. R.; Chou, C.; Chang, S. Y.; Ho, C. W. Excitation of Surface Plasma Wave at TiN/Air Interface in the Kretschmann Geometry. *J. Appl. Phys.* **2011**, *109*, 043104.
(330) Solovan, M. N.; Brus, V. V.; Maistruk, E. V.; Maryanchuk, P. D. Electrical and Optical Properties of TiN Thin Films. *Inorg. Mater.* **2014**, *50*, 40−45.
(331) Jeyachandran, Y. L.; Narayandass, S. K.; Mangalaraj, D.; Areva, S.; Mielczarski, J. A. Properties of Titanium Nitride Films Prepared by Direct Current Magnetron Sputtering. *Mater. Sci. Eng., A* **2007**, *445*−*446*, 223−236.
(332) Alvarez Barragan, A.; Ilawe, N. V.; Zhong, L.; Wong, B. M.; Mangolini, L. A Non-Thermal Plasma Route to Plasmonic TiN Nanoparticles. *J. Phys. Chem. C* **2017**, *121*, 2316−2322.
(333) Guler, U.; Suslov, S.; Kildishev, A. V.; Boltasseva, A.; Shalaev, V. M. Colloidal Plasmonic Titanium Nitride Nanoparticles: Properties and Applications. *Nanophotonics* **2015**, *4*, 269−276.
(334) Cortie, M. B.; Giddings, J.; Dowd, A. Optical Properties and Plasmon Resonances of Titanium Nitride Nanostructures. *Nanotechnology* **2010**, *21*, 115201.
(335) Guler, U.; Ndukaife, J. C.; Naik, G. V.; Nnanna, A. G. A.; Kildishev, A. V.; Shalaev, V. M.; Boltasseva, A. Local Heating with Lithographically Fabricated Plasmonic Titanium Nitride Nanoparticles. *Nano Lett.* **2013**, *13*, 6078−6083.
(336) Gui, L.; Bagheri, S.; Strohfeldt, N.; Hentschel, M.; Zgrabik, C. M.; Metzger, B.; Linnenbank, H.; Hu, E. L.; Giessen, H. Nonlinear Refractory Plasmonics with Titanium Nitride Nanoantennas. *Nano Lett.* **2016**, *16*, 5708−5713.
(337) Naik, G. V.; Kim, J.; Boltasseva, A. Oxides and Nitrides as Alternative Plasmonic Materials in the Optical Range. *Opt. Mater. Express* **2011**, *1*, 1090−1099.
(338) Lalisse, A.; Tessier, G.; Plain, J.; Baffou, G. Plasmonic Efficiencies of Nanoparticles Made of Metal Nitrides (TiN, ZrN) Compared with Gold. *Sci. Rep.* **2016**, *6*, 38647.
(339) Liu, Z.; Beaulac, R. Nature of the Infrared Transition of Colloidal Indium Nitride Nanocrystals: Nonparabolicity Effects on the Plasmonic Behavior of Doped Semiconductor Nanomaterials. *Chem. Mater.* **2017**, *29*, 7507−7514.
(340) Carrier Dynamics and Related Electronic Band Properties of InN Films. *Jpn. J. Appl. Phys.* **2014**, *53*, 100204.
(341) Davydov, V. Y.; Klochikhin, A. a.; Seisyan, R. p.; Emtsev, V. v.; Ivanov, S. v.; Bechstedt, F.; Furthmüller, J.; Harima, H.; Mudryi, A. v.; Aderhold, J.; et al. Absorption and Emission of Hexagonal InN. Evidence of Narrow Fundamental Band Gap. *Phys. Status Solidi B* **2002**, *229*, r1−r3.
(342) Wu, J.; Walukiewicz, W.; Yu, K. M.; Ager, J. W.; Haller, E. E.; Lu, H.; Schaff, W. J.; Saito, Y.; Nanishi, Y. Unusual Properties of the Fundamental Band Gap of InN. *Appl. Phys. Lett.* **2002**, *80*, 3967−3969.
(343) Palomaki, P. K.; Miller, E. M.; Neale, N. R. Control of Plasmonic and Interband Transitions in Colloidal Indium Nitride Nanocrystals. *J. Am. Chem. Soc.* **2013**, *135*, 14142−14150.
(344) Millot, M.; Ubrig, N.; Poumirol, J.-M.; Gherasoiu, I.; Walukiewicz, W.; George, S.; Portugall, O.; Léotin, J.; Goiran, M.; Broto, J.-M. Determination of Effective Mass in InN by High-Field Oscillatory Magnetoabsorption Spectroscopy. *Phys. Rev. B: Condens. Matter Mater. Phys.* **2011**, *83*, 125204.
(345) Demangeot, F.; Frandon, J.; Renucci, M. A.; Meny, C.; Briot, O.; Aulombard, R. L. Interplay of Electrons and Phonons in Heavily Doped GaN Epilayers. *J. Appl. Phys.* **1997**, *82*, 1305−1309.
(346) Khurgin, J. B. Surface Plasmon-Assisted Laser Cooling of Solids. *Phys. Rev. Lett.* **2007**, *98*, 177401.
(347) De Trizio, L.; Figuerola, A.; Manna, L.; Genovese, A.; George, C.; Brescia, R.; Saghi, Z.; Simonutti, R.; Van Huis, M.; Falqui, A. Size-Tunable, Hexagonal Plate-like Cu_3P and Janus-like Cu−Cu_3P Nanocrystals. *ACS Nano* **2012**, *6*, 32−41.
(348) Urso, C.; Barawi, M.; Gaspari, R.; Sirigu, G.; Kriegel, I.; Zavelani-Rossi, M.; Scotognella, F.; Manca, M.; Prato, M.; De Trizio, L.; et al. Colloidal Synthesis of Bipolar Off-Stoichiometric Gallium Iron Oxide Spinel-Type Nanocrystals with Near-IR Plasmon Resonance. *J. Am. Chem. Soc.* **2017**, *139*, 1198−1206.
(349) Bao, Q.; Hoh, H.; Zhang, Y. *Graphene Photonics, Optoelectronics, and Plasmonics*; CRC Press, 2017.
(350) Grigorenko, A. N.; Polini, M.; Novoselov, K. S. Graphene Plasmonics. *Nat. Photonics* **2012**, *6*, 749−758.
(351) Guo, Q.; Li, C.; Deng, B.; Yuan, S.; Guinea, F.; Xia, F. Infrared Nanophotonics Based on Graphene Plasmonics. *ACS Photonics* **2017**, *4*, 2989−2999.
(352) Huang, S.; Song, C.; Zhang, G.; Yan, H. Graphene Plasmonics: Physics and Potential Applications. *Nanophotonics* **2017**, *6*, 1191−1204.
(353) Cushing, B. L.; Kolesnichenko, V. L.; O'Connor, C. J. Recent Advances in the Liquid-Phase Syntheses of Inorganic Nanoparticles. *Chem. Rev.* **2004**, *104*, 3893−3946.
(354) Pileni, M.-P. The Role of Soft Colloidal Templates in Controlling the Size and Shape of Inorganic Nanocrystals. *Nat. Mater.* **2003**, *2*, 145−150.
(355) Murray, C. B.; Norris, D. J.; Bawendi, M. G. Synthesis and Characterization of Nearly Monodisperse CdE (E = Sulfur, Selenium, Tellurium) Semiconductor Nanocrystallites. *J. Am. Chem. Soc.* **1993**, *115*, 8706−8715.

DOI: 10.1021/acs.chemrev.7b00613
Chem. Rev. 2018, 118, 3121−3207

(356) Vossmeyer, T.; Katsikas, L.; Giersig, M.; Popovic, I. G.; Diesner, K.; Chemseddine, A.; Eychmueller, A.; Weller, H. CdS Nanoclusters: Synthesis, Characterization, Size Dependent Oscillator Strength, Temperature Shift of the Excitonic Transition Energy, and Reversible Absorbance Shift. *J. Phys. Chem.* **1994**, *98*, 7665−7673.
(357) Sooklal, K.; Cullum, B. S.; Angel, S. M.; Murphy, C. J. Photophysical Properties of ZnS Nanoclusters with Spatially Localized Mn^{2+}. *J. Phys. Chem.* **1996**, *100*, 4551−4555.
(358) Hines, M. A.; Guyot-Sionnest, P. Synthesis and Characterization of Strongly Luminescing ZnS-Capped CdSe Nanocrystals. *J. Phys. Chem.* **1996**, *100*, 468−471.
(359) Rogach, A. L.; Katsikas, L.; Kornowski, A.; Su, D.; Eychmüller, A.; Weller, H. Synthesis and Characterization of Thiol-Stabilized CdTe Nanocrystals. *Berichte Bunsenges. Für Phys. Chem.* **1996**, *100*, 1772−1778.
(360) Yin, Y.; Alivisatos, A. P. Colloidal Nanocrystal Synthesis and the Organic−inorganic Interface. *Nature* **2005**, *437*, 664−670.
(361) Owen, J. The Coordination Chemistry of Nanocrystal Surfaces. *Science* **2015**, *347*, 615−616.
(362) Mourdikoudis, S.; Liz-Marzán, L. M. Oleylamine in Nanoparticle Synthesis. *Chem. Mater.* **2013**, *25*, 1465−1476.
(363) Owen, J.; Brus, L. Chemical Synthesis and Luminescence Applications of Colloidal Semiconductor Quantum Dots. *J. Am. Chem. Soc.* **2017**, *139*, 10939−10943.
(364) Liu, H.; Owen, J. S.; Alivisatos, A. P. Mechanistic Study of Precursor Evolution in Colloidal Group II−VI Semiconductor Nanocrystal Synthesis. *J. Am. Chem. Soc.* **2007**, *129*, 305−312.
(365) Owen, J. S.; Chan, E. M.; Liu, H.; Alivisatos, A. P. Precursor Conversion Kinetics and the Nucleation of Cadmium Selenide Nanocrystals. *J. Am. Chem. Soc.* **2010**, *132*, 18206−18213.
(366) LaMer, V. K.; Dinegar, R. H. Theory, Production and Mechanism of Formation of Monodispersed Hydrosols. *J. Am. Chem. Soc.* **1950**, *72*, 4847−4854.
(367) Wang, F.; Richards, V. N.; Shields, S. P.; Buhro, W. E. Kinetics and Mechanisms of Aggregative Nanocrystal Growth. *Chem. Mater.* **2014**, *26*, 5−21.
(368) Gilroy, K. D.; Ruditskiy, A.; Peng, H. C.; Qin, D.; Xia, Y. Bimetallic Nanocrystals: Syntheses, Properties, and Applications. *Chem. Rev.* **2016**, *116*, 10414−10472.
(369) Xia, X.; Xie, S.; Liu, M.; Peng, H.-C.; Lu, N.; Wang, J.; Kim, M. J.; Xia, Y. On the Role of Surface Diffusion in Determining the Shape or Morphology of Noble-Metal Nanocrystals. *Proc. Natl. Acad. Sci. U. S. A.* **2013**, *110*, 6669−6673.
(370) Kwon, S. G.; Hyeon, T. Formation Mechanisms of Uniform Nanocrystals via Hot-Injection and Heat-Up Methods. *Small* **2011**, *7*, 2685−2702.
(371) van Embden, J.; Chesman, A. S. R.; Jasieniak, J. J. The Heat-Up Synthesis of Colloidal Nanocrystals. *Chem. Mater.* **2015**, *27*, 2246−2285.
(372) Franke, D.; Harris, D. K.; Chen, O.; Bruns, O. T.; Carr, J. A.; Wilson, M. W. B.; Bawendi, M. G. Continuous Injection Synthesis of Indium Arsenide Quantum Dots Emissive in the Short-Wavelength Infrared. *Nat. Commun.* **2016**, *7*, 12749.
(373) Chan, E. M.; Xu, C.; Mao, A. W.; Han, G.; Owen, J. S.; Cohen, B. E.; Milliron, D. J. Reproducible, High-Throughput Synthesis of Colloidal Nanocrystals for Optimization in Multidimensional Parameter Space. *Nano Lett.* **2010**, *10*, 1874−1885.
(374) Hendricks, M. P.; Cossairt, B. M.; Owen, J. S. The Importance of Nanocrystal Precursor Conversion Kinetics: Mechanism of the Reaction between Cadmium Carboxylate and Cadmium Bis-(Diphenyldithiophosphinate). *ACS Nano* **2012**, *6*, 10054−10062.
(375) Jun, Y.; Lee, J.-H.; Choi, J.; Cheon, J. Symmetry-Controlled Colloidal Nanocrystals: Nonhydrolytic Chemical Synthesis and Shape Determining Parameters. *J. Phys. Chem. B* **2005**, *109*, 14795−14806.
(376) Ito, D.; Yokoyama, S.; Zaikova, T.; Masuko, K.; Hutchison, J. E. Synthesis of Ligand-Stabilized Metal Oxide Nanocrystals and Epitaxial Core/Shell Nanocrystals via a Lower-Temperature Esterification Process. *ACS Nano* **2014**, *8*, 64−75.
(377) Pietryga, J. M.; Park, Y.-S.; Lim, J.; Fidler, A. F.; Bae, W. K.; Brovelli, S.; Klimov, V. I. Spectroscopic and Device Aspects of Nanocrystal Quantum Dots. *Chem. Rev.* **2016**, *116*, 10513−10622.
(378) Lee, J.; Zhang, S.; Sun, S. High-Temperature Solution-Phase Syntheses of Metal-Oxide Nanocrystals. *Chem. Mater.* **2013**, *25*, 1293−1304.
(379) Bronstein, L. M.; Huang, X.; Retrum, J.; Schmucker, A.; Pink, M.; Stein, B. D.; Dragnea, B. Influence of Iron Oleate Complex Structure on Iron Oxide Nanoparticle Formation. *Chem. Mater.* **2007**, *19*, 3624−3632.
(380) Kwon, S. G.; Piao, Y.; Park, J.; Angappane, S.; Jo, Y.; Hwang, N.-M.; Park, J.-G.; Hyeon, T. Kinetics of Monodisperse Iron Oxide Nanocrystal Formation by "Heating-Up" Process. *J. Am. Chem. Soc.* **2007**, *129*, 12571−12584.
(381) Zhang, Z.; Lu, M.; Xu, H.; Chin, W.-S. Shape-Controlled Synthesis of Zinc Oxide: A Simple Method for the Preparation of Metal Oxide Nanocrystals in Non-Aqueous Medium. *Chem. - Eur. J.* **2007**, *13*, 632−638.
(382) Narayanaswamy, A.; Xu, H.; Pradhan, N.; Kim, M.; Peng, X. Formation of Nearly Monodisperse In_2O_3 Nanodots and Oriented-Attached Nanoflowers: Hydrolysis and Alcoholysis vs Pyrolysis. *J. Am. Chem. Soc.* **2006**, *128*, 10310−10319.
(383) Pham, H. T.; Jeong, H.-D. Non-Monotonic Size Dependence of Electron Mobility in Indium Oxide Nanocrystals Thin Film Transistor. *Bull. Korean Chem. Soc.* **2014**, *35*, 2505−2511.
(384) Sowers, K. L.; Swartz, B.; Krauss, T. D. Chemical Mechanisms of Semiconductor Nanocrystal Synthesis. *Chem. Mater.* **2013**, *25*, 1351−1362.
(385) Hsu, S.-W.; Ngo, C.; Bryks, W.; Tao, A. R. Shape Focusing During the Anisotropic Growth of CuS Triangular Nanoprisms. *Chem. Mater.* **2015**, *27*, 4957−4963.
(386) Li, W.; Shavel, A.; Guzman, R.; Rubio-Garcia, J.; Flox, C.; Fan, J.; Cadavid, D.; Ibáñez, M.; Arbiol, J.; Ramon Morante, J.; et al. Morphology Evolution of $Cu_{2-x}S$ Nanoparticles: From Spheres to Dodecahedrons. *Chem. Commun.* **2011**, *47*, 10332−10334.
(387) Turo, M. J.; Macdonald, J. E. Crystal-Bound vs Surface-Bound Thiols on Nanocrystals. *ACS Nano* **2014**, *8*, 10205−10213.
(388) Pearson, R. G. Hard and Soft Acids and Bases. *J. Am. Chem. Soc.* **1963**, *85*, 3533−3539.
(389) Pearson, R. G. Acids and Bases. *Science* **1966**, *151*, 172−177.
(390) Ho, T.-L. Hard Soft Acids Bases (HSAB) Principle and Organic Chemistry. *Chem. Rev.* **1975**, *75*, 1−20.
(391) Yoshimura, M.; Byrappa, K. Hydrothermal Processing of Materials: Past, Present and Future. *J. Mater. Sci.* **2008**, *43*, 2085−2103.
(392) Darr, J. A.; Zhang, J.; Makwana, N. M.; Weng, X. Continuous Hydrothermal Synthesis of Inorganic Nanoparticles: Applications and Future Directions. *Chem. Rev.* **2017**, *117*, 11125−11238.
(393) Rabenau, A. The Role of Hydrothermal Synthesis in Preparative Chemistry. *Angew. Chem., Int. Ed. Engl.* **1985**, *24*, 1026−1040.
(394) Huang, Q.; Hu, S.; Zhuang, J.; Wang, X. $MoO_{(3-x)}$-Based Hybrids with Tunable Localized Surface Plasmon Resonances: Chemical Oxidation Driving Transformation from Ultrathin Nanosheets to Nanotubes. *Chem. - Eur. J.* **2012**, *18*, 15283−15287.
(395) Buonsanti, R.; Milliron, D. J. Chemistry of Doped Colloidal Nanocrystals. *Chem. Mater.* **2013**, *25*, 1305−1317.
(396) Ghosh, S.; Saha, M.; De, S. K. Tunable Surface Plasmon Resonance and Enhanced Electrical Conductivity of In Doped ZnO Colloidal Nanocrystals. *Nanoscale* **2014**, *6*, 7039−7051.
(397) Dalpian, G. M.; Chelikowsky, J. R. Self-Purification in Semiconductor Nanocrystals. *Phys. Rev. Lett.* **2006**, *96*, 226802.
(398) Liang, X.; Ren, Y.; Bai, S.; Zhang, N.; Dai, X.; Wang, X.; He, H.; Jin, C.; Ye, Z.; Chen, Q.; et al. Colloidal Indium-Doped Zinc Oxide Nanocrystals with Tunable Work Function: Rational Synthesis and Optoelectronic Applications. *Chem. Mater.* **2014**, *26*, 5169−5178.
(399) Tolman, C. A. Steric Effects of Phosphorus Ligands in Organometallic Chemistry and Homogeneous Catalysis. *Chem. Rev.* **1977**, *77*, 313−348.
(400) Lesnyak, V.; George, C.; Genovese, A.; Prato, M.; Casu, A.; Ayyappan, S.; Scarpellini, A.; Manna, L. Alloyed Copper Chalcogenide

DOI: 10.1021/acs.chemrev.7b00613
Chem. Rev. 2018, 118, 3121−3207

Nanoplatelets via Partial Cation Exchange Reactions. *ACS Nano* **2014**, *8*, 8407−8418.
(401) Akkerman, Q. A.; Genovese, A.; George, C.; Prato, M.; Moreels, I.; Casu, A.; Marras, S.; Curcio, A.; Scarpellini, A.; Pellegrino, T.; et al. From Binary Cu_2S to Ternary Cu−In−S and Quaternary Cu−In−Zn−S Nanocrystals with Tunable Composition via Partial Cation Exchange. *ACS Nano* **2015**, *9*, 521−531.
(402) Shanker, G. S.; Tandon, B.; Shibata, T.; Chattopadhyay, S.; Nag, A. Doping Controls Plasmonics, Electrical Conductivity, and Carrier-Mediated Magnetic Coupling in Fe and Sn Codoped In_2O_3 Nanocrystals: Local Structure Is the Key. *Chem. Mater.* **2015**, *27*, 892−900.
(403) Biswas, K.; Rao, C. N. R. Metallic ReO_3 Nanoparticles. *J. Phys. Chem. B* **2006**, *110*, 842−845.
(404) Ferretti, A.; Rogers, D. B.; Goodenough, J. B. The Relation of the Electrical Conductivity in Single Crystals of Rhenium Trioxide to the Conductivities of Sr_2MgReO_6 and Na_xWO_3. *J. Phys. Chem. Solids* **1965**, *26*, 2007−2011.
(405) Corà, F.; Stachiotti, M. G.; Catlow, C. R. A.; Rodriguez, C. O. Transition Metal Oxide Chemistry: Electronic Structure Study of WO_3, ReO_3, and $NaWO_3$. *J. Phys. Chem. B* **1997**, *101*, 3945−3952.
(406) Ghosh, S.; Biswas, K.; Rao, C. N. R. Core−shell Nanoparticles Based on an Oxide Metal: ReO_3@Au (Ag) and ReO_3@SiO_2 (TiO_2). *J. Mater. Chem.* **2007**, *17*, 2412−2417.
(407) Mattox, T. M.; Agrawal, A.; Milliron, D. J. Low Temperature Synthesis and Surface Plasmon Resonance of Colloidal Lanthanum Hexaboride (LaB_6) Nanocrystals. *Chem. Mater.* **2015**, *27*, 6620−6624.
(408) Xiao, L.; Su, Y.; Zhou, X.; Chen, H.; Tan, J.; Hu, T.; Yan, J.; Peng, P. Origins of High Visible Light Transparency and Solar Heat-Shielding Performance in LaB_6. *Appl. Phys. Lett.* **2012**, *101*, 041913.
(409) Zhang, M.; Yuan, L.; Wang, X.; Fan, H.; Wang, X.; Wu, X.; Wang, H.; Qian, Y. A Low-Temperature Route for the Synthesis of Nanocrystalline LaB_6. *J. Solid State Chem.* **2008**, *181*, 294−297.
(410) Yuan, Y.; Zhang, L.; Liang, L.; He, K.; Liu, R.; Min, G. A Solid-State Reaction Route to Prepare LaB_6 Nanocrystals in Vacuum. *Ceram. Int.* **2011**, *37*, 2891−2896.
(411) Zhou, J.; Gao, Y.; Zhang, Z.; Luo, H.; Cao, C.; Chen, Z.; Dai, L.; Liu, X. VO_2 Thermochromic Smart Window for Energy Savings and Generation. *Sci. Rep.* **2013**, *3*, 03029.
(412) Bergerud, A.; Buonsanti, R.; Jordan-Sweet, J. L.; Milliron, D. J. Synthesis and Phase Stability of Metastable Bixbyite V_2O_3 Colloidal Nanocrystals. *Chem. Mater.* **2013**, *25*, 3172−3179.
(413) Aetukuri, N. B.; Gray, A. X.; Drouard, M.; Cossale, M.; Gao, L.; Reid, A. H.; Kukreja, R.; Ohldag, H.; Jenkins, C. A.; Arenholz, E.; et al. Control of the Metal-Insulator Transition in Vanadium Dioxide by Modifying Orbital Occupancy. *Nat. Phys.* **2013**, *9*, 661−666.
(414) Grijalva, H.; Inoue, M.; Boggavarapu, S.; Calvert, P. Amorphous and Crystalline Copper Sulfides, CuS. *J. Mater. Chem.* **1996**, *6*, 1157−1160.
(415) Nozaki, H.; Shibata, K.; Ohhashi, N. Metallic Hole Conduction in CuS. *J. Solid State Chem.* **1991**, *91*, 306−311.
(416) Mazin, I. I. Structural and Electronic Properties of the Two-Dimensional Superconductor CuS with 1 1/3-Valent Copper. *Phys. Rev. B: Condens. Matter Mater. Phys.* **2012**, *85*, 115133.
(417) Yuan, K. D.; Wu, J. J.; Liu, M. L.; Zhang, L. L.; Xu, F. F.; Chen, L. D.; Huang, F. Q. Fabrication and Microstructure of P-Type Transparent Conducting CuS Thin Film and Its Application in Dye-Sensitized Solar Cell. *Appl. Phys. Lett.* **2008**, *93*, 132106.
(418) Morales-García, A.; Soares, A. L.; Dos Santos, E. C.; de Abreu, H. A.; Duarte, H. A. First-Principles Calculations and Electron Density Topological Analysis of Covellite (CuS). *J. Phys. Chem. A* **2014**, *118*, 5823−5831.
(419) Gotsis, H. J.; Barnes, A. C.; Strange, P. Experimental and Theoretical Investigation of the Crystal Structure of CuS. *J. Phys.: Condens. Matter* **1992**, *4*, 10461.
(420) Kumar, P.; Nagarajan, R.; Sarangi, R. Quantitative X-Ray Absorption and Emission Spectroscopies: Electronic Structure Elucidation of Cu_2S and CuS. *J. Mater. Chem. C* **2013**, *1*, 2448−2454.
(421) Zhang, H.; Zhang, Y.; Yu, J.; Yang, D. Phase-Selective Synthesis and Self-Assembly of Monodisperse Copper Sulfide Nanocrystals. *J. Phys. Chem. C* **2008**, *112*, 13390−13394.
(422) Wu, H.; Chen, W. Synthesis and Reaction Temperature-Tailored Self-Assembly of Copper Sulfide Nanoplates. *Nanoscale* **2011**, *3*, 5096−5102.
(423) Alam, R.; Labine, M.; Karwacki, C. J.; Kamat, P. V. Modulation of $Cu_{2-x}S$ Nanocrystal Plasmon Resonance through Reversible Photo-induced Electron Transfer. *ACS Nano* **2016**, *10*, 2880−2886.
(424) White, S. L.; Banerjee, P.; Jain, P. K. Liquid-like Cationic Sub-Lattice in Copper Selenide Clusters. *Nat. Commun.* **2017**, *8*, 14514.
(425) Li, W.; Zamani, R.; Ibanez, M.; Cadavid, D.; Shavel, A.; Morante, J. R.; Arbiol, J.; Cabot, A. Metal Ions to Control the Morphology of Semiconductor Nanoparticles: Copper Selenide Nanocubes. *J. Am. Chem. Soc.* **2013**, *135*, 4664−4667.
(426) Salje, E.; Güttler, B. Anderson Transition and Intermediate Polaron Formation in WO_{3-X} Transport Properties and Optical Absorption. *Philos. Mag. B* **1984**, *50*, 607−620.
(427) Deb, S. K. Opportunities and Challenges of Electrochromic Phenomena in Transition Metal Oxides. *Sol. Energy Mater. Sol. Cells* **1992**, *25*, 327−338.
(428) Greenblatt, M. Molybdenum Oxide Bronzes with Quasi-Low-Dimensional Properties. *Chem. Rev.* **1988**, *88*, 31−53.
(429) Deb, S. K. Opportunities and Challenges in Science and Technology of WO_3 for Electrochromic and Related Applications. *Sol. Energy Mater. Sol. Cells* **2008**, *92*, 245−258.
(430) Tan, X.; Wang, L.; Cheng, C.; Yan, X.; Shen, B.; Zhang, J. Plasmonic MoO_{3-X}@MoO_3 Nanosheets for Highly Sensitive SERS Detection through Nanoshell-Isolated Electromagnetic Enhancement. *Chem. Commun.* **2016**, *52*, 2893−2896.
(431) Li, Y.; Cheng, J.; Liu, Y.; Liu, P.; Cao, W.; He, T.; Chen, R.; Tang, Z. Manipulation of Surface Plasmon Resonance in Sub-Stoichiometry Molybdenum Oxide Nanodots through Charge Carrier Control Technique. *J. Phys. Chem. C* **2017**, *121*, 5208−5214.
(432) Mehra, S.; Bergerud, A.; Milliron, D. J.; Chan, E. M.; Salleo, A. Core/Shell Approach to Dopant Incorporation and Shape Control in Colloidal Zinc Oxide Nanorods. *Chem. Mater.* **2016**, *28*, 3454−3461.
(433) Hamza, M. K.; Bluet, J.-M.; Masenelli-Varlot, K.; Canut, B.; Boisron, O.; Melinon, P.; Masenelli, B. Tunable Mid IR Plasmon in GZO Nanocrystals. *Nanoscale* **2015**, *7*, 12030−12037.
(434) Kanehara, M.; Koike, H.; Yoshinaga, T.; Teranishi, T. Indium Tin Oxide Nanoparticles with Compositionally Tunable Surface Plasmon Resonance Frequencies in the Near-IR Region. *J. Am. Chem. Soc.* **2009**, *131*, 17736−17737.
(435) De Trizio, L.; Buonsanti, R.; Schimpf, A. M.; Llordes, A.; Gamelin, D. R.; Simonutti, R.; Milliron, D. J. Nb-Doped Colloidal TiO_2 Nanocrystals with Tunable Infrared Absorption. *Chem. Mater.* **2013**, *25*, 3383−3390.
(436) Kelchtermans, A.; Elen, K.; Schellens, K.; Conings, B.; Damm, H.; Boyen, H.-G.; D'Haen, J.; Adriaensens, P.; Hardy, A.; Van Bael, M. K. Relation between Synthesis Conditions, Dopant Position and Charge Carriers in Aluminium-Doped ZnO Nanoparticles. *RSC Adv.* **2013**, *3*, 15254−15262.
(437) Kemmitt, T.; Ingham, B.; Linklater, R. Optimization of Sol−Gel-Formed ZnO:Al Processing Parameters by Observation of Dopant Ion Location Using Solid-State ^{27}Al NMR Spectrometry. *J. Phys. Chem. C* **2011**, *115*, 15031−15039.
(438) Paudel, T. R.; Zakutayev, A.; Lany, S.; d'Avezac, M.; Zunger, A. Doping Rules and Doping Prototypes in A_2BO_4 Spinel Oxides. *Adv. Funct. Mater.* **2011**, *21*, 4493−4501.
(439) Shi, Y.; Ndione, P. F.; Lim, L. Y.; Sokaras, D.; Weng, T.-C.; Nagaraja, A. R.; Karydas, A. G.; Perkins, J. D.; Mason, T. O.; Ginley, D. S.; et al. Self-Doping and Electrical Conductivity in Spinel Oxides: Experimental Validation of Doping Rules. *Chem. Mater.* **2014**, *26*, 1867−1873.
(440) Shannon, R. D. Revised Effective Ionic Radii and Systematic Studies of Interatomic Distances in Halides and Chalcogenides. *Acta Crystallogr., Sect. A: Cryst. Phys., Diffr., Theor. Gen. Crystallogr.* **1976**, *32*, 751−767.

DOI: 10.1021/acs.chemrev.7b00613
Chem. Rev. 2018, 118, 3121−3207

(441) Ghosh, S.; Saha, M.; Dev Ashok, V.; Dalal, B.; De, S. K. Tunable Surface Plasmon Resonance in Sn-Doped Zn−Cd−O Alloyed Nanocrystals. *J. Phys. Chem. C* **2015**, *119*, 1180−1187.
(442) Guria, A. K.; Pradhan, N. Doped or Not Doped: Ionic Impurities for Influencing the Phase and Growth of Semiconductor Nanocrystals. *Chem. Mater.* **2016**, *28*, 5224−5237.
(443) Xia, Y.; Xiong, Y.; Lim, B.; Skrabalak, S. E. Shape-Controlled Synthesis of Metal Nanocrystals: Simple Chemistry Meets Complex Physics? *Angew. Chem., Int. Ed.* **2009**, *48*, 60−103.
(444) Polarz, S. Shape Matters: Anisotropy of the Morphology of Inorganic Colloidal Particles − Synthesis and Function. *Adv. Funct. Mater.* **2011**, *21*, 3214−3230.
(445) Herring, C. Some Theorems on the Free Energies of Crystal Surfaces. *Phys. Rev.* **1951**, *82*, 87−93.
(446) Vitos, L.; Ruban, A. V.; Skriver, H. L.; Kollár, J. The Surface Energy of Metals. *Surf. Sci.* **1998**, *411*, 186−202.
(447) Mackenzie, J. K.; Moore, A. J. W.; Nicholas, J. F. Bonds Broken at Atomically Flat Crystal Surfaces—I: Face-Centred and Body-Centred Cubic Crystals. *J. Phys. Chem. Solids* **1962**, *23*, 185−196.
(448) Mackenzie, J. K.; Nicholas, J. F. Bonds Broken at Atomically Flat Crystal Surfaces—II: Crystals Containing Many Atoms in a Primitive Unit Cell. *J. Phys. Chem. Solids* **1962**, *23*, 197−205.
(449) Walsh, A.; Catlow, C. R. A. Structure, Stability and Work Functions of the Low Index Surfaces of Pure Indium Oxide and Sn-Doped Indium Oxide (ITO) from Density Functional Theory. *J. Mater. Chem.* **2010**, *20*, 10438−10444.
(450) Manna, L.; Wang; Cingolani, R.; Alivisatos, A. P. First-Principles Modeling of Unpassivated and Surfactant-Passivated Bulk Facets of Wurtzite CdSe: A Model System for Studying the Anisotropic Growth of CdSe Nanocrystals. *J. Phys. Chem. B* **2005**, *109*, 6183−6192.
(451) Zhang, J.-M.; Ma, F.; Xu, K.-W. Calculation of the Surface Energy of FCC Metals with Modified Embedded-Atom Method. *Appl. Surf. Sci.* **2004**, *229*, 34−42.
(452) Khurshid, H.; Li, W.; Chandra, S.; Phan, M.-H.; Hadjipanayis, G. C.; Mukherjee, P.; Srikanth, H. Mechanism and Controlled Growth of Shape and Size Variant Core/Shell FeO/Fe_3O_4 Nanoparticles. *Nanoscale* **2013**, *5*, 7942−7952.
(453) Ung, D.; Tung, L. D.; Caruntu, G.; Delaportas, D.; Alexandrou, I.; Prior, I. A.; Thanh, N. T. K. Variant Shape Growth of Nanoparticles of Metallic Fe−Pt, Fe−Pd and Fe−Pt−Pd Alloys. *CrystEngComm* **2009**, *11*, 1309−1316.
(454) Xiong, Y.; McLellan, J. M.; Chen, J.; Yin, Y.; Li, Z.-Y.; Xia, Y. Kinetically Controlled Synthesis of Triangular and Hexagonal Nanoplates of Palladium and Their SPR/SERS Properties. *J. Am. Chem. Soc.* **2005**, *127*, 17118−17127.
(455) van der Stam, W.; Gradmann, S.; Altantzis, T.; Ke, X.; Baldus, M.; Bals, S.; de Mello Donega, C. Shape Control of Colloidal $Cu_{2-x}S$ Polyhedral Nanocrystals by Tuning the Nucleation Rates. *Chem. Mater.* **2016**, *28*, 6705−6715.
(456) Choi, D.-H.; Jeong, G.-H.; Kim, S.-W. Fabrication of Size and Shape Controlled Cadmium Oxide Nanocrystals. *Bull. Korean Chem. Soc.* **2011**, *32*, 3851−3852.
(457) Chen, L.; Sakamoto, M.; Haruta, M.; Nemoto, T.; Sato, R.; Kurata, H.; Teranishi, T. Tin Ion Directed Morphology Evolution of Copper Sulfide Nanoparticles and Tuning of Their Plasmonic Properties via Phase Conversion. *Langmuir* **2016**, *32*, 7582−7587.
(458) Wang, L.-S.; Sheng, T.-L.; Wang, X.; Chen, D.-B.; Hu, S.-M.; Fu, R.-B.; Xiang, S.-C.; Wu, X.-T. Self-Assembly of Luminescent Sn(IV)/Cu/S Clusters Using Metal Thiolates as Metalloligands. *Inorg. Chem.* **2008**, *47*, 4054−4059.
(459) Wang, X.; Sheng, T.-L.; Fu, R.-B.; Hu, S.-M.; Xiang, S.-C.; Wang, L.-S.; Wu, X.-T. Assembly of a Heterometallic Polynuclear Sn(IV)−CuI Cluster Based on $Sn(Edt)_2$ (Edt = Ethane-1,2-Dithiolate) as a Metalloligand. *Inorg. Chem.* **2006**, *45*, 5236−5238.
(460) van der Stam, W.; Akkerman, Q. A.; Ke, X.; van Huis, M. A.; Bals, S.; de Mello Donega, C. Solution-Processable Ultrathin Size- and Shape-Controlled Colloidal $Cu_{2-x}S$ Nanosheets. *Chem. Mater.* **2015**, *27*, 283−291.
(461) Nørby, P.; Johnsen, S.; Iversen, B. B. In Situ X-Ray Diffraction Study of the Formation, Growth, and Phase Transition of Colloidal $Cu_{2-x}S$ Nanocrystals. *ACS Nano* **2014**, *8*, 4295−4303.
(462) van der Stam, W.; Rabouw, F. T.; Geuchies, J. J.; Berends, A. C.; Hinterding, S. O. M.; Geitenbeek, R. G.; van der Lit, J.; Prévost, S.; Petukhov, A. V.; de Mello Donega, C. In Situ Probing of Stack-Templated Growth of Ultrathin $Cu_{2-x}S$ Nanosheets. *Chem. Mater.* **2016**, *28*, 6381−6389.
(463) Kovalenko, M. V.; Bodnarchuk, M. I.; Lechner, R. T.; Hesser, G.; Schäffler, F.; Heiss, W. Fatty Acid Salts as Stabilizers in Size- and Shape-Controlled Nanocrystal Synthesis: The Case of Inverse Spinel Iron Oxide. *J. Am. Chem. Soc.* **2007**, *129*, 6352−6353.
(464) Peng, X. Mechanisms for the Shape-Control and Shape-Evolution of Colloidal Semiconductor Nanocrystals. *Adv. Mater.* **2003**, *15*, 459−463.
(465) Goniakowski, J.; Finocchi, F.; Noguera, C. Polarity of Oxide Surfaces and Nanostructures. *Rep. Prog. Phys.* **2008**, *71*, 016501.
(466) Noguera, C. Polar Oxide Surfaces. *J. Phys.: Condens. Matter* **2000**, *12*, R367.
(467) Rempel, J. Y.; Trout, B. L.; Bawendi, M. G.; Jensen, K. F. Density Functional Theory Study of Ligand Binding on CdSe (0001), (0001), and (1120) Single Crystal Relaxed and Reconstructed Surfaces: Implications for Nanocrystalline Growth. *J. Phys. Chem. B* **2006**, *110*, 18007−18016.
(468) Bealing, C. R.; Baumgardner, W. J.; Choi, J. J.; Hanrath, T.; Hennig, R. G. Predicting Nanocrystal Shape through Consideration of Surface-Ligand Interactions. *ACS Nano* **2012**, *6*, 2118−2127.
(469) Yang, H. G.; Sun, C. H.; Qiao, S. Z.; Zou, J.; Liu, G.; Smith, S. C.; Cheng, H. M.; Lu, G. Q. Anatase TiO_2 Single Crystals with a Large Percentage of Reactive Facets. *Nature* **2008**, *453*, 638−641.
(470) Liu, Y. Q.; Wang, F. X.; Xiao, Y.; Peng, H. D.; Zhong, H. J.; Liu, Z. H.; Pan, G. B. Facile Microwave-Assisted Synthesis of Klockmannite CuSe Nanosheets and Their Exceptional Electrical Properties. *Sci. Rep.* **2015**, *4*, 5998.
(471) Millstone, J. E.; Wei, W.; Jones, M. R.; Yoo, H.; Mirkin, C. A. Iodide Ions Control Seed-Mediated Growth of Anisotropic Gold Nanoparticles. *Nano Lett.* **2008**, *8*, 2526−2529.
(472) Magnussen, O. M. Ordered Anion Adlayers on Metal Electrode Surfaces. *Chem. Rev.* **2002**, *102*, 679−726.
(473) Gao, Y.; Cao, C.; Dai, L.; Luo, H.; Kanehira, M.; Ding, Y.; Wang, Z. L. Phase and Shape Controlled VO2 Nanostructures by Antimony Doping. *Energy Environ. Sci.* **2012**, *5*, 8708−8715.
(474) Cao, C.; Gao, Y.; Luo, H. Pure Single-Crystal Rutile Vanadium Dioxide Powders: Synthesis, Mechanism and Phase-Transformation Property. *J. Phys. Chem. C* **2008**, *112*, 18810−18814.
(475) Mehra, S.; Chan, E. M.; Salleo, A. Modular Synthetic Design Enables Precise Control of Shape and Doping in Colloidal Zinc Oxide Nanorods. *J. Mater. Chem. C* **2015**, *3*, 7172−7179.
(476) Mangolini, L.; Kortshagen, U. Selective Nanoparticle Heating: Another Form of Nonequilibrium in Dusty Plasmas. *Phys. Rev. E* **2009**, *79*, 026405.
(477) Hirasawa, M.; Orii, T.; Seto, T. Size-Dependent Crystallization of Si Nanoparticles. *Appl. Phys. Lett.* **2006**, *88*, 093119.
(478) Daugherty, J. E.; Graves, D. B. Particulate Temperature in Radio Frequency Glow Discharges. *J. Vac. Sci. Technol., A* **1993**, *11*, 1126−1131.
(479) Boufendi, L.; Bouchoule, A.; Porteous, R. K.; Blondeau, J. P.; Plain, A.; Laure, C. Particle−particle Interactions in Dusty Plasmas. *J. Appl. Phys.* **1993**, *73*, 2160−2162.
(480) Zhang, L.; Yin, L.; Wang, C.; lun, N.; Qi, Y.; Xiang, D. Origin of Visible Photoluminescence of ZnO Quantum Dots: Defect-Dependent and Size-Dependent. *J. Phys. Chem. C* **2010**, *114*, 9651−9658.
(481) Kaftelen, H.; Ocakoglu, K.; Thomann, R.; Tu, S.; Weber, S.; Erdem, E. EPR and Photoluminescence Spectroscopy Studies on the Defect Structure of ZnO Nanocrystals. *Phys. Rev. B: Condens. Matter Mater. Phys.* **2012**, *86*, 014113.
(482) Whitaker, K. M.; Ochsenbein, S. T.; Polinger, V. Z.; Gamelin, D. R. Electron Confinement Effects in the EPR Spectra of Colloidal n-Type ZnO Quantum Dots. *J. Phys. Chem. C* **2008**, *112*, 14331−14335.

DOI: 10.1021/acs.chemrev.7b00613
Chem. Rev. 2018, 118, 3121−3207

(483) Cohn, A. W.; Kittilstved, K. R.; Gamelin, D. R. Tuning the Potentials of "Extra" Electrons in Colloidal n-Type ZnO Nanocrystals via Mg^{2+} Substitution. *J. Am. Chem. Soc.* **2012**, *134*, 7937−7943.
(484) Thimsen, E.; Kortshagen, U. R.; Aydil, E. S. Nonthermal Plasma Synthesis of Metal Sulfide Nanocrystals from Metalorganic Vapor and Elemental Sulfur. *J. Phys. D: Appl. Phys.* **2015**, *48*, 314004.
(485) Li, J.; Gao, L.; Sun, J.; Zhang, Q.; Guo, J.; Yan, D. Synthesis of Nanocrystalline Titanium Nitride Powders by Direct Nitridation of Titanium Oxide. *J. Am. Ceram. Soc.* **2001**, *84*, 3045−3047.
(486) Takada, N.; Sasaki, T.; Sasaki, K. Synthesis of Crystalline TiN and Si Particles by Laser Ablation in Liquid Nitrogen. *Appl. Phys. A: Mater. Sci. Process.* **2008**, *93*, 833−836.
(487) Karan, N. S.; Chen, Y.; Liu, Z.; Beaulac, R. Solution−Liquid−Solid Approach to Colloidal Indium Nitride Nanoparticles from Simple Alkylamide Precursors. *Chem. Mater.* **2016**, *28*, 5601−5605.
(488) Oliva-Chatelain, B. L.; Ticich, T. M.; Barron, A. R. Doping Silicon Nanocrystals and Quantum Dots. *Nanoscale* **2016**, *8*, 1733−1745.
(489) Oliva, B. L.; Barron, A. R. Thin Films of Silica Imbedded Silicon and Germanium Quantum Dots by Solution Processing. *Mater. Sci. Semicond. Process.* **2012**, *15*, 713−721.
(490) Veinot, J. G. C. Synthesis, Surface Functionalization, and Properties of Freestanding Silicon Nanocrystals. *Chem. Commun.* **2006**, 4160−4168.
(491) Ghosh, B.; Shirahata, N. Colloidal Silicon Quantum Dots: Synthesis and Luminescence Tuning from the near-UV to the near-IR Range. *Sci. Technol. Adv. Mater.* **2014**, *15*, 014207.
(492) English, D. S.; Pell, L. E.; Yu, Z.; Barbara, P. F.; Korgel, B. A. Size Tunable Visible Luminescence from Individual Organic Monolayer Stabilized Silicon Nanocrystal Quantum Dots. *Nano Lett.* **2002**, *2*, 681−685.
(493) Hessel, C. M.; Henderson, E. J.; Veinot, J. G. C. Hydrogen Silsesquioxane: A Molecular Precursor for Nanocrystalline Si−SiO_2 Composites and Freestanding Hydride-Surface-Terminated Silicon Nanoparticles. *Chem. Mater.* **2006**, *18*, 6139−6146.
(494) Yu, Y.; Rowland, C. E.; Schaller, R. D.; Korgel, B. A. Synthesis and Ligand Exchange of Thiol-Capped Silicon Nanocrystals. *Langmuir* **2015**, *31*, 6886−6893.
(495) Baldwin, R. K.; Zou, J.; Pettigrew, K. A.; Yeagle, G. J.; Britt, R. D.; Kauzlarich, S. M. The Preparation of a Phosphorus Doped Silicon Film from Phosphorus Containing Silicon Nanoparticles. *Chem. Commun.* **2006**, *0*, 658−660.
(496) Murthy, T. U. M. S.; Miyamoto, N.; Shimbo, M.; Nishizawa, J. Gas-Phase Nucleation during the Thermal Decomposition of Silane in Hydrogen. *J. Cryst. Growth* **1976**, *33*, 1−7.
(497) Wilson, W. L.; Szajowski, P. F.; Brus, L. E. Quantum Confinement in Size-Selected, Surface-Oxidized Silicon Nanocrystals. *Science* **1993**, *262*, 1242−1244.
(498) Brus, L. Luminescence of Silicon Materials: Chains, Sheets, Nanocrystals, Nanowires, Microcrystals, and Porous Silicon. *J. Phys. Chem.* **1994**, *98*, 3575−3581.
(499) Gao, Y.; Pi, X.; Wang, X.; Yuan, T.; Jiang, Q.; Gresback, R.; Lu, J.; Yang, D. Structures, Oxidation, and Charge Transport of Phosphorus-Doped Germanium Nanocrystals. *Part. Part. Syst. Charact.* **2016**, *33*, 271−278.
(500) Degoli, E.; Cantele, G.; Luppi, E.; Magri, R.; Ninno, D.; Bisi, O.; Ossicini, S. Ab Initio structural and electronic properties of hydrogenated silicon nanoclusters in the ground and excited state. *Phys. Rev. B: Condens. Matter Mater. Phys.* **2004**, *69*, 155411.
(501) Niesar, S.; Stegner, A. R.; Pereira, R. N.; Hoeb, M.; Wiggers, H.; Brandt, M. S.; Stutzmann, M. Defect Reduction in Silicon Nanoparticles by Low-Temperature Vacuum Annealing. *Appl. Phys. Lett.* **2010**, *96*, 193112.
(502) Viswanatha, R.; Sapra, S.; Sen Gupta, S.; Satpati, B.; Satyam, P. V.; Dev, B. N.; Sarma, D. D. Synthesis and Characterization of Mn-Doped ZnO Nanocrystals. *J. Phys. Chem. B* **2004**, *108*, 6303−6310.
(503) Liu, J.; Katahara, J.; Li, G.; Coe-Sullivan, S.; Hurt, R. H. Degradation Products from Consumer Nanocomposites: A Case Study on Quantum Dot Lighting. *Environ. Sci. Technol.* **2012**, *46*, 3220−3227.
(504) Novo, C.; Funston, A. M.; Gooding, A. K.; Mulvaney, P. Electrochemical Charging of Single Gold Nanorods. *J. Am. Chem. Soc.* **2009**, *131*, 14664−14666.
(505) Ung, T.; Giersig, M.; Dunstan, D.; Mulvaney, P. Spectroelectrochemistry of Colloidal Silver. *Langmuir* **1997**, *13*, 1773−1782.
(506) Huttanus, H. M.; Graugnard, E.; Yurke, B.; Knowlton, W. B.; Kuang, W.; Hughes, W. L.; Lee, J. Enhanced DNA Sensing via Catalytic Aggregation of Gold Nanoparticles. *Biosens. Bioelectron.* **2013**, *50*, 382−386.
(507) Yockell-Lelièvre, H.; Lussier, F.; Masson, J.-F. Influence of the Particle Shape and Density of Self-Assembled Gold Nanoparticle Sensors on LSPR and SERS. *J. Phys. Chem. C* **2015**, *119*, 28577−28585.
(508) Becker, J.; Trügler, A.; Jakab, A.; Hohenester, U.; Sönnichsen, C. The Optimal Aspect Ratio of Gold Nanorods for Plasmonic Bio-Sensing. *Plasmonics* **2010**, *5*, 161−167.
(509) Lin, S.-Y.; Wu, S.-H.; Chen, C. A Simple Strategy for Prompt Visual Sensing by Gold Nanoparticles: General Applications of Interparticle Hydrogen Bonds. *Angew. Chem., Int. Ed.* **2006**, *45*, 4948−4951.
(510) Shim, M.; Guyot-Sionnest, P. n-Type Colloidal Semiconductor Nanocrystals. *Nature* **2000**, *407*, 981−983.
(511) Valdez, C. N.; Schimpf, A. M.; Gamelin, D. R.; Mayer, J. M. Proton-Controlled Reduction of ZnO Nanocrystals: Effects of Molecular Reductants, Cations, and Thermodynamic Limitations. *J. Am. Chem. Soc.* **2016**, *138*, 1377−1385.
(512) Padilha, L. A.; Stewart, J. T.; Sandberg, R. L.; Bae, W. K.; Koh, W.-K.; Pietryga, J. M.; Klimov, V. I. Carrier Multiplication in Semiconductor Nanocrystals: Influence of Size, Shape, and Composition. *Acc. Chem. Res.* **2013**, *46*, 1261−1269.
(513) Koh, W.; Koposov, A. Y.; Stewart, J. T.; Pal, B. N.; Robel, I.; Pietryga, J. M.; Klimov, V. I. Heavily Doped *n*-Type PbSe and PbS Nanocrystals Using Ground-State Charge Transfer from Cobaltocene. *Sci. Rep.* **2013**, *3*, 02004.
(514) Sturaro, M.; Della Gaspera, E.; Michieli, N.; Cantalini, C.; Emamjomeh, S. M.; Guglielmi, M.; Martucci, A. Degenerately Doped Metal Oxide Nanocrystals as Plasmonic and Chemoresistive Gas Sensors. *ACS Appl. Mater. Interfaces* **2016**, *8*, 30440−30448.
(515) Diroll, B. T.; Schramke, K. S.; Guo, P.; Kortshagen, U. R.; Schaller, R. D. Ultrafast Silicon Photonics with Visible to Mid-Infrared Pumping of Silicon Nanocrystals. *Nano Lett.* **2017**, *17*, 6409−6414.
(516) Mridha, S.; Basak, D. Aluminium Doped ZnO Films: Electrical, Optical and Photoresponse Studies. *J. Phys. D: Appl. Phys.* **2007**, *40*, 6902.
(517) Gavrilyuk, A. I. Photochromism in WO3 Thin Films. *Electrochim. Acta* **1999**, *44*, 3027−3037.
(518) Guyot-Sionnest, P.; Hines, M. A. Intraband Transitions in Semiconductor Nanocrystals. *Appl. Phys. Lett.* **1998**, *72*, 686−688.
(519) Shim, M.; Shilov, S. V.; Braiman, M. S.; Guyot-Sionnest, P. Long-Lived Delocalized Electron States in Quantum Dots: A Step-Scan Fourier Transform Infrared Study. *J. Phys. Chem. B* **2000**, *104*, 1494−1496.
(520) Schimpf, A. M.; Thakkar, N.; Gunthardt, C. E.; Masiello, D. J.; Gamelin, D. R. Charge-Tunable Quantum Plasmons in Colloidal Semiconductor Nanocrystals. *ACS Nano* **2014**, *8*, 1065−1072.
(521) Liu, W. K.; Whitaker, K. M.; Smith, A. L.; Kittilstved, K. R.; Robinson, B. H.; Gamelin, D. R. Room-Temperature Electron Spin Dynamics in Free-Standing ZnO Quantum Dots. *Phys. Rev. Lett.* **2007**, *98*, 186804.
(522) Cohn, A. W.; Schimpf, A. M.; Gunthardt, C. E.; Gamelin, D. R. Size-Dependent Trap-Assisted Auger Recombination in Semiconductor Nanocrystals. *Nano Lett.* **2013**, *13*, 1810−1815.
(523) Braten, M. N.; Gamelin, D. R.; Mayer, J. M. Reaction Dynamics of Proton-Coupled Electron Transfer from Reduced ZnO Nanocrystals. *ACS Nano* **2015**, *9*, 10258−10267.
(524) Hayoun, R.; Whitaker, K. M.; Gamelin, D. R.; Mayer, J. M. Electron Transfer Between Colloidal ZnO Nanocrystals. *J. Am. Chem. Soc.* **2011**, *133*, 4228−4231.

DOI: 10.1021/acs.chemrev.7b00613
Chem. Rev. 2018, 118, 3121−3207

(525) Schrauben, J. N.; Hayoun, R.; Valdez, C. N.; Braten, M.; Fridley, L.; Mayer, J. M. Titanium and Zinc Oxide Nanoparticles Are Proton-Coupled Electron Transfer Agents. *Science* **2012**, *336*, 1298−1301.
(526) Johns, R. W.; Blemker, M. A.; Azzaro, M. S.; Heo, S.; Runnerstrom, E. L.; Milliron, D. J.; Roberts, S. T. Charge Carrier Concentration Dependence of Ultrafast Plasmonic Relaxation in Conducting Metal Oxide Nanocrystals. *J. Mater. Chem. C* **2017**, *5*, 5757−5763.
(527) Guo, P.; Schaller, R. D.; Ketterson, J. B.; Chang, R. P. H. Ultrafast Switching of Tunable Infrared Plasmons in Indium Tin Oxide Nanorod Arrays with Large Absolute Amplitude. *Nat. Photonics* **2016**, *10*, 267−273.
(528) Della Valle, G.; Scotognella, F.; Kandada, A. R. S.; Zavelani-Rossi, M.; Li, H.; Conforti, M.; Longhi, S.; Manna, L.; Lanzani, G.; Tassone, F. Ultrafast Optical Mapping of Nonlinear Plasmon Dynamics in $Cu_{2-x}Se$ Nanoparticles. *J. Phys. Chem. Lett.* **2013**, *4*, 3337−3344.
(529) Scotognella, F.; Della Valle, G.; Srimath Kandada, A. R.; Dorfs, D.; Zavelani-Rossi, M.; Conforti, M.; Miszta, K.; Comin, A.; Korobchevskaya, K.; Lanzani, G.; et al. Plasmon Dynamics in Colloidal $Cu_{(2)-X}Se$ Nanocrystals. *Nano Lett.* **2011**, *11*, 4711−4717.
(530) Kinsey, N.; DeVault, C.; Kim, J.; Ferrera, M.; Shalaev, V. M.; Boltasseva, A. Epsilon-near-Zero Al-Doped ZnO for Ultrafast Switching at Telecom Wavelengths. *Optica* **2015**, *2*, 616.
(531) Ludwig, J.; An, L.; Pattengale, B.; Kong, Q.; Zhang, X.; Xi, P.; Huang, J. Ultrafast Hole Trapping and Relaxation Dynamics in p-Type CuS Nanodisks. *J. Phys. Chem. Lett.* **2015**, *6*, 2671−2675.
(532) Nishiyama, Y.; Imaeda, K.; Imura, K.; Okamoto, H. Plasmon Dephasing in Single Gold Nanorods Observed By Ultrafast Time-Resolved Near-Field Optical Microscopy. *J. Phys. Chem. C* **2015**, *119*, 16215−16222.
(533) Jain, P. K.; Qian, W.; El-Sayed, M. A. Ultrafast Electron Relaxation Dynamics in Coupled Metal Nanoparticles in Aggregates. *J. Phys. Chem. B* **2006**, *110*, 136−142.
(534) Sönnichsen, C.; Franzl, T.; Wilk, T.; von Plessen, G.; Feldmann, J.; Wilson, O.; Mulvaney, P. Drastic Reduction of Plasmon Damping in Gold Nanorods. *Phys. Rev. Lett.* **2002**, *88*, 077402.
(535) Roller, E.-M.; Besteiro, L. V.; Pupp, C.; Khorashad, L. K.; Govorov, A. O.; Liedl, T. Hotspot-Mediated Non-Dissipative and Ultrafast Plasmon Passage. *Nat. Phys.* **2017**, *13*, 761−765.
(536) Hogan, N. J.; Urban, A. S.; Ayala-Orozco, C.; Pimpinelli, A.; Nordlander, P.; Halas, N. J. Nanoparticles Heat through Light Localization. *Nano Lett.* **2014**, *14*, 4640−4645.
(537) Tian, Q.; Jiang, F.; Zou, R.; Liu, Q.; Chen, Z.; Zhu, M.; Yang, S.; Wang, J.; Wang, J.; Hu, J. Hydrophilic Cu_9S_5 Nanocrystals: A Photothermal Agent with a 25.7% Heat Conversion Efficiency for Photothermal Ablation of Cancer Cells in Vivo. *ACS Nano* **2011**, *5*, 9761−9771.
(538) Barile, C. J.; Slotcavage, D. J.; McGehee, M. D. Polymer−Nanoparticle Electrochromic Materials That Selectively Modulate Visible and Near-Infrared Light. *Chem. Mater.* **2016**, *28*, 1439−1445.
(539) Moon, H. C.; Lodge, T. P.; Frisbie, C. D. Solution Processable, Electrochromic Ion Gels for Sub-1 V, Flexible Displays on Plastic. *Chem. Mater.* **2015**, *27*, 1420−1425.
(540) zum Felde, U.; Haase, M.; Weller, H. Electrochromism of Highly Doped Nanocrystalline SnO_2:Sb. *J. Phys. Chem. B* **2000**, *104*, 9388−9395.
(541) Boschloo, G.; Fitzmaurice, D. Spectroelectrochemistry of Highly Doped Nanostructured Tin Dioxide Electrodes. *J. Phys. Chem. B* **1999**, *103*, 3093−3098.
(542) Nguyen, W. H.; Barile, C. J.; McGehee, M. D. Small Molecule Anchored to Mesoporous ITO for High-Contrast Black Electrochromics. *J. Phys. Chem. C* **2016**, *120*, 26336−26341.
(543) Wang, J.; Polleux, J.; Lim, J.; Dunn, B. Pseudocapacitive Contributions to Electrochemical Energy Storage in TiO_2 (Anatase) Nanoparticles. *J. Phys. Chem. C* **2007**, *111*, 14925−14931.
(544) Granqvist, C. G. Electrochromics for Smart Windows: Oxide-Based Thin Films and Devices. *Thin Solid Films* **2014**, *564*, 1−38.
(545) Hotchandani, S.; Kamat, P. V. Photoelectrochemistry of Semiconductor ZnO Particulate Films. *J. Electrochem. Soc.* **1992**, *139*, 1630−1634.
(546) Hoyer, P.; Weller, H. Potential-Dependent Electron Injection in Nanoporous Colloidal ZnO Films. *J. Phys. Chem.* **1995**, *99*, 14096−14100.
(547) Wang, C.; Shim, M.; Guyot-Sionnest, P. Electrochromic Nanocrystal Quantum Dots. *Science* **2001**, *2*, 2390−2392.
(548) Keuleyan, S.; Kohler, J.; Guyot-Sionnest, P. Photoluminescence of Mid-Infrared HgTe Colloidal Quantum Dots. *J. Phys. Chem. C* **2014**, *118*, 2749−2753.
(549) Wehrenberg, B. L.; Guyot-Sionnest, P. Electron and Hole Injection in PbSe Quantum Dot Films. *J. Am. Chem. Soc.* **2003**, *125*, 7806−7807.
(550) Liu, H.; Keuleyan, S.; Guyot-Sionnest, P. N- and p-Type HgTe Quantum Dot Films. *J. Phys. Chem. C* **2012**, *116*, 1344−1349.
(551) Boehme, S. C.; Wang, H.; Siebbeles, L. D. A.; Vanmaekelbergh, D.; Houtepen, A. J. Electrochemical Charging of CdSe Quantum Dot Films: Dependence on Void Size and Counterion Proximity. *ACS Nano* **2013**, *7*, 2500−2508.
(552) Llordés, A.; Wang, Y.; Fernandez-Martinez, A.; Xiao, P.; Lee, T.; Poulain, A.; Zandi, O.; Saez Cabezas, C. A.; Henkelman, G.; Milliron, D. J. Linear Topology in Amorphous Metal Oxide Electrochromic Networks Obtained via Low-Temperature Solution Processing. *Nat. Mater.* **2016**, *15*, 1267−1273.
(553) DeForest, N.; Shehabi, A.; Selkowitz, S.; Milliron, D. J. A Comparative Energy Analysis of Three Electrochromic Glazing Technologies in Commercial and Residential Buildings. *Appl. Energy* **2017**, *192*, 95−109.
(554) DeForest, N.; Shehabi, A.; O'Donnell, J.; Garcia, G.; Greenblatt, J.; Lee, E. S.; Selkowitz, S.; Milliron, D. J. United States Energy and CO_2 Savings Potential from Deployment of Near-Infrared Electrochromic Window Glazings. *Build. Environ.* **2015**, *89*, 107−117.
(555) Llorente, V. B.; Dzhagan, V. M.; Gaponik, N.; Iglesias, R. A.; Zahn, D. R. T.; Lesnyak, V. Electrochemical Tuning of Localized Surface Plasmon Resonance in Copper Chalcogenide Nanocrystals. *J. Phys. Chem. C* **2017**, *121*, 18244−18253.
(556) van der Stam, W.; Gudjonsdottir, S.; Evers, W. H.; Houtepen, A. J. Switching between Plasmonic and Fluorescent Copper Sulfide Nanocrystals. *J. Am. Chem. Soc.* **2017**, *139*, 13208−13217.
(557) Abb, M.; Wang, Y.; Papasimakis, N.; de Groot, C. H.; Muskens, O. L. Surface-Enhanced Infrared Spectroscopy Using Metal Oxide Plasmonic Antenna Arrays. *Nano Lett.* **2014**, *14*, 346−352.
(558) Huck, C.; Neubrech, F.; Vogt, J.; Toma, A.; Gerbert, D.; Katzmann, J.; Härtling, T.; Pucci, A. Surface-Enhanced Infrared Spectroscopy Using Nanometer-Sized Gaps. *ACS Nano* **2014**, *8*, 4908−4914.
(559) Adato, R.; Altug, H. In-Situ Ultra-Sensitive Infrared Absorption Spectroscopy of Biomolecule Interactions in Real Time with Plasmonic Nanoantennas. *Nat. Commun.* **2013**, *4*, 2154.
(560) Ishikawa, A.; Hara, S.; Tanaka, T.; Hayashi, Y.; Tsuruta, K. Cross-Polarized Surface-Enhanced Infrared Spectroscopy by Fano-Resonant Asymmetric Metamaterials. *Sci. Rep.* **2017**, *7*, 3205.
(561) Kundu, J.; Le, F.; Nordlander, P.; Halas, N. J. Surface Enhanced Infrared Absorption (SEIRA) Spectroscopy on Nanoshell Aggregate Substrates. *Chem. Phys. Lett.* **2008**, *452*, 115−119.
(562) Hu, H.; Yang, X.; Zhai, F.; Hu, D.; Liu, R.; Liu, K.; Sun, Z.; Dai, Q. Far-Field Nanoscale Infrared Spectroscopy of Vibrational Fingerprints of Molecules with Graphene Plasmons. *Nat. Commun.* **2016**, *7*, 12334.
(563) Schlücker, S. Surface-Enhanced Raman Spectroscopy: Concepts and Chemical Applications. *Angew. Chem., Int. Ed.* **2014**, *53*, 4756−4795.
(564) Stiles, P. L.; Dieringer, J. A.; Shah, N. C.; Van Duyne, R. P. Surface-Enhanced Raman Spectroscopy. *Annu. Rev. Anal. Chem.* **2008**, *1*, 601−626.
(565) Yang, Z.; Li, Q.; Ruan, F.; Li, Z.; Ren, B.; Xu, H.; Tian, Z. FDTD for Plasmonics: Applications in Enhanced Raman Spectroscopy. *Chin. Sci. Bull.* **2010**, *55*, 2635−2642.

DOI: 10.1021/acs.chemrev.7b00613
Chem. Rev. 2018, 118, 3121−3207

(566) Akselrod, G. M.; Weidman, M. C.; Li, Y.; Argyropoulos, C.; Tisdale, W. A.; Mikkelsen, M. H. Efficient Nanosecond Photoluminescence from Infrared PbS Quantum Dots Coupled to Plasmonic Nanoantennas. *ACS Photonics* **2016**, *3*, 1741−1746.
(567) Marin, B. C.; Hsu, S.-W.; Chen, L.; Lo, A.; Zwissler, D. W.; Liu, Z.; Tao, A. R. Plasmon-Enhanced Two-Photon Absorption in Photoluminescent Semiconductor Nanocrystals. *ACS Photonics* **2016**, *3*, 526−531.
(568) Park, J.; Estrada, A.; Sharp, K.; Sang, K.; Schwartz, J. A.; Smith, D. K.; Coleman, C.; Payne, J. D.; Korgel, B. A.; Dunn, A. K.; et al. Two-Photon-Induced Photoluminescence Imaging of Tumors Using near-Infrared Excited Gold Nanoshells. *Opt. Express* **2008**, *16*, 1590−1599.
(569) Adato, R.; Yanik, A. A.; Amsden, J. J.; Kaplan, D. L.; Omenetto, F. G.; Hong, M. K.; Erramilli, S.; Altug, H. Ultra-Sensitive Vibrational Spectroscopy of Protein Monolayers with Plasmonic Nanoantenna Arrays. *Proc. Natl. Acad. Sci. U. S. A.* **2009**, *106*, 19227−19232.
(570) Li, W.; Chen, X. Gold Nanoparticles for Photoacoustic Imaging. *Nanomedicine* **2015**, *10* (2), 299−320.
(571) Nie, L.; Chen, X. Structural and Functional Photoacoustic Molecular Tomography Aided by Emerging Contrast Agents. *Chem. Soc. Rev.* **2014**, *43*, 7132−7170.
(572) Pan, D.; Kim, B.; Wang, L. V.; Lanza, G. M. A Brief Account of Nanoparticle Contrast Agents for Photoacoustic Imaging. *Wiley Interdiscip. Rev. Nanomed. Nanobiotechnol.* **2013**, *5*, 517−543.
(573) Zha, Z.; Zhang, S.; Deng, Z.; Li, Y.; Li, C.; Dai, Z. Enzyme-Responsive Copper Sulphide Nanoparticles for Combined Photoacoustic Imaging, Tumor-Selective Chemotherapy and Photothermal Therapy. *Chem. Commun.* **2013**, *49*, 3455−3457.
(574) Yang, W.; Guo, W.; Le, W.; Lv, G.; Zhang, F.; Shi, L.; Wang, X.; Wang, J.; Wang, S.; Chang, J.; et al. Albumin-Bioinspired Gd:CuS Nanotheranostic Agent for In Vivo Photoacoustic/Magnetic Resonance Imaging-Guided Tumor-Targeted Photothermal Therapy. *ACS Nano* **2016**, *10*, 10245−10257.
(575) Jiang, W.; Kim, B. Y. S.; Rutka, J. T.; Chan, W. C. W. Nanoparticle-Mediated Cellular Response Is Size-Dependent. *Nat. Nanotechnol.* **2008**, *3*, 145−150.
(576) Song, G.; Shen, J.; Jiang, F.; Hu, R.; Li, W.; An, L.; Zou, R.; Chen, Z.; Qin, Z.; Hu, J. Hydrophilic Molybdenum Oxide Nanomaterials with Controlled Morphology and Strong Plasmonic Absorption for Photothermal Ablation of Cancer Cells. *ACS Appl. Mater. Interfaces* **2014**, *6*, 3915−3922.
(577) Zhou, Z.; Kong, B.; Yu, C.; Shi, X.; Wang, M.; Liu, W.; Sun, Y.; Zhang, Y.; Yang, H.; Yang, S. Tungsten Oxide Nanorods: An Efficient Nanoplatform for Tumor CT Imaging and Photothermal Therapy. *Sci. Rep.* **2015**, *4*, 3653.
(578) Choi, H. S.; Liu, W.; Misra, P.; Tanaka, E.; Zimmer, J. P.; Itty Ipe, B.; Bawendi, M. G.; Frangioni, J. V. Renal Clearance of Quantum Dots. *Nat. Biotechnol.* **2007**, *25*, 1165−1170.
(579) Cui, J.; Xu, S.; Guo, C.; Jiang, R.; James, T. D.; Wang, L. Highly Efficient Photothermal Semiconductor Nanocomposites for Photothermal Imaging of Latent Fingerprints. *Anal. Chem.* **2015**, *87*, 11592−11598.
(580) Zhang, S.; Sun, C.; Zeng, J.; Sun, Q.; Wang, G.; Wang, Y.; Wu, Y.; Dou, S.; Gao, M.; Li, Z. Ambient Aqueous Synthesis of Ultrasmall PEGylated $Cu_{2-x}Se$ Nanoparticles as a Multifunctional Theranostic Agent for Multimodal Imaging Guided Photothermal Therapy of Cancer. *Adv. Mater.* **2016**, *28*, 8927−8936.
(581) Yang, G.; Lv, R.; He, F.; Qu, F.; Gai, S.; Du, S.; Wei, Z.; Yang, P. A Core/Shell/Satellite Anticancer Platform for 808 NIR Light-Driven Multimodal Imaging and Combined Chemo-/Photothermal Therapy. *Nanoscale* **2015**, *7*, 13747−13758.
(582) Sun, C.; Liu, M.; Zou, Y.; Wei, J.; Jiang, J. Synthesis of Plasmonic Au−CuS Hybrid Nanocrystals for Photothermal Transduction and Chemical Transformations. *RSC Adv.* **2016**, *6*, 26374−26379.
(583) Robinson, J. T.; Welsher, K.; Tabakman, S. M.; Sherlock, S. P.; Wang, H.; Luong, R.; Dai, H. High Performance in Vivo Near-IR (>1 μm) Imaging and Photothermal Cancer Therapy with Carbon Nanotubes. *Nano Res.* **2010**, *3*, 779−793.
(584) Zhang, Y.; Wei, T.; Dong, W.; Huang, C.; Zhang, K.; Sun, Y.; Chen, X.; Dai, N. Near-Perfect Infrared Absorption from Dielectric Multilayer of Plasmonic Aluminum-Doped Zinc Oxide. *Appl. Phys. Lett.* **2013**, *102*, 213117.
(585) Boriskina, S. V.; Tong, J. K.; Huang, Y.; Zhou, J.; Chiloyan, V.; Chen, G. Enhancement and Tunability of Near-Field Radiative Heat Transfer Mediated by Surface Plasmon Polaritons in Thin Plasmonic Films. *Photonics* **2015**, *2*, 659−683.
(586) Bermel, P.; Boriskina, S. V.; Yu, Z.; Joulain, K. Control of Radiative Processes for Energy Conversion and Harvesting. *Opt. Express* **2015**, *23*, A1533.
(587) Wang, L. V.; Wu, H.-I. *Biomedical Optics*; John Wiley & Sons, Inc., 2009; pp i−xiv.
(588) Yan, C.; Tian, Q.; Yang, S. Recent Advances in the Rational Design of Copper Chalcogenide to Enhance the Photothermal Conversion Efficiency for the Photothermal Ablation of Cancer Cells. *RSC Adv.* **2017**, *7*, 37887−37897.
(589) Ding, X.; Liow, C. H.; Zhang, M.; Huang, R.; Li, C.; Shen, H.; Liu, M.; Zou, Y.; Gao, N.; Zhang, Z.; et al. Surface Plasmon Resonance Enhanced Light Absorption and Photothermal Therapy in the Second Near-Infrared Window. *J. Am. Chem. Soc.* **2014**, *136*, 15684−15693.
(590) Tsai, M.-F.; Chang, S.-H. G.; Cheng, F.-Y.; Shanmugam, V.; Cheng, Y.-S.; Su, C.-H.; Yeh, C.-S. Au Nanorod Design as Light-Absorber in the First and Second Biological Near-Infrared Windows for in Vivo Photothermal Therapy. *ACS Nano* **2013**, *7*, 5330−5342.
(591) Maestro, L. M.; Haro-González, P.; de Rosal, B.; Ramiro, J.; Caamaño, A. J.; Carrasco, E.; Juarranz, A.; Sanz-Rodríguez, F.; Solé, J. G.; Jaque, D. Heating Efficiency of Multi-Walled Carbon Nanotubes in the First and Second Biological Windows. *Nanoscale* **2013**, *5*, 7882−7889.
(592) Zhu, H.; Wang, Y.; Chen, C.; Ma, M.; Zeng, J.; Li, S.; Xia, Y.; Gao, M. Monodisperse Dual Plasmonic Au@Cu_{2-x}E (E= S, Se) Core@Shell Supraparticles: Aqueous Fabrication, Multimodal Imaging, and Tumor Therapy at in Vivo Level. *ACS Nano* **2017**, *11*, 8273−8281.
(593) Wang, S.; Riedinger, A.; Li, H.; Fu, C.; Liu, H.; Li, L.; Liu, T.; Tan, L.; Barthel, M. J.; Pugliese, G.; et al. Plasmonic Copper Sulfide Nanocrystals Exhibiting Near-Infrared Photothermal and Photodynamic Therapeutic Effects. *ACS Nano* **2015**, *9*, 1788−1800.
(594) Wen, L.; Chen, L.; Zheng, S.; Zeng, J.; Duan, G.; Wang, Y.; Wang, G.; Chai, Z.; Li, Z.; Gao, M. Ultrasmall Biocompatible WO_{3-x} Nanodots for Multi-Modality Imaging and Combined Therapy of Cancers. *Adv. Mater.* **2016**, *28*, 5072−5079.
(595) Zhou, M.; Tian, M.; Li, C. Copper-Based Nanomaterials for Cancer Imaging and Therapy. *Bioconjugate Chem.* **2016**, *27*, 1188−1199.
(596) Ku, G.; Zhou, M.; Song, S.; Huang, Q.; Hazle, J.; Li, C. Copper Sulfide Nanoparticles As a New Class of Photoacoustic Contrast Agent for Deep Tissue Imaging at 1064 Nm. *ACS Nano* **2012**, *6*, 7489−7496.
(597) Ding, K.; Zeng, J.; Jing, L.; Qiao, R.; Liu, C.; Jiao, M.; Li, Z.; Gao, M. Aqueous Synthesis of PEGylated Copper Sulfide Nanoparticles for Photoacoustic Imaging of Tumors. *Nanoscale* **2015**, *7*, 11075−11081.
(598) Liu, J.; Han, J.; Kang, Z.; Golamaully, R.; Xu, N.; Li, H.; Han, X. In Vivo Near-Infrared Photothermal Therapy and Computed Tomography Imaging of Cancer Cells Using Novel Tungsten-Based Theranostic Probe. *Nanoscale* **2014**, *6*, 5770−5776.
(599) Li, B.; Wang, X.; Wu, X.; He, G.; Xu, R.; Lu, X.; Wang, F. R.; Parkin, I. P. Phase and Morphological Control of MoO_{3-x} Nanostructures for Efficient Cancer Theragnosis Therapy. *Nanoscale* **2017**, *9*, 11012−11016.
(600) Cheng, L.; Wang, C.; Feng, L.; Yang, K.; Liu, Z. Functional Nanomaterials for Phototherapies of Cancer. *Chem. Rev.* **2014**, *114*, 10869−10939.
(601) Goel, S.; Chen, F.; Cai, W. Synthesis and Biomedical Applications of Copper Sulfide Nanoparticles: From Sensors to Theranostics. *Small* **2014**, *10*, 631−645.
(602) Chang, J.-Y.; Basu, S.; Wang, L. Indium Tin Oxide Nanowires as Hyperbolic Metamaterials for Near-Field Radiative Heat Transfer. *J. Appl. Phys.* **2015**, *117*, 054309.

DOI: 10.1021/acs.chemrev.7b00613
Chem. Rev. 2018, 118, 3121−3207

(603) Clavero, C. Plasmon-Induced Hot-Electron Generation at Nanoparticle/Metal-Oxide Interfaces for Photovoltaic and Photocatalytic Devices. *Nat. Photonics* **2014**, *8*, 95−103.
(604) Xie, W.; Schlücker, S. Hot Electron-Induced Reduction of Small Molecules on Photorecycling Metal Surfaces. *Nat. Commun.* **2015**, *6*, 7570.
(605) Mukherjee, S.; Libisch, F.; Large, N.; Neumann, O.; Brown, L. V.; Cheng, J.; Lassiter, J. B.; Carter, E. A.; Nordlander, P.; Halas, N. J. Hot Electrons Do the Impossible: Plasmon-Induced Dissociation of H_2 on Au. *Nano Lett.* **2013**, *13*, 240−247.
(606) Lee, H. W.; Papadakis, G.; Burgos, S. P.; Chander, K.; Kriesch, A.; Pala, R.; Peschel, U.; Atwater, H. A. Nanoscale Conducting Oxide PlasMOStor. *Nano Lett.* **2014**, *14*, 6463−6468.
(607) Park, J.; Kang, J.-H.; Liu, X.; Brongersma, M. L. Electrically Tunable Epsilon-Near-Zero (ENZ) Metafilm Absorbers. *Sci. Rep.* **2015**, *5*, 15754.
(608) Runnerstrom, E. L.; Kelley, K. P.; Sachet, E.; Shelton, C. T.; Maria, J.-P. Epsilon-near-Zero Modes and Surface Plasmon Resonance in Fluorine-Doped Cadmium Oxide Thin Films. *ACS Photonics* **2017**, *4*, 1885−1892.
(609) Campione, S.; Wendt, J. R.; Keeler, G. A.; Luk, T. S. Near-Infrared Strong Coupling between Metamaterials and Epsilon-near-Zero Modes in Degenerately Doped Semiconductor Nanolayers. *ACS Photonics* **2016**, *3*, 293−297.
(610) Campione, S.; Liu, S.; Benz, A.; Klem, J. F.; Sinclair, M. B.; Brener, I. Epsilon-Near-Zero Modes for Tailored Light-Matter Interaction. *Phys. Rev. Appl.* **2015**, *4*, 044011.
(611) Campione, S.; Brener, I.; Marquier, F. Theory of Epsilon-near-Zero Modes in Ultrathin Films. *Phys. Rev. B: Condens. Matter Mater. Phys.* **2015**, *91*, 121408.

DOI: 10.1021/acs.chemrev.7b00613
Chem. Rev. 2018, 118, 3121−3207